



A study of the large-scale structure of the universe with galaxy clusters: from Planck to Euclid

van Tuan Bui

► To cite this version:

van Tuan Bui. A study of the large-scale structure of the universe with galaxy clusters: from Planck to Euclid. Physics [physics]. Université Sorbonne Paris Cité, 2019. English. NNT : 2019USPCC022 . tel-02614091

HAL Id: tel-02614091

<https://theses.hal.science/tel-02614091>

Submitted on 20 May 2020

HAL is a multi-disciplinary open access archive for the deposit and dissemination of scientific research documents, whether they are published or not. The documents may come from teaching and research institutions in France or abroad, or from public or private research centers.

L'archive ouverte pluridisciplinaire **HAL**, est destinée au dépôt et à la diffusion de documents scientifiques de niveau recherche, publiés ou non, émanant des établissements d'enseignement et de recherche français ou étrangers, des laboratoires publics ou privés.

UNIVERSITÉ SORBONNE PARIS CITÉ



UNIVERSITÉ PARIS DIDEROT

École doctorale des Sciences de la Terre et de l'Environnement
et Physique de l'Univers, Paris

DOCTORAL THESIS

A study of the large-scale structure of the universe with galaxy clusters: from Planck to Euclid

BÙI Văn Tuấn

Thèse de doctorat de Physique de l'Univers
dirigée par M. Volker BECKMANN et M. Cyrille ROSSET

Soutenue publiquement le 21 juin 2019
devant un jury composé de :

- | | |
|---------------------------|--|
| <i>Président</i> | - Delphine HARDIN (Professeure - Sorbonne Université, LPNHE) |
| <i>Rapporteur</i> | - Réza ANSARI (Professeur - Université Paris-Sud, LAL) |
| <i>Rapporteur</i> | - Juan MACIAS-PEREZ (Directeur de recherche - CNRS, LPSC) |
| <i>Examineur</i> | - Jean-Baptiste MELIN (Chercheur - CEA, IRFU / DPhP) |
| <i>Directeur de thèse</i> | - Volker BECKMANN (Ingénieur de recherche - CNRS / IN2P3) |
| <i>Co-encadrant</i> | - Cyrille ROSSET (Chargé de recherche - CNRS, APC) |

“This work is dedicated to my family.”

BVT

UNIVERSITÉ PARIS DIDEROT

Abstract

UFR de Physique
AstroParticle and Cosmology Laboratory

Doctor of Philosophy

**A study of the large-scale structure of the universe with galaxy clusters:
from Planck to Euclid**

by BÙI Văn Tuấn

Studying the large-scale structure of the universe is one of the most important elements to understand the origin and evolution of the universe. Galaxy clusters which formed from gravitational collapses in the cosmic density field are the largest gravitationally bound structures. Using the two-point correlation we can quantify the clustering of galaxy clusters in both spatial and angular scales. Many galaxy surveys have been carried out for similar purpose.

The *Planck* Sunyaev-Zel'dovich (SZ) cluster catalog contains sources detected through the SZ effect from the 29 month full sky *Planck* mission. This is the largest SZ cluster catalog and it covers about 85% of the sky. In this thesis, we investigate the angular two-point correlation function $w(\theta)$ of the *Planck* SZ cluster catalog. We obtained an indication of clustering signal of *Planck* clusters with redshift smaller than 0.4 and signal-to-noise ratio $SNR \geq 6$. We detected a significant clustering signal of clusters with redshift $z < 0.2$ and $SNR \geq 6$. The correlation of *Planck* SZ clusters turns out quite compatible with our prediction.

We also explore the potential of the two-point correlation function $\xi(r)$ of the *Euclid* Flagship simulation dark matter halo catalog. *Euclid* is a space mission under development to study dark energy and dark matter by measuring the accelerated expansion of the universe. We found that the correlation of Flagship simulation dark matter halos evolves with redshift. On scales less than $60 h^{-1}$ Mpc, the correlation of dark matter halo is well fitted by a power law with a correlation length from 16 to $19 h^{-1}$ Mpc depending on the redshift. We also found the Baryonic Acoustic Oscillations (BAO) signature in the groups with redshift $z > 0.2$. Furthermore, we found the halo bias, which can be used as a tracer of dark matter and which also evolves with redshift.

Finally, we also show the results of the validation of external simulation data in the context of Science Challenge 3 of *Euclid* consortium. In this part, we present methods to measure the photometry, the astronomical tools to measure astrometry, extract objects from astronomical image.

Keywords: Cosmology, large-scale structure, galaxy clusters, Planck SZ cluster catalog, Baryonic Acoustic Oscillations, dark matter, dark energy, two-point correlation function.

Résumé

Étude de la structure à grande échelle de l'Univers avec des amas de galaxies: de Planck à Euclid.

par BÙI Văn Tuấn

L'étude de la structure à grande échelle de l'univers est l'un des éléments les plus importants pour comprendre l'origine et l'évolution de l'Univers. Les amas de galaxies qui se sont formés à partir d'effondrements gravitationnels dans le champ de densité cosmique sont les plus grandes structures gravitationnelles liées. En utilisant la corrélation à deux points, nous pouvons quantifier le regroupement des galaxies aux échelles spatiale et angulaire.

Le catalogue d'amas de la mission Planck contient des sources détectées par l'effet Sunyaev-Zel'dovich (SZ) pendant les 29 mois d'observation de la mission. C'est le plus grand catalogue d'amas SZ existant. Il couvre environ 85% du ciel. Dans cette thèse, nous étudions la fonction de corrélation angulaire à deux points $w(\theta)$ de ce catalogue. Nous avons obtenu une indication d'un signal de regroupement des amas de Planck avec décalage vers le rouge inférieur à 0,4 et un rapport signal sur bruit $SNR \geq 6$. Nous avons aussi détecté significatif pour un décalage vers le rouge $z < 0.2$ et $SNR \geq 6$. La corrélation des amas de Planck s'avère tout à fait compatible avec notre prédiction.

Nous explorons également le potentiel de la fonction de corrélation à deux points $\xi(r)$ du catalogue de halos de matière noire de la simulation Flagship Euclid. Euclid est une mission spatiale en cours de développement visant à étudier l'énergie noire et la matière noire en mesurant l'expansion accélérée de l'univers. Nous avons trouvé que la corrélation entre les halos de matière noire de la simulation Flagship évolue avec le décalage vers le rouge. Sur des échelles inférieures à $60 \text{ h}^{-1} \text{ Mpc}$, la corrélation du halo de matière noire est bien ajustée par une loi de puissance avec une longueur de corrélation entre 16 et $19 \text{ h}^{-1} \text{ Mpc}$ selon le décalage vers le rouge. Nous avons également mis en évidence la signature BAO (Baryonic Acoustic Oscillations) dans les groupes avec décalage vers le rouge $z > 0,2$.

Enfin, nous montrons également, dans le contexte du défi scientifique 3 du consortium Euclid, les résultats de la validation de données de simulations des données externes nécessaires à Euclid. Dans cette partie, nous présentons des méthodes pour mesurer la photométrie, des outils astronomiques pour mesurer l'astrométrie, extraire des objets d'une image astronomique.

Mots clefs: Cosmologie, structure à grande échelle, amas de galaxies, catalogue des amas de Planck SZ, oscillations acoustiques des baryons, matière noire, énergie noire, fonction de corrélation à deux points.

Acknowledgements

First of all, I would like to thank the jury members, and in particular Prof. Réza Ansari, and Dr. Juan Macias-Perez for reading my manuscript . . .

I would like to thank my Ph.D. advisors, Dr. Cyrille Rosset and Dr. Volker Beckmann for supporting me during these last three years. Cyrille is a patient advisor and he gave me a lot of advice and spent a lot of time to work with me on this thesis. He also encouraged me to learn French. Volker is an enthusiastic advisor and has worked out plans to help me achieve the results in this study. I was very impressed that he answered my emails very quickly regarding any of my questions about this research.

I sincerely thank Prof. Michel Cr     who also helped me a lot on this thesis. We have many discussion and he gave me much advice and reviews about the work on the two-point correlation function in Chapter 4.

I would like to thank Prof. James Bartlett (Jim). He is a very knowledgeable person in the field of galaxy clusters who also helped me a lot with discussions and suggestions on the two-point correlation function.

I would like to thank Dr. Jean-Baptiste Melin who provided the selection function of the *Planck* survey. He also gave many ideas and comments for the work reported in Chapter 4.

I am especially grateful to Dr. Yannick Giraud-H  raud who helped me with a lot of useful advice and feedback in my research, with his great humanity. He also helped me to improve my French language and understanding French culture. My special thanks go to Professor St  phane Jacquemoud for his optimism and encouragement, and who also gave me a lot of opportunities to discover French culture.

I would like to thank all members of the cosmology group at the Laboratory Astroparticle and Cosmology (APC). I really enjoyed the seminars of our cosmology journal club where I have learned a lot about cosmology from great scientists. My special thank goes to all the members of the *Euclid* group at APC, and especially to Dr. R  mi Fahed who helped me in the work of validation of the *Euclid* external simulation data.

I greatly appreciate the support from the *Euclid* France, the *Euclid* Consortium who gave me the opportunities to participate in great *Euclid* summer schools and conferences. These schools and conferences not only helped me to enhance my knowledge in cosmology but also to connect with new colleagues and international collaborations.

I would like to thank the University of Science and Technology of Hanoi (USTH), the Vietnam International Education Development (VIED) for providing me the fellowship to do this research. I would like to thank the Laboratory Astroparticle and Cosmology, the University Paris Diderot have facilitated me to work in a professional working environment and who provided part of the financial support for my thesis.

I want to thank all my labmates: Over the last three years I had the chance to discuss a lot of fun things about research, life, movies, and also to hang out with very friendly and helpful friends: Eleonora, Camille, Mikhail, Cyrille,

Pierros, Thường, Dũng, Alessandro, Ranajoy, Calum, Thomas, Louise, Bastien, Guillaume, Clara, Dominic, Hamza, and Jie. In particular, I had a lot of interesting discussions about my research related to the large-scale structure and galaxy clusters with Calum and Pierros who work also on the *Euclid* mission. Calum is a very funny Scottish friend and also helped me a lot to improve my English. Thường is my best friend that we often share and help each other in every aspect of life in Paris. I want to thank all my friends during the time we had together in Paris.

Finally, I would like to thank my Mum who always encourages me and supports me to follow my dreams without conditions.

Contents

Abstract	v
Acknowledgements	vii
Introduction	1
1 An overview of modern cosmology	3
1.1 A brief time-line of modern cosmological observation	3
1.2 The standard cosmological model	9
1.3 Cosmological probes	10
1.3.1 Cosmic microwave background	11
1.3.2 Galaxy clustering	12
1.3.3 Supernovae	16
1.3.4 Weak gravitational lensing	16
1.3.5 Galaxy clusters	18
2 Galaxy clusters as a cosmological probes	21
2.1 An overview of galaxy clusters	21
2.2 Methods of galaxy cluster detection	22
2.2.1 Optical surveys	22
2.2.2 X-ray telescopes	25
2.2.3 The SZ effect	28
2.3 Cosmology with galaxy clusters	32
2.3.1 Halo mass function	33
2.3.2 Cluster counts	35
2.3.3 Scaling relations	38
2.3.4 Clustering of clusters	42
3 ESA's Euclid and Planck mission	45
3.1 The Euclid mission	45
3.1.1 An overview	45
3.1.2 Scientific objectives	47
3.1.3 Satellite and scientific instruments	48
The VIS instrument	50
The NISP instrument	51
3.2 The <i>Planck</i> mission	54
3.2.1 Overview	54
3.2.2 Scientific objectives	54
3.2.3 Telescope and scientific instruments	55

3.3	<i>Planck</i> results	56
3.3.1	Maps and angular power spectra	57
3.3.2	Cosmological parameters	59
3.3.3	Cosmology from <i>Planck</i> galaxy clusters detected by SZ effect	61
4	Preparation of data processing for Euclid	63
4.1	Scientific context	63
4.2	CCD imaging in astronomy	65
4.3	Software and tools	68
4.4	Validation of Euclid external data simulations	69
4.4.1	Unit test	69
	Background test	70
	Stars	71
	Galaxies	76
	Conclusions	79
4.4.2	Validation of KiDS image simulation	80
	Overview of KiDS CCDs	80
	Input catalog	80
	Image validation	80
4.5	Conclusion	85
5	Studying the large-scale structure of the universe using galaxy clusters	87
5.1	The clustering correlation of existing cluster catalogs	88
5.2	The two-point correlation function	91
5.2.1	Estimators of the two-point correlation function	92
5.2.2	Error estimation of the two-point correlation function	93
5.2.3	The power law approximation of the two-point correlation function.	96
5.3	The angular two-point correlation function of the <i>Planck</i> SZ cluster catalog	98
5.3.1	<i>Planck</i> SZ cluster catalog	98
5.3.2	Random catalog	100
5.3.3	Results: Detection of clustering of <i>Planck</i> SZ cluster catalog	103
5.3.4	Redshift dependence	107
	Low redshift sample	107
	High redshift sample	109
	Null test	110
5.3.5	Conclusions	111
5.4	The two-point correlation function of the Euclid Flagship dark matter halo catalog	114
5.4.1	Euclid Flagship dark matter halo catalog	114
5.4.2	Data selection	115
5.4.3	Results	115
5.4.4	Fitting power law	118

5.4.5	Fitting BAO	118
5.4.6	Discussion on bias evolution	124
5.4.7	Conclusions	124
5.5	Conclusions	125
6	Conclusions and outlook	127
6.1	Conclusions	127
6.2	Outlook	128
A	The angular two-point correlation function of <i>Planck</i> SZ clusters and their coefficient correlation matrices	129
B	Coefficient matrix of the two-point correlation of <i>Euclid</i> dark matter halo catalog	133
	Bibliography	137

List of Figures

1.1	The plot of the velocity-distance relation for galaxies (nebulae) as presented by Hubble (1929)	4
1.2	CMB map as measured by <i>COBE</i> , <i>WMAP</i> and <i>Planck</i>	5
1.3	The diagram of distance as a function of red-shift for Type Ia Supernovae.	7
1.4	The distribution of galaxies from the Two-degree-Field Galaxy Redshift Survey (2dF)	7
1.5	Localization of gravitational-wave, gamma-ray, and optical signals for GW170817.	8
1.6	The measured angular power spectra of <i>Planck</i> , 9 year <i>WMAP</i> data, ACT, and SPT.	12
1.7	The BAO signal detected from the two-point correlation function of SDSS galaxies. Figure from Eisenstein et al. (2005). . . .	13
1.8	Distance measurements using BAO compared to the prediction given by the best-fit cosmological parameters of Planck as function of redshift	14
1.9	The redshift-space distortion as seen under the two-dimensional redshift space correlation function from 2dFGRS	15
1.10	The magnitude-redshift plot of Type Ia Supernovae with data points from the HZT and SCP collaborations	17
1.11	Illustration of a gravitational lensing system	18
2.1	The galaxy cluster Abell 1935 observed in the X-ray and optical domain, and through the SZ effect	22
2.2	Number of clusters at and above a given redshift expected to be detected by <i>Euclid</i>	26
2.3	Diagram of atmospheric absorption to various wavelengths of electromagnetic radiation	27
2.4	A Voronoi tessellation consists of cell polygons of a random field. Figure from Ebeling and Wiedenmann, 1993.	28
2.5	CMB intensity spectrum distorted by the SZ effect in comparison with the undistorted spectrum.	29
2.6	Galaxy cluster Abell 2319 as observed in seven different frequency channels with <i>Planck</i>	30
2.7	Mass of galaxy clusters detected through SZ effect by ACT, SPT, and <i>Planck</i> (PSZ1 and PSZ2) as a function of redshift.	31
2.8	The mass function of simulation dark matter halos. Also shown are predictions from the fitting halo mass function	35

2.9	Constraints from <i>Planck</i> SZ clusters: the contours at 95% for different signal-to-noise limits applied to the <i>Planck</i> 2015 SZ clusters	36
2.10	Tension between the determination of cosmological parameters based on the CMB and on clusters measurements. Figure from Douspis et al. (2019).	38
2.11	Constraints at the 68 per cent confidence level on the parameters Ω_m and σ_8 and on the parameters w_0 and w_a for the dark energy equation of state evolution	39
2.12	The scaling relation of cluster mass and temperature from two cluster samples at r_{500}	41
2.13	Comparison of halo bias $b(M)$ model with different observational data as the function of redshift	42
3.1	The regions of the sky that will be covered by <i>Euclid</i> shown in Mollweide projection in ecliptic coordinates	46
3.2	Overview of the <i>Euclid</i> PLM sub-systems	49
3.3	The normalized transmission curve of VIS and Y, J, H filters of <i>Euclid</i>	50
3.4	Overview of the subsystems composing the <i>Euclid</i> VIS instrument	51
3.5	An overview of the <i>Euclid</i> NISP instrument	52
3.6	Artist's impression of the <i>Planck</i> satellite	54
3.7	The <i>Planck</i> LFI instrument	56
3.8	The fluctuation of sky emission at nine frequency channels after removal of a common dipole component by <i>Planck</i> 2018	57
3.9	The sky polarization in seven frequency channels between 30 and 353 GHz of <i>Planck</i>	58
3.10	The 2018 <i>Planck</i> CMB map created by SMICA method	59
3.11	The 2018 <i>Planck</i> temperature power spectra (TT, TE, EE).	60
3.12	Marginalized joint 68% and 95% confidence level regions for spectral index n_s and tensor-to-scalar ratio r at $k = 0.002 \text{ Mpc}^{-1}$ from <i>Planck</i> alone and in combination with BK14 (BICEP2/Keck) or BK14 plus BAO data, compared to the theoretical predictions of selected inflationary models	62
4.1	Sky coverage area of <i>Euclid</i> and of some other surveys	64
4.2	One of the <i>Euclid</i> VIS CCDs that will be used on the science payload of ESA's <i>Euclid</i> mission	66
4.3	Unit test diagram	69
4.4	Distribution of flux in a simulated image containing only sky background flux.	71
4.5	Distribution of difference of the pixel position between the input and output objects. The center of distribution for both coordinates is 0 pixel. Only some matching objects have ΔX from 0.1 to 0.4 pixels.	72

4.6	Histogram of difference of the pixel position for each axis between the input and output objects.	73
4.7	Distribution of difference of the world coordinate position between the input and output objects.	73
4.8	Distribution of estimated sky background flux.	75
4.9	Distribution of estimated flux. The estimated flux is less than the expected flux by about 5%	76
4.10	Distribution of estimated flux by <i>Sextractor</i> . The estimated flux is less than the expected flux about 5.6%	77
4.11	The distribution of standard deviation of the shape of output objects.	78
4.12	Distribution of the standard deviation of the shape of galaxy output.	78
4.13	Distribution of difference of the world coordinate position between the galaxy-like input and output objects.	79
4.14	The arrangement of KiDS CCDs. Credit: M. J. Neeser.	80
4.15	Display of the first CCD of the KiDS simulation image.	81
4.16	Distribution of input and output objects in the KiDS simulation image. All input objects are selected within the footprint of the KiDS CCDs.	82
4.17	Magnitude distribution of input and output objects of KiDS simulation image	83
4.18	Positions of some matching objects on the first CCD of the simulation image	84
4.19	Position difference of matching objects on all CCDs of simulation image. While the position difference of matching objects in Y dimension is centered around 0 pixel, the difference in X dimension is shifted by about 1 pixel.	84
5.1	The distribution of galaxies from the SDSS survey	88
5.2	Comparison of the different estimators and their uncertainty of two-point correlation function of the simulated mock galaxy samples of the Sloan Digital Sky Survey	93
5.3	An example of the illustration of counting number of pairs of objects in small angular separation	94
5.4	The distribution of the 1,271 PSZ2 MMF3 sources and the <i>Planck</i> mask in Galactic coordinates	99
5.5	Redshift distribution of 443 Planck SZ clusters with $SNR \geq 6$ and redshift $z \leq 0.4$	100
5.6	Mass and redshift distribution of Planck SZ clusters	101
5.7	The hit map (total number of clusters in a pixel) distribution of the random clusters catalog.	101
5.8	A map of standard deviation of SZ flux Y_{500} in galactic coordinates of a <i>Planck</i> cluster.	102
5.9	Angular two-point correlation function of 442 clusters with redshift $z < 0.4$	103

5.10	Distribution of angular two-point correlation function of 10,000 bootstrap resamples of clusters with redshift $z < 0.4$ of the first 4 angular bins	104
5.11	The angular two-point correlation function estimated from <i>Planck</i> clusters with redshift $z < 0.4$	105
5.12	The prediction of the angular two-point correlation function of <i>Planck</i> clusters with redshift $z < 0.4$	106
5.13	The angular two-point correlation function measured from the <i>Planck</i> clusters with redshift $z < 0.4$ (same plot of Figure 5.11 in log scale), including the fit of the predicted angular correlation function of <i>Planck</i> clusters in this redshift range	106
5.14	The angular two-point correlation function of <i>Planck</i> clusters with redshift $z < 0.2$. The fitting lines are fitted excluding the first two angular bins	108
5.15	The angular two-point correlation function of <i>Planck</i> clusters with redshift $z < 0.2$ in log-log scale	108
5.16	Angular two-point correlation function of <i>Planck</i> clusters with redshift $0.2 \leq z < 0.4$. The fitting lines are derived excluding the first three angular bins.	109
5.17	The angular two-point correlation function of <i>Planck</i> clusters with redshift $0.2 \leq z < 0.4$ in log-log scale, showing the power law of the predicted angular correlation of <i>Planck</i> in the same redshift range	110
5.18	The mean and median of angular correlation function of 5000 mock cluster catalogs.	111
5.19	The angular correlation function of the first four angular bins of 5000 mock cluster catalogs.	112
5.20	The parameter fit a of the angular correlation function of 5000 mock cluster catalogs	112
5.21	Distribution of <i>Euclid</i> Flagship dark matter halos after applying the <i>Euclid</i> survey mask and star mask	115
5.22	Distribution of <i>Euclid</i> Flagship dark matter halos mass in redshift range [0-0.8].	116
5.23	The predicted correlation function of matter computed from the linear matter power spectrum at different redshifts	117
5.24	The correlation functions of <i>Euclid</i> flagship dark matter halos in different redshift groups.	118
5.25	The correlation of <i>Euclid</i> dark matter halos and the power law fitting lines over scales $R < 60 h^{-1} \text{ Mpc}$	119
5.26	The effect of varying the smooth parameter Σ_{nl} to the correlation function and the BAO signal.	121
5.27	The correlation function of <i>Euclid</i> flagship dark matter halos and the BAO fitting lines	122
5.28	The correlation function of <i>Euclid</i> flagship dark matter halos and the BAO fitting lines. In this case, the smooth parameter $\Sigma_{nl} = 10 h^{-1} \text{ Mpc}$	123

5.29 Halo bias as a function of redshift.	124
A.1 Coefficient correlation matrix of the angular two-point correlation function of <i>Planck</i> clusters with $z < 0.4$ and $SNR > 6$. .	129
A.2 Coefficient correlation matrix of the angular two-point correlation function of <i>Planck</i> clusters with $z < 0.2$ and $SNR > 6$. .	130
A.3 Coefficient correlation matrix of correlation function of <i>Planck</i> clusters with $0.2 < z < 0.4$ and $SNR > 6$	130
B.1 Coefficient correlation matrix of the two-point correlation function of <i>Euclid</i> dark matter halos $z < 0.2$	133
B.2 Coefficient correlation matrix of the two-point correlation function of <i>Euclid</i> dark matter halos with $0.2 < z < 0.4$	134
B.3 Coefficient correlation matrix of the two-point correlation function of <i>Euclid</i> dark matter halos with $0.4 < z < 0.6$	134
B.4 Coefficient correlation matrix of the two-point correlation function of <i>Euclid</i> dark matter halos with $0.6 < z < 0.8$	135

List of Tables

1.1	Results of parameter best fit, marginalized means and 68% errors for the Λ -CDM model from <i>Planck</i> TT,TE,EE+lowE+lensing (Planck Collaboration et al., 2018b)	11
3.1	Overview of <i>Euclid</i> surveys.	46
3.2	<i>Euclid</i> filter specifications.	48
3.3	Overview of the subsystems composing the <i>Euclid</i> VIS instrument	50
3.4	Description of <i>Euclid</i> NISP main elements.	53
3.5	Summary of <i>Planck</i> instrument characteristic	55
4.1	Overview of photometry bands and telescopes of <i>Euclid</i> and of some complementary surveys.	65
4.2	Simulation input catalog	81
5.1	The values of 14 angular distance bins, and the number of pairs of <i>Planck</i> clusters in each bin based on the selection of redshift.	102
5.2	Cosmological parameters used in the <i>Euclid</i> Flagship dark matter halo simulation.	114
5.3	Number of selected <i>Euclid</i> flagship dark matter halos in different redshift bins	116
5.4	The best fit results of the power law of the correlation function of <i>Euclid</i> dark matter halos over scales $R < 60 h^{-1}$ Mpc.	119
5.5	Values of χ^2 of the BAO fit when vary the value of the smooth parameter Σ_{nl} . The lowest χ^2 value in each redshift groups are bold.	123
A.1	Statistics of the angular two-point correlation function of <i>Planck</i> clusters in all 14 angular bins of different redshift groups from 10,000 bootstrap resamples.	131
B.1	The best fit parameters and their uncertainties of the BAO fit in different redshift groups.	133

List of Abbreviations

ACT	Atacama Cosmology Telescope
AGN	Active Galactic Nuclei
BAO	Baryonic Acoustic Oscillations
BCG	Brightest Cluster Galaxy
BOSS	SDSS' Baryon Oscillation Spectroscopic Survey
CFIS	Canadian France Hawaii Telescope
CMB	Cosmic Microwave Background
COBE	COsmic Background Explorer
DES	Dark Energy Survey
ESA	European Space Agency
FLRW	Friedmann-Lemaître-Robertson-Walker
ICM	Intra-Cluster Medium
JPAS	Javalambre Physics of the Accelerating Universe Astrophysical Survey
KiDS	Kilo-Degree Survey
LSST	Large Synoptic Survey Telescope
MCMC	Monte Carlo Markov Chain
NIR	Near Infrared
NISP	Near Infrared Spectrometer and Photometer
Pan-STARRS	Panoramic Survey Telescope and Rapid Response System
Rockstar	Robust Overdensity Calculation using K-Space Topologically Adaptive Refinement
RSD	Redshift Space Distortion
SDSS	Sloan Digital Sky Survey
SGS	Science Ground Segment
SPT	South Pole Telescope
SZ	Sunyaev–Zel'dovich
VIS	Visible instrument (<i>Euclid</i>)
VTP	Voronoi Tessellation and Percolation algorithms
WFIRST	Wide Field Infrared Survey Telescope
WMAP	Wilkinson Microwave Anisotropy Probe

Introduction

Studying the large-scale structure of the universe is one of the most important tools in cosmology to help us understand the content and evolution of the universe. Observations show that our universe is made of only 5% of ordinary (baryonic) matter, and that the main components are 27% of dark matter and 68% of dark energy. Baryonic matter is the known substance that makes up human, planets, stars, while dark matter and dark energy are still the two most puzzling components of the universe. Dark matter is responsible for the cosmic structure formation such as galaxies and galaxy clusters. Dark matter does not emit or absorb electromagnetic waves but exerts gravitational force. Dark energy is responsible for the accelerating expansion and the growth of structure of the universe. Observing the large-scale structure as a function of time is a powerful tool to study the distribution of dark matter and the nature of dark energy. The upcoming large-scale surveys such as the ones that are going to be performed by *Euclid*, by the Large Synoptic Survey Telescope (LSST), and by the Wide Field Infrared Survey Telescope (WFIRST) will investigate the nature of the dark universe. There are various ways to investigate the large-scale structure, such as weak gravitational lensing, Baryon Acoustic Oscillations (BAO), Redshift-Space Distortion (RSD) effects, and galaxy clustering. I will present an overview of these methods in this thesis.

In the paradigm of the evolution of the universe, galaxy clusters are among the largest structures of the universe. Many surveys have been conducted to study the clustering and distribution of galaxy clusters. In this thesis, I will address these important questions: How do these structures evolve? How can we quantify the clustering of these structures? I will present the findings about the clustering of galaxy clusters and the constraints of the cosmological parameters from previous observations and measurements. Then recent data from an all-sky space survey, from the *Planck* galaxy cluster catalog will be used to check the clustering of these sources and to compare with the prediction. In a second step, my work demonstrates the potential of the *Euclid* space mission which will be launched in 2022 by the European Space Agency (ESA). It is designed to map the geometry of the universe over the past 10 billion years and accurately measure the expansion of the universe.

This thesis is organized as follows:

In Chapter 1, I will give an overview of modern cosmology. I will start with a short time-line of the most important cosmological observations. Then I will introduce the fundamental principles and the parameters to describe the universe in cosmological terms in this chapter. Also the most powerful cosmological probes to derive cosmological parameters will be presented.

In Chapter 2, I will provide an overview about galaxy clusters, e.g. the physical properties, how we detect them. In addition, the methods, which use galaxy clusters as a tool to constrain cosmological parameters, will be summarized.

In Chapter 3, I will describe the two space missions *Euclid* and *Planck* that are most relevant for my thesis.

Euclid will measure the shape of galaxies with high precision using VIS broad band measurements and need the distance information (redshift) to map the three dimensional distribution of dark matter. It will derive the redshift information using its NIR band photometry and also complementary photometric data from ground-based surveys. The *Euclid* consortium is developing pipelines to process the future data of the satellite and also the external data provided by ground-based telescopes. In Chapter 4, I will show in detail the context and the results on the validation of *Euclid* external simulation data.

In Chapter 5, I will summarize the results of studying the large-scale structure of the universe using galaxy cluster catalogs from previous measurements. Then the two-point correlation function, which is a tool to quantify the clustering of galaxy clusters, will be discussed in detail. I will present our results of the angular two-point correlation function of the *Planck* cluster catalog. Finally, I will demonstrate the potential of the two-point correlation using the *Euclid* flagship simulation dark matter halo catalog.

The conclusions and outlook are presented in Chapter 6.

Chapter 1

An overview of modern cosmology

In this first chapter, I will start with presenting a short time-line of important recent discoveries in modern cosmology. I will then introduce briefly the standard model of modern cosmology, which we are using to describe the origin, the structure formation, and the evolution of the universe. Our understanding of the universe has been rapidly improving based on the results obtained with different cosmological probes. In this chapter I will also summarize the basics of these probes, and their application in cosmology.

1.1 A brief time-line of modern cosmological observation

Cosmology is the study of the origin, the structure, and evolution of the universe. Since ancient times, humans have looked at the night sky to find out where we are in the universe. But humans started to observe the universe with very simple tools - naked eyes - for a very long time of human history. In 1609, Galileo was the first person to use a telescope for astronomical purposes (Galilei, 1610). Over the last century more and more powerful, advanced and various types of telescopes and detectors have been developed that help us to explore the universe deeper and to achieve tremendous progress in the discovery and understanding of the universe.

Let us begin to explore some of these important results with the observation of galaxies by the American astronomer Edwin Powell Hubble in 1925. Hubble used the reflector telescopes of the Mount Wilson Observatory to study the distance of Cepheid variables (a type of star which periodically varies diameter and luminosity) of our Milky Way galaxy, and in the spiral nebulae Messier 31 (Andromeda galaxy) and M33 (Hubble, 1925). This was a confirmation of spectroscopic observations by Vesto Slipher of nebulae in the early 20th century that revealed that some of these show redshifted lines indicating they are moving relative to the Milky Way at velocities exceeding the escape velocity of our Galaxy (Slipher, 1913). Before this time, most astronomers assumed that M31 and M33 were spiral nebulae within our galaxy,

and that the Milky Way was the only galaxy in the universe¹. Hubble found that the Cepheids of these nebulae are far beyond the Milky Way. This means that M31 and M33 must reside outside of our galaxy. This discovery changed the scientific, and not only the scientific, view of our universe because the Milky Way turned out to be not the unique galaxy and that our universe is much much larger than assumed previously.

In 1927, the Belgian priest and astronomer Georges Lemaître was the first to predict the distance-redshift relation and the expansion of the universe (Lemaître, 1927). In 1929, Edwin Hubble then indeed discovered that many galaxies are moving away from us (Hubble, 1929). Figure 1.1 represents the velocity-distance relation of galaxies as observed by Hubble. He found that the redshift-distance to a galaxy is proportional to its recessional velocity:

$$v = H \times d \quad (1.1)$$

where H is Hubble's parameter in unit of $\text{km s}^{-1} \text{Mpc}^{-1}$. This is known as Hubble's law or as Hubble-Lemaître's law. Hubble estimated the value of H to be about $H = 500 \text{ km s}^{-1} \text{Mpc}^{-1}$. Although this result is far from the results of recent observations, which give a Hubble's parameter in the range from 67 to 72 $\text{km s}^{-1} \text{Mpc}^{-1}$, the finding that the universe is expanding was indeed very important.

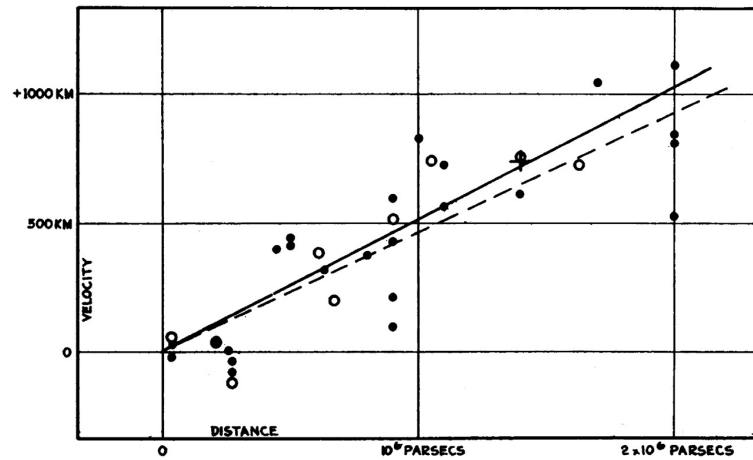


FIGURE 1.1: The plot of the velocity-distance relation for galaxies (nebulae) as presented by Hubble (1929). The black circles represent observed radial velocities of individual galaxies corrected for solar motion, and the black line shows the linear fit. The white circles are velocities of groups of galaxies, and the dashed line shows the fit to those. The black cross is the mean velocity corresponding to the mean distance of 22 galaxies.

In 1933, the Swiss astronomer Fritz Zwicky at the California Institute of Technology studied the redshift of galaxies (nebulae at that epoch) of the

¹although as early as in the 18th century the astronomer Thomas Wright speculated that some of the nebulae observed by then in the sky were actually not part of the Milky Way, but rather independent Milky Ways (Wright, 1750)

Coma cluster and used the virial theorem to infer the existence of dark matter (Zwicky, 1933). The virial theorem postulates that the average value of kinetic energy of the particle system moving in a confined space under the effect of gravitational forces is proportional to the half of the average of the gravitational potential energy. Using this theorem, Zwicky was able to measure the mass of the Coma Cluster from the velocity of galaxies. He noticed that the observed velocity dispersion along the line of sight of galaxies in the Coma cluster is much larger than the estimated average velocity. This means that the stars and gas within the galaxies could not have enough gravitational force to hold cluster together. He inferred that this gives rise to the surprising result that huge amount of dark matter should exist inside the galaxy cluster.

The cosmic microwave background (CMB) radiation is a uniform black body radiation coming from all directions of the sky. It was predicted in 1948 by Ralph Alpher and Robert Herman in the frame of the Big Bang model. In 1965, Arno Penzias and Robert Woodrow Wilson (Penzias and Wilson, 1965) discovered the CMB using a 6 meter horn antenna when they were actually trying to detect the radio waves (at a frequency of about 4 GHz) from the Echo balloon satellites. They measured a CMB temperature of about $T = 3.5$ K. Their discovery of the CMB was important evidence for a hot early universe (Big Bang theory). They were awarded the Nobel Prize in Physics in 1978 for this work.

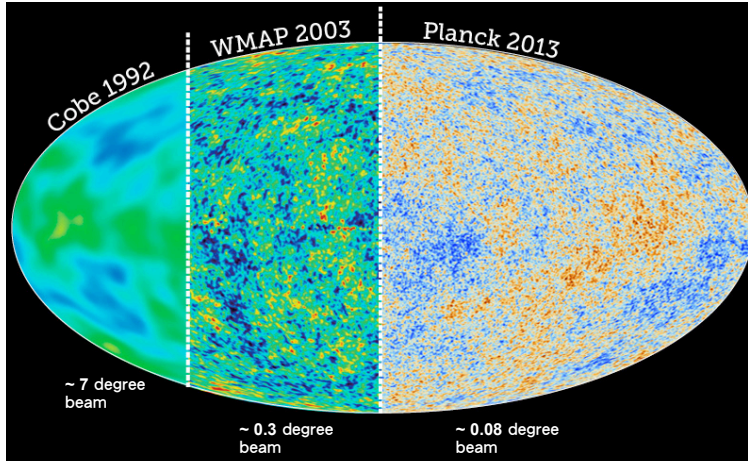


FIGURE 1.2: CMB map as measured by *COBE*, *WMAP* and *Planck* from left to right. The anisotropies of the CMB came into sharper focus when the angular resolutions and sensitivities of detectors were increased from *COBE* to *WMAP*, then *Planck*. Figure from Chluba (2018).

Afterwards, there were more precise measurements of the CMB radiation to help cosmologists understand better the initial conditions of the universe. The Cosmic Background Explorer (*COBE*) satellite was launched in 1989 by NASA to study the CMB of the universe across the sky. This mission has precisely measured CMB spectrum and its compatibility with a blackbody spectrum at $T = 2.725 \pm 0.001$ K (Fixsen and Mather, 2002). On the same

satellite, the Differential Microwave Radiometers (DMR) instrument detected for the first time the primary anisotropies of the CMB at the 7° scale (Smoot et al., 1992). These results confirmed the Big Bang theory of the origin of universe. In 2006, John Cromwell Mather and George Fitzgerald Smoot were awarded the Nobel prize in physics for these discoveries. The following space missions, such as the Wilkinson Microwave Anisotropy Probe (WMAP) by NASA (2001) and the *Planck* satellite by the European Space Agency (ESA) 2009 helped us to map in much more detail the CMB on the full sky, and also to determine with higher accuracy the age, energy, composition, and future of the universe. Figure 1.2 shows the remarkable improvement of CMB maps as measured by COBE, WMAP and *Planck* in terms of angular resolution and temperature sensibility.

In 1998, the *Supernova Cosmology Project* lead by Saul Perlmutter, and the *High-Z Supernova Search Team* lead by Adam Riess and Brian Schmidt discovered the accelerated expansion of the universe using distant supernovae as standard candles (Riess et al., 1998; Perlmutter et al., 1999). Standard candles are astronomical objects where the intrinsic luminosity (or absolute magnitude) of the object is known. By measuring how much light from these objects (apparent luminosity or magnitude) reaches us and by comparison with their absolute magnitude one can determine their distance. The discovery of the accelerated cosmic expansion provided first direct evidence for the existence of a non-zero cosmological constant or dark energy, which is responsible for the accelerated expansion of universe. Figure 1.3 shows the diagram of distance versus redshift of Type IA Supernovae obtained by these two projects. These observational data are consistent with the expected models (dotted lines) of a universe with matter and cosmological constant or dark energy. The leaders of the two groups were awarded the Nobel prize in Physics in 2011 for this discovery.

More and more galaxy surveys of higher resolution and higher sensitivity have been implemented to help us exploring further and to learn more about the detailed picture of the universe. One of the main goals of cosmology is to understand the origin and evolution of the large-scale structure of the universe. Galaxy clusters, filaments and voids are the largest structures of the universe. We need to understand how these structures evolved from the initial conditions, and how the initial spectrum of density fluctuations led to these structures. In order to answer to these questions we need large sky surveys to test the cosmological models.

The results from the *Two-degree-Field Galaxy Redshift Survey* (2dF²) and from the *Sloan Digital Sky Survey* (SDSS³) showed us clearly the picture of the large-scale structure. Figure 1.4 shows the galaxy distribution from the 2dF survey. The current surveys, such as the *Dark Energy Survey* (DES; The Dark Energy Survey Collaboration, 2005), the *Kilo-Degree Survey* (KiDS; de Jong et al., 2013), and the upcoming surveys like the one that will be performed by the *Large Synoptic Survey Telescope* (LSST; LSST Science Collaboration et al.,

²2dF survey: <http://www.2dfgrs.net/>

³SDSS survey: <https://www.sdss.org/>

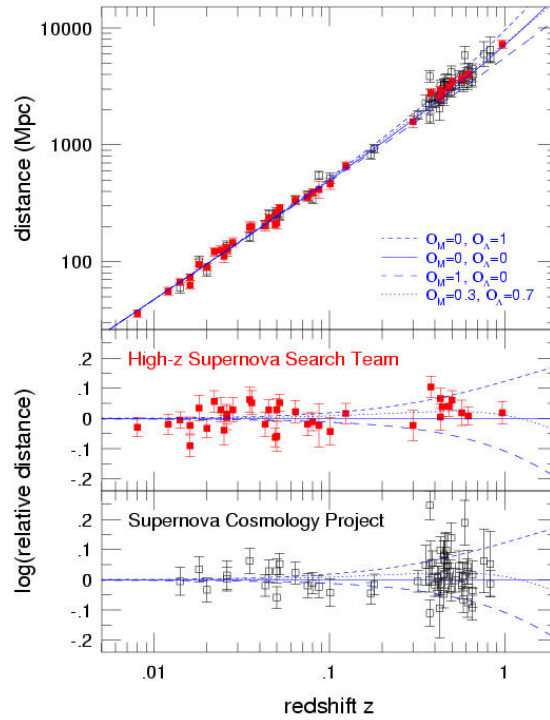


FIGURE 1.3: The diagram of distance as a function of redshift for Type Ia Supernovae. The observed Supernovae data from the Supernova Cosmology Project and the *High-Z Supernova Search Team* shown here are consistent with the expected model (dotted lines) for a universe with dark matter and cosmological constant ($\Omega_m = 0.3$, $\Omega_\Lambda = 0.7$). Credit: Leibundgut and Sollerman, 2002.

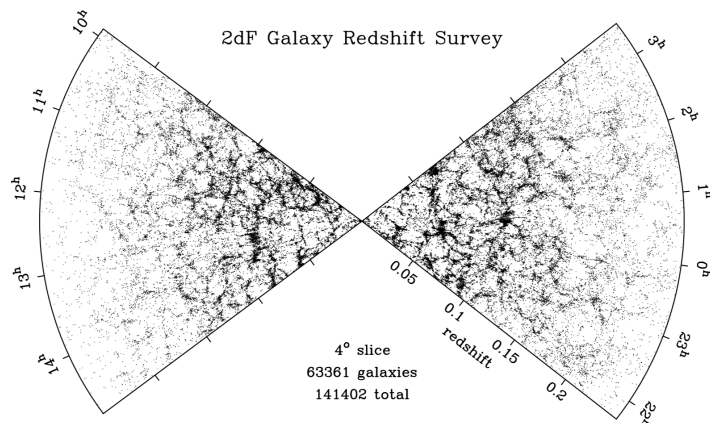


FIGURE 1.4: The distribution of galaxies from the Two-degree-Field Galaxy Redshift Survey (2dF). Credit: Peacock et al., 2001.

2009), ESA's *Euclid* mission (Laureijs et al., 2011), and by NASA's *Wide Field Infrared Survey Telescope* (WFIRST; Spergel et al., 2015) are needed to help us understand the most mysterious components of our universe: dark energy and dark matter.

On February 11, 2016, the LIGO Scientific Collaboration together with the Virgo Collaboration announced the first confirmed observation of gravitational waves from colliding black holes. These gravitational wave event called GW150914 was observed on September 14, 2015 by both LIGO observatories (Abbott et al., 2016). This confirmed the prediction of Einstein's theory of general relativity about the gravitational waves are the ripples in space-time which are created by violent events such as the collision of two black holes. On 17 August 2017, Advanced LIGO and Advanced Virgo detected gravitational waves from a binary neutron star merger for the very first time (Abbott et al., 2017b). About 1.7 seconds after the merger, a gamma-ray burst (GRB 170817A) was detected independently within a region of the sky consistent with the LIGO-Virgo-derived location of the gravitational-wave source by the Fermi Gamma-Ray Burst Monitor, and *INTEGRAL*. The event also was observed in the electromagnetic spectrum subsequently (Abbott et al., 2017c). The location of this event is shown in Figure 1.5.

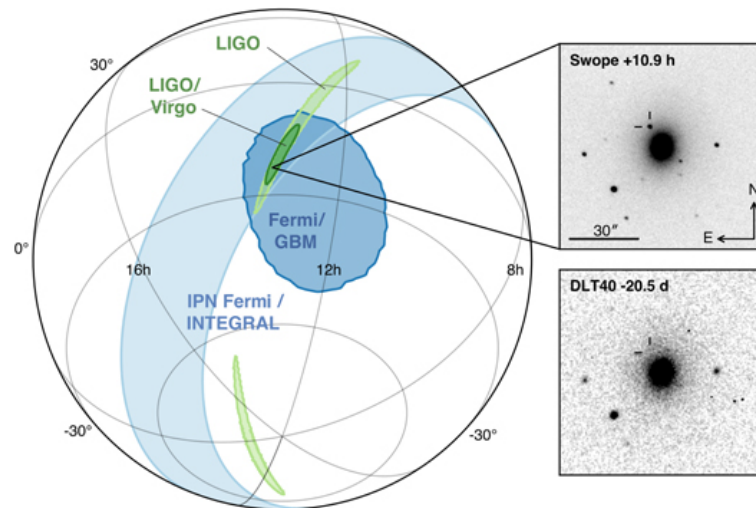


FIGURE 1.5: Localization of the gravitational-wave, gamma-ray, and optical signals for GW170817: from LIGO (light green), the initial LIGO-Virgo localization (dark green), IPN triangulation from the time delay between *Fermi* and *INTEGRAL*/ACS (light blue), and *Fermi*/GBM (dark blue). The inset shows the location of the apparent host galaxy NGC 4993 in the Swope optical discovery image at 10.9 hr after the merger (top right) and the DLT40 pre-discovery image from 20.5 days prior to the merger (bottom right). Credit: Abbott et al. (2017b).

The observations of this event marked the beginning of new era in multi-messenger, time-domain astronomy (Abbott et al., 2017c). Abbott et al. (2017a) used these multi-messenger observations of GW170817 as a standard siren to measure the Hubble parameter. They determined the Hubble constant

to be $H_0 = 70.0_{-8}^{+12.0} \text{ km s}^{-1} \text{ Mpc}^{-1}$, which is consistent with existing measurements from CMB data (Planck Collaboration et al., 2016b), and Cepheid variables (Riess et al., 2016).

1.2 The standard cosmological model

In 1915, Einstein published his paper “Die Feldgleichungen der Gravitation” (Einstein, 1915), which contains the Einstein field equations to describe how space time geometry is curved by mass and energy.

$$R_{\mu\nu} - \frac{1}{2}Rg_{\mu\nu} + \Lambda g_{\mu\nu} = \frac{8\pi G}{c^4}T_{\mu\nu} \quad (1.2)$$

where: $R_{\mu\nu}$ is the Ricci curvature tensor, R is the scalar curvature, $g_{\mu\nu}$ is the metric tensor, Λ is the cosmological constant, G is Newton’s gravitational constant, c is the speed of light in vacuum, and $T_{\mu\nu}$ is the stress–energy tensor.

The fundamental assumption of modern cosmology is that our universe is homogeneous and isotropic at large scales. Homogeneity means that the universe has the same properties on average at every point in space. Isotropy means that the universe is the same in all directions. The spacetime of such a universe can be described by the Friedmann-Lemaître-Robertson-Walker (FLRW) metric as in Equation 1.3:

$$ds^2 = c^2 dt^2 - a^2(t) \left[\frac{dr^2}{1 - kr^2} + r^2(d\theta^2 + \sin^2\theta d\phi^2) \right] \quad (1.3)$$

with the scale factor $a(t)$, which is the relative expansion of the universe at a given time t , the curvature of space k , radial distance r , polar angle θ , and azimuthal angle ϕ . The space curvature k might take a value of 1, -1 , or 0 respectively, which corresponds to a close (spherical), open (hyperbolic) or flat universe. The FLRW metric depends on the coordinates of the observer, which are called comoving coordinates (r, θ, ϕ) because they do not change under the expansion or contraction of the universe: the solid angle $d\Omega^2 = d\theta^2 + \sin^2\theta d\phi^2$.

Using the FLRW metric under the assumption of the cosmological principle, Friedmann (1922) obtained the equations for modeling the universe from Einstein’s field equations:

$$H = \frac{\dot{a}}{a} = \frac{8\pi G}{3}\rho(t) - \frac{kc^2}{a^2} + \frac{\Lambda c^2}{3} \quad (1.4)$$

and

$$\frac{\ddot{a}}{a} = -\frac{4\pi G}{3}\left(\rho(t) + \frac{3p}{c^2}\right) + \frac{\Lambda c^2}{3} \quad (1.5)$$

with H being the Hubble parameter, ρ is the mass density, and p is the pressure of cosmic fluids. For simplicity, the term c can be set to unity. The Hubble parameter (Equation 1.4 indicates the expansion rate of the universe,

and it is one of the most fundamental cosmological parameters. However, we are still aiming for a more accurate value. When we evaluate the Hubble parameter at present time t_0 , it can be written as H_0 , and it is often expressed in the form:

$$H_0 = 100 h \text{ km s}^{-1} \text{ Mpc}^{-1} \quad (1.6)$$

with h being a dimensionless parameter. The value of H_0 derived from the recent results concerning the CMB by the *Planck* collaboration is about $H_0 = 67.36 \pm 0.54 \text{ km s}^{-1} \text{ Mpc}^{-1}$ (Planck Collaboration et al., 2018b), while the value of H_0 as measured using Type Ia supernovae is about $H_0 = 73.24 \pm 1.74 \text{ km s}^{-1} \text{ Mpc}^{-1}$ (Riess et al., 2016). The discrepancy between these values of the Hubble parameter from independent measurements is a tension that still needs to be clarified.

For a flat universe with $k = 0$, one defines the critical density:

$$\rho_c = \frac{3H^2}{8\pi G} \quad (1.7)$$

and the relative cosmological densities:

$$\Omega_i = \frac{\rho_i}{\rho_c} = \frac{8\pi G \rho_i}{3H_0^2} \quad (1.8)$$

where i stands for different species that contribute to the universe, Ω_b is the baryon density, Ω_c is the cold dark matter density, Ω_r represents the radiation density (photons and relativistic neutrinos), and $\Omega_\Lambda = \Lambda c^2 / (3H_0^2)$ or Ω_{DE} for dark energy, except $\Omega_k = -k/H_0^2$.

Using the notation of density parameters, the first Friedmann Equation 1.4 can be written as:

$$H^2 = H_0^2 (\Omega_\Lambda + \Omega_k a^{-2} + \Omega_m a^{-3} + \Omega_r a^{-4}) \quad (1.9)$$

where $\Omega_m = \Omega_c + \Omega_b$ is the total matter density.

Recent results from *WMAP* (Hinshaw et al., 2013) and *Planck* (Planck Collaboration et al., 2018b) have shown that with only six parameters one can fit very well the $\Lambda - \text{CDM}$ model. Table 1.1 shows the results of best fit cosmological parameters for the $\Lambda - \text{CMD}$ model from the Planck Collaboration et al. (2018b).

1.3 Cosmological probes

One of the most important goals in cosmology is to determine precisely the cosmological parameters to derive the most accurate model of our universe. In recent years, many observational cosmological surveys have been built. In this section, I will summarize and describe shortly what are the most powerful cosmological probes that cosmologists are using today, and the main constraints on the cosmological models they got from them.

1.3. Cosmological probes

TABLE 1.1: Results of parameter best fit, marginalized means and 68% errors for the Λ -CDM model from *Planck* TT,TE,EE+lowE+lensing (Planck Collaboration et al., 2018b). The first six parameters are independent parameters, while the others are derived from these first six.

Parameter	TT+lowE 68% limits	TE+lowE 68% limits	EE+lowE 68% limits	TT,TE,EE_lowE 68% limits	TT,TE,EE+lowE+lensing 68% limits	TT,TE,EE+lowE+lensing+BAO 68% limits
$\Omega_b h^2$	0.02212 ± 0.00022	0.02249 ± 0.00025	0.0240 ± 0.00015	0.02236 ± 0.00015	0.02237 ± 0.00015	0.02242 ± 0.00014
$\Omega_c h^2$	0.1206 ± 0.0021	0.1177 ± 0.0020	0.1156 ± 0.0046	0.1200 ± 0.0014	0.1200 ± 0.0012	0.11933 ± 0.00091
$100 \theta_{MC}$	1.04077 ± 0.0047	1.04139 ± 0.00049	1.03999 ± 0.00089	1.04090 ± 0.00031	1.04092 ± 0.00031	1.04101 ± 0.00029
τ	0.0522 ± 0.0080	0.0496 ± 0.0085	0.0527 ± 0.0090	$0.0544^{+0.0070}_{-0.0081}$	0.0544 ± 0.0073	0.0561 ± 0.0071
$\ln(10^{10} A_s)$	3.040 ± 0.016	$3.018^{+0.020}_{-0.018}$	3.052 ± 0.022	3.045 ± 0.016	3.044 ± 0.014	3.047 ± 0.014
n_s	0.9626 ± 0.00957	0.967 ± 0.011	0.980 ± 0.015	0.9649 ± 0.0044	0.9649 ± 0.0042	0.9665 ± 0.0038
H_0 [km s ⁻¹ Mpc ⁻¹]	66.88 ± 0.92	68.44 ± 0.91	69.9 ± 2.7	67.27 ± 0.60	67.36 ± 0.54	67.66 ± 0.42
Ω_{Λ}	0.679 ± 0.013	0.699 ± 0.012	$0.711^{+0.033}_{-0.026}$	0.6834 ± 0.0084	0.6847 ± 0.0073	0.6889 ± 0.0056
Ω_m	0.321 ± 0.013	0.301 ± 0.012	$0.289^{+0.026}_{-0.033}$	0.3166 ± 0.0084	0.3153 ± 0.0073	0.3111 ± 0.0056
$\Omega_m h^2$	0.1434 ± 0.0020	0.1408 ± 0.0019	$0.1404^{+0.0034}_{-0.0039}$	0.1432 ± 0.0013	0.01430 ± 0.0011	0.14240 ± 0.00087
σ_8	0.8118 ± 0.0089	0.793 ± 0.011	0.796 ± 0.0018	$0.00730.8120 \pm$	0.811 ± 0.0060	0.8120 ± 0.0060

1.3.1 Cosmic microwave background

Our universe started about 14 billion years ago from a extremely hot and dense state. The universe started to expand exponentially during a very short period known as inflation which ended at $t \simeq 10^{-32}$ s. For a recent review on inflation, see e.g. Linde (2014) and Vázquez et al. (2018). At the beginning the universe was so hot that only plasma existed. Quantum fluctuation during this period were later imprinted on the universe as density fluctuation, which seeded the formation of large-scale structures that we can observe today.

During the era of recombination, which started about 200,000 years after the Big Bang, the free nuclei and electrons began to combine into atoms. About 380,000 years after the Big Bang, the universe had cooled down enough and the universe became transparent for the photons that now were able to travel freely in space. This could be called the first light of the universe, which is uniformly distributed over the entire sky we observe today, giving rise to the Cosmic Microwave Background (CMB).

The precise measurement of the CMB is very important in cosmology because it will affect the cosmological model which explain this radiation. The CMB has a thermal blackbody spectrum, which was predicted by Gamow (1948) and confirmed by Dicke et al. (1965). The spectral radiance of the CMB is expressed in Planck's law:

$$B_\nu(\nu, T) = \frac{2h\nu^3}{c^2} \frac{1}{e^{\frac{h\nu}{k_B T}} - 1} \quad (1.10)$$

where k_B is the Boltzmann constant, h is the Planck constant, and c is the speed of light in vacuum.

The CMB contains information about the conditions at the last scattering surface (primary anisotropies) but is also affected by the large scale structures of the universe. These cause several observable effects, such as gravitational redshift (Sachs–Wolfe effect; Sachs and Wolfe, 1967), gravitational lensing, and inverse Compton scattering on ionized gas (Sunyaev–Zel’dovich - SZ effect). Therefore the received light from the CMB probes density fluctuations

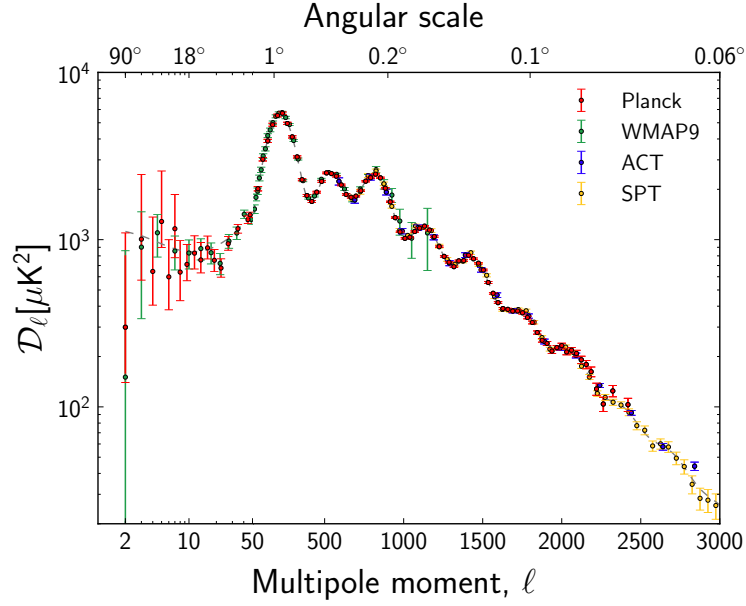


FIGURE 1.6: The measured angular power spectra of *Planck*, 9 year *WMAP* data, ACT, and SPT. The best-fit cosmological model provides an excellent fit to the spectra of these surveys. The horizontal axis is logarithmic up to $\ell = 50$, and linear beyond. Figure from *Planck* 2013 results. I.

at large-scale.

CMB observations help us to constrain the cosmological parameters. For example, measurements of temperature and polarization anisotropy of the CMB performed by the *WMAP* and *Planck* space missions have shown excellent agreement with the Λ -CDM cosmological model by constraining 6 cosmological parameters. Figure 1.6 presents the angular power spectra of the CMB based on different CMB surveys. All these measurements are in concordance with the cosmological model. The multiple peaks of the CMB temperature power spectrum can be interpreted as fluctuations in density and temperature in the early universe: the position of the peaks depends on the geometry of the universe and the height of the peaks depends on the density of the universe (Spergel, 2005).

1.3.2 Galaxy clustering

In the last decades there were many galaxy surveys to measure the large-scale structure of the universe, such as the 2dF Galaxy Redshift Survey⁴, SDSS⁵, and the Galaxy And Mass Assembly⁶ survey (GAMA). However, galaxies are considered as a bias tracer of matter density because of the structure we are observing with galaxies is just a small part of an underlying structure which

⁴2dF survey: <http://www.2dfgrs.net/>

⁵SDSS survey: <https://www.sdss.org/surveys/>

⁶GAMA survey: <http://www.gama-survey.org/>

is dominated by dark matter clustering (Kaiser, 1984). Therefore, it is very important to understand this bias in order to infer cosmological information.

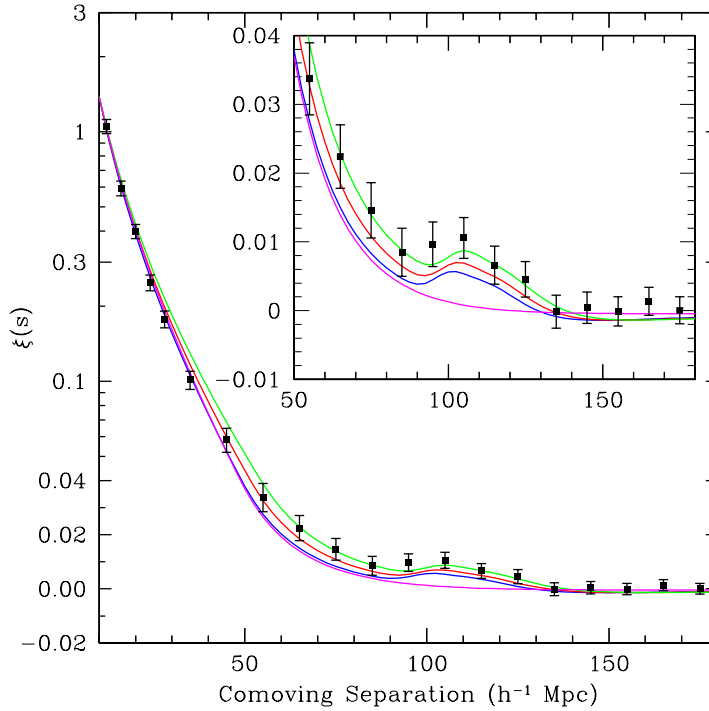


FIGURE 1.7: The BAO signal detected from the two-point correlation function of SDSS galaxies. Figure from Eisenstein et al. (2005).

In order to quantify the clustering one can use the two-point correlation function as a quantitative tool to trace the amplitude of clustering as a function of scale (angular or spatial distance): the angular two-point correlation function $w(\theta)$, and the spatial two-point correlation function $\xi(r)$. The Fourier transform of the two-point correlation function is the power spectrum, which is often used to present the density fluctuation of CMB or density field such as galaxies, galaxy clusters. I will present the two-point correlation function in more detail in Chapter 5.

A powerful tool related to galaxy clustering are the Baryonic Acoustic Oscillations (BAO) that are the typical acoustic peaks that appear in the two-point correlation function or in the power spectrum. The BAO are the acoustic waves propagating in the early universe due to the counteracting forces of the pressure created by the heat of matter radiation falling into the overdensity regions and the gravity. As galaxies formed in the matter overdensity regions, we can see this density fluctuation of the BAO signal imprinted on the large scale of the universe through the galaxy correlation function. This feature has been measured using 46,748 luminous red galaxies from the SDSS (Eisenstein et al., 2005). The estimated power spectrum of galaxies from the 2dF Galaxy Redshift Survey also showed an evidence of BAO (Cole et al., 2005). Since then the BAO were measured using quasars between redshift

$z = 0.8$ and $z = 2.2$ (Ata et al., 2018) and Ly- α forests (Bautista et al., 2017). The distance measurements using BAO normalized to the prediction using the *Planck* cosmological model are shown in Figure 1.8.

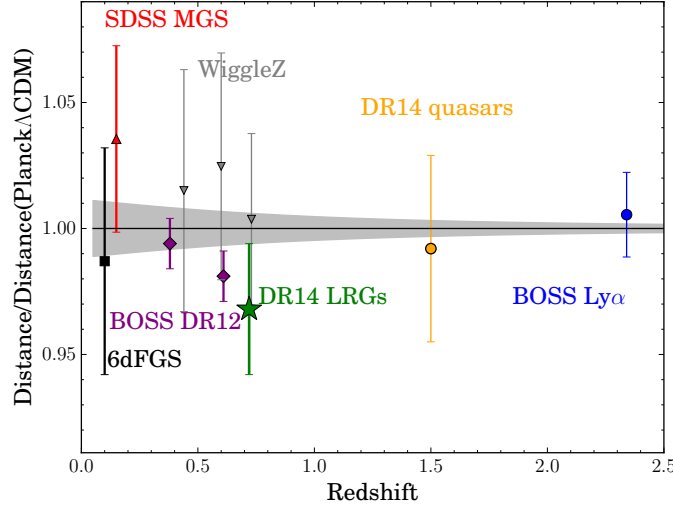


FIGURE 1.8: Distance measurements using BAO compared to the prediction given by the best-fit cosmological parameters of *Planck* (Planck Collaboration et al., 2016b) as function of redshift. The BAO measurements are: 6dFGRS at $z = 0.11$ (Beutler et al., 2011), SDSS MGC at $z = 0.15$ (Ross et al., 2015), BOSS DR12 at $z = [0.38, 0.61]$ (Alam et al., 2017), WiggleZ at $z = [0.44, 0.6, 0.73]$ (Blake et al., 2011), eBOSS DR14 QSO sample at $z = 1.52$ (Ata et al., 2018), and BOSS DR12 Lyman- α sample at $z = 2.3$ (Bautista et al., 2017; du Mas des Bourboux et al., 2017). Figure from Bautista et al. (2018).

Because of the typical features of the BAO imprinted on the distribution of galaxies, BAO can act as a "standard ruler" to measure the angular distance and the Hubble parameter directly. The acoustic length scale or sound horizon at the recombination is defined as the comoving distance of sound waves traveled from the Big Bang to recombination at redshift $z = z_*$ (Eisenstein and Hu, 1998a):

$$r_s = \int_0^{t_*} \frac{c_s(t)}{a(t)} dt = \int_{z_*}^{\infty} \frac{c_s(z)}{H(z)} dz \quad (1.11)$$

where t_* is the time at recombination, the sound speed: $c_s = 1/[3(1+R)^2]^2$ with R being the ratio of the baryon to the photon momentum density. The angular size of the sound horizon, which appears as the first acoustic peak in the CMB temperature power spectrum, can be defined as:

$$\theta_* = \frac{r_s}{D_A(z_*)} \quad (1.12)$$

The sound horizon has been well constrained by the Planck Collaboration et al. (2014a) with $\theta_s = 0.596724^\circ \pm 0.00038^\circ$ and $r_s = 147.9 \pm 0.59$ Mpc for a flat Λ CDM cosmological model.

Measurements of BAO at low and intermediate redshift combined with CMB measurements allow us to constrain models of dark energy with time-dependent equation of state (Said et al., 2013).

Through galaxy clustering we can measure:

- The Baryonic acoustic oscillations (BAO) as a standard ruler of the universe.
- Redshift-space distortion: powerful measurement of the growth rate of universe (Kaiser, 1987).

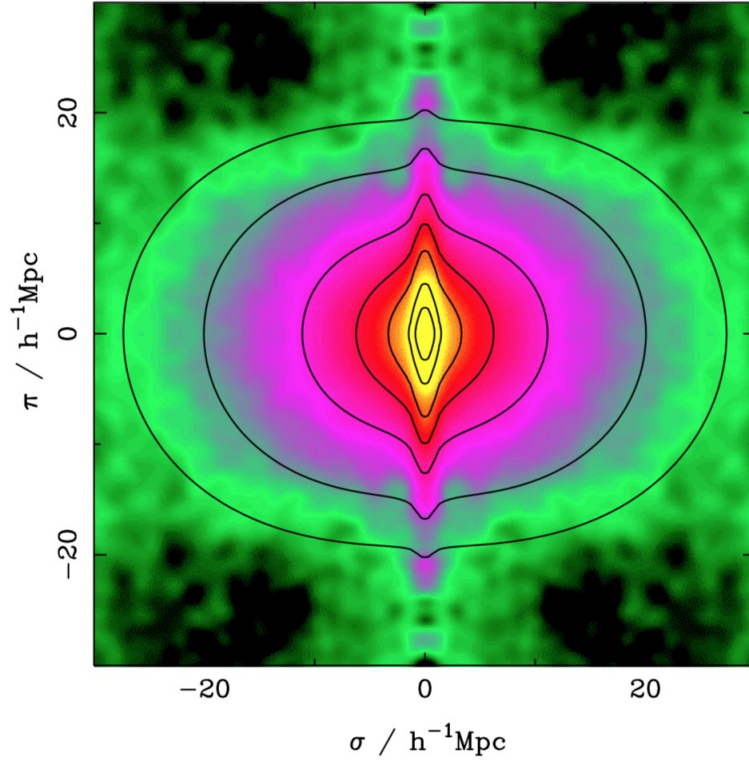


FIGURE 1.9: The redshift-space distortion as seen under the two-dimensional redshift space correlation function from 2dFGRS (Peacock et al., 2001).

On large scales ($> 1 \text{ Mpc h}^{-1}$) of the universe, the spatial distribution of galaxies as seen by an observer is distorted due to the peculiar velocity of galaxies in the flow of overdensities of gravity combined with the redshift of galaxies caused by the comical expansion. This is called redshift-space distortion. This effect can be clearly seen from galaxy clustering analysis in Peacock et al. (2001) and Reid et al. (2012). Figure 1.9 shows the two-dimensional clustering as a function of separation perpendicular to and along the line-of-sight of 2dFGRS galaxy clustering.

1.3.3 Supernovae

A supernova is the explosion at the end of life of certain types of massive stars. Supernovae Type Ia occur in a binary star system that contains a white dwarf star and a giant star or a smaller white dwarf star. A white dwarf star is a dense, carbon remain, which has approximately the size of the Sun. When the dwarf star pulls of matter from the companion star and its mass reaches about $1.4 M_{\odot}$, a nuclear chain reaction sets on, causing the dwarf star to explode. The typical characteristic of the spectrum of a supernovae type Ia is the absence of silicon absorption features at $\lambda = 6150 \text{ \AA}$ (Perlmutter and Schmidt, 2003). What is important with the type Ia supernovae is that they have constant or at least standardized intrinsic luminosity. They could be used as standard candles.

The brightness of a supernova can be as high as that of an entire galaxy for several weeks. By measuring the light intensity varying over time of supernovae, then converting to luminosity distance d_L , they can be used as standard candles.

$$d_L = \sqrt{\frac{L}{4\pi F}} \quad (1.13)$$

where L is the luminosity [erg s^{-1}], and F is the observed flux.

Using data of observations of 16 high-redshift supernovae in combination with a set of 34 nearby supernovae, Riess et al. (1998) discovered the accelerated expansion of the universe (see also Perlmutter et al., 1999). These observations were the first revolutionary evidence for the need for dark energy (or modification to the law of gravity).

1.3.4 Weak gravitational lensing

Gravitational lensing is the apparent distortion of images of distant galaxies or the distortion of the light path, which is caused by large gravitational potential wells such as stars, galaxies, and galaxy clusters in the line of sight. Figure 1.11 illustrates the gravitational lensing effect.

There are three different regimes of lensing: weak lensing, strong lensing, and microlensing. Depending on the position of the source, lens and observer; also the mass and shape of the lens might give us these different kinds of lensing. Strong lensing happens when the light of the source is distorted by very massive sources in the line of sight and produces multiples images, arcs, or even Einstein rings. In some cases the image of the source is not distorted in shape but appears brighter due to a small mass lens such as a star. In this case the effect is called microlensing. Most of the observed cases of lensing are weak lensing in which the lens is not strong enough to produce multiple images but the source will be magnified in size and brightness (convergence κ) and stretched tangentially around the lens (shear γ).

Weak gravitational lensing can be used to trace the large-scale structure of the universe by measuring galaxy shape correlations or similarly to measure

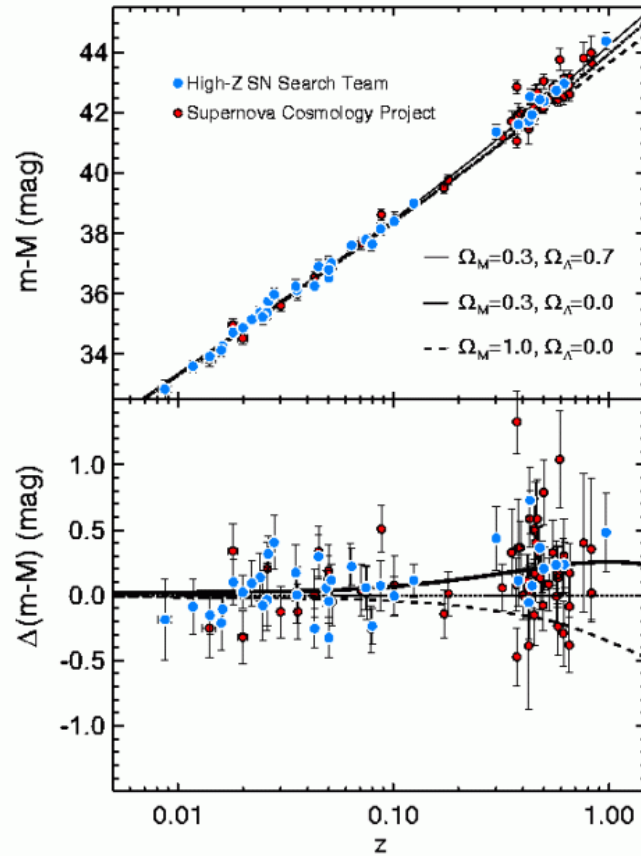


FIGURE 1.10: The magnitude-redshift plot of Type Ia Supernovae with data points from the HZT and SCP collaborations. Reproduced from Riess et al. (1998). Figure from: O’Raifeartaigh et al. (2018).

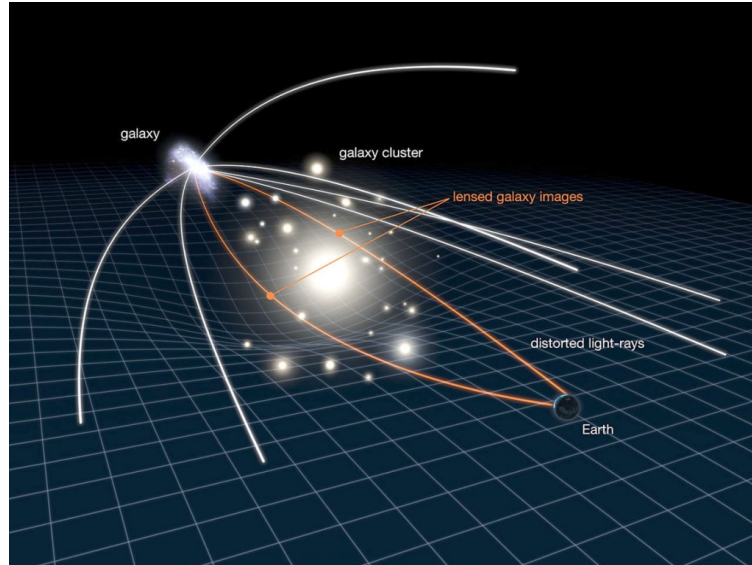


FIGURE 1.11: Illustration of a gravitational lensing system. The light from a distant galaxy that travels through a galaxy cluster will be distorted and this can create lensed galaxy images caused by the large gravitational potential well as seen from the Earth. Credit: NASA/ESA.

the matter power spectrum in the linear regime. The weak lensing by large-scale structure is called cosmic shear (Serjeant, 2010). The induced correlations between shapes of galaxies are directly related to the statistical properties of the total matter distribution. With an estimate of the redshift distribution of the lensed galaxies, theoretical predictions of weak lensing observables can be tested to obtain constraints on cosmological parameters and models (Kilbinger et al., 2013).

Weak gravitational lensing will be one of the two primary cosmological probes of the ESA M2 *Euclid* mission (see Chapter 3).

1.3.5 Galaxy clusters

Galaxy clusters are valuable cosmological probes because they are massive objects and can be detected by different methods: optical and X-ray observations, SZ effect, and gravitational lensing. These methods are described in Section 2.2.

Galaxy clusters were first used as cosmological probes with the discovery of dark matter by Fritz Zwicky in 1933. Since that time, galaxy clusters have been used as a powerful cosmological probe with different methods and aspects. One of the methods that has been used widely is the number density count. By counting the abundance of clusters with known mass and redshift in a given volume one is able to obtain cosmological constraints.

Galaxy clusters are the largest structures that collapsed on themselves by gravity. They can be used to trace the evolution of large-scale structures of the universe. They also provide information about nucleosynthesis in the

universe because they retain all the enriched material information. Moreover, the determination of the mass of galaxy clusters through the measurement of their X-ray emission and through gravitational lensing effects has provided us with strong evidence for dark matter. When combining results based on the SZ effect with observations of X-ray emission, with optical measurements and with gravitational lensing results of galaxy clusters we can determine main cosmological parameters. We can do cosmology with these statistics using galaxy clusters:

- Number counts, mass function to provide cosmological constraints.
- Scaling relation: for example SZ clusters - X-ray

I will present more details about this in Section [2.3](#).

Chapter 2

Galaxy clusters as a cosmological probes

Galaxy clusters are the largest gravitational bound objects in the universe. The study of galaxy clusters will help us to understand the standard model of cosmology, and especially dark matter and dark energy, the two main components we have only a limited understanding of. In this chapter I will introduce the study of galaxy clusters. Then I will present different methods which cosmologists are using to detect them. Finally I will describe how we can use galaxy clusters as a tool to constrain cosmological parameters.

2.1 An overview of galaxy clusters

Galaxies are not distributed randomly in space but bound together in clusters by gravity. Galaxy clusters consist of from hundreds to thousands of galaxies. The mass of galaxy cluster ranges from $10^{14} M_{\odot}$ to $10^{16} M_{\odot}$ (with M_{\odot} being the solar mass). The typical size of a galaxy cluster is from a few to hundreds Mpc. Unlike point source objects, galaxy clusters are observed with a large variety in shape and mass, so that it can be difficult to define their structures. Our galaxy, the Milky Way, is located in the Local Group with a diameter of 3.1 Mpc which contains about 54 galaxies (Karachentsev and Kashibadze, 2006). The Local Group belongs to a bigger cluster, the Virgo Cluster, which contains about 1300 - 2000 galaxies and which is classified as a rich cluster. The Laniakea Supercluster is a supercluster that is home to the Milky Way. It encompasses approximately 100,000 other nearby galaxies stretched out over 160 Mpc (Tully et al., 2014) with a total mass of about $10^{17} M_{\odot}$. It includes the Virgo cluster, the Norma, Hydra and Centaurus clusters, the Pavo-Indus filament and a number of voids.

Galaxy clusters comprise of 3 main components:

- Visible objects: galaxies which make up only about 1% of the total mass of a galaxy cluster.
- Hot gas makes up about 12% of the mass of a cluster, which can be observed in the X-ray domain.



FIGURE 2.1: From left to right: the galaxy cluster Abell 1935 ($z = 0.25$) observed in the X-ray and optical domain, and through the SZ effect. Image from Allen et al. (2011)

- Dark matter is the main component of a galaxy cluster. However it cannot be observed directly, because dark matter does not emit or absorb electromagnetic waves.

Because galaxy clusters are the largest gravitationally bound objects in the universe that formed from the density fluctuation, studying galaxy clusters is of great importance to cosmology.

2.2 Methods of galaxy cluster detection

Galaxy clusters can be observed not only with optical light but also in another wavebands. Primarily there are 4 main different methods to detect galaxy clusters:

- with optical telescopes,
- with X-rays satellite observations,
- using the SZ effect,
- through the gravitational lensing effect induced on background galaxy emission.

In Figure 2.1, I show as an example three different observations of the Abell 1935 galaxy cluster observed at different wavelengths. I will describe in the next sections these different approaches.

2.2.1 Optical surveys

The first method to detect galaxy clusters is to look for over density of galaxies in patches on the sky. The pioneer of this method was George Abell. He used the images taken with photographic plates obtained with the 48-inch Schmidt telescope of the Palomar Observatory from the National Geographic Society Palomar Observatory Sky Survey. He inspected visually the

plates and counted galaxies within certain region and between certain apparent magnitude to group in catalog of 2712 rich clusters of galaxies (Abell, 1958). This catalog was extended later to southern hemisphere (Abell et al., 1989a). Another larger galaxy cluster catalog using the photographic plates which was updated in many years is the Zwicky catalog (Zwicky et al., 1961–1968).

The more advanced method to detect galaxy clusters from imaging is automated detection developed by Shectman (1985), Dodd and MacGillivray (1986), Lumsden et al. (1992), and Dalton et al. (1997). However both methods have some limitations in magnitude depth, completeness not covering equally wide areas of the sky (Puddu et al., 2001). More accurate and deeper catalogs were created by using CCD (charge-coupled devices) imaging with photometry filters such as Postman et al. (1996), Olsen et al. (1999), Lobo et al. (2000), Goto et al. (2002), and Gladders and Yee (2005).

The algorithms to detect galaxy clusters in the optical band are evolving as the development of the detectors of optical telescope progress. With these methods a detected cluster can be defined as a contrast above the local background. I summarize some algorithms to detect galaxy clusters in the optical as described in Gal (2006).

1. Count in cells

This is a simple and the oldest technique to detect galaxy clusters. Most of the early catalogs using this method were detected by eye. We count the number of galaxies in a band of magnitude, within a fixed angular size or a physical distance and compare the result with the mean background. The cluster detected using this method can be defined with an eye contrast parameter σ_{cl} :

$$\sigma_{cl} = \frac{N_{\text{cluster}} - \bar{N}_{\text{field}}}{\sigma_{\text{field}}} \quad (2.1)$$

where N_{cluster} is the number of galaxies within an angular size θ , \bar{N}_{field} is the mean number of field galaxies within a disk of radius θ , and σ_{field} is the standard deviation of N_{cluster} . However this technique has some disadvantages. Because it strongly depends on the visual inspection of overdensities, it can induce some contamination. The count in cells at a given magnitude and redshift range make the limitation in the radius detection of clusters and assuming the same galaxy luminosity function of the same redshift is not correct. Overall, this technique is unsuitable for modern cosmological surveys.

2. Percolation Algorithm:

The percolation or the friends-of-friends (FOF) technique is a structure-finding algorithm. The original idea of this method was introduced by (Huchra and Geller, 1982). This technique is used to identify structure in galaxy distribution based on physical proximity. It looks for

galaxy pairs within a given cut-off separation. Many galaxy cluster catalogs have been created using this method such as Dalton et al., 1997, Berlind et al., 2006, Farrens et al., 2011. This method is widely used in N-body simulation to identify halo structures (Efsthathiou et al., 1985), (Knebe et al., 2011). Botzler et al. (2004) have developed an extended friends-of-friends algorithm that allows to deal with photometric redshift galaxy surveys. The FOF algorithm is often used in N-body simulations (Cole and Lacey, 1996) or in surveys which have spectroscopic redshift (Tucker et al., 2001; Ramella et al., 2002) because this method strongly depends on the precise distance information of objects.

3. The matched filter

The matched filter method was first introduced by (Postman et al., 1996) when the CCD imaging emerged. This method uses the positions and photometric information of galaxies to construct a matched filter from which a cluster likelihood map is generated to test how well galaxies in a given sky region match this model at various redshifts. It allows to optimally enhances the contrast of a cluster galaxy distribution with respect to the foreground and background galaxy distributions. The adaptive matched filter is another technique based on this method with the adoption of a full likelihood function and the incorporation of redshift information (Kepner et al., 1999). Kim et al. (2002) made a comparison of these two techniques and found that the matched filter is more efficient in detecting faint clusters while the adaptive matched filter evaluates the redshift and richness more accurately.

4. Red-sequence galaxy cluster finder

The *red-sequence galaxy cluster finder* was developed to identify a large sample of galaxy clusters over a wide range of redshifts in two-band optical/near-IR imaging data (Gladders and Yee, 2000). This method relies on the morphology of galaxies which evolves with redshift. The bulk of early-type cluster galaxies has a linear relation of color-magnitude and is referred as the red sequence. Therefore clusters are detected as overdensities in projected angular position, colour, and magnitude at the same time.

5. maxBCG

The maxBCG (Koester et al., 2007) method is a powerful cluster finder which was developed to detect galaxy clusters in the Sloan Digital Sky Survey (SDSS; York et al., 2000). In fact, maxBCG is a based red-sequence galaxy cluster finder of bright massive clusters using multi-band CCD imaging data. The advantage of this method is that it is able to exploit 3 main features of galaxy clusters: the spatial clustering, the most luminous cluster galaxy in a tight sequence in colour-magnitude E/S0 (E - elliptic and S - spiral are two types of galaxy) ridge-line (Bower et al., 1992), and existing a unique brightest galaxy which gives the center positions and redshift of cluster.

The individual objects in the photometric catalog are assessed by a likelihood of redshift-dependent in order to find the cluster members and the brightest cluster galaxy (BCG): Each object is tested by an array of redshift for the likelihood function. Redshift is assigned to each galaxy when it maximizes the likelihood. Objects are ranked by this maximum likelihood. The object with the highest likelihood defines the center of the cluster. During the process, the galaxies within $1h^{-1}$ Mpc, within $\pm 2\sigma$ of the E/S0 ridgeline, and brighter than some minimum luminosity L_{\min} regardless of redshift are kept and used for the richness estimation. L_{\min} is measured to be the lowest value for each cluster which satisfies the condition that the estimation of galaxy colors(g-r and r-i) are within 3σ of the predicted colors.

The *Euclid* space mission will have the possibility to detect galaxy clusters using 3 different probes: photometric data, spectroscopic data, and through gravitational lensing. The maxBCG or Red-Sequence approaches could be some efficient methods to detect galaxy cluster with *Euclid*. Figure 2.2 shows the distribution of number of clusters $N_{500,c}$ within radius $r_{500,c}$ versus redshifts which is expected to be detected at given redshift using photometric data (Sartoris et al., 2016). The radius r_{500} is defined as the radius of a sphere that encloses an average mass density 500 times the critical density of the universe at the cluster redshift. *Euclid* is expected to detect about 100,000 galaxy clusters up to redshift $z = 2$ with the photometric surveys Laureijs et al. (2011).

Besides the above methods, there are many others to detect galaxy clusters in optical surveys such as: the adaptive kernel, surface brightness enhancements, cut-and-enhance. None of them are perfect, but they were designed to adapt with the evolution of optical surveys. Along the optical surveys we also have been developing the algorithms to detect distant galaxy clusters in X-Ray imaging, and radio observations of the SZ effect.

2.2.2 X-ray telescopes

Most of the baryons in clusters are present in the form of hot gas. The temperature of hot gas between the Intra-Cluster Medium reaches around several 10^7 K for a typical cluster mass of $M = 10^{14} M_{\odot}$ to $M = 10^{15} M_{\odot}$ (Rosati et al., 2002). Due to the high temperature the gas is fully ionized, and therefore emits in the X-ray wavelengths via thermal bremsstrahlung. The emissivity (the energy released per unit time, frequency and volume) at frequency ν and temperature T_x is given by (Borgani and Guzzo, 2001):

$$\epsilon(\nu) = n_e \times n_i \times \sqrt{T_x} \exp \frac{-h\nu}{k_B T_x} \quad (2.2)$$

where n_e, n_i is the number density of electrons and ions, T_x is the temperature of gas, k_B is the Boltzmann's constant, and h is the Planck constant.

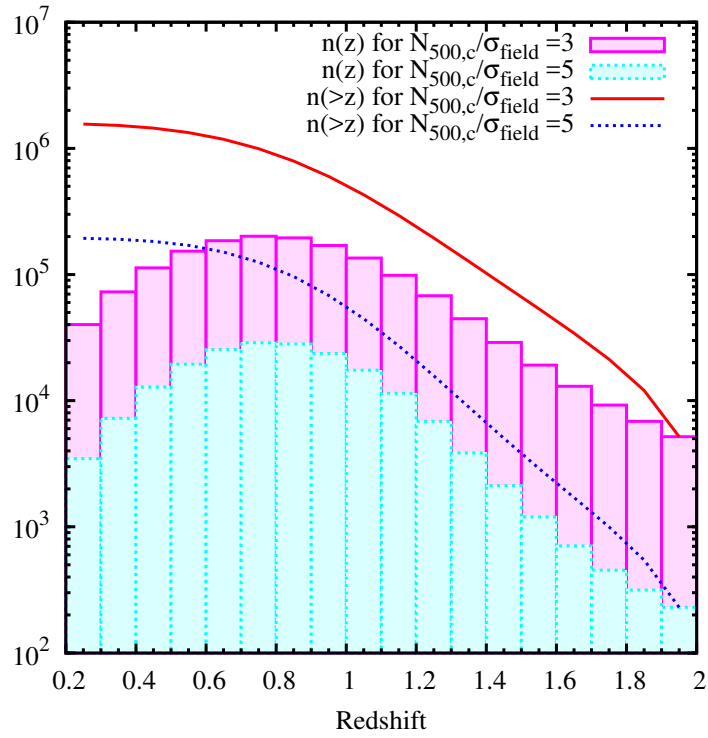


FIGURE 2.2: Number of clusters at and above a given redshift expected to be detected by *Euclid* with overdensities $N_{500,c}/\sigma_{field} > 5$ and > 3 in the *Euclid* photometric survey (dotted blue and solid red lines, respectively), where σ_{field} is the root mean square of the field counts within the same radius $r_{500,c}$. Figure from (Sartoris et al., 2016).

2.2. Methods of galaxy cluster detection

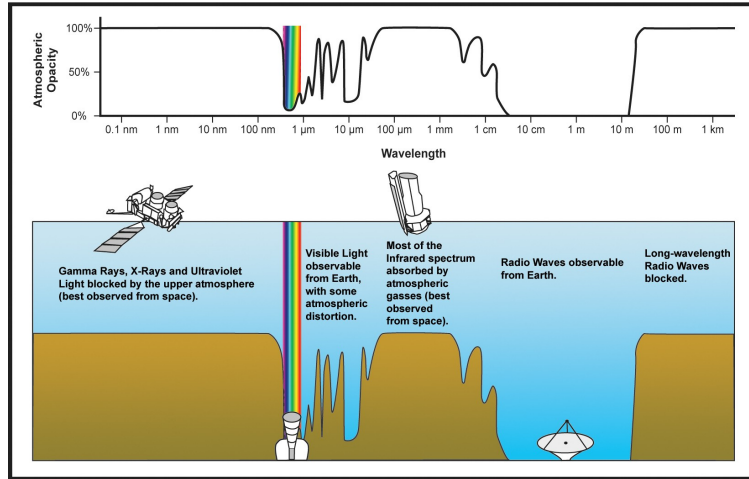


FIGURE 2.3: Diagram of atmospheric absorption to various wavelengths of electromagnetic radiation. X-rays are blocked by the Earth's atmosphere. Credit: NASA/Wikipedia.

X-rays have wavelengths from 0.01 to 10 nanometers, equivalent to photon energies of 100 eV to 100 keV. X-ray radiation from space is blocked by the upper atmosphere of the Earth. Therefore, all X-ray telescopes have to be embedded on satellites orbiting above the Earth's atmosphere. Figure 2.3 illustrates the Earth's atmospheric transmittance to various wavelengths of electromagnetic radiation.

The first X-ray measurements of AGN¹ were made with detectors onboard an Aerobee rocket in April 1965, which provided evidence for high-energy emission from Cygnus A and M87 (Byram et al., 1966). The first all-sky survey in the X-ray domain by the *Uhuru* satellite experiment found galaxy clusters to be bright extended sources in the X-rays (Giacconi et al., 1972). With time, more and more galaxy clusters were detected with more accurate properties and redshift information by projects such as: *Einstein*, *Chandra*, *XMM-Newton*, REFLEX Cluster Survey (Böhringer et al., 2004), ROSAT All-Sky Survey (RASS; Voges et al., 1999), Meta-Catalogue X-ray galaxy Clusters (MCXC; Piffaretti et al., 2011).

The Voronoi Tessellation and Percolation (VTP) algorithms (Ebeling and Wiedenmann, 1993) are often used together to detect point-like X-ray sources and more generally extended sources, in particular galaxy clusters (Perlman et al., 2002; Barkhouse et al., 2006). By applying these methods one can search for both, the extended and point-like X-ray sources in the cluster areas by identifying higher peaks of number of photons and discard random fluctuation of the background. The steps of the VTP method can be summarized as follows:

- A Voronoi tessellation for a given spatial distribution of photons is defined as a set of convex cells. The Voronoi tessellation is computed for the original photon distribution.

¹for a review on AGN see Beckmann and Shrader, 2012

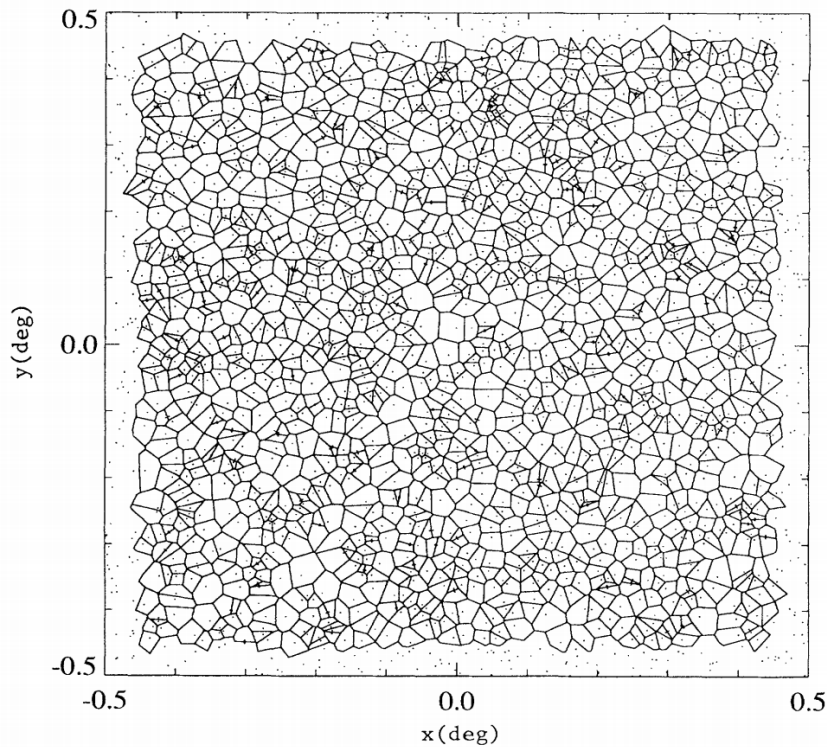


FIGURE 2.4: A Voronoi tessellation consists of cell polygons of a random field. Figure from Ebeling and Wiedenmann, 1993.

- Comparing the cumulative surface brightness distribution of resulting Voronoi cells with the expectation from a Poisson distribution. A global threshold of the surface brightness distribution in a given field is determined.
- The spatial percolation algorithm groups the adjacent cells whose surface brightness exceeds the threshold value.
- The background fluctuations are eliminated applying a threshold on the number of photons.

Besides the VTP algorithms, the matched filters or wavelet techniques (Rosati et al., 1995) are also used to detect galaxy clusters in X-ray surveys.

2.2.3 The SZ effect

Another method to detect galaxy clusters is through the Sunyaev-Zeldovich (SZ) effect. The SZ effect is the result of the distortion of CMB spectrum when the CMB photons travel through the hot gas of the intra-cluster medium (ICM) of galaxy clusters. They gain energy from high energy electrons in the hot gas medium of galaxy clusters through inverse Compton scattering effect. Figure 2.5 shows the change in intensity of the CMB spectrum due to

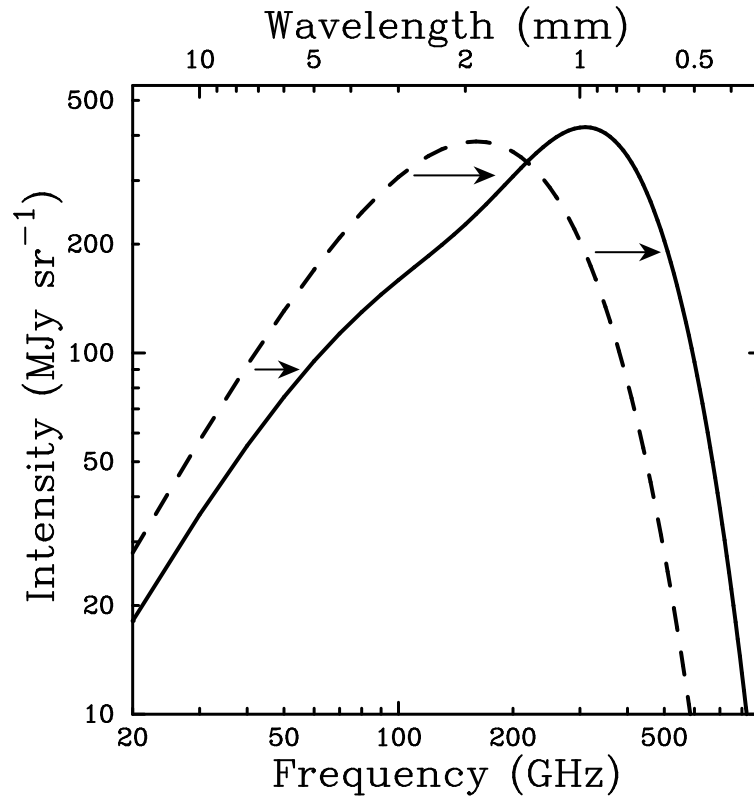


FIGURE 2.5: The dashed line represents the undistorted CMB intensity spectrum, and the solid line represents the distorted CMB spectrum caused by the SZ effect. The SZ effect causes a decrease of the CMB intensity at frequencies $\nu < 218$ GHz and an increase at higher frequencies. Figure from Carlstrom et al., 2002.

the SZ effect. The intensity of the CMB is increased at frequencies larger than $\nu = 218$ GHz and decreased at lower frequencies.

The change in temperature of CMB photons caused by the SZ effect is given by:

$$\frac{\Delta T_{SZE}}{T_{CMB}} = f(x)y = f(x) \int \sigma_T n_e \frac{kT_e}{m_e c^2} dl \quad (2.3)$$

where y is the Compton y -parameter, $f(x)$ is the frequency dependence of the SZ effect, n_e is the electron number density, σ_T is the Thomson cross-section, T_e is the electron temperature, k_B is the Boltzmann constant, $m_e c^2$ is the electron rest mass energy, and the integration is along the line of sight l . The Compton y -parameter is proportional to the ICM pressure (i.e. $P_e = k_B T_e n_e$) integrated along the line of sight. The SZ effect causes a decrement in CMB temperature at low frequencies (below 218 GHz) and an increment at high frequencies due to the upscattering of photons by the hot electrons (LaRoque et al., 2006). Figure 2.6 shows galaxy cluster Abell 2319 as observed in 7 different frequency channels from 44 GHz to 545 GHz by the *Planck* satellite.

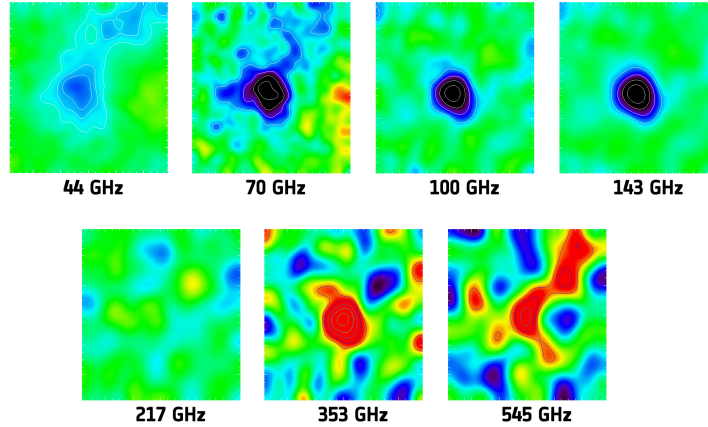


FIGURE 2.6: Galaxy cluster Abell 2319 as observed in seven different frequency channels with *Planck*. The cluster appears colder (or negative signal in blue) than the average CMB signal at low frequencies and hotter at high frequencies (positive signal in red). No signal is seen at 217 GHz which is a characteristic of SZ effect. Credit: ESA.

The South Pole Telescope (SPT; Staniszewski et al., 2009), the Atacama Cosmology Telescope (ACT; Hilton et al., 2018), and the *Planck* surveys (Planck Collaboration et al., 2016d) have found hundreds to thousands of clusters using the SZ effect. Figure 2.7 shows the number of clusters detected using the SZ effect by ACT, SPT, CARMA (Combined Array for Research in Millimeter-wave Astronomy - Bonamente et al., 2012), and by *Planck*. The angular resolution at the relevant frequencies of *Planck* is between 5 and 10 arcmin while for the ACT and for the SPT the resolution is about 1 arcmin, but the sky coverage of *Planck* is much larger. That is why *Planck* detected larger, more massive, and lower redshift clusters than those found by ACT and SPT (Planck Collaboration et al., 2014b).

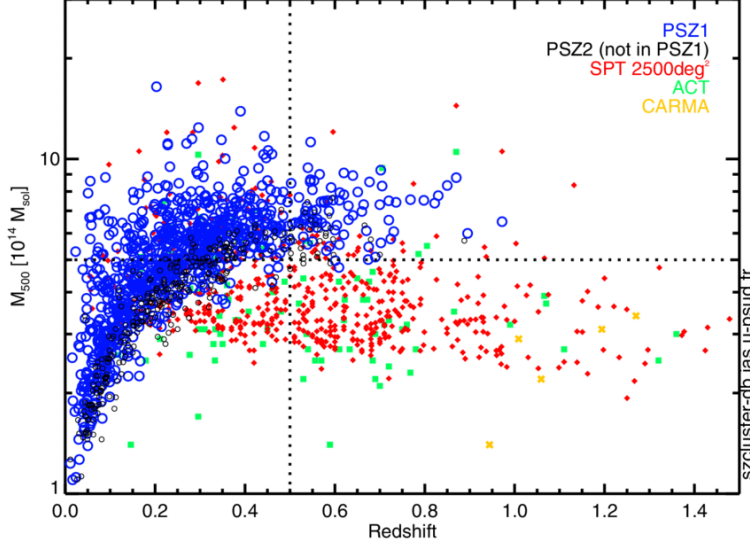


FIGURE 2.7: Mass of galaxy clusters detected through SZ effect by ACT, SPT, and *Planck* (PSZ1 and PSZ2) as a function of redshift. The *Planck* SZ cluster catalog is detected with an all-sky survey, while SZ clusters detected from ACT survey covers only 504 deg^2 and the SPT survey covers 2500 deg^2 . Figure from Battistelli et al., 2016.

The SZ effect has two main forms: thermal and kinetic effects. The thermal effect directly measures the integrated thermal pressure of high energy electrons along the light of sight. The kinetic SZ effect is caused by the motion of the galaxy clusters with respect to the rest frame of the CMB. In another words, the CMB spectrum is shifted to higher or lower frequencies if the cluster moves towards or away from observer. Both effects have redshift-independent with surface brightness ($\Delta T_{SEZ} / \Delta T_{CMB}$ is independent of the redshift). This unique feature of SZ effects offer a powerful tool to observe the universe at high redshift.

Besides, these two effects of the SZ effect also generate linear polarization in the CMB (Carlstrom et al., 2002; Lavaux et al., 2004). Polarization describes the orientation of the light perpendicular to the direction of propagation. The polarization of the SZ effect is caused entirely from the quadrupole component of the local radiation field experienced by the scattering electron. In principle, this effect could be used to measure the optical depth of the cluster. In addition, the CMB as seen by the cluster electrons will have a quadrupole component and get a linear polarization due to the electron scattering. We can use this mechanism to trace the evolution of the CMB quadrupole if polarization measurements could be obtained for a large number of clusters binned in direction and redshift.

The method to detect galaxy clusters with the SZ effect should combine different frequency maps into a synthesized thermal SZ map (stacking CMB maps) and find the significant signal in that map. However the SZ signal is too small compared to the background noise, this stacking method is not

efficient enough.

The multifrequency filtering techniques were introduced which optimize the detection of SZ clusters and reduce the background signal. Herranz et al. (2002) showed that the filtering techniques are useful tools to detect the discrete objects in multifrequency data. These techniques work well with not only the sources have circular symmetry, but also the extended sources which have asymmetry structures.

The Matched Multifilter Methods (MMF; Melin et al., 2006) are effective methods to detect SZ clusters. The MMF methods were used to construct the *Planck* SZ cluster catalog. There are also many others methods to detect SZ clusters such as: Bayesian Methods, Internal Linear Combination Methods (ILC), Generalized Morphological Component Analysis (GMCA). Each of them was designed to adapt under different circumstances, and was developed with different algorithms. Melin et al. (2012) made the comparison for some of them using Plank's instrumental characteristics to detect SZ galaxy clusters. They also classified them into two classes: direct methods that produce a cluster catalog applying filters directly to a set of frequency maps, and indirect methods that first extract a thermal SZ map and then apply source finding algorithms. It turned out that the indirect methods seem to offer greater opportunity for optimization with a larger number of tuning parameters. They are also less model dependent for the SZ map construction and the cluster detection. On the other hand, the direct methods are linear, easy to implement and robust. They can be optimized to detect objects of a given shape (SZ profile) and and a given spectral energy distribution - SED - (SZ spectrum).

2.3 Cosmology with galaxy clusters

Over the last decades, many galaxy cluster surveys at different wavelengths have been done to map from low to high redshifts and to find more massive clusters in our universe. Studying clusters has helped us to build and constrain the cosmological standard model, and to investigate one of the most important issues in modern cosmology: the nature of dark matter and dark energy.

The formation of galaxy clusters is the result of the gravitational collapse of overdensities of the initial density field fluctuations. The overdensity field or the matter density contrast at spatial scale or at a given position x can be defined as:

$$\delta(\vec{x}) = \frac{\rho(\vec{x}) - \bar{\rho}_m}{\bar{\rho}_m} \quad (2.4)$$

where $\rho(\vec{x})$ is the density at a given position \vec{x} and $\bar{\rho}_m$ is the background density or the mean density in the universe as defined in Equation 1.7. The regions with:

- $\delta(x) > 0$ are overdense and tend to collapse to form objects such as galaxies and clusters of galaxies.

2.3. Cosmology with galaxy clusters

- $\delta(x) < 0$ are underdense and tend to create voids.

The Fourier transform of the density contrast is given by:

$$\delta(\vec{k}) = \int d^3x \rho(\vec{x}) e^{i\vec{k} \cdot \vec{x}} \quad (2.5)$$

where $k = 2\pi/x$ is the wavenumber.

The abundance of objects depends on the amplitude of the density fluctuations which is defined as the variance of density contrast, $\sigma^2(R)$ smoothed on some scale R or in terms of mass M :

$$\delta_R(\vec{x}) = \int d^3x' W_R(\vec{x} - \vec{x}') \delta(\vec{x}') \quad (2.6)$$

where $W_R(\vec{x})$ is the top-hat window function (or filter function) that weights the density field:

$$W_R(\vec{x}) = W_R(x) = \begin{cases} \frac{3}{4\pi R^3}, & x \leq R \\ 0, & x > R \end{cases} \quad (2.7)$$

The density fluctuation field is assumed to be a Gaussian random variable, and thus the smoothed density fluctuation field is also a Gaussian random variable (Zentner, 2007). The variance of the density contrast is often expressed in terms of mass scales rather than distance scales R (Bartlett, 1997):

$$\langle \delta_R^2 \rangle = \sigma^2(R) \equiv \sigma^2(M) = \frac{1}{2\pi^2} \int dk k^2 P(k) |W_R(k)|^2 \quad (2.8)$$

where $W_R(k) = 3/(kR)^3 [\sin(kR) - kR \cos(kR)]$ is the Fourier transform of the top-hat window function, $P(k)$ is the matter power spectrum which quantifies the density contrast in the Fourier scale k . In other words, it measures the power of fluctuations on a given scale k . It is related to the two-point correlation function which will be described in Section 5.2.

The probability of obtaining a smooth density contrast over scale M is:

$$p(\delta_M) = \frac{1}{\sqrt{2\pi}\sigma(M)} \exp \left[-\frac{\delta_M^2}{2\sigma^2(M)} \right] \quad (2.9)$$

The predictions of the abundance of collapsed objects are usually quantified by the mass function $dn(M, z)$ described in the following section.

We can constrain cosmological models based on the galaxy cluster properties - their abundance and the evolution of there abundance.

2.3.1 Halo mass function

The halo mass function (HMF) describes the number density of clusters of given mass as a function of redshift. It was first analytically quantified by Press and Schechter (1974). Let $p(\delta)$ be the probability that a given volume

V contains a mass whose fractional deviation from the ensemble average is between δ and $\delta + d\delta$. Considering Gaussian fluctuations, this probability has the form as given in Equation 2.9. Then the probability that a given region within the initial overdensity field smoothed on a mass scale M will collapse into a halo of mass or larger than M is:

$$F(M) = \int p(\delta) d\delta = \frac{1}{2} \text{erfc}\left[\frac{\nu}{\sqrt{2}}\right] \quad (2.10)$$

where erfc is the complementary error function, $\nu = \frac{\delta_c}{\sigma_M}$ with δ_c the linear overdensity evaluated at the virialization time, σ_M is the rms amplitude of the matter fluctuations at a given mass scale M (i.e. the square root of Equation 2.8).

The mass function can be derived as number of objects collapsing into halos of mass between M and $M + dM$ at redshift z :

$$\frac{dn(M, z)}{dM} = \frac{\bar{\rho}_m}{M} \left| \frac{dF}{dM} \right| = \frac{\bar{\rho}_m}{M} f(M, z), \quad (2.11)$$

where dn is the number density of halos mass range dM , z is the redshift of the halo, and $\bar{\rho}_m$ is the background matter density in a comoving volume, the multiplicity function $f(M, z)$ encoding information of non linear collapse of halos (the matter evolved non-linearly and formed large-scale structures such as galaxy clusters).

Bond et al. (1991) proposed solutions to the mass function based on the excursion set formalism. There are other analytic versions of halo mass function such as Lacey and Cole (1993) and Sheth et al. (2001). Given the limitation of the spherical collapse model, N-body simulations are used to obtain more accurate mass functions and also to test its universality such as Jenkins et al. (2001), Tinker et al. (2008), Despali et al. (2016), and Courtin et al. (2011). For example, Springel et al. (2005) presented the Millennium Simulation which is the largest simulation of the growth of dark matter structure. They showed that the mass function of Jenkins et al. (2001) reproduces remarkably well numerical results over a wide range of sampled halo masses and redshifts. Figure 2.8 shows the differential halo number density as a function of mass at different redshifts.

Tinker et al. (2008) showed that the evolution of halo concentrations is mostly driven by the change in Ω_m with redshift. The halo mass function allows us to constrain on the matter power spectrum and on the linear growth rate of density perturbations as summarized by Borgani (2008). The abundance of massive halos is sensitive to the amplitude of mass fluctuations and also to cosmological parameters. Besides, an accurate model of halos is needed in order to understand galaxy formation as it is the core component for the concentration of gas and matter for galaxy formation. For these reasons, it is essential to accurately model the halo mass function. Murray et al. (2013) presented the online tool *HMFcalc* for calculating the Halo Mass Function using various models.

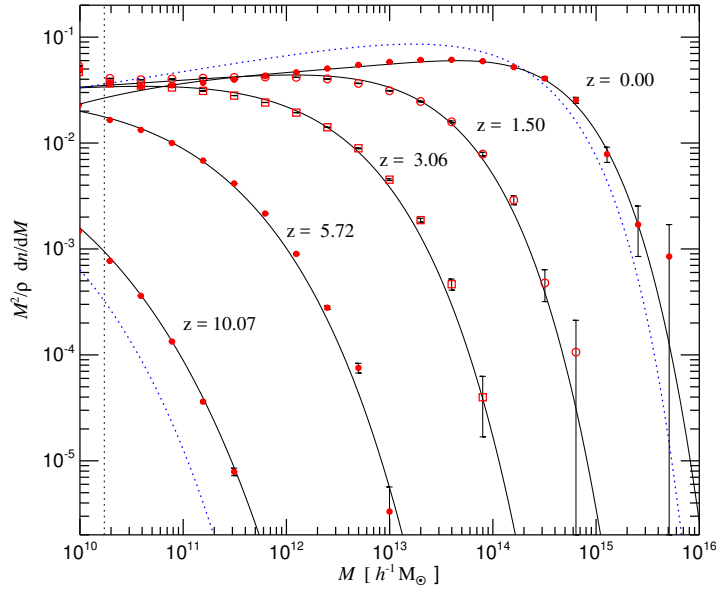


FIGURE 2.8: The mass function of simulation dark matter halos (dots). Solid lines are predictions from the fitting halo mass function proposed by Jenkins et al. (2001), dashed lines are predictions from model mass function by Press and Schechter (1974). Figure from Springel et al. (2005).

2.3.2 Cluster counts

Reviews on this topic can be found in Battistelli et al. (2016) on galaxy clusters as probes for dark matter, and in Blanchard et al. (2018) concerning the cosmological cluster tension.

Recently, many galaxy clusters catalogs have been produced using the SZ effect such as from the Atacama Cosmology Telescope (Hasselfield et al., 2013), the South Pole Telescope (Reichardt et al., 2013), and the *Planck* satellite (Planck Collaboration et al., 2016d). Since then the abundance of galaxy clusters or cluster counts have been shown to be a powerful cosmological probe of matter density Ω_m , and the present amplitude of density fluctuations σ_8 (the root mean square - rms linear overdensity in spheres of radius $8 h^{-1}$ Mpc). Figure 2.9 shows the constraints from *Planck* SZ cluster counts (Planck Collaboration et al., 2016c) combined with the BAO and BBN priors.

Cluster counts formalism: The general idea of cluster count analysis is comparing a catalog of clusters to some model prediction: the models predict number of clusters in mass-redshift space; then in a cosmological likelihood analysis, varying cosmological parameters to obtain the best values which maximize the likelihood. I will briefly summarize the way we can constrain on Ω_m and σ_8 using cluster counts as studied in Planck Collaboration et al., 2016c.

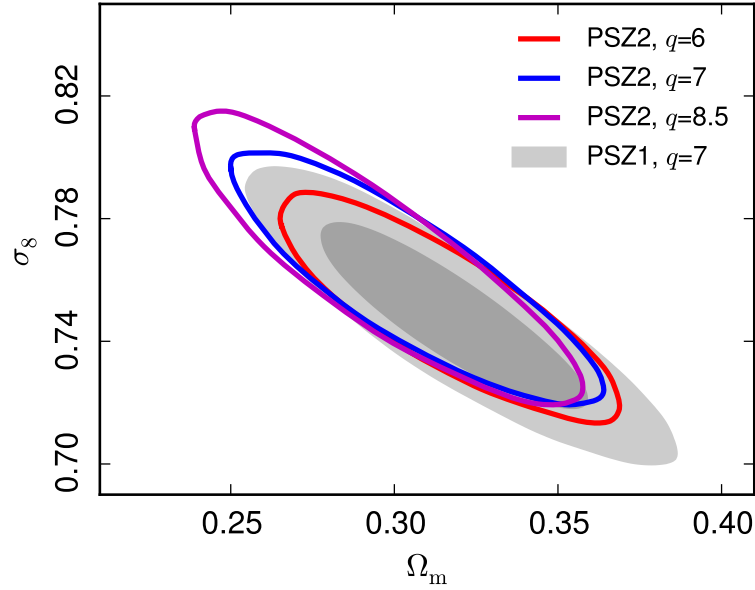


FIGURE 2.9: Constraints from *Planck* SZ clusters: the contours at 95% for different signal-to-noise limits applied to the *Planck* 2015 SZ clusters, the filled light grey contour ellipses at 68% and 95% from *Planck* 2013 constraints (Planck Collaboration et al., 2014b). Figure from Planck Collaboration et al., 2016c

The predicted number of galaxy clusters to be observed by a survey in a given redshift interval $[z_i, z_{i+1}]$:

$$n_i = \int_{z_i}^{z_{i+1}} dz \frac{dN}{dz}, \quad (2.12)$$

The redshift distribution of clusters detected at given signal to noise $q > q_{cut}$ ($q_{cut} > 6$):

$$\frac{dN}{dz}(q > q_{cut}) = \int_{q_{cut}}^{\infty} dq \frac{dN}{dz dq} = \int d\Omega \int dM_{500} \hat{\chi}(M_{500}, z, l, b) \frac{dN}{dz dM_{500} d\Omega}, \quad (2.13)$$

where:

- $d\Omega$ is the solid angle element.
- M_{500} is the mass within the radius where the mean density is 500 times the critical density.
- $\hat{\chi}(M_{500}, z, l, b)$ is the survey completeness at a given location (l : longitude, b : latitude) on the sky:

$$\hat{\chi}(M_{500}, z, l, b) = \int_{q_{cut}}^{\infty} dq P[q | \bar{q}_m(M_{500}, z, l, b)], \quad (2.14)$$

- Y_{500}, θ_{500} is the SZ flux and size of a cluster of redshift z and mass M_{500} .

2.3. Cosmology with galaxy clusters

- $\chi(Y_{500}, \theta_{500}, l, b)$ is the survey selection function which refers directly to the observed quantities.
- $P[q|\bar{q}_m(M_{500}, z, l, b)]$ is the predicted distribution of q given the mean signal-to-noise value, \bar{q}_m for a cluster with a mass M_{500} and redshift z at coordinates (l, b) . \bar{q}_m depends on the mean SZ signal expected for a cluster $\bar{Y}_{500}(M_{500}, z)$ and the detection filter noise σ_f . The details of these terms are defined in Planck Collaboration et al., 2016c.

The quantity $\frac{dN}{dzdM_{500}d\Omega} = \frac{dN}{dVdM_{500}} \frac{dV}{dzd\Omega}$ is the dark matter halo mass function times the volume element. We can adapt with the mass function such as Tinker et al. (2008), Courtin et al. (2011), etc.

In short, we need the following inputs to get a prediction of the counts expected in a survey given cosmological assumption:

- A mass function predict the number distribution of clusters with given mass and redshift
- Scaling relations predicts observable quantities from the mass and redshift.
- The completeness of the survey.

When we have all these ingredients we need to construct cluster counts likelihood function following a Poisson distribution:

$$\ln L = \sum_{i,j=1}^{N_z N_q} [N_{ij} \ln(\bar{N}_{ij}) - \bar{N}_{ij} - \ln[N_{ij}!]], \quad (2.15)$$

where N_z and N_q are the total number of redshift and signal to noise bins, respectively. \bar{N}_{ij} is the mean number of objects in each bins as predicted from theory:

$$\bar{N}_{ij} = \frac{dN}{dzdq}(z_i, q_j) \delta z, \delta q \quad (2.16)$$

We can use the Monte Carlo Markov Chain (MCMC) to map the likelihood surface around the maximum and establish confidence limits. Cluster counts constraints are most sensitive to Ω_m and σ_8 , so when analyzing the cluster counts we need to apply additional observational constraints as priors on other parameters: the Big Bang nucleosynthesis $\Omega_b h^2$, the BAO to constrain H_0 , *Planck* CMB prior on n_s .

However, cluster count constraints are limited by uncertainties on scaling relations - mass bias. The abundance of SZ clusters as measured by *Planck* have been found to be in tension with the primary CMB. This tension has also been found between the constraints of CMB and the measurement of clusters from X-ray to optical. Figure 2.10 shows the tension of cosmological parameters Ω_m , and σ_8 between CMB and clusters. The cosmological constraints from primary CMB alone give is away about 2.4σ from SZ clusters.

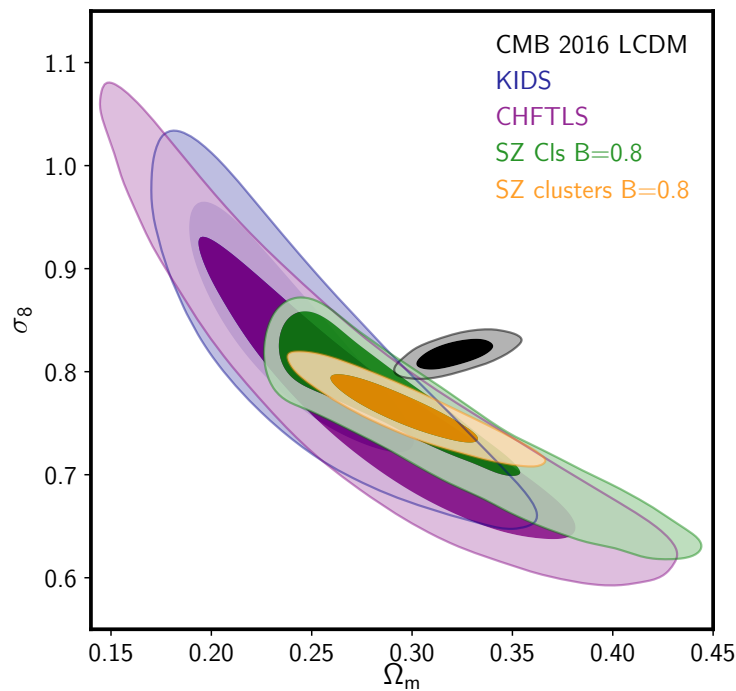


FIGURE 2.10: Tension between the determination of cosmological parameters based on the CMB and on clusters measurements. Figure from Douspis et al. (2019).

The level of tension between SZ clusters and CMB could be reduced by lower the value of optical depth τ from Thomson scatter after reionization (Planck Collaboration et al., 2016c) or adding the sum of neutrino masses as a free parameter to combine with cluster data (de Haan et al., 2016).

Future experiments such as *Euclid*, LSST, and *WFIRST* (Wide Field Infrared Survey Telescope) will provide additional data which will have a potential impact of a 1% determination of the mass scale calibration. Figure 2.11 shows the predicted constraints from *Euclid* photometric clusters on suitable pairs of cosmological parameters. Based on the Fisher matrix approach, Sartoris et al. (2016) derived these constraints. The Fisher matrix is a Gaussian approximation of the likelihood around the maximum to second order. It is often used in cosmology to forecast the accuracy of the estimation of a vector of parameters from various data sets. By combining cluster power spectrum with cluster number counts Fisher matrix, the constraints on σ_8 and Ω_m are significantly improved compared to cluster number counts only.

2.3.3 Scaling relations

Galaxy clusters were formed in the densest regions of the universe during the early structure formation of the universe. Understanding the physical processes of galaxy clusters is a key issue to understand the evolution of the universe. Measuring accurately the total mass of clusters is very important in order to study the halo mass function and also cluster counts as we have seen

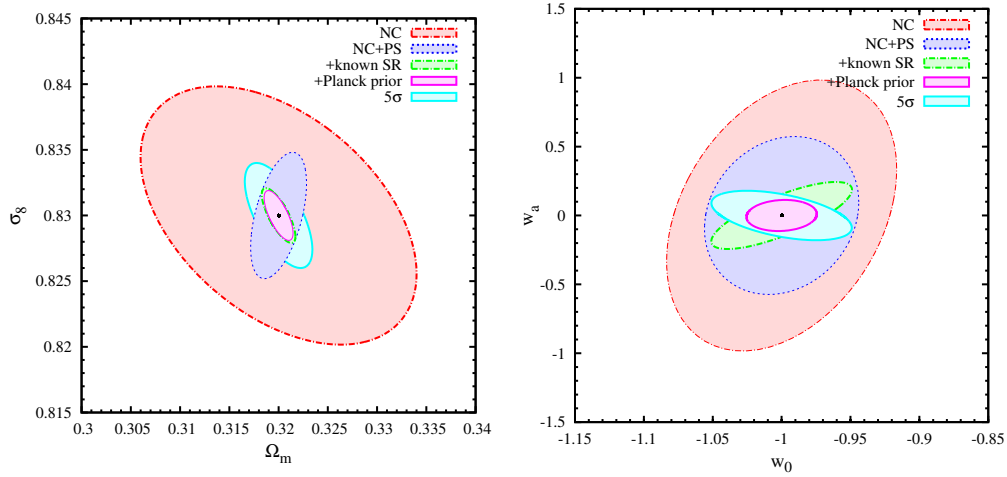


FIGURE 2.11: Constraints at the 68 per cent (1σ) confidence level on the parameters Ω_m and σ_8 (left panel) and on the parameters w_0 and w_a for the dark energy equation of state evolution (right panel). In each panel, the forecasts for the $N_{500,c}/\sigma_{\text{field}} \leq 3$ *Euclid* photometric cluster selection obtained by number counts (NC), the Fisher Matrix (FM) number counts (red dash-dotted contours), FM + cluster power spectrum (PS), the combination of FM NC and power spectrum (PS) information (blue dotted contours), NC+PS+known SR (scaling relation), i.e. by additionally assuming a perfect knowledge of the nuisance parameters (green dash-dotted contours), and NC+PS+known SR+*Planck* prior, i.e. by also adding information from *Planck* CMB data (magenta solid contours). The cyan solid lines present forecasts for the $N_{500,c}/\sigma_{\text{field}} \geq 5$ *Euclid* photometric cluster selection in the case NC+PS+known SR+*Planck* prior (labelled 5σ). *Planck* information includes prior on Λ CDM parameters and the DE EoS parameters. Figure from Sartoris et al., 2016.

in previous sections. As we already stated, we can observe galaxy clusters from X-ray, optical surveys and using SZ effect. Hence, the cluster mass can be measured from different ways such as galaxies-richness (optical), velocity dispersion, gravitational lensing, SZ effects to probe the gas properties, X-ray by measuring the gas density and temperature profiles (Allen et al., 2011). These cluster mass measurement methods have been studied as scaling relations of clusters to put the constraints on cosmological parameters.

The self-similarity relations of clusters was first described by Kaiser (1986). The self similar model assumes that cluster properties are determined by gravitational collapse of dark matter halos, and the shock heating of the ICM created by the infall of galaxies and gas by gravity. When we describe clusters as self-similarity, it means that the observable quantities such as temperature and luminosity naturally scale with respect to the mass.

Based on that, power law scaling relations have been used to derive scaling relation between cluster properties (typically using X-ray clusters) (Maughan et al., 2012): X-ray luminosity (L_x) which is obtained by integrating the surface brightness profile of the cluster from X-ray imaging data, gas temperature (kT) of the ICM which is determined from X-ray spectroscopic data, metal abundances in the ICM. Many works have used X-ray clusters to study the scale relations from these properties.

The $L_x - kT$ relation has been well studied, for example by Markevitch (1998), Allen et al. (2011), and Maughan et al. (2012). The total mass and temperature ($M - T$) relation has also been determined (Reiprich and Böhringer, 2002; Vikhlinin et al., 2006; Zhang et al., 2007). As an example, Figure 2.12 shows the strong scaling relation of clusters between total mass and temperature.

In the last decades, the mean mass-to-light ratio M/L of galaxy clusters has been used as a method to infer matter density parameter Ω_m (Peebles, 1986; Bahcall et al., 1995; Tinker et al., 2005):

$$\Omega_m = \langle M/L \rangle \times \rho_{lum} / \rho_{crit} \quad (2.17)$$

where ρ_{lum} is the luminosity density and ρ_{crit} is the critical density.

In Tinker et al. (2005), cluster M/L ratios depend not only on the matter density but also on the amplitude of the density fluctuations, σ_8 , once the galaxy bias model is constrained to match the projected galaxy correlation function $w_p(r_p)$.

The Planck Collaboration et al. (2011b) showed that the measured SZ signal from *Planck* is in excellent agreement over the whole explored luminosity range with the X-ray data from the Meta-Catalogue of X-ray detected Clusters of galaxies (MCXC) and also with the predictions based on X-ray data. The intrinsic scatter in the scaling relation between SZ signal and X-ray luminosity is measured and found to be consistent with the one in the luminosity – mass relation from X-ray studies. These results underlines the robustness and consistency of our overall view of ICM properties.

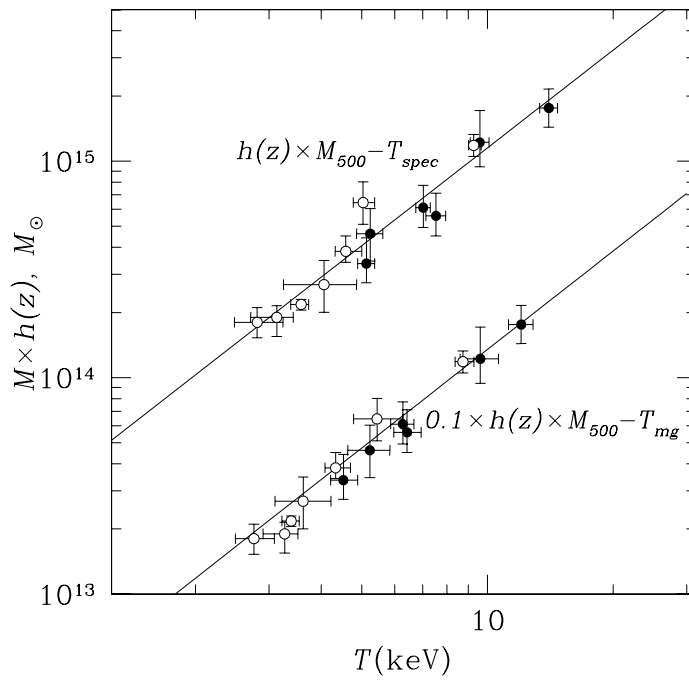


FIGURE 2.12: The scaling relation of cluster mass and temperature from two cluster samples at r_{500} : the combined *XMM-Newton* (open circles) and *Chandra* (solid circles) sample. (T_{spec} : spectroscopic temperature, T_{mg} : computed the gas mass-weighted average). Figure from Kotov and Vikhlinin, 2006

2.3.4 Clustering of clusters

Galaxy clustering measurements offer a unique window into the distribution of dark matter in the universe. However, one of the main impediments to the use of galaxy clustering for inferring cosmological information is galaxy bias it is likely that the distribution of galaxies differs from the distribution of dark matter. Thus both the amplitude and shape of the galaxy clustering signal are biased relative to the clustering of dark matter at quasi-linear and nonlinear scales. This bias is degenerate with cosmology in such a way that a bias model can be constructed to match the observed real-space galaxy or cluster two-point correlation function for a range of cosmological models. As we saw above, the spherical collapse model indicates that the probability of forming a halo depends on the initial density field. Large scale density field acts as the background which is surround the high density of halo regions. Therefore, halos are considered as the biased tracers of the “background” dark matter field with a bias $b(M, z)$. The halo bias can be calculated from spherical collapse and the form of the mass function. Mo and White (1996) have derived the first description of bias of dark matter halos:

$$b(M, z) = \frac{\xi_{hh}(r)}{\xi_m(r)} \quad (2.18)$$

where $\xi_{hh}(r)$ is the correlation function of halos as function of the spatial distance r , $\xi_m(r)$ is the correlation function of mass.

Under the assumption of Press-Schechter halo mass function, the bias is given by:

$$b(M) = 1 - \frac{v^2 - 1}{\delta_c} \quad (2.19)$$

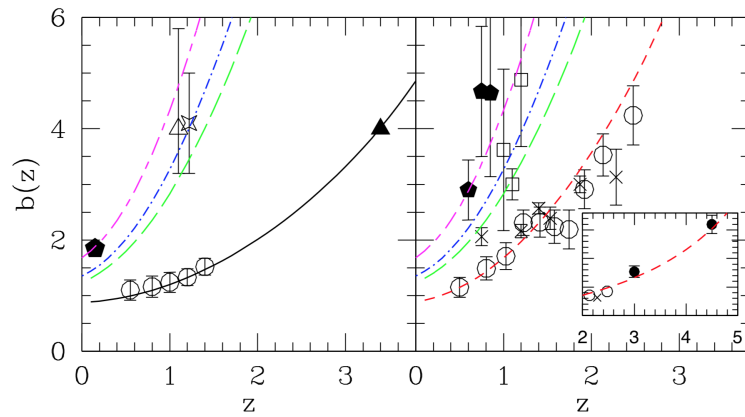


FIGURE 2.13: Comparison of halo bias $b(M)$ model with different observational data as the function of redshift. Figure from Basilakos et al. (2008)

Based on linear perturbation theory and the Friedmann-Lemaître solutions of the cosmological field equations, Basilakos et al. (2008) showed that

halo bias evolves with redshift. Figure 2.13 shows the bias model as the function of redshift with different observational data.

A dark matter halo as a collapsed, virialized object with a mean interior density of 200 times the critical density. Distinct cosmologies produce distinct populations of dark matter halos (Zheng et al., 2002). Mana et al. (2013) demonstrated that we can use the clustering of galaxy clusters as a useful addition to the common set of cosmological observables.

In Chapter 5, we will give more details on the cluster length measurement of galaxy clusters in the literature. In short, on scales smaller than $60 h^{-1} \text{ Mpc}$, the correlation of galaxy clusters can be well fitted by a power law.

Chapter 3

ESA's Euclid and Planck mission

In this chapter I will briefly introduce two space missions, *Euclid*¹ and *Planck*², which are most relevant to my thesis.

Euclid is an European Space Agency (ESA) mission that will be launched in 2022. In the frame of the *Euclid* mission:

- I contributed to the external data simulation.
- I studied the potential of measuring clustering of the *Euclid* mock cluster catalog.

In the context of ESA's *Planck* mission (launched in 2009), I used the *Planck* SZ cluster catalog to study the clustering of galaxy clusters using the angular two-point correlation function as presented in Chapter 5.

3.1 The Euclid mission

3.1.1 An overview

Euclid was selected as the second Medium Class (M2) mission in 2011 by the Science Program Committee of the member states of ESA for the Cosmic Vision 2015-2025 program. The main mission goal is to investigate the accelerating expansion of the Universe, which is believed to be caused by dark energy. *Euclid* will take images of about 1.5 billion galaxies and take spectroscopy of about 50 million galaxies (Laureijs et al., 2011). Figure 3.1 shows the sky areas that will be covered by the *Euclid* mission's surveys.

The *Euclid* mission will perform two main surveys during 6 years of observations. An overview of the *Euclid* surveys is presented in Table 3.1.

The first survey is called the "*Euclid* Wide Survey", covering 15,000 deg² of the sky. This survey will cover the darkest part of the sky which excludes the regions dominated by light from the Solar System and from the Milky Way. The two main scientific objectives of this survey are to study dark energy using gravitational lensing effects on galaxies (Weak Lensing), and the properties of galaxy clustering (Baryonic Acoustic Oscillations and Redshift Space

¹<http://sci.esa.int/euclid/>

²<http://sci.esa.int/planck/>

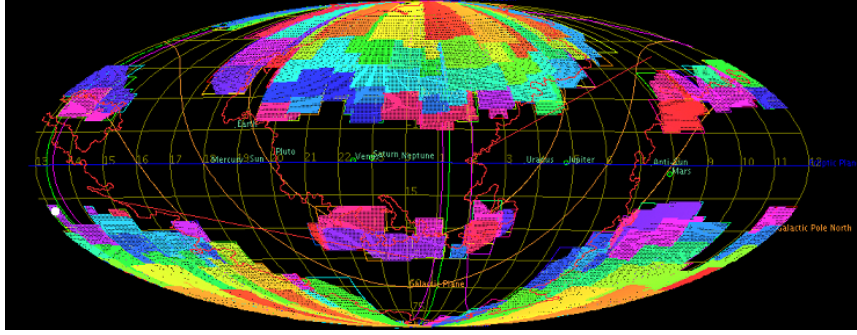


FIGURE 3.1: The regions of the sky that will be covered by *Euclid* shown in Mollweide projection in ecliptic coordinates during 6 years nominal mission. Different colors correspond to different observation periods of the mission. Credit: ESA/Euclid consortium.

TABLE 3.1: Overview of Euclid surveys.

SURVEYS					
	Area deg ²		Description		
Wide survey	15,000 deg ²		The core of dark energy mission out of which weak lensing, BAO, RSD will be measured		
Deep survey	40 deg ²		Primarily for calibration of the wide survey but also extending the scientific scope of the mission to faint high redshift galaxies, quasars and AGNs.		
Wavelength range	VIS (550 - 900 nm)	Y (920 - 1146 nm)	J (1146 - 1372 nm)	H (1372 - 2000 nm)	NISP (1100 - 2000 nm)
Sensitivity	24.5 mag	24 mag	24 mag	24 mag	3 10^{-16} erg cm ⁻² s ⁻¹
	10 σ extended source	5 σ point source	5 σ point source	5 σ point source	3.5 σ unresolved line flux

Distortion). The wide survey will take galaxy images in a single VIS wide filter for high precision galaxy shape measurements needed for cosmic shear survey. It will also perform photometry of galaxies through 3 NIR filters (Y, J, H) to determine the redshifts. In order to obtain sufficient galaxy redshifts for weak lensing analysis, *Euclid* needs to include all types of galaxies with redshift at $0 < z < 2$. The *Euclid* broad-band data alone are not sufficient to achieve the required photometric redshift accuracy and precision for weak lensing analysis. Therefore, *Euclid* needs complementary photometric redshifts data from ground-based surveys covering at least the full wavelength range 420 - 930 nm, with an overlap between the filters less than $\sim 10\%$.

The second survey is the "*Euclid* Deep Survey" covering 40 deg² of the sky. It will be used to calibrate the wide survey and to extend the scientific scope of the mission to faint high-redshift galaxies, quasars, and other Active Galactic Nuclei (AGN). The *Euclid* Deep Survey will observe three separated areas: one near the north ecliptic pole (EDS-N), one near the south ecliptic pole (EDS-S) and a third overlapping the Chandra Deep Fields South (EDS-Fornax). The EDS-N will have 10 visits covering an area of 20 deg² for calibration purposes, and 30 visits covering an area of 10 deg² during a five year period. The EDS-S will cover an area of 20 deg² and the same total number of visits as the EDS-N. In addition the EDS-Fornax will scan 56 times and cover an area of 10 deg².

In order to prepare the future data processing, the *Euclid* consortium is

developing the software and program pipelines that will be needed for data analysis. One of the development activities is to simulate the data of the VIS and NISP *Euclid* instruments and also what could be called the third instrument: the ground based telescopes' external data. These data, which are similar to the expected data from *Euclid* which are mandatory to estimate the photometric redshifts of 1.5 billion galaxies which will be used for weak lensing studies. During my PhD, I contributed to the development of this external data simulation.

The *Euclid* Consortium comprises more than 100 laboratories from 13 European countries: Austria, Denmark, France, Finland, Germany, Italy, Netherlands, Norway, Spain, Switzerland, Portugal, Romania and the UK. Several US laboratories also participate in this consortium. Concerning to the preparation of the mission, the *Astroparticle and Cosmology laboratory* (APC) is one of the *Euclid* consortium members involved in the development of the software platform to simulate the external data for *Euclid*. At APC we are also involved in the Science Ground Segment for the contribution of the development of the *Euclid* Galaxy Cluster Likelihood to constrain cosmological parameters.

3.1.2 Scientific objectives

What is the nature of dark energy and dark matter? This is one of the main issues of cosmology today and *Euclid*'s primary objective is to investigate their properties. As mentioned in the introduction of this chapter, *Euclid* will study their effects using at least two cosmological probes:

- Weak Lensing by measuring the shape and photometric redshifts of 1.5 billion galaxies.
- Galaxy Clustering: Baryonic Acoustic Oscillations (BAO) and Redshift Space Distortion (RSD) by measuring the 3-dimensional distribution of 50 million galaxies using spectroscopic redshifts.

Weak Lensing: *Euclid* will measure the shape of about 1.5 billion galaxies (about 30 resolved galaxies per arcmin²), and derive the photometric redshift of these galaxies with a precision of $\sigma_z/(1+z) < 0.05$. In order to achieve this goal, *Euclid* will do imaging in one broad visible (VIS) band (550-920 nm) down to AB mag 24.5 (10σ), get photometry in 3 *Euclid* Near Infrared (NIR) bands (Y, J, H in the range 920-2000 nm) of the Near Infrared Spectrometer and Photometer (NISP) instrument, and get the additional ground based photometry from collaborations of projects³ such as the Dark Energy Survey (DES; The Dark Energy Survey Collaboration, 2005), the Kilo-Degree Survey (KiDS; de Jong et al., 2013), the Large Synoptic Survey Telescope (LSST; LSST Dark Energy Science Collaboration, 2012), the Panoramic Survey Telescope and Rapid Response System (Pan-STARRS; Kaiser et al., 2002), the Canadian France Hawaii Telescope Imaging Survey (CFIS), and the Javalambre Physics of the Accelerating Universe Astrophysical Survey (JPAS; Benítez et al., 2015).

³*Euclid* Data Processing, Martin Kümmel, 2018

Galaxy Clustering: *Euclid* will determine about 50 million spectroscopic redshifts of galaxies with $0.001(1+z)$ accuracy. The three dimensional galaxy distribution of the universe can be quantified through the power spectrum or the two-point correlation function. *Euclid* will exploit the BAO signature and therefore put constraints on the properties of dark energy. Using the same data set, *Euclid* will perform a measurement of RSD (Redshift space distortion) to provide an additional measurement of the growth of structure in the universe.

These probes will enable us to track the observational signatures of dark matter and dark energy on the geometry of the universe, and the cosmic evolution of structure formation.

Besides these two primary probes, *Euclid* will also extract a number of complementary cosmological probes such as clusters of galaxies, combining with the CMB data from *Planck*, type Ia Supernovae in the deep survey. Using photometric survey data, *Euclid* is expected to find about 100,000 galaxy clusters with signal to noise ratio $S/N > 3$ between redshift from $z = 0.2$ to $z = 2.0$ in which 10,000 clusters will have a redshift larger than 1.

3.1.3 Satellite and scientific instruments

Euclid will be launched to the second Lagrangian point L2. The satellite has a total mass of about 2020 kg with a power budget of 1920 W. It will be about 4.5 metres tall and 3.1 metres in 'diameter'. The nominal mission lifetime is six years. The Payload Module (PLM) comprises the telescope, the PLM thermal control system, the Fine Guidance Sensor (FGS), the visible (VIS) instrument, and Near Infrared Spectrometer and Photometer (NISP) instruments (delivered to Airbus Defence and Space division by the *Euclid* Consortium). An overview of the PLM sub-systems is shown in Figure 3.2. The telescope is based on 3-mirror Korsch operating at temperature below 130 K, with a primary mirror of 1.2 m diameter.

The VIS and NISP are the two main scientific instruments: the VIS provides the wide-band visible image and the NISP will be able to provide both NIR imaging and slitless spectroscopy. They can be operated simultaneously thanks to a dichroic filter which splits the incident light from the telescope in the exit pupil. Both instruments cover a common field of view of 0.54 deg^2 . In Figure 3.3 and Table 3.2 are given the normalized filter transmission of VIS and Y, J, H filters of NISP, and the specifications of *Euclid* filters.

TABLE 3.2: *Euclid* filter specifications.

Filter name	Central wavelength [Å]	Width [Å]
VIS	7150	3550
Y	10850	2750
J	13750	4300
H	17725	5250

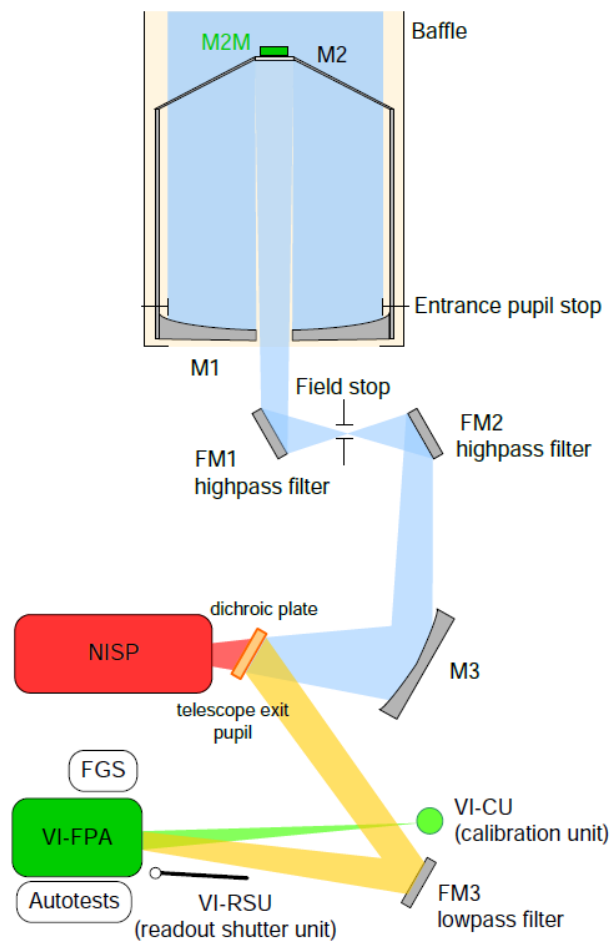


FIGURE 3.2: Overview of the PLM sub-systems. Credit: *Euclid* consortium / Airbus Defence and Space.

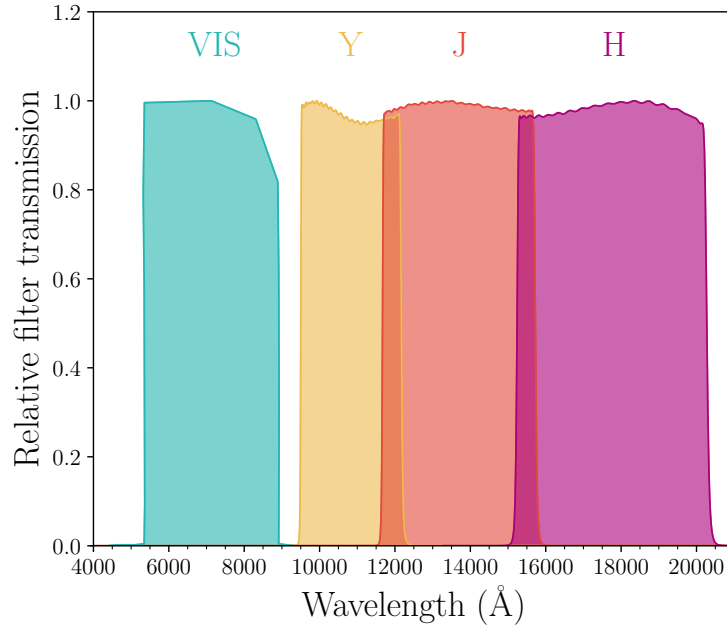


FIGURE 3.3: The normalized transmission curve of VIS and Y, J, H filters of *Euclid*. Figure from Inserra et al. (2018).

The VIS instrument

The VIS is an assembly of the subsystems units listed in Table 3.3. The layout of these units is shown in Figure 3.4.

TABLE 3.3: Overview of the subsystems composing the *Euclid* VIS instrument.

Name	Unit	Function
VI-FPA	VIS Focal Plane Assembly	Detection of visible light for imaging
VI-RSU	VIS Read-out Shutter	Close VIS optical path for read out Close VIS optical path for dark calibration
VI-CU	VIS Calibration Unit	Illuminate the FPA with Flat Field for calibration
VI-CDPU	Control and Data Processing Unit	Control Instrument Perform data processing Interface with Spacecraft for data handling
VI-PMCU	Power and Mechanism Control Unit	Control Units
VI-FH	Flight Harness	Connection of units

The VIS has a wide wavelength band from 550 - 900 nm. Its focal plane consists of a matrix 6x6 e2v CCDs (Charge Coupled Devices). Each CCD has the size of 4096×4132 pixels covering 0.57 deg^2 field of view. The VIS will be used to measure the shapes of galaxies for weak lensing with very high quality (with a mean image quality of resolution better than 0.2 arc-second).

The VI-FPA is a thermal-mechanical structure to support the CCDs array and its associated Read Out Electronics units. It also ensures mechanical and stability of the temperature of CCD array and on the whole extent of the focal plane array at temperature $153 \pm 5 \text{ K}$.

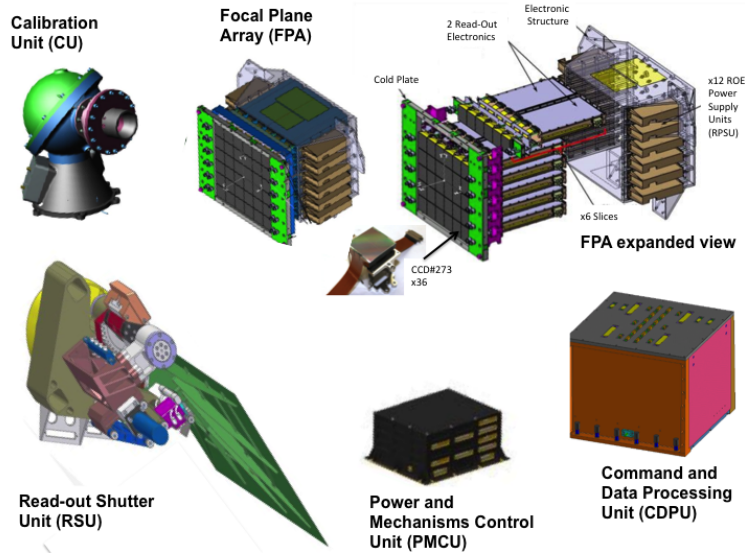


FIGURE 3.4: Overview of the subsystems composing the *Euclid* VIS instrument. Credit: *Euclid* Consortium/VIS team.

The VI-CU calibration unit allows flat fields of the visible channel to be obtained. This structure encloses a 12-LEDs panel illuminating a diffusing panel inside an integrating sphere which has a high reflectivity over the wavelength range from $\lambda = 600$ nm to $\lambda = 900$ nm.

The RSU is designed to stop the light beam before entering the VIS focal plane in order to prevent trails in the images during the readout of the visible detector array.

The VI-CDPU controls the instrument and compresses the scientific data before transfer to the payload mass memory.

The VI-PMCU controls the VIS mechanisms as well as the calibration units.

The NISP instrument

The NISP instrument is the near-infrared Spectrometer and Photometer operating from 900-2000 nm wavelength at a temperature below 140 K. It has two main observing modes: the photometric mode to take images with 3 filters Y, J, H (Fig. 3.3); and the spectroscopic mode to acquire the slitless dispersed images.

The NISP photometer is equipped with 16 HgCdTe NIR detectors with 0.3 arc-second pixels. The NISP spectroscopic channel operates in the wavelength from 1100 - 2000 nm at a mean spectral resolution $\lambda/\delta\lambda \sim 250$, employing 0.3 arc-second pixels. The NISP with the VIS and ground based external data will be combined to derive the photometric redshift of galaxies.

An overview of NISP instrument is shown in Figure 3.5. The main elements of NISP instrument are shown in Table 3.4. The NISP instrument includes six main Opto-mechanical modules, to be mounted on a common structure:

1. Corrector lens (NI-CoLA)
2. Mechanism dedicated to the selection of filters (NI-FWA)
3. Mechanism dedicated to the selection of grisms (NI-GWA)
4. Three lenses camera optics (NI-CaLA)
5. Focal plane with mosaic of 16 (2k x 2k) infrared detectors and associated proximity electronics (NI-DS)
6. Calibration unit (NI-CU)
7. Electronic for the data acquisition and processing (NI-DPU)
8. Electronic for the instrument control and interface with the satellite (NI-ICU)

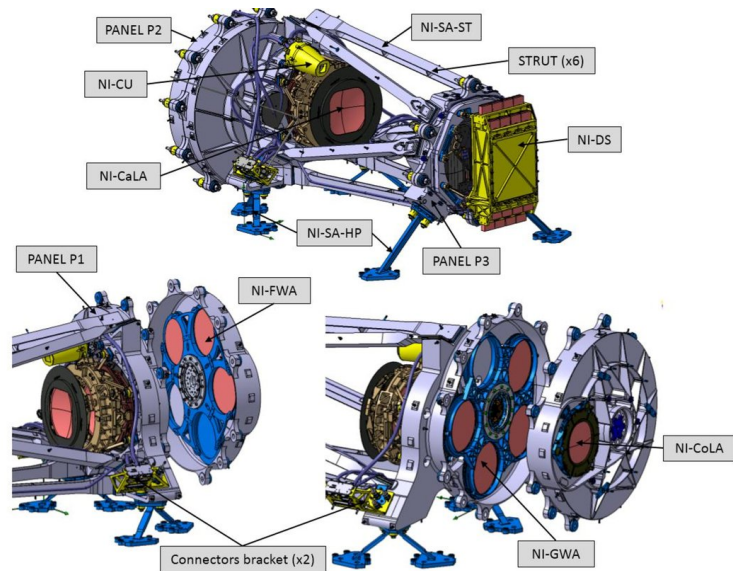


FIGURE 3.5: An overview of the NISP instrument. Figure from Bougoin et al. (2017).

TABLE 3.4: Description of *Euclid* NISP main elements.

Name	Unit	Function
NI-OMA	NISP Opto-Mechanical Assembly	Holds the optical elements and the Focal Plane Array
NI-GWA	NISP Grism Wheel Assembly	Holds the four dispersing elements for the spectroscopic mode and it allows them to be placed in the optical beam.
NI-FWA	NISP Filter Wheel Assembly	Holds the three filters for the photometric mode and it allows them to be placed in the optical beam. It provides also a closed and open position.
NI-CU	NISP Calibration Unit	Injects calibration signal in the optical beam for calibration purposes
NI-DS	NISP Detector system	Provides detection of the NIR signal in photometric and spectroscopic mode
NI-WE	NISP Warm Electronics	Composed of the NI-DCU, NI-DPU and NI-ICU.
NI-DCU	NISP Detector Control Unit	Provides the data and command interface to NI-DS and also detector acquisition and cosmic ray identification.
NI-DPU	NISP Data Processing Units	Provides data compression and packeting as well as the interface to S/C Mass Memory and to the NI-DCU
NI-ICU	NISP Instrument Control Unit	Controls the instrument, powers and controls mechanisms, provides instrument thermal control, and the command interface with NI-DPU and NI-DCU.

3.2 The *Planck* mission

3.2.1 Overview

Planck is a space mission which was developed by ESA with participation of NASA. The *Planck* satellite was launched in 2009 to the Lagrangian point L2. It was operated for 4 years and 5 months from May, 2009 to October, 2013. *Planck* operated beyond its nominal operational lifetime of fifteen months from the end of the Calibration and Performance Verification Phase. An artist's impression of the *Planck* satellite is shown in Figure 3.6.

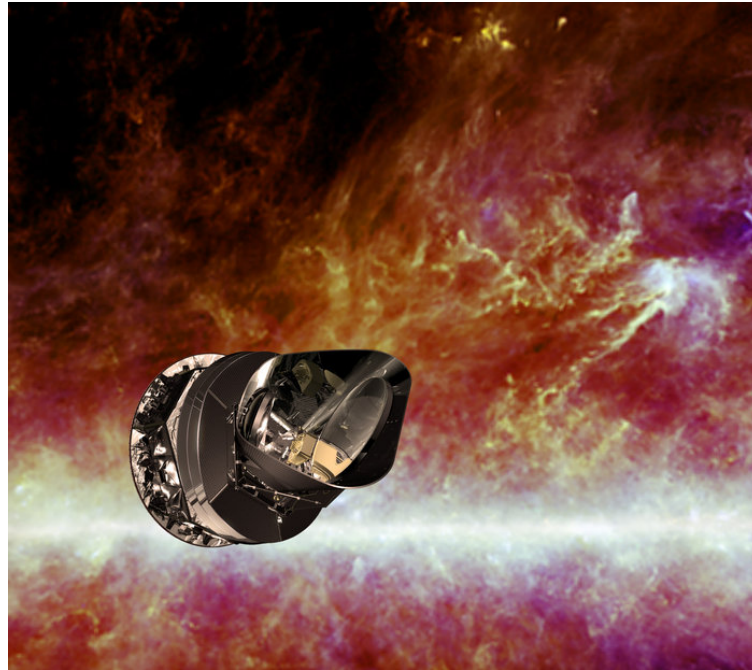


FIGURE 3.6: Artist's impression of the *Planck* satellite. Credit: ESA.

The main goal of the mission was to measure the temperature anisotropies of the CMB with an accuracy set by fundamental astrophysical limits using sensitive radio receivers operating at extremely low temperatures. *Planck* improved the observations of CMB with higher resolution and sensitivity compared to the previous space missions *WMAP* (2001) and *COBE* (1989). Therefore, *Planck* allowed to probe much smaller scales of the power spectrum of the CMB. Moreover, *Planck* was also able to reduce significantly the impact of foreground radiation using a wide range of 9 frequency detector channels.

3.2.2 Scientific objectives

The main scientific objectives of the *Planck* mission were:

- Measure the anisotropies of the CMB with high resolution and sensitivity detection, derive the cosmological parameters, and measure the non-Gaussianity the CMB.

- Produce and analyze a catalog of galaxy clusters via the SZ effect.
- Characterize the reionization history of the Universe.
- Observation of the large-scale structure matter distribution through the gravitational lensing of the CMB and the integrated Sachs-Wolfe effect.
- In addition, *Planck* was also dedicated to observe and analyze extra-galactic sources and the solar system.

3.2.3 Telescope and scientific instruments

The *Planck* satellite operated at the L2 orbit with a reflector telescope of $1.9 \text{ m} \times 1.5 \text{ m}$. The spacecraft spun at $\sim 1 \text{ rpm}$ around an axis offset by $\sim 85^\circ$ from the telescope boresight. The spin axis continuously pointed in the opposite direction of the Sun. The satellite itself was used to protect the payload from solar illumination. The instruments swept through the sky at a rate of 1° per day. Therefore the whole sky was completely scanned in about more than 6 months. The nominal duration of the mission was 15 months but the satellite operated until October, 2013.

Planck has two main scientific instruments: the Low Frequency Instrument (LFI) covering the frequency range 30–100 GHz, and the High Frequency Instrument (HFI) covering the frequency range 100–857 GHz (The Planck Collaboration, 2006). Table 3.5 shows the characteristic of these channels including angular resolution and sensitivity. Among them all of the 3 LFI channels, and four of the 6 HFI channels were designed to measure linear polarization of the radiation as well as intensity.

TABLE 3.5: Summary of *Planck* instrument characteristic

Frequency [GHz]	Bandwidth ($\Delta\nu/\nu$)	Angular Resolution [arcmin]	Sensitivity (total intensity) $\Delta T/T$ per pixel	Sensitivity (polarization) $\Delta T/T$ per pixel
30	0.2	33	2.0	2.8
44	0.2	24	2.7	3.9
70	0.2	14	4.7	6.7
100	0.33	10	2.5	4.0
143	0.33	7.1	2.2	4.0
217	0.33	5.5	4.8	9.8
353	0.33	5.0	14.7	29.8
545	0.33	5.0	147	N/A
857	0.33	5.0	6700	N/A

- The Low Frequency Instrument: The LFI consists of 11 radiometric receivers with ultra-low-noise amplifiers based on high-electron-mobility transistors (HEMTs). The LFI was designed to scan the sky (including polarized components) at 30, 44 and 70 GHz, covering the microwave to infra-red regions of the electromagnetic spectrum. It is cooled to 20 K using a closed-cycle hydrogen sorption cryocooler to minimize power dissipation in the focal plane. The LFI horns are located in a ring around the HFI as shown in Figure 3.7.

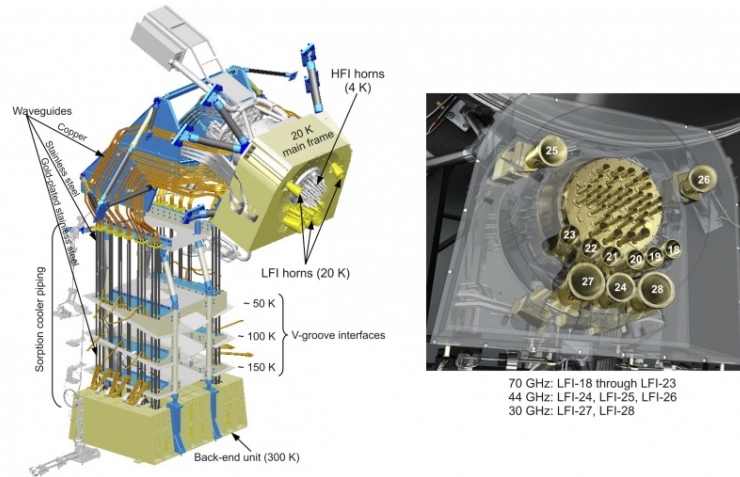


FIGURE 3.7: Left figure: The LFI instrument with main thermal stages, focal plane, waveguides and sorption cooler piping highlighted. Right: labelling of feed horns on the LFI focal plane. Credit: *Planck*/ESA.

- The High Frequency Instrument: The HFI observed the sky at six frequency bands: 100, 143, 217, 353, 545, and 857 GHz. The HFI consists of an array of 52 bolometer detectors (Bock et al., 1995), and cooled down to a temperature of 100 mK by using a space qualified dilution cooler coupled to a high precision temperature control system. There are two types of bolometers: twenty of the them (spider-web bolometers or SWBs) are sensitive to total power, and 32 bolometers are sensitive to the polarisations which are used for the four lower frequency bands. In order to get high sensitivity for the HFI bolometers they need to operate at 0.1 K. To reach this very low temperature, *Planck* used a chain of three cryo-coolers: a hydrogen sorption cooler which provides 20 K to LFI and 18 K to HFI, a Joule-Thomson refrigerator precooled to 18 K by the sorption cooler, and which provides 4 K to HFI; and an open-loop dilution refrigerator to provides 0.1 K.

3.3 *Planck* results

A first early result of *Planck* was published in 2011 (Planck Collaboration et al., 2011a). The complete results were made public in December 2014 and published in early 2015 (Planck Collaboration et al., 2016a). On July 2018 ESA and the *Planck* Collaboration have released to the public a new and improved version of the data acquired by the *Planck* satellite, which constitutes the final official release from *Planck* (Planck Collaboration et al., 2018a). The cosmological parameters that describe the current universe and its history such as the age of the universe and its initial composition, have been refined thanks to the unmatched precision of the data collected by *Planck*. These elements make it possible to better understand certain aspects of the physics of the

primordial universe, as well as the mode of formation of the large structures of the universe. Overall, *Planck*'s data confirm the theory of cosmic inflation, one of the pillars of the standard model of cosmology, the most commonly accepted theory regarding the mode of formation of the observable universe.

In this section, I will present very brief overview of the main cosmological results of *Planck* 2018 as presented by the Planck Collaboration et al. (2018a).

3.3.1 Maps and angular power spectra

Planck observed sky emission in nine frequency channels. *Planck* produced the maps of the whole sky in these 9 frequency channels after 5 surveys from which the CMB maps and astrophysical foregrounds (Galactic and extra-galactic) have been extracted.

Figure 3.8 shows the *Planck* 2018 sky maps in these nine different frequency channels. The CMB emission is most evident at frequencies from 30 to 217 GHz. The observations at low frequencies are affected by the foreground radio emission of synchrotron radiation emitted by electrons that spiral along the lines of the Galactic magnetic field from the interstellar material in the Milky Way, while at higher frequencies, the observations is dominated by the foreground emission from interstellar dust in the Milky Way.

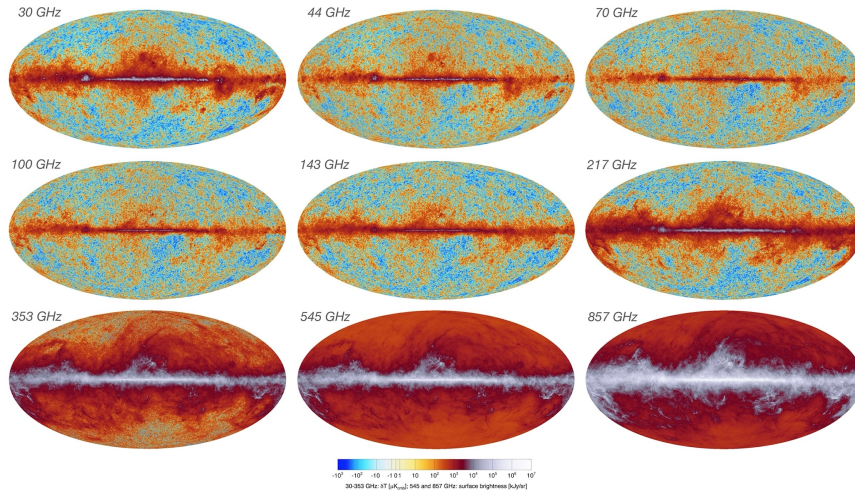


FIGURE 3.8: The fluctuation of sky emission at nine frequency channels after removal of a common dipole component by *Planck* 2018. The units are in μT_{CMB} for the first 7 frequencies, and in kJy sr^{-1} (conventional unit) for the two highest frequencies which monitor the dust emission.

The polarization of the CMB is due to Thomson scattering by free electrons of the local quadrupole at last scattering surface. It brings the key information of early stages of the universe such as the epoch of re-ionization, the inflation time and also the primordial gravitational waves produced at the end of inflation. Polarization can be decomposed into two independent modes: the gradient component E-modes, and curl component B-modes.

Planck has measured the CMB polarization at very low multipoles (large-scale) compared to previous *WMAP* and *COBE* missions. The sky polarization maps measured by *Planck* are shown in Figure 3.9.

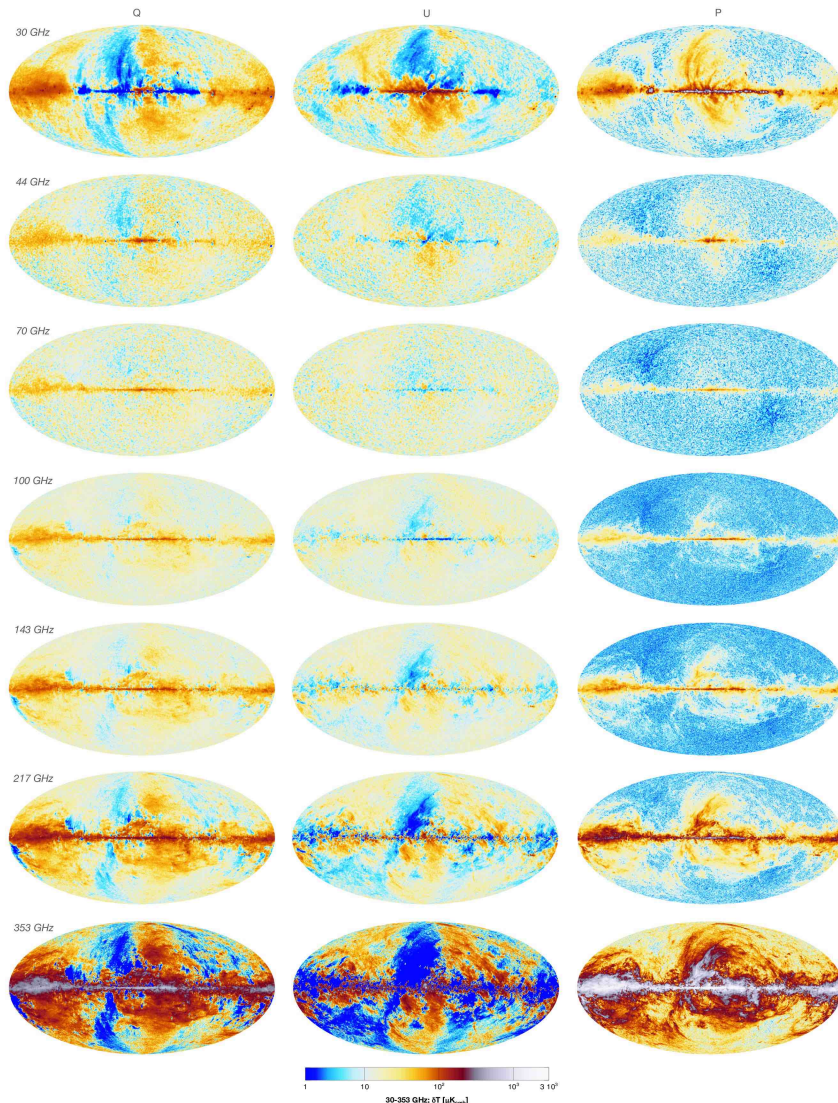


FIGURE 3.9: The sky polarization in seven frequency channels between 30 and 353 GHz of *Planck*, shown in Stokes Q and U, and well as in total polarized intensity $P = \sqrt{Q^2 + U^2}$.

Planck has used four different methods to combine the different frequency maps and separate the contribution of the CMB signal from all the astrophysical contaminants:

- Commander: a pixel-based parameter and template fitting procedure (Eriksen et al., 2008).
- NILC: a needlet-based internal linear combination approach (Basak and Delabrouille, 2013).

- SEVEM which employs template fitting (Leach et al., 2008; Fernández-Cobos et al., 2012).
- SMICA which uses an independent component analysis of power spectra (Delabrouille et al., 2003).

The polarization state of an incoming transverse electromagnetic wave is be fully described by four Stokes parameters: I (total intensity), Q and U describe the linearly polarized part, and V gives the circularly polarized part of radiation. Each method produces: CMB maps in Stokes I , Q , and U ; mask maps; an effective beam; and a noise estimate map, together characterizing the CMB. The differences between four maps can be use to estimate the uncertainty in the recovery of the CMB. The 2018 *Planck* CMB anisotropies map is shown in Figure 3.10.

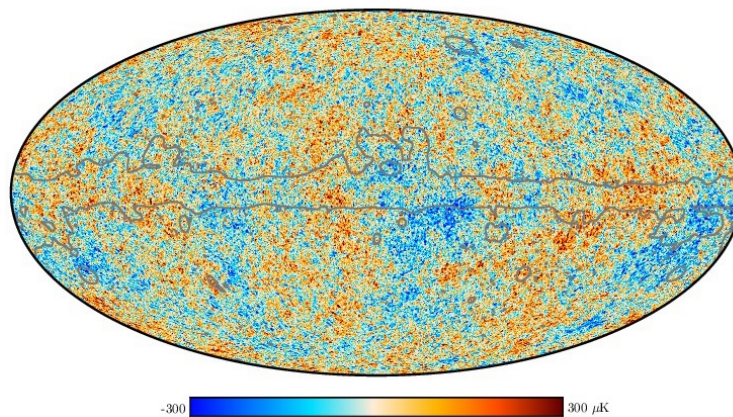


FIGURE 3.10: The 2018 *Planck* CMB map created by SMICA method. The grey line areas indicate the regions mostly around the Galactic plane where residuals from foreground emission are expected to be substantial.

The CMB angular power spectrum which is used to characterize the statistics of the tiny fluctuations in the CMB temperature is shown in Figure 3.11. This was done by a hybrid likelihood: an exact likelihood at large scales ($l < 50$), and a pseudo-spectral C_l power spectrum at smaller scales ($50 < l < 2500$; Planck Collaboration, 2016). The theoretical spectrum lines computed from the Λ CMB are very well fitted over all angular scales.

3.3.2 Cosmological parameters

The CMB temperature anisotropies discovered by Smoot et al. (1992) has become one of the most powerful tools to constraint the parameters, and describing the cosmological model. The CMB data from *Planck* were remarkable consistent with the flat Λ CDM model. This model is described by only 6 key parameters: baryon density parameter, dark matter density parameter, the age of the universe, scalar spectral index, curvature fluctuation amplitude,

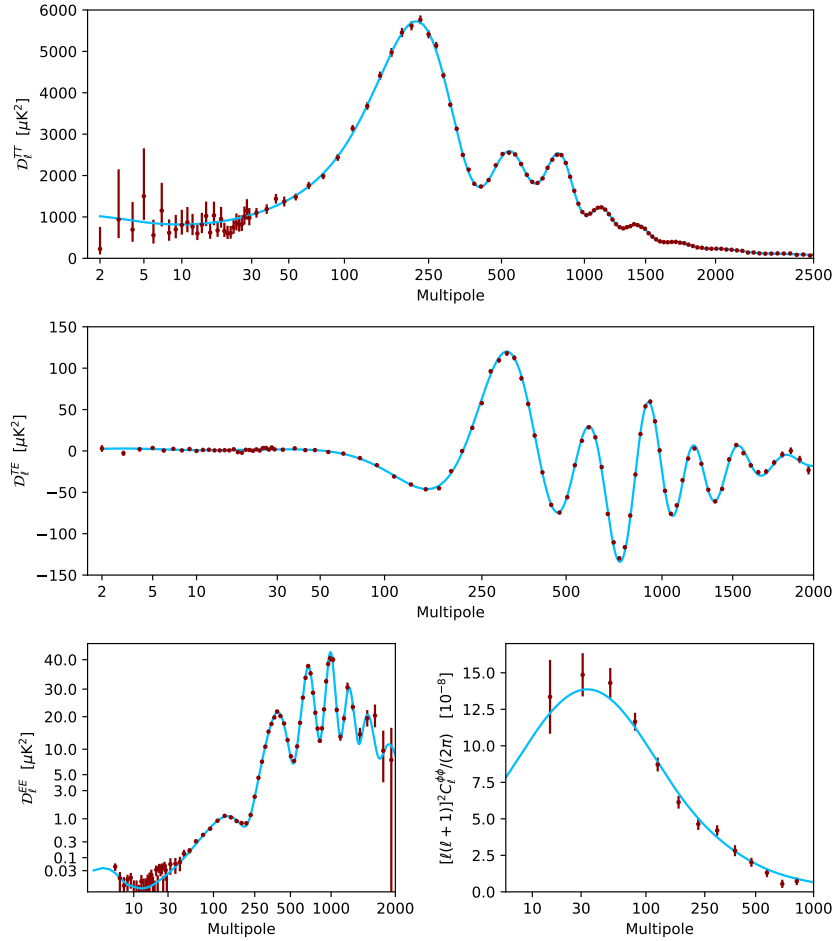


FIGURE 3.11: The 2018 *Planck* temperature power spectra (TT, TE, EE). These are foreground-subtracted, frequency-averaged, cross-half-mission angular power spectra for temperature (top), the temperature-polarization cross-spectrum (middle), the E mode of polarization (bottom left) and the lensing potential (bottom right). The red dots correspond to the measurement by *Planck*. The blue lines are the best-fitting model base Λ CDM.

The error bars show $\pm 1\sigma$ uncertainties.

and reionization optical depth. The *Planck* data alone, and in combination with other probes such as BAO, Type Ia supernovae, or the growth of structure determined by redshift-space distortions provided precise constraints on *Planck* cosmological models. To summarize these results, the constraint on the cosmological parameters measured by *Planck* 2018 are presented in Table 1.1. I give below some of the main conclusions presented by the Planck Collaboration et al. (2018b):

- The 6-parameter base- Λ CDM model provides a very good fit to the *Planck* TT, TE, and EE power spectra and to the *Planck* CMB lensing measurements, either individually or in combination with each other.
- The CMB angular acoustic scale $\theta_* = 0.5965$ deg is measured robustly at 0.03% precision, and is one of the most accurately measured parameters in cosmology.
- The *Planck* best fit base- Λ CDM cosmology is in very good agreement with BAO, supernovae, redshift-space distortion measurements and BBN predictions for element abundance observations. There is some tension at about 2.5σ with high-redshift BAO measurements from quasar Ly α observations, but no standard extension of the base- Λ CDM cosmology improves the fit to these data.
- The primordial fluctuations are consistent with Gaussian purely adiabatic scalar perturbations characterized by a power spectrum, consistent with the predictions of slow-roll, single-field, inflation. Combining with BICEP/Keck data on B-mode polarization *Planck* found a 95 % upper limit on the tensor-to-scalar ratio $r_{0.002} < 0.07$ (Planck Collaboration et al., 2018c). The predictions to the lowest order in the slow-roll approximation for spectral index n_s and tensor-to-scalar ratio r at $k = 0.002 \text{ Mpc}^{-1}$ of *Planck* and a few inflationary models are shown in Figure 3.12.
- The Hubble parameter determined by *Planck* $H_0 = 67.4 \pm 0.5 \text{ km s}^{-1} \text{ Mpc}^{-1}$ is in tension of 3.6σ with the latest local determination using Cepheids by Riess et al. (2018). But we have to consider that the Planck estimate is not a direct measurement but depends on the cosmological model.
- *Planck* combined with Pantheon supernovae (Scolnic et al., 2018) and BAO data provided a tight constraint on the equation of state of dark energy.

3.3.3 Cosmology from *Planck* galaxy clusters detected by SZ effect

Planck has constructed the thermal SZ (tSZ) all-sky maps from the individual *Planck* frequency maps, and also updated a catalog of 1653 sources, of which

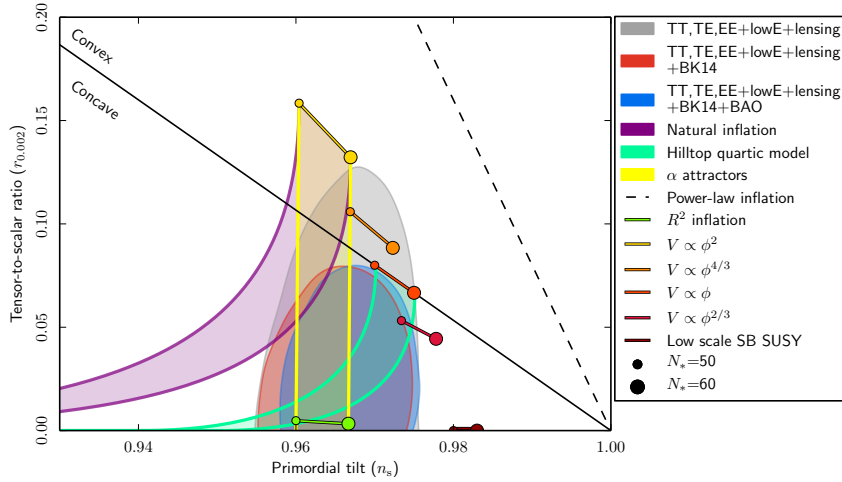


FIGURE 3.12: Marginalized joint 68% and 95% confidence level regions for spectral index n_s and tensor-to-scalar ratio r at $k = 0.002 \text{ Mpc}^{-1}$ from *Planck* alone (grey area) and in combination with BK14 (BICEP2/Keck) or BK14 plus BAO data, compared to the theoretical predictions of selected inflationary models. The lines show the predictions of a number of models as a function of the number of e-folds, N_* till the end of inflation. The black line divide between the concave and convex potentials. Credit: Planck Collaboration et al. (2018c).

1203 are confirmed galaxy clusters using the tSZ effect (Planck Collaboration et al., 2015). It was also the first SZ cluster catalog with more than 1000 confirmed galaxy clusters.

The *Planck* collaboration has published a number of articles to discuss how to do cosmology using *Planck* SZ clusters. *Planck* has shown that we can study the physics of hot gas in the Coma cluster (Planck Collaboration et al., 2013), or study the scaling relations of SZ flux Y_{500} and X-ray derived gas mass $M_{g,500}$, temperature T_X , and luminosity L_X (Planck Collaboration et al., 2011c). Besides, SZ cluster counts have been used to constrain the cosmological parameters σ_8 , and Ω_m as presented in Planck Collaboration et al. (2014b), and Planck Collaboration et al. (2016c).

In Chapter 5, I will present our results of studying the large-scale structure of the universe using the *Planck* SZ cluster catalog.

Chapter 4

Preparation of data processing for Euclid

As mentioned in Chapter 3, *Euclid* will perform imaging in VIS (wide band) and NIR. In order to achieve its scientific goals, it will also need narrow band imaging in the visible domain covering the same sky areas as studied by the *Euclid* mission in order to obtain high-precision photometric redshifts. Therefore, *Euclid* will need external data from ground based surveys. In order to prepare for the mission, the *Euclid* consortium has launched a number of Scientific Challenges and defined a series of milestones.

My work for this validation was done in the context of the External Simulation (SIM-EXT) in the period of the *Euclid* Scientific Challenge 3 (SC3). SC3 was one of the scientific challenges of the Science Ground Segment (SGS) team, which was the test of a realistic flow of operations among the different *Euclid* pipelines¹.

The result of this work was reported in the "Euclid SGS SIM Software Test Plan & Test Report, 2017" as an internal report of the *Euclid* Consortium and also at the *Euclid* Consortium Meeting in Bonn (Germany) in June 2018.

4.1 Scientific context

The discovery of the accelerated expansion of the Universe in 1998 is believed to be caused by an unknown mysterious component of the Universe: dark energy. Dark energy leaves imprints on cosmological observations via two regimes (DES Collaboration et al., 2018): modifying the curvature of the Universe which increases the distances and volumes over time in the universe, and suppresses the growth of cosmic structure. In order to understand the nature of dark energy we need to combine different cosmological probes (Frieman et al., 2008; Weinberg et al., 2013; Huterer and Shafer, 2018). That requires us to have more data with a deeper view (higher redshift) of wide sky area. The ongoing and upcoming sky surveys together will cover almost the full sky. Figure 4.1 presents the sky coverage area of *Euclid* and of some other surveys whose photometric redshift data will be additional data for the *Euclid* mission.

¹The Euclid Consortium Newsletter - Winter 2017

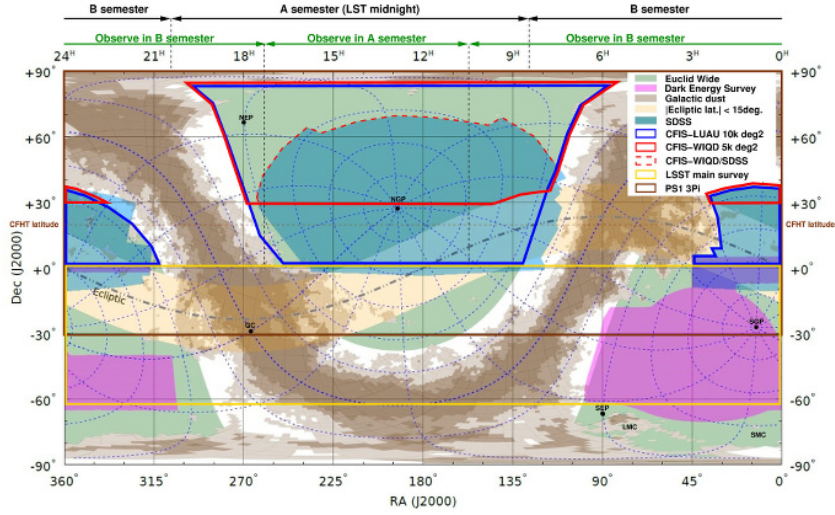


FIGURE 4.1: Sky coverage area of *Euclid* and of some other surveys. Credit: Jean-Charles Cuillandre.

Euclid is going to provide one of the sky surveys with the goal to discover the nature of dark matter and dark energy using the two main cosmological probes: Weak Lensing and Galaxy Clustering as mentioned in Section 3.1.2. *Euclid* will use the effect of Weak Lensing in order to map the three dimensional distribution of dark matter. That requires very high precision measurement of galaxy shapes which will be imaged with *Euclid* VIS. The galaxy distances will be inferred from the photometric redshifts. *Euclid* will perform NIR band photometry in 3 colors (Y, J, H). *Euclid* will also need complementary data for photometry from ground-based surveys² in optical bands:

- The Dark Energy Survey (DES): g, r, i, z in the south.
- The Kilo-Degree Survey (KiDS): u, g, r, i, z in the south.
- The Large Synoptic Survey Telescope (LSST): u, g, r, i, z, y in the south and partial or the north.
- The Javalambre Physics of the Accelerating Universe Astrophysical Survey (JPAS): g in the north.
- The Canadian France Hawaii Telescope (CFHT) CFIS survey: u, r in the north.
- PAN-STARRS: i, z in the north.

Table 4.1 shows the comparison of telescopes and photometry bands of *Euclid* and some complementary surveys.

The *Euclid* consortium is developing the scientific pipelines to process not only the future data of the satellite experiment, but also the external photometric data. At APC, we developed the image simulator for observations

²Euclid Data Processing, Martin Kümmel, 2018

4.2. CCD imaging in astronomy

TABLE 4.1: Overview of photometry bands and telescopes of *Euclid* and of some complementary surveys.

	Euclid		LSST	DES	KiDS	CFIS (Ibata et al., 2017)
	VIS	NISP				
Telescope	1.2 m		8.4 m (6.5 m effective)	Blanco 4 m	OmegaCAM / VST (VLT Survey Telescope)	3.6 m CFHT
Location	L2 (Space)		Cerro Pachón, Chile	Cerro Tololo Inter-American Observatory (CTIO), Chile	Paranal Observatory Cerro Paranal, Chile	Maunakea, Hawaii USA
Survey area (deg ²)	15,000 (Wide survey) 40 (Deep survey)		30,000	5000	780 N / 720 S (1500)	u-band: 10,000 r-band: 5000
FOV deg ²	0.53		9.6	2.2	1	1
Magnitude limit	24.5 (Wide survey) 26.5 (Deep survey)	24 (Wide survey) 26 (Deep survey)	r ~ 27.5	r ~ 24	u:24.8,g:25.4,r:25.2,i:24.2	u: 23.6 r: 24.1
Number of CCDs	36 (6x6)	16 (4x4)	189	74	32	40
Size of CCD	(4096 x 4132)	(2040 x 2040)	(4k x 4k) 3.2 Gp	519 Mp	(2k x 4k) 300 Mp	(2048 x 4612)
Size of pixel	0.1"	0.3"	0.2 "	0.27"	0.2"	0.187"
Filters	Wide band	y,j,h	u, g, i, r, z, y	g, r, i, z, y	u, g, r, i	u, r
PSF (Seeing)	0.1"	0.3"	0.6"	0.65"	0.7" - 0.9" (g)	0.6"

from the ground telescopes using their real instrumentation parameters as well as the effects of the observing process, such as the distortion of the telescope optics and the sky background.

The main objective of SC3 was to perform the following activities:

- To design and implement the first prototypes of the MER (Euclid and External data merging) and EXT (EXT-DES and EXT-KIDS) Processing Functions (PFs).
- To integrate them with the SGS Infrastructure components (Euclid Archive System, IAL, COORS) and with the other PF's : SIM (Image simulations), VIS (VIS image processing), NIR (NISP photometry image processing), SIR (NISP spectroscopy image processing).
- To deploy each PF on every SDCProd (Science Data Centre Production) through the CODEEN system.
- To run these PF's with input simulated data products : VIS/NIR/SIR/EXT (External data ingestion) on the various SDC's Prods.
- To analyze / check the output data products of MER
- To validate some scientific requirements.
- To prepare the Science Performance Review
- To store the output data in the EAS (Euclid Archive System).

At the moment, we are using the EXT simulator for KiDS, DES, and LSST. The simulator software and the output images need to be validated before being delivered to the next steps in the data processing pipeline (MER, PHZ, ...).

4.2 CCD imaging in astronomy

In this section, I will give very brief information about CCDs imaging in astronomy and also the definition of the useful terms which are used in this work.

Most astronomical detectors in use today are CCDs (Charge-Coupled Devices). A CCD is a light-sensitive integrated circuit device which converts the incoming light (photons) into electrons in each pixel during a certain exposure time. The charge-coupled device was introduced in 1970 by Amelio et al. (1970) and Boyle and Smith (1970) at Bell labs. The first astronomical image taken by CCDs was the planet Uranus taken by the scientists from the Jet Propulsion Laboratory (JPL) (Janesick and Blouke, 1987).

Before the invention of CCDs, the photographic plates were commonly used in astronomical imaging. However they have some limitation such as limited dynamical range and their response to the brightness of the illuminating light was non-linear, leading to persistent calibration problems. On the other hands, the CCDs have many advantages such as high sensitivity, high speed, low-power, low-noise CCD constrollers, large dynamical range and high quality image at the pixel resolution level. As a results, overtime CCDs have been improved and became very common in astronomical imaging. Figure 4.2 shows an example of a CCD manufactured by Teledyne E2v company which will be used on the science payload of ESA's *Euclid* mission.

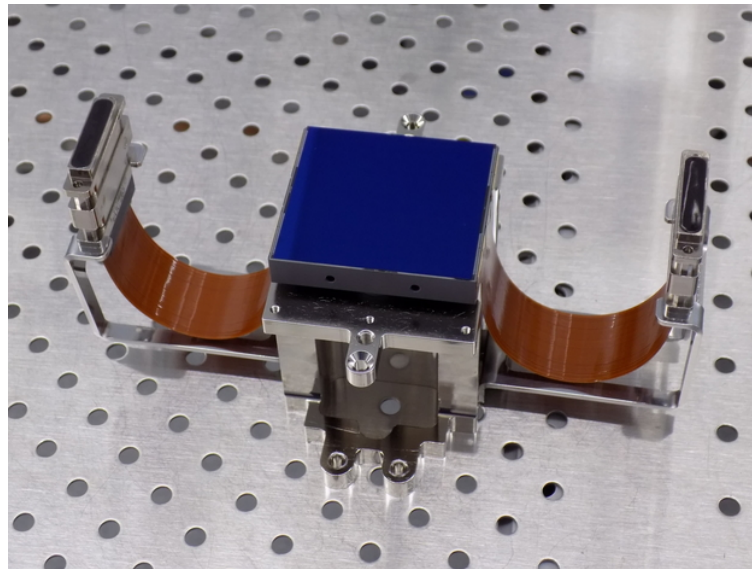


FIGURE 4.2: One of the *Euclid* VIS CCDs that will be used on the science payload of ESA's *Euclid* mission. Credit: ESA.

CCDs are manufactured in different sizes and shapes by different companies. CCDs may have sizes in square shapes such as 512 by 512 pixels, 2048 by 2048 pixels, or in rectangular shapes such as 2048 by 4096 pixels. The name of CCDs are usually a combination of the company name and the size of CCDs, for example: SITe4096, 4K x 2K e2v (Howell, 2000).

The spectral response of the CCD is defined by the quantum efficiency (QE). It is defined as the ratio of incoming photons to electrons actually detected or stored in the depletion region of the detector. Because CCDs are made of silicon which has a band gap energy of 1.14 electron volts (eV), so it

easily absorbs light of energy from 1.1 to 4 eV (300 nm to 1100 nm). Therefore, the band-pass available of a CCD is about 300 nm to 1100 nm (with QE of about 10% or more) (Howell, 2000).

The voltage of each pixel caused by electrons is measured and digitized, giving a number of counts or ADU (Analog-to-Digital Units) proportional to the number of electrons collected during the exposure time. The gain of a CCD represents how the amount of charge collected in each pixel will be assigned to a digital number in the output image. Gain values are given by the number of electrons needed to produce one ADU within the A/D converter:

$$G = \frac{\text{Number of electrons per pixel}}{\text{Number of counts per pixel}} \quad (4.1)$$

and the gain has unit of e^- / ADU .

There are some prior process needed to be taken into account to correct the raw image from CCD before using them for data analysis. The correction includes bias level, flat-fielding, overscan. These terms will be explained below.

In fact, before taking images with CCD, a CCD should undergo a process known as "wipping the array". The purpose of this process is to remove any residual dark current or photoelectron collection on the detector that may have happened during idle times between obtaining images. It also to ensure that the A/D converter will not have a negative number for the charge estimate due to read noise when the absorbed number of photons in a given pixel is small or zero. This process is called bias calibration.

There are two common process to evaluate the bias level: using overscan regions, or usage of bias frames. Bias frames are done by fast reading of unexposed pixel (shutter closes) of CCD. Overscan regions are virtual strips of rows or columns that are added to and stored with each image frame when CCD is read out. The mean level of overscan pixels or overscan level gives a measure of the average signal introduced when reading the CCD. Then we subtract the overscan level for all pixels within the CCD image. In practice, we usually take multiple bias frames and use the average of these frames to create a "master bias" to reduce the noise. Then we use the master bias to de-bias all other images.

Sometimes, when signal is recorded in each pixel of CCD, there is an additional component affects the image. This signal is called dark current or thermal noise due to the heat of the material in the CCD causes some charge deposition in the pixels. The amount of dark current depends on the operating temperature of CCDs. In order to limit this effect, all CCDs used in astronomy are cooled down to very low temperatures. This can be accomplished via the use of liquid nitrogen to cool the metal dewar in which CCD and associated electronics are placed inside. The devices are cooled down to temperatures near -100°C (173 K). A less expensive cooling method is the usage of thermo-electric cooling methods that allow CCD systems to operate at temperatures of -20° to -50°C (or 253 K to 223 K).

There are several other effects or unusual sources that may also affect images obtained from CCD such as cosmic rays, cross-talk, hot pixels, overexposure of bright sources... These effects must be taken into account when analyzing astronomical images. In this work I will not go into details of these effects. There are three main sources of noise in CCD measurements:

- Readout noise: generated by the electronics as the charge present in the pixels which is converted to a voltage on the CCD output (on-chip amplifier).
- Photon noise or shot noise: caused by the inherent natural variation of the flux of the incident photons which hit to the silicon's layer of CCD.
- Dark noise (dark current): arises from the statistical variation of thermally generated electrons within the silicon constituting the CCD.

4.3 Software and tools

In order to validate the simulation image, we have to detect objects in the image. In this work, I used *SExtractor* (Source Extractor³), which is a software to detect astronomical objects and create a catalog of sources (stars and galaxies).

SExtractor analyzes an image in 6 steps: estimation of sky background, thresholding, deblending, filtering of the detection, photometry, and star/galaxy separation (Bertin and Arnouts, 1996). Output catalog extracted from *SExtractor* contains information of image coordinates, world coordinates, magnitude, flux, sizes,.. of the objects.

The input configuration of *SExtractor* is very important for the object detection. It directly affects the quality of output parameters such as magnitude, flux, background, PSF, sky positions, image positions, and the classification of objects (for example to separate stars from galaxies). The complete configuration can be found in Bertin and Arnouts (1996) or in Holwerda (2005). The default `.sex` configuration file is usually used with modification of some parameters depending on the needs of the output catalog and the configuration of the input instrumentation.

In addition I also used DS9⁴, an astronomical imaging and data visualization application to check visually the output image.

All the unit test modules and image validation tests are written in Python. The unit test pipeline codes are published on *Euclid* GitLab⁵.

³*SExtractor*: <https://www.astromatic.net/software/sextractor>

⁴SAOImageDS9: <http://ds9.si.edu/site/Home.html>

⁵SIM-EXT Validator: https://gitlab.euclid-sgs.uk/PF-SIM/SIM_EXT

4.4 Validation of Euclid external data simulations

In this section, I will present the main results of my work on the validation of *Euclid* external data simulations. There are two main validations that are needed: the unit validation test and the image validation test.

- The unit validation test: unit tests in general are made to check the implemented features of the software independently. In our case, unit tests consist of individual module tests to check whether the associated input data fit with the expected output.
- The image validation test: to check quality of the output image and expected out parameters of a full simulation.

4.4.1 Unit test

The idea of the unit test is to test the code itself using simple parameters and check that the properties of output images are confirmed to what is expected. It helps us to track the errors in the simulation code and to improve the precision of the output simulation.

The input parameters are configured depending on the feature to be tested: background, astrometry, photometry, PSF (Point-Spread Function), and noise. The configuration of the input for this image simulation will be as minimal as possible.

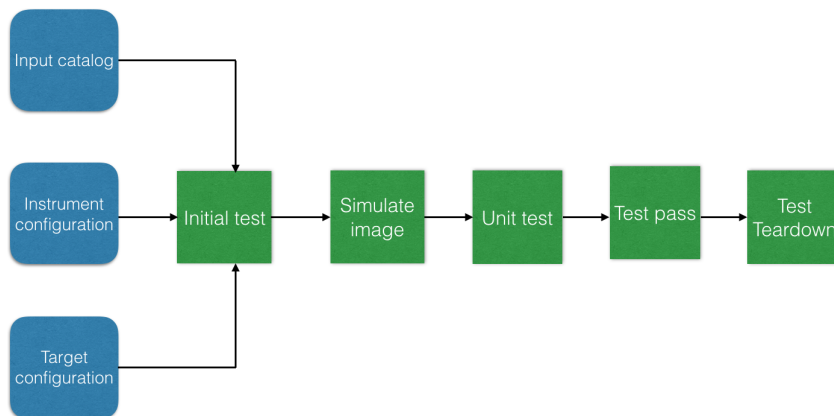


FIGURE 4.3: Unit test diagram

Figure 4.3 presents the unit test diagram. The input catalog is either an empty catalog (background test) or a catalog, which contains information of the sky positions, magnitude, and type of objects. The instrument configuration is a JSON⁶ (JavaScript Object Notation) file containing all information of telescope and CCDs. The target configuration is also a JSON file containing information on the telescope location, pointing direction, and filters mainly.

⁶<https://en.wikipedia.org/wiki/JSON>

Once we have all the necessary input files the program will simulate the image output file in the FITS (Flexible Image Transport System) format. The FITS format was first described by Wells et al. (1981). This format is characterized by pixel logical record, and formatted as N-dimensional arrays or tables with the use of substructure header. The header is stored in a human-readable ASCII format to present the image metadata. All the output images and configuration will be written to a work-space directory. The next step is to extract source information of output such as positions, or photometry, and size from the images and to provide this as input to the different unit test cases.

The output of the unit test is written in a separate folder. Depending on the success of the test, the data can be deleted or kept for further inspection.

The unit test was performed using KiDS and DES instrument parameters.

Background test

The first unit test I am going to describe is the background test. The purpose of this test is to check the simulation of the sky background signal. The way of the test is performed by using uniform sky signal which is defined by its magnitude per sky area, with zero bias, unity flat and no objects.

In our simulation each input object or sky background has a certain magnitude value. In order to test the flux in the output image we need to convert the magnitude to a flux value. Equation 4.2 shows the way to transform a magnitude value into total data numbers (DN) for each pixel or the pixel's value during an exposure time.

$$DN_{bg} = 10^{\frac{m_{zp} - m_{sky}}{2.5}} \times t_{exp} \times p_s^2 \quad (4.2)$$

where m_{zp} is the zero point corresponding to each CCD, m_{sky} is the sky background magnitude, t_{exp} represents the exposure time, and p_s is the size of a CCD pixel in arcsec unit.

We use this equation to convert the sky background from magnitude per unit area (surface magnitude) to pixel's value (unit of ADU or in counts), then compare to the flux (counts) of the background in the simulated image.

The noise of the measurement from the image consists of the photon noise (Poisson noise of the sky background) and the readout noise. Dark noise was not simulated so this parameter can be neglected.

$$\sigma_{counts} = \sqrt{\frac{1}{Gain} \times (DN_{bg} + Readout_{Noise})} \quad (4.3)$$

In this unit test the following set of parameters has been used: $m_{zp} = 24.95$, $m_{bg} = 24.35 \text{ mag arcsec}^{-2}$, $t_{exposure} = 180 \text{ s}$, $Gain = 2.49$, $Readout_{Noise} = 2.08$, and $p_s = 0.27''$. Therefore the expected noise is equal to 2.56 ADUs.

Figure 4.4 shows the distribution of flux of the background in ADU. It is a Gaussian distribution with the standard deviation of 2.5, which is slightly

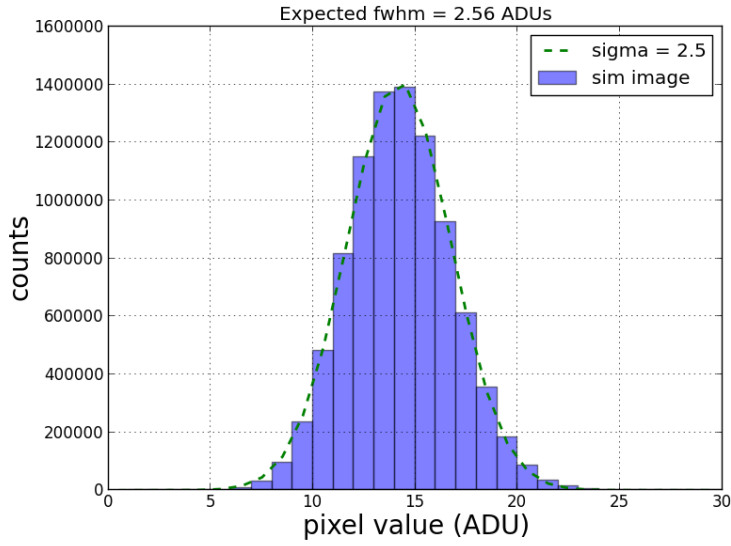


FIGURE 4.4: Distribution of flux in a simulated image containing only sky background flux.

smaller than the expected value. Therefore, this test demonstrated that the sky background simulation was acceptable.

Stars

In the next step we are going to simulate an output image with some starlike objects included. Stars are considered to be point sources in the sky because they appear to be a point as they are very far. Three main unit tests are considered for the simulated image: positions, photometry, and shape.

In order to simulate the image of star objects, an input catalog of objects of only starlike objects with magnitude $m = 18$ mag was created. This magnitude value is within the magnitude limit detection of KiDS photometric system. Then, we simulate the image and use *SExtractor* to extract the output catalog from the image.

Position test The point spread function (PSF) describes the response of an imaging system to a point source. Because stars are point sources, they give a measurement of the PSF. The purpose of this test is to check the position of output objects compared to the input position of these objects. It includes the test of position in image coordinates, and also in world coordinates or in equatorial coordinates. The header of FITS image can contain information about one or more scientific coordinate systems: Cartesian coordinate system that describes the location of each pixel in the image, and World Coordinate System (WCS) to present the relationship between pixel coordinates in the image and sky coordinates such as the equatorial coordinate system. Therefore, we check the position of objects in both coordinate systems.

- Positions in image coordinates

We match the input and output objects within the distance of 3 pixels and make the subtraction of position between the input and output objects. Figure 4.5 and Fig. 4.6 show the distribution of pixel position difference between the input and output.

As can be seen in Fig. 4.5, the difference of positions between the input and output is less than 0.1 pixels and are centered at 0 in both dimensions, X and Y of the image. What is important is that on average they are zero (with a precision of 0.1 pixels)

Figure 4.6 shows more clearly in each dimension of the distributions of the difference between the input and output positions which have Gaussian shapes with centers at 0 pixel. There are very few matching objects which have a difference of positions larger than 0.1 pixels and smaller than 0.1 pixels. The position of these objects are not very well detected by *SEXtractor*. They are the objects near the edges of the CCD inducing layer uncertainty in the position measurement.

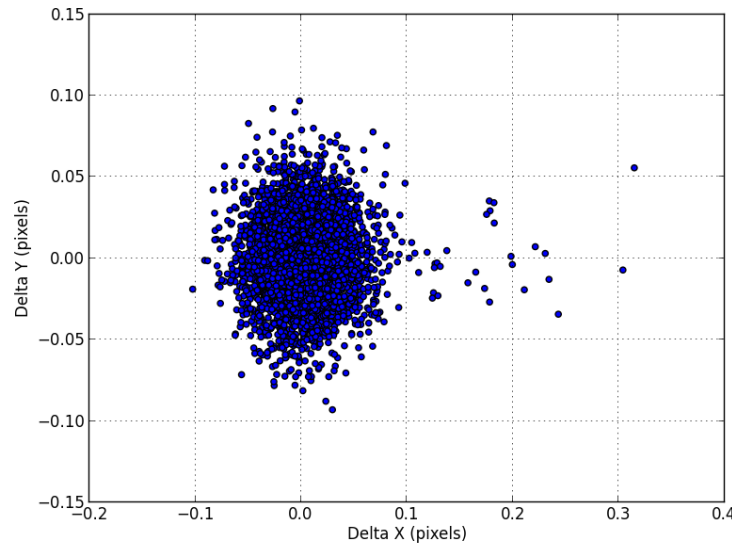


FIGURE 4.5: Distribution of difference of the pixel position between the input and output objects. The center of distribution for both coordinates is 0 pixel. Only some matching objects have ΔX from 0.1 to 0.4 pixels.

- Position in world coordinates

We match the input and output objects within the distance 0.72'' (about 3 pixels). Figure 4.7 shows the histogram of the difference in sky coordinates between the input and output objects. In both histograms the differences are less than 0.05 arcsecond and have the center of histogram at 0 arcsecond. These differences of sky coordinate distance are consistent with the differences of image pixel distances.

In summary, the position of stars of the simulation is very good and pass our test.

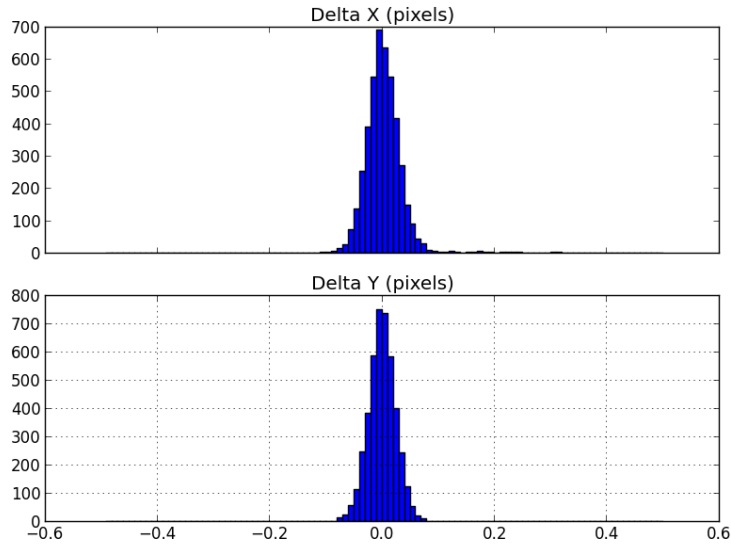


FIGURE 4.6: Histogram of difference of the pixel position for each axis between the input and output objects.

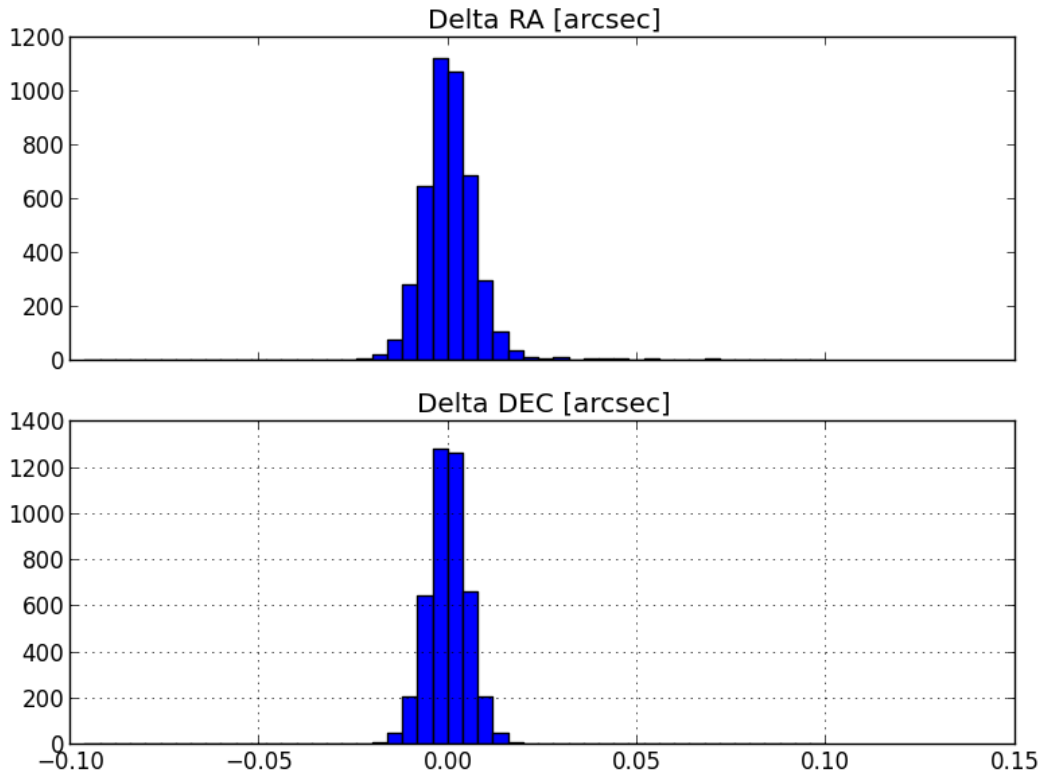


FIGURE 4.7: Distribution of difference of the world coordinate position between the input and output objects. The center of distribution for both RA and DEC axis are 0 arcsec. Similar as pixel coordinates test, some matching objects have delta RA from 0.025'' to 0.075'' (about 0.3 pixels).

Star photometry We create an input catalog with only stars at magnitude $m = 18$. As we mentioned above we choose arbitrary value of magnitude in the limit detection of KiDS photometric system. Each star is distributed at every 100 pixels. The relation between magnitude and flux of object is:

$$F = 10^{\frac{m_{zp}-m}{2.5}} \times t_{exp} \quad (4.4)$$

We use this equation to estimate the expected flux of simulation object.

How do we estimate the photometry?

Photometry is a technique to measure the flux or intensity of astronomical objects. A simple method to measure the photometry from astronomical image is the aperture photometry as presented in Mighell (1999). The four main steps of this method are:

- Determining the centers of the objects.
- Determining the nearby background.
- Summing the pixel counts within an aperture centered on the object.
- Subtracting the product of the nearby average sky count per pixel and the number of pixels within the aperture.

In our unit test, we already had the image position of input objects. This is the center position of the simulated object derived from the image. Next step is to determine the aperture radius of objects. A small aperture will not contain all the flux. In practice, the optimize aperture radius is in order of the PSF value to compromise between systematic centering errors and reducing signal-to noise ratios typically obtained with large aperture radii. However, we know precisely the positions of starlike objects and the distances between them in our simulation, therefore we can make larger aperture radius. We integrate the flux around the center position of each object within the radius of 4 times the PSF of the input object (about 13 pixels) to ensure that we cover almost 100 % flux of object. This is the aperture radius of object.

We estimate the background flux by summing pixels in an annulus between 25 and 30 pixels from the source. The background flux per pixel is the total background flux of the annulus divided by the area of the annulus. Thus the estimated flux of the object is the aperture flux minus the background flux in the aperture.

Figure 4.8 shows the distribution of estimated sky background flux using the method described above. It can be clearly seen that this is a Gaussian distribution with the mean about 15 ADUs which is same value of the background flux in background test as shown above.

The estimated flux of all objects is around 5 % lower than the expected flux as shown in Figure 4.9. We also compare the flux of output catalog by *SExtractor* with the expected flux.

Figure 4.10 shows the distribution of the estimated flux by *SExtractor*. The estimated flux by *SExtractor* is also about 5% lower than the expected flux.

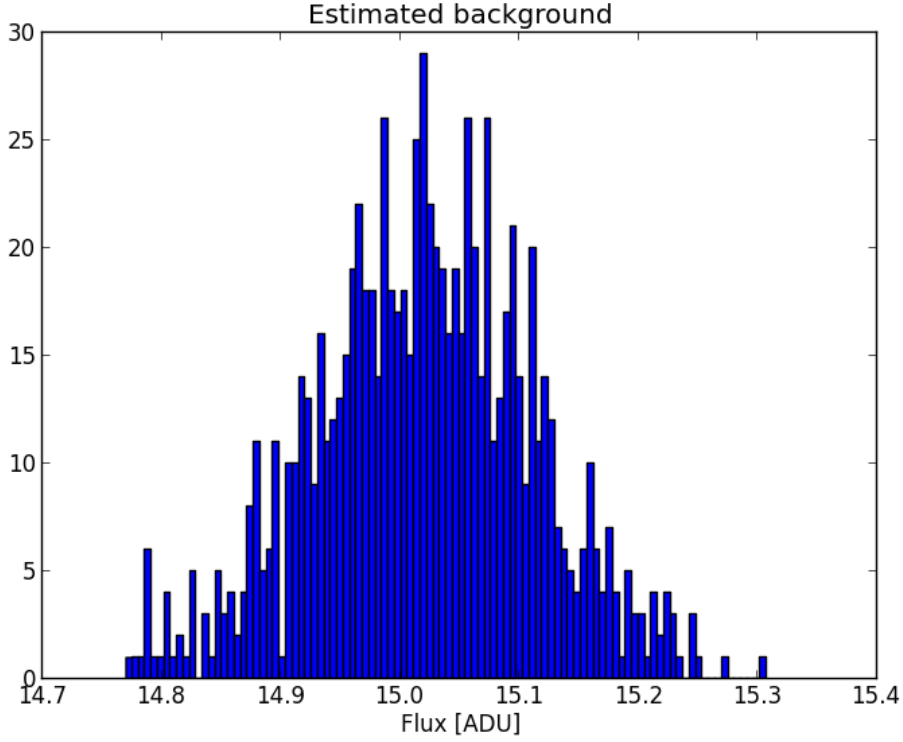


FIGURE 4.8: Distribution of estimated sky background flux.

There is a problem with the simulation image which cause the discrepancy of flux between input and output. In fact, this was due to the scattering of atmospheric aerosol parameter. We have checked again in unit test and found that if we don't use this parameter in the unit test simulation, we obtain the correct output flux.

Shape We used the constant PSF (point spread function) so whatever configuration of the PSF of the input does not effect to the output. The 2D Gaussian PSF can be described as:

$$f(x, y) = A \times \exp \left\{ - \left[\frac{(x - x_0)^2}{2\sigma_x^2} + \frac{(y - y_0)^2}{2\sigma_y^2} \right] \right\} + B \quad (4.5)$$

where:

- A is the amplitude of the PSF, with the unit in ADU.
- x_0, y_0 are the center of the distribution, unit in pixel.
- σ_x, σ_y are the spread of the PSF in x and y . In the case of symmetric Gaussian PSF: $\sigma_x = \sigma_y$.
- B : the background noise, unit in ADU.

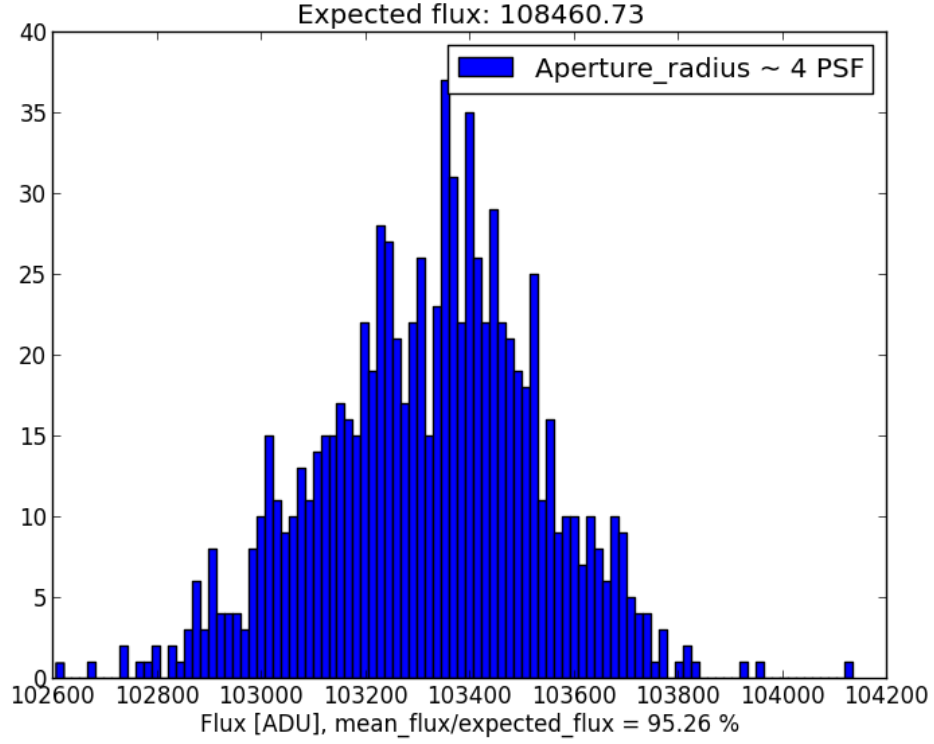


FIGURE 4.9: Distribution of estimated flux. The estimated flux is less than the expected flux by about 5%

In this test, we set the KiDs-like parameters: $m_{zp} = 24.95$, $m_{bg} = 24.35$ mag arcsec⁻², $t_{exp} = 180$ s, and pixel size is $p_s = 0.27''$. The input PSF (or FWHM) of KiDS optical system of the telescope and the atmosphere is $0.9''$. We have $FWHM = 2\sqrt{2 \times \ln(2)}\sigma = 0.9''$, so the expected standard deviation is $\sigma = 0.382$.

The distribution of the standard deviation of the shapes of output objects is shown in Figure 4.11. As can be seen in this figure, we obtained a Gaussian distribution of the standard deviation with the mean is about 0.38 in both dimensions. The small differences between expected σ and output is due to the contribution of the background.

Galaxies

The purpose of a unit test is to validate that each function of the code works properly. We performed an extra test using galaxy-like objects. In this subsection, we will present the results of the distribution of the difference in positions of output compared to input, and the distribution of the standard deviation of the shape of output.

Galaxies are considered to be extended sources. The surface brightness of a galaxy decreases with increasing radius. The two most common profiles to describe the surface brightness of galaxies are the exponential and Sersic

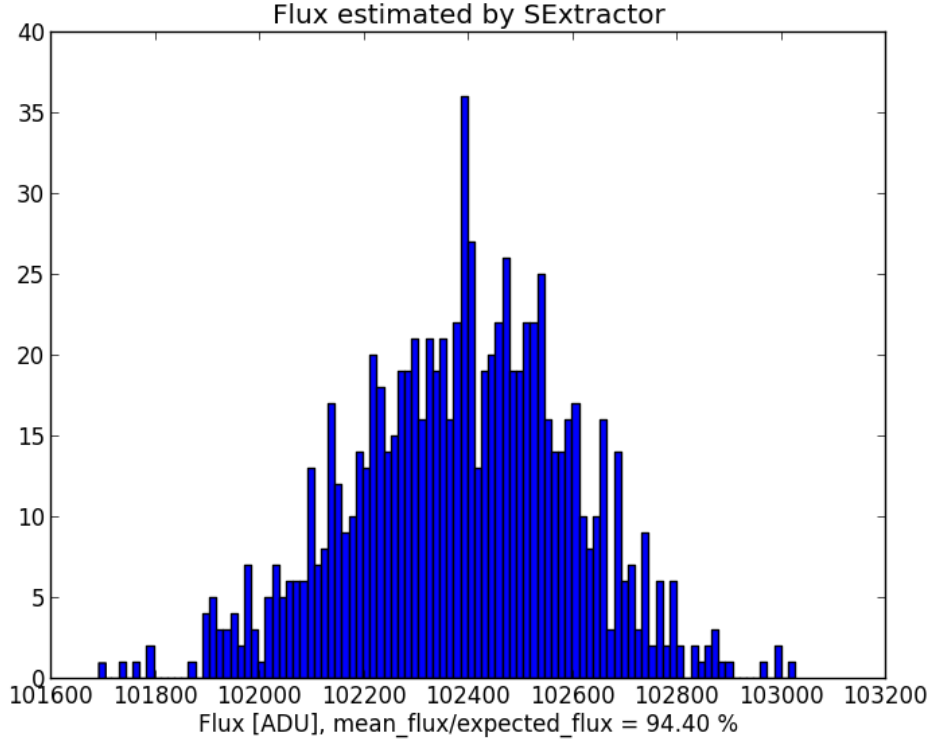


FIGURE 4.10: Distribution of estimated flux by *SExtractor*. The estimated flux is less than the expected flux about 5.6%

profiles (Trujillo et al., 2001). However, we are only interested in testing the code in this case, thus the exact shape of the galaxies is not relevant. Therefore we created and applied the most simple galaxy profile. We considered the intensity distribution of a galaxy to be a 2-D symmetric Gaussian. It can then be described as in Equation 4.5 with background $B = 0$.

The output galaxy image is the convolution of the input galaxy with the PSF of the instrument. We created an input galaxy catalog with magnitude $m = 17$, which also corresponds to the detection limit of the KiDS instrument. The stamp galaxy file profile is simulated using the distribution in Equation 4.5 with $A = 0.05$ and $\sigma_x = \sigma_y = 30$ pixels. The pixel size of the stamp is 0.05 arcsec. The size of the stamp is 300×300 pixels². The PSF of the telescope is 0.9". Each galaxy is arranged at every 100 pixels.

The expected standard deviation of the shape of the output in each axis is: $\sigma_{x'} = \sqrt{\sigma_{PSF}^2 + \sigma_x^2} = 1.548$ arcsec. The distribution of $\sigma_{x'}$ and $\sigma_{y'}$ of the output is shown in Figure 4.12. As can be seen in this figure, the mean values of the standard deviation of the shape of the output in both axes are slightly larger than the expected value.

The distribution of difference of the position between the input catalog and the output catalog is shown in Figure 4.13. It can be seen that the difference is centered at 0.

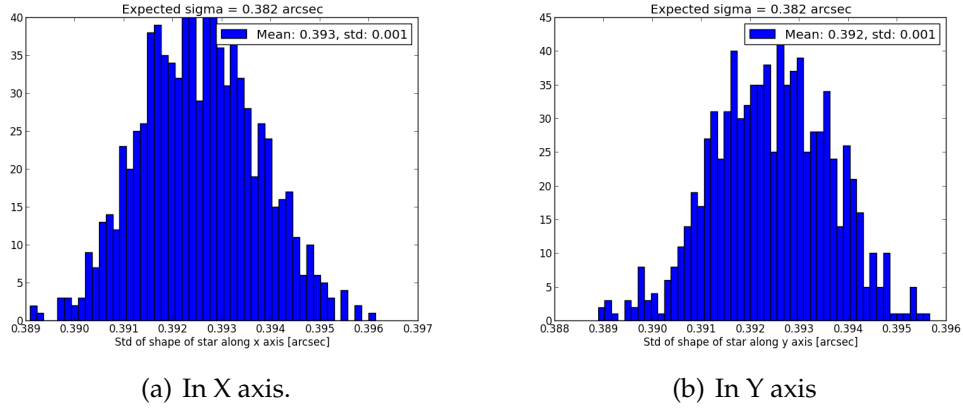


FIGURE 4.11: The distribution of standard deviation of the shape of output objects.

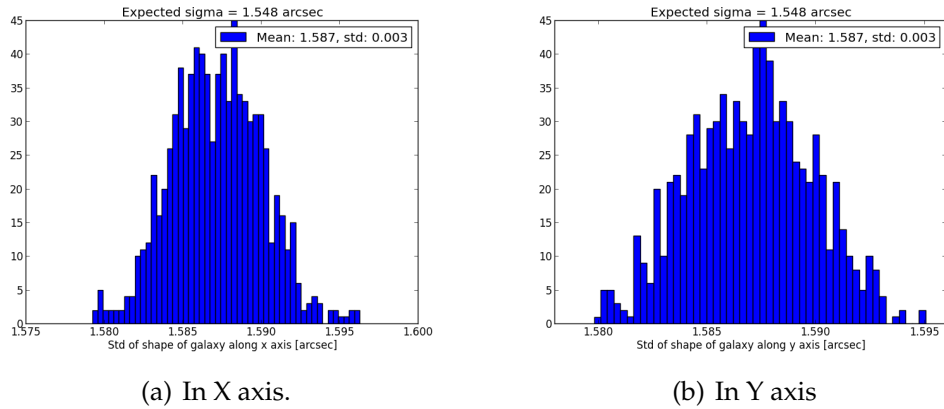


FIGURE 4.12: Distribution of the standard deviation of the shape of galaxy output.

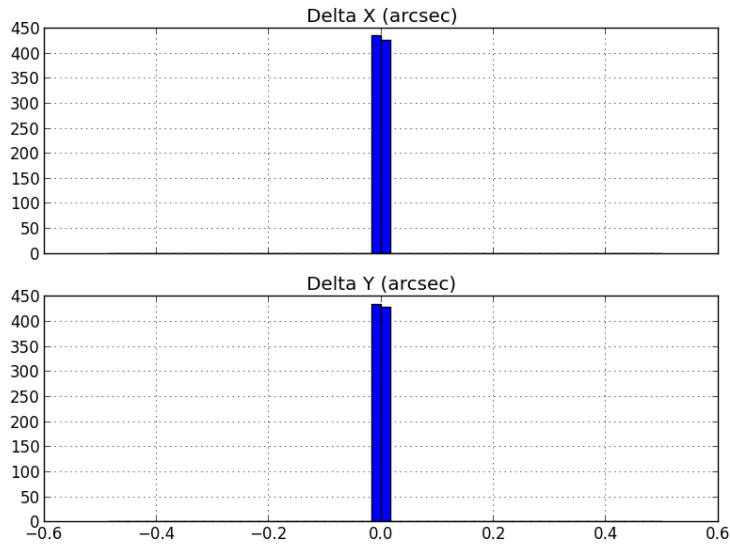


FIGURE 4.13: Distribution of difference of the world coordinate position between the galaxy-like input and output objects.

Conclusions

These tests are part of the unit test which executed automatically after each modification of the code to ensure the quality of the code. We tested the output of the image simulator by checking functions with the simplest parameters in turn. We found the problem with the position of output image as presented in next section. We fixed this problem with the unit test. We have demonstrated that the unit test is necessary and useful in next stages of Science Challenges for *Euclid* when we re-factorize the code.

4.4.2 Validation of KiDS image simulation

Overview of KiDS CCDs

The Kilo-Degree Survey (KiDS) is a large optical imaging survey in the Southern sky. This survey uses the 2.6-m VLT Survey Telescope (VST), which is installed at the Paranal Observatory of the European Southern Observatory (ESO) on Cerro Paranal in Chile. The KiDS cover a total of 1500 square degrees of the extragalactic sky in 4 bands (u, g, i, r). The primary science goal of this survey is dedicated to weak gravitational lensing (de Jong et al., 2013).

The KiDS detector is the wide-field OmegaCam imager of VST. The OmegaCam consists of 32 2k x 4k CCDs, for a total mosaic detector of 16k x 16k pixels. The pixel size on the sky is 0.21 arcsec. Figure 4.14 shows the layout of the 32 CCDs of OmegaCAM of KiDs.

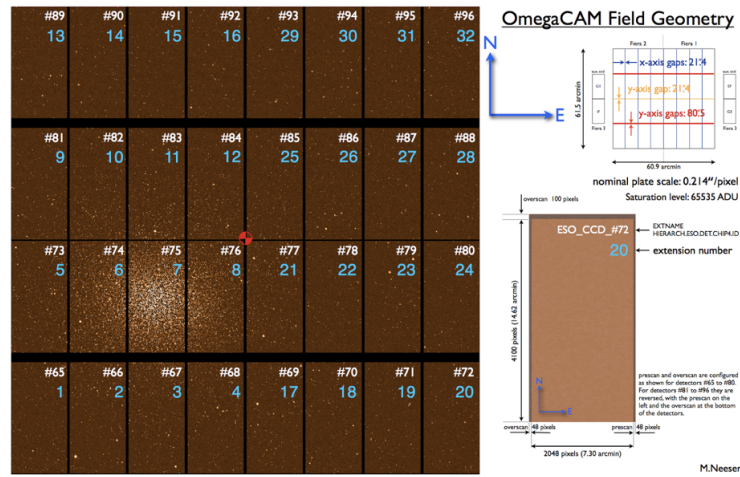


FIGURE 4.14: The arrangement of KiDS CCDs. Credit: M. J. Neeser.

Input catalog

The input catalog consists of stars and galaxies. The input parameters of galaxies are from a flagship simulation in which is called the "True Universe", and the input parameters of stars were from another simulation using the Besançon model (Debray et al., 2006). Table 4.2 shows the information about the input catalog.

Image validation

This part is about the validation of the KiDS image in the g filter, which was released on April 20, 2017.

Figure 4.15 shows the image of the first CCD. The magenta area is the overscan area of the CCD. Most part of the image shows a green color, which is the sky background which have the pixel value below 290 ADUs. The simulated objects appear in yellow colors.

4.4. Validation of Euclid external data simulations

Number	Name	Unit / Type	Description
1	OBJTYPE	Integer	Type of object: star=0, galaxy=1
2	X_WORLD	Deg	Right ascension
3	Y_WORLD	Deg	Declination
4	MAG	Float	Magnitude of object
5	STAMPFILE		Thumbnail of object
6	STAMPID	Integer	Id of thumbnail

TABLE 4.2: Input catalog

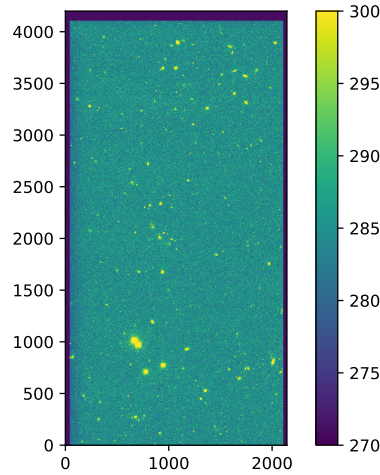


FIGURE 4.15: Display of the first CCD of the KiDS simulation image. The magenta area is the overscan area of the CCD. The yellow points are the display of the simulated objects.

The original input catalog contains 109,410 objects. We select only objects that fall on the footprint of CCDS, and exclude objects in the overscan areas of CCDs. After this selection, we got 52,476 input objects.

First, we use *SExtractor* to extract an output catalog from the simulation image. We get 28,964 output objects, which is about 55.2% of the objects in the input catalog. Figure 4.16 shows the spatial distribution of input and output objects. Step by step we are going to check the output catalog and to compare with the input catalog the magnitudes and positions of objects.

Figure 4.17 shows the distribution of magnitude in the input and output catalog. As we can see from this figure, the most of the magnitude distribution of the input and output objects is relatively consistent with each other in the magnitude bins of bright objects (magnitude bins $m < 23$). There are only few magnitude bins in which the number of output objects is slightly larger than the number of input objects. In higher magnitude bins (i.e. for fainter objects), we detected less output objects. This is because of the noise which masks the objects and also part of the problem of flux simulation of output objects as we saw in the unit test. Because we loss about 5% of flux of

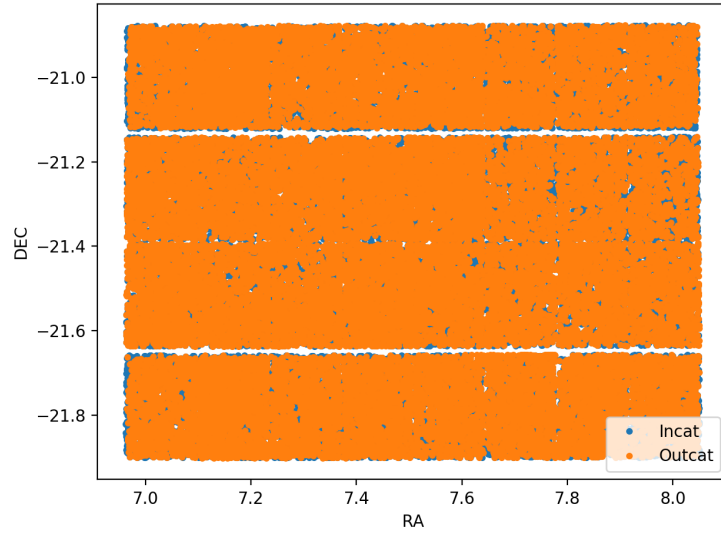


FIGURE 4.16: Distribution of input and output objects in the KiDS simulation image. All input objects are selected within the footprint of the KiDS CCDs. The two big white gap areas are the gaps of the CCDs layout.

output objects so the faint input objects became even fainter and not detected by *SExtractor*.

We search for the matching objects between the input and output catalog: finding the closest output object around each input object within a distance: $\leq 0.36''$ (at a pixel size of 1 pixel = $0.214''$) of all CCDs. We choose a matching distance smaller than 2 pixel to ensure that we have less surrounding objects that have similar positions. We derive 20,314 matching objects which are about 39 % of the input catalog and 60 % of the output catalog.

Figure 4.18 shows the positions of some matching objects on the first CCD of the simulation image. As we can see, the positions of output objects (represented by circle symbols) seem to be correct, which are in the center of simulation objects (yellow points). On the other hand, the output positions are shifted with respect to the input objects.

Figure 4.19 represents the distribution of the difference of positions of matching in all CCDs. The distribution of the difference of matching objects in Y dimension is centered around 0. However, most of the matching output positions in the X dimension of the image are shifted to the right by about 1 pixel compared to the matching input objects. This indicates that there was a problem in the generation of the simulation output.

In conclusion, the simulated KiDS images were not correctly generated. Two main problems are apparent concerning the simulation image:

- There is a discrepancy between the output and input flux. This discrepancy has been detected through the unit test. The reason for this problem came from the configuration of the SkyMarker part of the SIM EXT simulation pipeline.

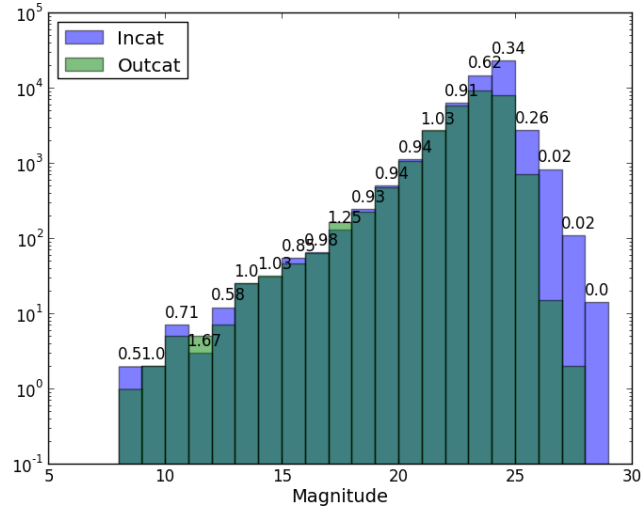


FIGURE 4.17: Magnitude distribution of input and output objects of KiDS simulation image. The numbers on top of each bin are the ratio of number of output objects with respect to the input objects.

- The position of the output objects is shifted by 1 pixel in X dimension of the image compared to the input objects. This has been identified to be an error in the simulation code to simulate the position of output.

Both problems were detected in the unit test and have been fixed.

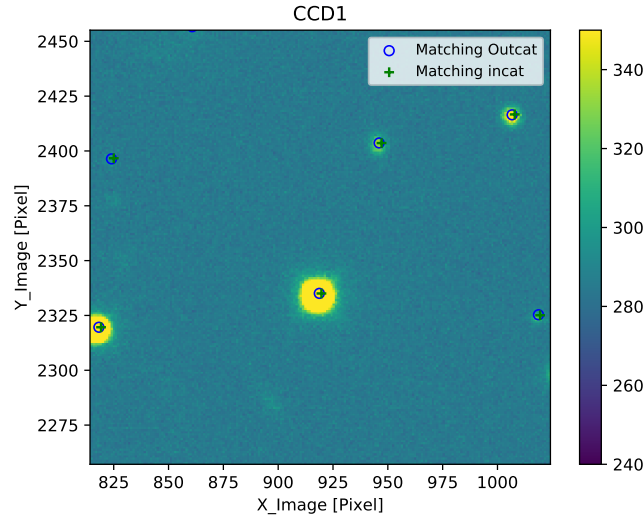


FIGURE 4.18: Positions of some matching objects on the first CCD of the simulation image. The yellow bright points are the simulation objects. The blue circles are the matching output objects, and the green crosses are the matching input objects.

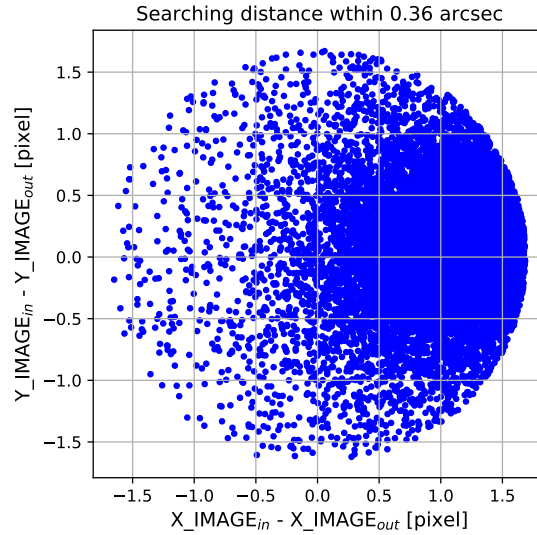


FIGURE 4.19: Position difference of matching objects on all CCDs of simulation image. While the position difference of matching objects in Y dimension is centered around 0 pixel, the difference in X dimension is shifted by about 1 pixel.

4.5 Conclusion

The unit test and image simulation test show how effective we can use these tools to verify simulated images. Especially, the unit test is very useful to check individual components of the simulation code.

The result of the unit test has been reported to the *Euclid* SIM EXT simulation team during the SC3 challenge. It was also extremely useful for the next simulation stages when the simulation team re-factorized the simulation code. The SIM-EXT simulation team decided to change to the new simulation code using the core simulation code from GALSIM (Rowe et al., 2015) instead of SkyMarker. Because the SkyMarker is an outdated code while GALSIM is a new project of simulating astronomical objects and is now widely used and frequently updated by a large astronomical community.

Chapter 5

Studying the large-scale structure of the universe using galaxy clusters

Modern cosmology observations have found strong evidence to support the cosmological principle, which states that the distribution of matter in the universe is both isotropic and homogeneous on large scales. The most obvious evidence comes from observations of the CMB and the distribution of galaxies. The CMB observations by the *COBE*, *WMAP* and *Planck* satellites have shown that the relic radiation from the Big Bang is well approximated as a uniform blackbody radiation distribution in all directions of the sky with a temperature of about $T = 2.725$ K (Fixsen and Mather, 2002). There are very tiny fluctuations in the temperature of the CMB (at about one over one million level) which correspond to the different densities of the sky. These fluctuations seen in the CMB result from the short period of inflation when the quantum fluctuations happened that seeded the formation of structures we observe in the universe today. Large-scale structures of the universe refer to the scales larger than the scale of galaxies (Coil, 2013). On these scales, due to gravity, galaxies gather into galaxy clusters, superclusters, and filaments, leaving voids between filaments. Figure 5.1 shows the distribution of galaxies from the SDSS survey¹. As we can see from this figure, galaxies are distributed in groups and filaments, creating the large structure of the cosmic web.

On the largest scales, still in the linear regime, this distribution is uniquely characterized by the two-point correlation function (or, equivalently, the power spectrum). Riding the highest peaks in the density field, galaxy clusters are effective tracers of the matter distribution, and their two-point correlation function is consequently an important cosmological observable.

Many large-scale galaxy redshift surveys have been carried out to cover large volumes and scales in which galaxy clusters catalogs were conducted to study the clustering and distribution of clusters. I will summarize in Section 5.1 basic properties of some large galaxy cluster catalogs and the results of investigations using them as a tracer of the large-scale structure of the universe.

¹<https://www.sdss.org/science/orangepie/>

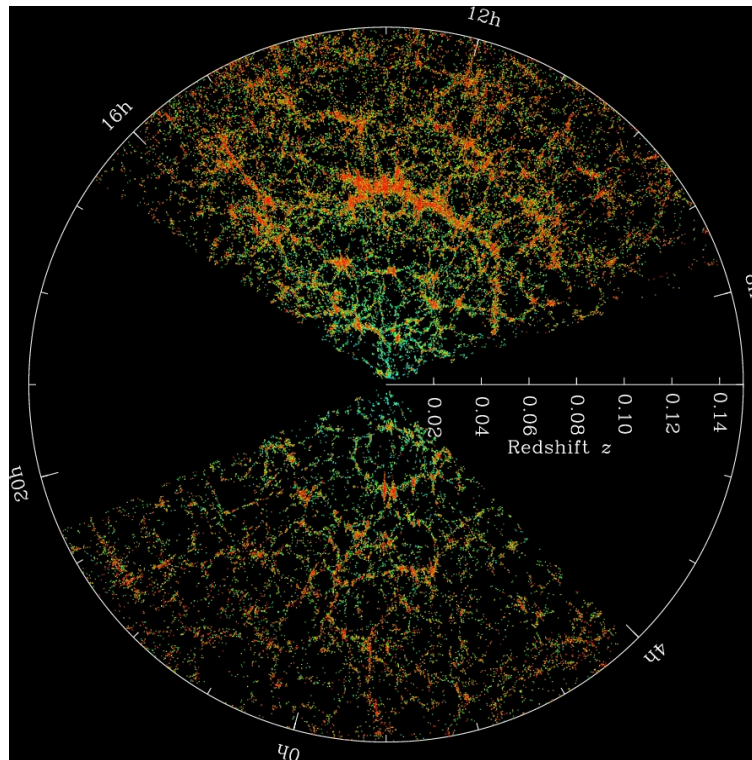


FIGURE 5.1: The distribution of galaxies from the SDSS survey. Each dot is a galaxy, and the color of each galaxy presents the g-r color of that galaxy. Credit: M. Blanton and SDSS.

I will present the estimators of the two-point correlation function in Section 5.2, and how to estimate the correlation length in Section 5.2.3. I will show the result on the two-point angular correlation function of the *Planck* SZ cluster catalog in Section 5.3. In Section 5.4, I explore the potential of measuring the two-point correlation function of the *Euclid* flagship simulation dark matter halo catalog.

5.1 The clustering correlation of existing cluster catalogs

A major step of measurements of the large-scale structure with galaxy clusters catalog have been accomplished by Abell (1958). This first Abell cluster catalog contained 2712 rich clusters of galaxies. It was based on detections by means of a visual inspection of the photographic plates of the Palomar Observatory Sky Survey (POSS). This catalog covers the sky from the north celestial pole down to declination -27° . Each cluster has at least 50 members with magnitudes in the range m_3 to $m_3 + 2$, where m_3 is the magnitude of the third brightest galaxy. This is how Abell defined the richness of clusters. Abell classified them into 6 richness groups. The redshifts of objects in the Abell cluster catalog are in the range $0.02 \leq z \leq 0.2$. The Abell catalog gives information such as the clusters' position on the sky, the distance group

D from 1 to 6 according to the magnitudes of their tenth-brightest members, and the richness classification R from 0 to 5. Bahcall and Soneira (1983) found that the clustering of clusters in the Abell catalog can be approximated by a power law of the two-point correlation function with a correlation length of $25 h^{-1} \text{Mpc}$. I will explain in detail the definition of the correlation length in the power law approximation of the two-point correlation in the next section. Abell et al. (1989b) extended their catalog with 1361 clusters in the southern hemisphere using the Deep Southern Sky Survey plates taken with the Schmidt telescope at Siding Spring in Australia.

A larger catalog of 9134 galaxy clusters was compiled along with a catalog of galaxies by Zwicky et al. (1961–1968). This cluster catalog also was identified based on the POSS fields. This is also a rich clusters catalog, each object having at least 50 galaxy members within 3 magnitudes of the brightest member². However, the definition of clusters in the Abell catalog is more exact than the one in the Zwicky catalog (Einasto, 2001). The Zwicky catalog has many more clusters than Abell catalog due to lower density and less rich systems. Postman et al. (1986) found large-scale inhomogeneities in the Zwicky catalog, which may be caused by the variations in the depth of Palomar Sky Survey plates. They also showed that the angular correlation function of nearby Zwicky clusters is about 10 times smaller than that for nearby Abell clusters, and at depths, the angular correlation functions of both cluster catalogs are the same.

Shectman (1985) presented 646 galaxy clusters that have been selected from the Shane-Wirtanen counts of galaxies using the Lick Observatory survey (Shane and Wirtanen, 1967), which have magnitudes brighter than (lower than) 19 mag. The Shectman clusters were selected by finding local density maxima above a threshold value, after lightly smoothing the data to reduce the effect of the sampling grid. The clusters of the Shectman catalog are located at galactic latitudes above 40° and declinations larger than 22.5° . The clusters in this catalog have a higher space density than the Abell clusters. About 40% of the Shectman clusters are also members of the Abell catalog. There are about 70% of Shectman clusters that are Abell clusters at distance class $D = 4$. The two-point angular correlation function of the Shectman clusters catalog is two times weaker than the angular correlation of Abell $D \leq 4$ clusters (Shectman, 1985).

Lumsden et al. (1992) presented a cluster catalog selected from the Edinburgh/Durham Southern Galaxy Catalogue (EDSGC; Collins et al., 1989). As described in Lumsden et al. (1992), the galaxy data from the EDSGC catalog were constructed from accurate calibration, better star-galaxy separation, and using a powerful deblending routine to discriminate between different galaxies in rich cluster cores. As a result, the Edinburgh/Durham cluster catalog has been constructed through a combined Shectman-Abell approach with reducing projection effects. Projection effects refer to the unwanted effects caused by foreground and background galaxies which may create false

²<https://heasarc.gsfc.nasa.gov/W3Browse/all/zwclusters.html>

cluster detection in over-dense regions. This cluster catalog contains 737 clusters of galaxies covering 1500 deg^2 of the sky, centred on the South Galactic Pole. About 70% of clusters in this catalog are brighter than magnitude 18.75, which is approximately 1 magnitude fainter than the Abell catalog. In comparison with the Abell clusters in the same region, 80% of the Abell clusters are brighter than the Edinburgh/Durham clusters. Nichol et al. (1992) studied the two-point correlation function of this catalog. They found the correlation length of these clusters to be about $16.4 h^{-1} \text{ Mpc}$, which is lower than the correlation length of the Abell clusters. Dalton et al. (1994) obtained a similar result on the two-point correlation function of 364 rich clusters selected from the APM galaxy survey (Maddox et al., 1990) with a clustering length of $14.3 h^{-1} \text{ Mpc}$.

The different results between rich Abell clusters and the others are caused by the richness dependence of the correlation function, as shown by Park and Lee (1998). When using the correlation function on the APM clusters, increasing the richness limit from $R = 53$ to $R = 80$, the correlation length increases from 17.5 to $28.9 h^{-1} \text{ Mpc}$.

Over the last decades, the development of multi-color CCD photometry has enabled further advances in galaxy surveys with more precise measurements of redshift and also providing the galaxy color. A large optical catalog, the MaxBCG, with 13,823 galaxy clusters (Koester et al., 2007) from the Sloan Digital Sky Survey (SDSS; York et al., 2000) was selected using the maxBCG red-sequence method, based on the color of the galaxies as explained in Section 2.2. This catalog covers $7,500 \text{ deg}^2$ of the North Galactic cap, with a redshift range from $z = 0.1$ to $z = 0.3$. The two-point correlation function of the MaxBCG cluster catalog and some early clusters selected from the SDSS have been studied by Bahcall et al. (2003), Basilakos and Plionis (2004), and Estrada et al. (2009). The results from these work showed that the correlation length of SDSS clusters correlated with the richness of the clusters: richer clusters have larger correlation lengths. Besides, Hong et al. (2012) using a catalog of 13904 galaxy clusters at $z \leq 0.4$ extracted from the SDSS by Wen et al. (2009) found a strong BAO signal on scales of $20 h^{-1} \text{ Mpc} \leq r \leq 200 h^{-1} \text{ Mpc}$, demonstrating again the value of clusters in tracing the matter distribution on large scales.

In parallel with the optical cluster catalogs, also X-ray cluster catalogs, and SZ cluster catalogs have been studied. While the X-ray clusters are detected based on the strong emission produced from the ICM in the X-ray band by thermal Bremsstrahlung radiation of hot electrons, SZ clusters are detected through the distortion in the CMB spectrum caused by the inverse Compton scattering of CMB photons on the same electrons. Both methods help us to detect clusters not only at higher redshifts compared to the optical surveys, but are also less sensitive to projection effects (Basilakos et al., 2003).

Many X-ray clusters have been found through X-ray surveys, such as the *Einstein Observatory Extended Medium Sensitivity Survey* (EMSS) catalog by Gioia and Luppino (1994), the *X-ray-brightest Abell-type clusters of galaxies* (XBACs) from the ROSAT All-Sky Survey by Ebeling et al. (1996), Romer et al. (2000),

Böhringer et al. (2000), and Böhringer et al. (2004). Using the two-point correlation function of X-ray cluster data, the studies in Borgani et al. (1999), Moscardini et al. (2000), and Collins et al. (2000) also found a correlation length of 12-26 $h^{-1}\text{Mpc}$, which depends on the brightness or flux limit of the cluster samples.

Recently, the CMB surveys provided by the ACT, SPT and *Planck* missions with high angular resolution compared to the *COBE* and *WMAP* missions have constructed SZ cluster catalogs based on the signature of the SZ effect when the CMB photons pass through galaxy clusters. See for example Hasselfield et al. (2013), Bleem et al. (2015), and Planck Collaboration et al. (2016d). As I mentioned in Chapter 2, *Planck* has detected larger, more massive, and lower redshift clusters, and also covers a larger sky area compared to ACT and SPT.

I present the results on the angular two-point correlation function of *Planck* clusters in Section 5.3.

5.2 The two-point correlation function

As mentioned briefly in Section 1.3.2, the two-point correlation function is used as a statistical tool to quantify the clustering of large-scale structures such as galaxies, galaxy clusters, voids, etc. It is used to trace the clustering as function of scale either in spatial distance r or in angular distance θ : two-point spatial correlation $\xi(r)$ or two-point angular correlation function $w(\theta)$. When we speak about the two-point correlation function, we usually refer to the spatial correlation. The two-point correlation is defined as the excess of joint probability dP of finding a pair of objects in volume elements dV_1 and dV_2 at separation $r_{12} = |\vec{r}_1 - \vec{r}_2|$ compared to a uniform random distribution (Peebles, 1980):

$$dP = n^2[1 + \xi(r_{12})]dV_1dV_2 \quad (5.1)$$

where n is the mean number density of the object sample. For a uniform random distribution ($\xi = 0$), the probability of finding pair of objects is the square of mean density and volume elements and independent of the distance. The object positions are correlated if $\xi > 0$, and anti-correlated if $\xi < 0$. In general the measurement of $\xi(r)$ is performed in comoving distance with r having the unit of $h^{-1}\text{Mpc}$. The two-point correlation function is related to the power spectrum $P(k)$ (Baugh and Efstathiou, 1993) by:

$$\xi(r) = \frac{1}{2\pi^2} \int_0^\infty P(k) \frac{\sin(kr)}{kr} k^2 dk \quad (5.2)$$

where k is a comoving wavenumber. The two-point correlation function and power spectrum are the Fourier transform of each other. Both give same statistics to quantify the clustering of the matter density distribution but in different forms.

5.2.1 Estimators of the two-point correlation function

Many estimators of two-point correlation function have been studied in the literature. The most early and simple estimator was defined by Peebles and Hauser (1974) using the ratio of the number of pairs of data with number of pair of random in different distance bins:

$$\hat{\xi}_{PH}(r) = \frac{DD}{RR} - 1 \quad (5.3)$$

where:

- $DD = \frac{2 \times P_{DD}}{n_d(n_d-1)}$ is the normalized number of data pairs separated by a spatial distance comprised in the interval $[r - dr/2, r + dr/2]$.
- $RR = \frac{2 \times P_{RR}}{n_r(n_r-1)}$ is the normalized number of random pairs separated by $[r - dr/2, r + dr/2]$.
- n_d, n_r are the total number of data and random points in the survey volume.

In 1982, Davis and Peebles (1983a) introduced another estimator to estimate the two-point correlation of the Center for Astrophysics (CfA) Redshift Survey:

$$\hat{\xi}_{DP}(r) = \frac{DD}{DR} - 1 \quad (5.4)$$

where: $DR = \frac{P_{DR}}{n_d \times n_r}$ is the normalized number of cross data - random pairs. This estimator has an advantage compared to the first estimator because the edge effects are automatically accounted for because it uses the cross count sum between the random and data samples.

A better estimator of the two-point correlation function was presented by Hamilton (1993):

$$\hat{\xi}_H(r) = \frac{DD \times RR}{DR^2} - 1 \quad (5.5)$$

They showed that this estimator has a second order uncertainty in the mean density while David-Peebles estimator has a first order uncertainty. Therefore Hamilton estimator has smaller bias on larger scales. There are other estimators such as Hewett (1982), Szapudi and Szalay (1998), Landy and Szalay (1993). Kerscher et al. (2000) made the comparison of several estimators of two-point correlation. They showed that the Hamilton estimator and Landy-Szalay estimator display the smallest deviation and the best edge correction on large scales. In practice, the most commonly used estimator is the Landy-Szalay estimator:

$$\begin{aligned} \hat{\xi}_{LS}(r) &= \frac{DD - 2DR + RR}{RR} \\ &= \frac{P_{DD}}{P_{RR}} \frac{n_r(n_r-1)}{n_d(n_d-1)} - \frac{P_{DR}}{P_{RR}} \frac{n_r-1}{n_d} + 1 \end{aligned} \quad (5.6)$$

5.2. The two-point correlation function

Landy and Szalay have shown that this estimator has a lower variance which is nearly Poisson. Besides, the Landy-Szalay estimator is recommended to use because of it has small variance, as shown by Pons-Bordería et al. (1999), and by Kerscher et al. (2000). Figure 5.2 shows the comparison of different estimators of two-point correlation functions and their uncertainties of simulated mock galaxy samples of the SDSS survey from the study by Labatie et al. (2010). The Landy-Szalay and the Hamilton estimators have the smallest uncertainties.

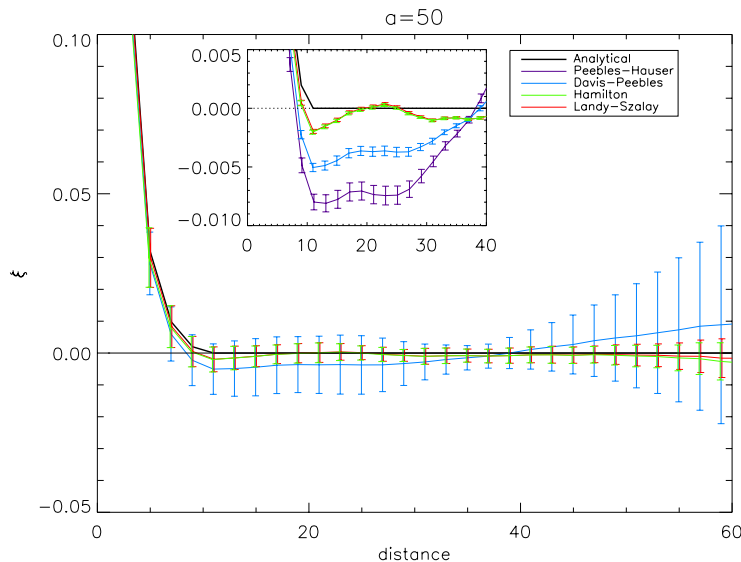


FIGURE 5.2: Comparison of the different estimators and their uncertainty of two-point correlation function of the simulated mock galaxy samples of the Sloan Digital Sky Survey for a cube size $a = 50 h^{-1}$ Mpc. The error bars are estimated using 512 realizations. The Landy-Szalay estimator (red bars) has the lowest uncertainties in all scales. The Hamilton estimator has similar values as Landy-Szalay estimator. The inset shows the bias of each estimator (error bars are equal σ/\sqrt{N} with N being the number of realizations). Figure from Labatie et al. (2010).

The angular two-point correlation function is defined similarly, simply replacing the 3-dimensional spatial distance r by the angular separation between pairs θ . Figure 5.3 illustrates counting number of pairs in a projected separation of radius $[\theta, d\theta]$. The angular two-point correlation function is especially used when the redshift information of the data sample is not available to derive the spatial correlation function or too few samples in the catalog.

5.2.2 Error estimation of the two-point correlation function

There are different ways to determine the statistical uncertainties of the two-point correlation function. Norberg et al. (2009) explained some of them and classify them into two different categories:

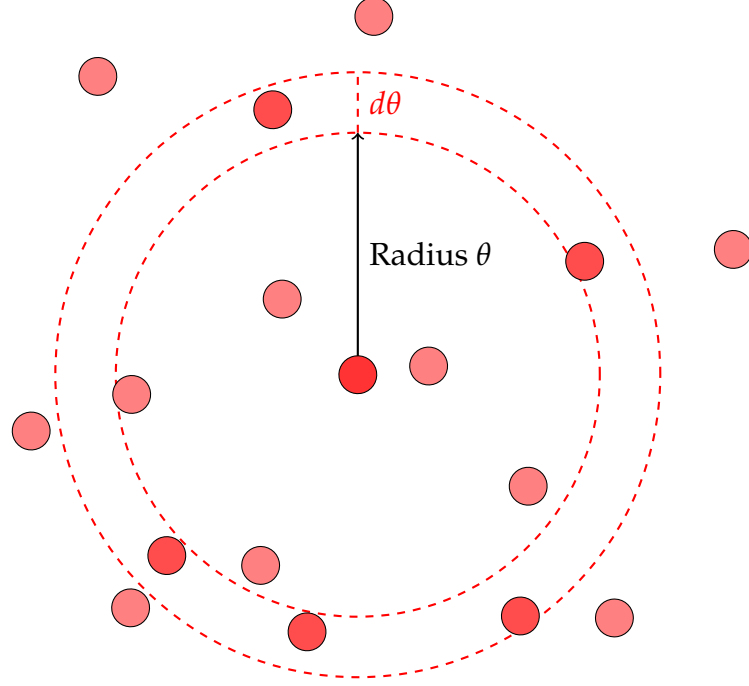


FIGURE 5.3: An example of the illustration of counting number of pairs of objects in small angular separation $d\theta$. Each circle represents for an object on the sky, and we count the number of bold red objects in small angular separation $d\theta$.

- External method: Monte Carlo realizations or mock simulation.
- Internal methods: the sub-sample, the jackknife, the bootstrap

The Monte Carlo realizations is a method to create mock sample by assuming we know the underlying statistical and physical processes which shaped the observed data. We use N-body simulation to model the clustering evolution in the universe, and also apply the observational effects. In fact, it is hard to account for all these effects and these are the difficulties with N-body simulations, which are very costly in terms of computational time.

In the **sub-sample method** we split the sample into N_{sub} independent sub-samples, and the covariance matrix then is given by:

$$C(x_i, x_j) = \frac{1}{N} \sum_{k=1}^N (x_i^k - \bar{x}_i)(x_j^k - \bar{x}_j) \quad (5.7)$$

where x_i^k, x_j^k are the estimated correlation at the i^{th} and j^{th} bins of the k^{th} of N subsamples; \bar{x}_i and \bar{x}_j are the mean of all sub-samples measurements at the i^{th} and j^{th} bins. However, this method has major drawback because for galaxy clustering studies in the universe the sub-samples are never fully independent of each other regardless of the clustering scales. This is because

of presence of long-range modes in the density fluctuations, making all sub-samples to some extent correlated with each other. This causes false assumption to study the clustering in the universe.

The jackknife (Efron, 1982) is a method to estimate the variance and bias originally invented by Quenouille (1956) and refined by Tukey (1958). A jackknife sample is defined by systematically leaving out a sub-sample in which the data has been split into N sub-samples from the original sample. The jackknife estimator is estimated by take the average of the estimates of each $(N - 1)$ remaining sub-sample. In order to estimator the error the two-point correlation function of cluster sample, a jackknife resample X is generated by omitting a sub-region of which the survey's area is divided into N regions which have the same cluster densities. The covariance matrix of N jackknife resamplings is given by (Norberg et al., 2009):

$$C_{ij} = \frac{N-1}{N} \sum_{k=1}^N (\xi_i^k - \bar{\xi}_i)(\xi_j^k - \bar{\xi}_j) \quad (5.8)$$

where: ξ_i^k, ξ_j^k are the estimated correlation at the i^{th} and j^{th} bins of the k^{th} sub-sample; $\bar{\xi}_i$ and $\bar{\xi}_j$ are the mean of all jackknife measurements at the i^{th} and j^{th} bins. The factor $N - 1$ on the numerator of the above equation takes into account the lack of independence between the N resamplings of the data. The errors of jackknife resamplings are the square-root of the diagonal elements of the covariance matrix. The advantage of this method is that we can estimate the uncertainties correctly on large scales. However this method significantly overestimates the variance on small scales.

A similar method of the jackknife is **the bootstrap method** (Efron, 1979). The bootstrap method is widely used to estimate the bias and standard error of an estimate. The idea of this method is that the clusters in original catalog are drawn randomly to create N bootstrap resamples in which each bootstrap resample has the same total number of clusters as the original sample. We choose N - the number of bootstrap re-samples in which the error of our estimator is converge. The covariance matrix of N bootstrap resamplings of data is computed by:

$$C_{ij} = \frac{1}{N-1} \sum_{k=1}^N (\xi_i^k - \bar{\xi}_i)(\xi_j^k - \bar{\xi}_j), \quad (5.9)$$

where ξ_i^k, ξ_j^k are the values of the two-point correlation function at the i^{th} , and j^{th} bins respectively of the k^{th} bootstrap resample; and $\bar{\xi}_i, \bar{\xi}_j$ are the mean value of all bootstrap resamples at the i^{th} , and j^{th} bins. The common advantage of the bootstrap and jackknife methods is that we do not need to implement mock simulations which require a lot of computational time and also have to well define underlying physics of the evolution of matters and selection functions. Besides, in principle with the bootstrap method we can create arbitrary number of resamples. In practice, the variance on a measurement

converges relatively slowly.

The errors σ_{θ_i} in each bin of the two-point correlation are obtained from the diagonal elements of the covariance matrix:

$$\sigma_{\theta_i} = \sqrt{C_{ii}} \quad (5.10)$$

In this work, I will use the bootstrap method to calculate the error of our correlation function. There is a problem with bootstrap method that we might obtain asymmetry distribution of the number of pairs of clusters in some certain bins because there might be few or no clusters in these bins. As consequence, I will not use these bins for power law fitting in our analysis. However, I will check under the null hypothesis test to verify the clustering of our result as I will present in next section.

In the analysis of the two-point correlation function of our data to compare with the previous works and also fitting the power law, we perform the chi-square minimization to obtain the best fit of the two-point correlation function.

$$\chi^2 = \sum_{i,j} [w(\theta_i) - w_m(\theta_i)]^T C_{ij}^{-1} [w(\theta_i) - w_m(\theta_i)] \quad (5.11)$$

where: θ_i , and θ_j are bins i and j angular bins, C_{ij}^{-1} is the inverse covariance matrix of the correlation function of clusters resamples, and w_m is a model.

5.2.3 The power law approximation of the two-point correlation function.

In the literature, many studies have shown that at the scale $r \leq 60 h^{-1} \text{Mpc}$ the two-point correlation function is well modelled by a power law (Peebles, 1980; Estrada et al., 2009):

$$\xi(r) = \left(\frac{r}{r_0}\right)^{-\gamma} \quad (5.12)$$

where r_0 is the correlation length of clustering that at this scale $\xi(r) = 1$ and the clustering strength becomes comparable to the probability of the homogeneous distribution, and $\gamma > 0$ is the scaling exponent or the power index.

The power law of two-point correlation function of galaxies is sometimes referred to as the 1.8 power law on scales smaller than $10 h^{-1} \text{Mpc}$ because the power law index $\gamma = 1.8$ was first found by Totsuji and Kihara (1969). In other studies, the value of γ was also close or equal to 1.8, for example in Peebles (1980) and Davis and Peebles (1983b).

However, the power law of correlation of galaxies as the function of spatial distance does not exactly follow this power law index. Baugh (1996) found that the correlation of galaxies in APM galaxy survey (Maddox et al., 1990) fitted very well with the power law in Equation 5.12, in which $\gamma = 1.7$ and $r_0 = 4.1$ on scales $r \leq 4 h^{-1} \text{Mpc}$. Baugh found a "shoulder", which is a rising of correlation function above that power law at scales $4 h^{-1} \text{Mpc} \leq r \leq 25 h^{-1} \text{Mpc}$. The power index and also the correlation

length of the power law of the correlation function depend on luminosity and spectral type of the galaxies. For example, Norberg et al. (2002) showed that the power law index varies between $\gamma = 1.69$ and $\gamma = 2.01$, and that r_0 varies between 5.19 to $9.74 h^{-1}$ Mpc when they investigate the dependence of galaxy clustering on luminosity and spectral type using the 2dF Galaxy Redshift Survey (2dFGRS).

The two-point correlation function is well fitted by a power law not only in galaxy surveys but also in galaxy cluster surveys. Many galaxy surveys based on optical and X-ray data showed that the exponent index γ varies from 1.6 to 2.1 depending on the richness of clusters as well as on the analyzed sample. Moreover, Watson et al. (2011) found that the power law of the correlation function not only depends on the mass of galaxies, which is equivalent to the luminosity of galaxies, but also depends on redshift.

As Efstathiou (1993) summarized of the studies from Bahcall and Soneira (1983) that the power law correlation of Abell clusters catalog (Abell, 1958) and its extension to the Southern hemisphere (Abell et al., 1989a) can be approximated by a power law shown in Equation 5.12 with $r_0 = 25 h^{-1}$ Mpc and $\gamma = 1.8$ over scale $r < 100 h^{-1}$ Mpc. Using 13,904 galaxy clusters from the SDSS survey, Hong et al. (2012) obtained a larger correlation length which depends on the richness of clusters: $r_0 = 18.84 \pm 0.27 h^{-1}$ Mpc for clusters with richness $R > 15$, $r_0 = 16.15 \pm 0.13 h^{-1}$ Mpc for clusters with richness $R \leq 5$; here the power index $\gamma = 2.1$ is almost the same for all cluster sub-samples. Another study by Estrada et al. (2009) using the MaxBCG galaxy clusters from the SDSS survey have found that the correlation length is in range of 14 to 20 h^{-1} Mpc which depends on the richness. Their results are also consistent with the previous studies.

Many studies, such as Peebles (1980), Calzetti et al. (1992), and Connolly et al. (2002), showed that the angular two-point correlation function is also related to an angular power law correlation:

$$w(\theta) = A\theta^{1-\gamma} \quad (5.13)$$

where: A is the clustering amplitude, and $1 - \gamma$ is the slope of angular correlation function, γ is the same scaling exponent in Equation 5.12.

Peebles (1980) introduced a way to relate the spatial two-point correlation function $\xi(r)$ with the angular two-point correlation $w(\theta)$ function using an approximation by Limber's equation (Limber, 1953). Baugh and Efstathiou (1993) presented this relation in the sense of selection function of survey:

$$w(\theta') = \frac{2 \int_0^\infty \int_0^\infty x^4 F^{-2} a^6 p^2(x) \xi(r) dx du}{[\int_0^\infty x^2 F^{-1} a^3 p(x) dx]^2} \quad (5.14)$$

where: $\theta' = 2\sin(\theta/2)$, with θ is the separation angle between object pairs, the selection function $p(x)$ is the probability of detection of galaxy at coordinate distance x in the survey, u is the difference of distance between objects,

a is the scale factor, and x is the comoving distance given by:

$$x = \frac{2}{H_0} \left(1 - \frac{1}{\sqrt{1+z}} \right) \quad (5.15)$$

The physical separation between object pairs, separated by an angle θ on the sky, is:

$$r^2 = a^2 \sqrt{u^2 + x^2 \theta'^2} \quad (5.16)$$

Baugh and Efstathiou (1993) showed that $F(x)$ depends on the cosmological model. For a universe with $\Omega_0 = 1$, $F(x)$ is equal to 1. Then Equation 5.14 can be simplified as:

$$w(\theta') = \frac{2 \int_0^\infty \int_0^\infty x^4 a^6 p^2(x) \xi(r) dx du}{[\int_0^\infty x^2 a^3 p(x) dx]^2} \quad (5.17)$$

We will use this equation to make the prediction of angular two-point correlation function of *Planck* SZ cluster catalog in the next section.

5.3 The angular two-point correlation function of the *Planck* SZ cluster catalog

5.3.1 *Planck* SZ cluster catalog

The second *Planck* SZ cluster catalog (PSZ2) is an all-sky catalog of clusters detected in the full mission dataset based on 29 months of observation (Planck Collaboration et al., 2016c). I focus on the MMF3 (Matched Multi-Filters) sub-sample of the PSZ2, for which we possess an accurate description of its selection function that enables us to generate the required unclustered random samples. The *Planck* selection function comprises of two complementary functions: the completeness defines the probability that a given real object will be detected, and the statistical reliability (or purity) defines the probability that a given detection corresponds to a real object. The completeness is a function of underlying SZ observables θ_{500} , and Y_{500} (see more in chapter 2). The reliability is a statistical function of detection attributes and is presented as a function of detection SNR (signal-to-noise ratio). Two algorithms were used to detect *Planck* SZ clusters (Planck Collaboration et al., 2016c): MMF1 and MMF3, based on the same technique (matched multi-filters; Melin et al., 2006) but have been implemented independently, and the PwS (PowellSnakes). The MMF3 sub-sample contains 1271 SZ sources, among which 926 are confirmed clusters with redshift estimates. *Planck* SZ clusters were cross checked of the completeness, positions, and also get the compilation of redshift information using other clusters surveys such as the MCXC catalog (Piffaretti et al., 2011), the redMaPPer catalog (Rykoff et al., 2014), SPT, and ACT.

The PSZ2 presents a number of advantages over other cluster catalogs for our purposes. First, as a space mission *Planck* observed over a larger range of frequencies than the other SZ surveys from the ground. Therefore, it provides sufficient information to separate the SZ signal of large cluster from the background. *Planck* detected more massive and lower redshift clusters than those detected by ACT and SPT as was mentioned in Section 2.2.3. Finally, the full-sky survey produced a catalog covering most of the sky, except for regions masked around the Galactic plane and bright point sources.

The *Planck* mask was constructed as a threshold on the level of Galactic dust emission. In addition, bright point sources with $SNR > 10$ are masked out to a radius of 3σ of the beam. In total, only 16.4% of the sky are masked.

Figure 5.4 shows the distribution of clusters in the PSZ2 MMF3 sample and the masked sky area. In order to reduce the use of some contaminated clusters in the *Planck* SZ cluster catalog, we keep only clusters which have $SNR \geq 6$.

Clusters with $SNR \geq 6$, and redshift $z < 0.4$ were used to estimate the angular two-point correlation function. The reason for the selection of redshift $z < 0.4$ is that all the *Planck* clusters (PSZ1) were compared and crossed checked with clusters in the SDSS DR8 RedMaPPer cluster catalog (Rykoff et al., 2014). RedMaPPer is a catalog of 25,000 galaxy clusters with redshift in range $[0.08 - 0.55]$ detected from SDSS DR8 data. Rozo et al. (2015) showed that *Planck* SZ clusters within the redMaPPer’s footprint, and within the redMaPPer’s redshift range are found in the redMaPPer cluster catalog. They also showed that the redMaPPer cluster richness produces a well defined, tight scaling relation with SZ mass proxies. In addition, we limit the redshift of our data to the same range of redshift of the SDSS data used in the study of Hong et al. (2012). Moreover, there are only 42 *Planck* clusters with $SNR \geq 6$ and in the range of redshift $0.4 \leq z \leq 0.55$. The clustering signal will be diluted if we add these distance clusters in our analysis.

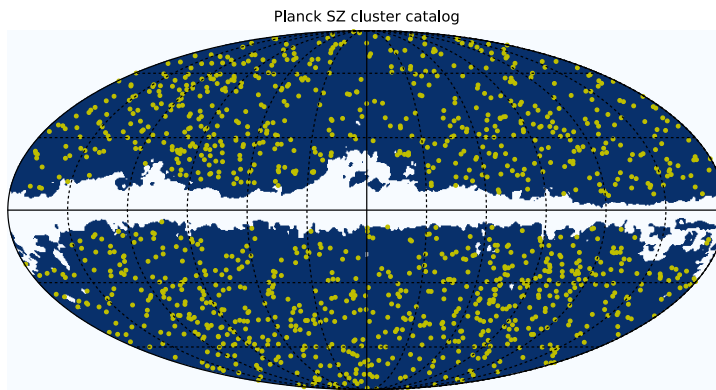


FIGURE 5.4: The distribution of the 1,271 PSZ2 MMF3 sources (yellow points) and the *Planck* mask (white area) in Galactic coordinates.

Figure 5.5 gives the redshift distribution for the 423 clusters with $SNR \geq 6$, and redshift $z < 0.4$. These clusters were used to estimate the angular two-point correlation function. The mass-redshift distribution of Planck SZ clusters is shown in Figure 5.6. As we can see that *Planck* detected some very massive clusters at low redshift. The mean mass of all clusters (blue points) is $4.96 \times 10^{14} M_{\odot}$. The mean mass of 423 clusters with $SNR \geq 6$, and redshift $z < 0.4$ (orange points) is $5.27 \times 10^{14} M_{\odot}$.

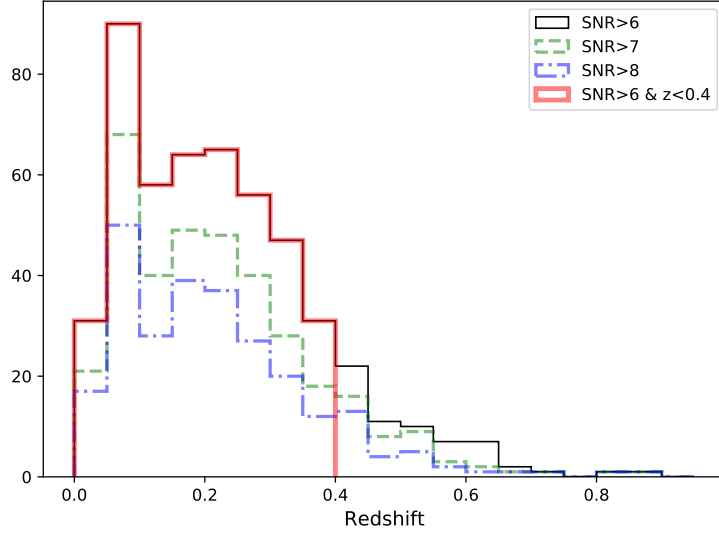


FIGURE 5.5: Redshift distribution of 443 Planck SZ clusters with $SNR \geq 6$ and redshift $z \leq 0.4$

5.3.2 Random catalog

Similar to the spatial two-point correlation, the angular two-point correlation function, usually denoted $w(\theta)$, quantifies the excess probability of finding two objects at an angular separation of θ with respect to a random uniform distribution.

Thus, we need a reference random uniform sample to measure the correlation function. The reference sample must represent a uniform distribution of points *as observed by the Planck survey*, which means modified by the *Planck* selection function, which varies in depth across the sky and depends on cluster size, θ_s and total SZ amplitude, Y_{500} ; these selection effects must be incorporated into the random sample.

The reference sample was generated by randomly drawing clusters in mass and redshift according to the halo mass function. To do so, we must adopt a reference cosmology, for which we take the *Planck* 2015 baseline cluster cosmological model. We then translate mass and redshift for each cluster into θ_s and Y_{500} using the *Planck* 2015 cluster SZ scaling relations. In this process, we randomly scatter the Y_{500} values with a log-normal distribution with the variance given in the selection function maps. The sky mask and *Planck*

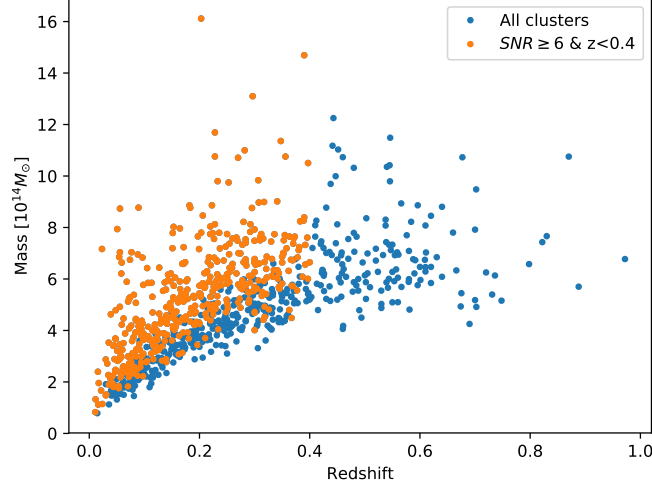


FIGURE 5.6: Mass and redshift distribution of Planck SZ clusters with redshift estimates (926 clusters). Clusters with $z < 0.4$ and $SNR \geq 6$ are presented as orange points.

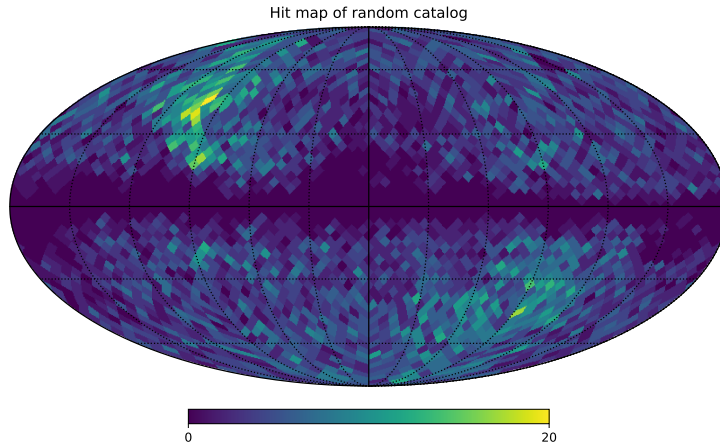


FIGURE 5.7: The hit map (total number of clusters in a pixel) distribution of the random clusters catalog.

selection function are then applied to produce the final reference random catalog. Figure 5.7 shows the hit map of the random cluster catalog. Figure 5.8 shows a map of standard deviation of SZ flux Y_{500} in galactic coordinates.

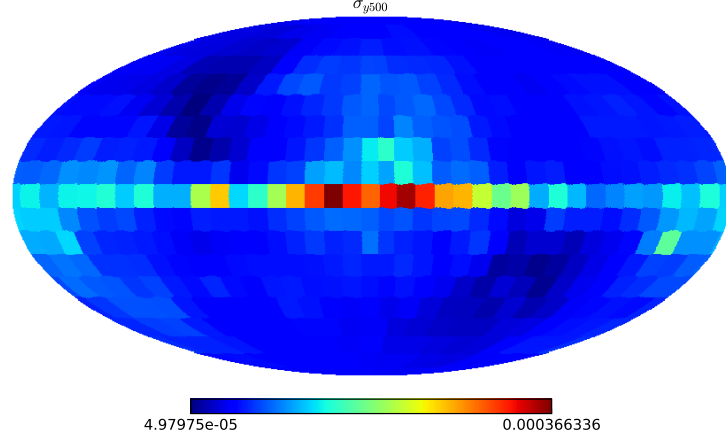


FIGURE 5.8: A map of standard deviation of SZ flux Y_{500} in galactic coordinates of a *Planck* cluster.

We focus on angular distances less than 50 degrees, and divide the interval $[0.1, 50]$ degrees into 20 bins spaced logarithmically. We use the bootstrap method to estimate uncertainties, creating 10,000 resampled data catalogs with the same total number of galaxy clusters as in the PSZ2 by randomly drawing objects with replacement from the PSZ2; in each bootstrap catalog, some clusters are replicated several times, while some clusters do not appear at all. In order to avoid the duplication of the number of pairs at angular distance $\theta = 0$ in the estimation of two-point correlation, we shift the edge of the first θ bin to 0.05 degrees instead of 0 degree. We merged some small angular bins together to avoid null or very few number of pairs at small angular bins: bins 1, 2, 3 and 4 into 1 bin; similarly with bins 5, 6, and 7; and bins 8 and 9. Therefore, we end up with 14 bins of angular distance.

TABLE 5.1: The values of 14 angular distance bins, and the number of pairs of *Planck* clusters in each bin based on the selection of redshift.

Bin Number	1	2	3	4	5	6	7	8	9	10	11	12	13	14
Angular distance θ [degree]	0.20	0.61	1.26	1.94	2.64	3.61	4.92	6.71	9.16	12.5	17.06	23.27	31.75	43.32
$z < 0.4$	1	5	33	30	44	75	136	264	515	878	1536	2852	4796	8052
$z < 0.2$	1	4	15	8	15	28	42	81	168	259	484	855	1507	2369
$0.2 \leq z < 0.4$	0	0	5	10	11	17	24	53	95	186	302	548	978	1623

Table 5.1 gives the values of the bin centers and the number of pairs of clusters in each bin. There are only few pairs of *Planck* clusters in the first two bins of angular distance in the redshift groups $z < 0.4$ and $z < 0.2$. In the cluster group $0.2 \leq z < 0.4$, there is no pair of clusters in the first two angular bins and 5 pairs of clusters in the third angular bin. Note that this is the number of pairs of clusters, not the number of clusters.

5.3.3 Results: Detection of clustering of Planck SZ cluster catalog

The angular two-point correlation function of 442 *Planck* clusters with redshift $z < 0.4$ is shown in Figure 5.9. The error bars are estimated using the bootstrap method of 10,000 re-samples from data catalog.

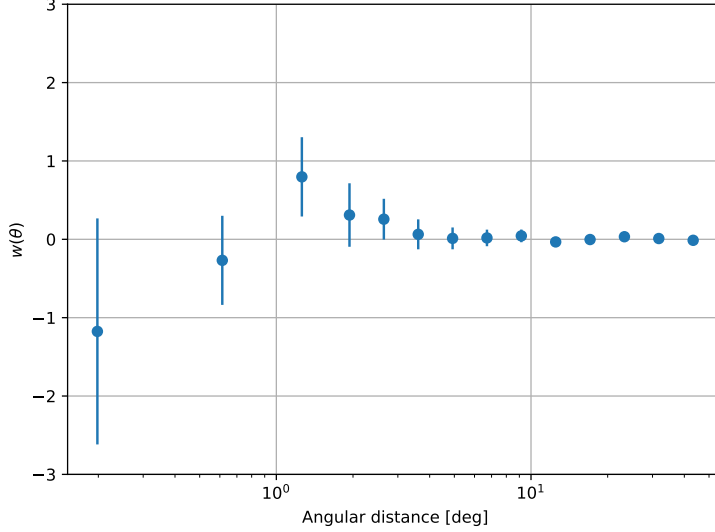


FIGURE 5.9: Angular two-point correlation function of 442 clusters with redshift $z < 0.4$. Error bars are estimated using the bootstrap method using the bootstrap procedure.

As can be seen in this figure at angular distance smaller than 1 degrees, the angular correlation of *Planck* clusters is negative. The large error bars in small angular distance bins is due to the small number of pairs of clusters. The number of pairs of clusters for each angular bins is shown in Table 5.1. There is only 1 pair in the first bin and 5 pairs in the second bins. At higher angular distance we obtain a positive correlation. A positive peak of angular correlation function is obtained at angular distance about 1.3 degrees. At angular distance larger than 3 degrees, the correlation function of clusters is compatible with zero.

The coefficient matrix of correlation function of *Planck* clusters with redshift $z < 0.4$ is shown in Figure A.1 in Appendix A.

The distribution of angular correlation function of 10,000 *Planck* bootstraps was examined in the first four angular bins as shown in Figure 5.10. As can be seen the distribution of angular correlation function of the first two bins of angular distance are asymmetric. This is a characteristic of a bias due to small number of pairs at small distances as can be expected from a sample of 442 clusters covering about 85% of the sky.

Due to the low number of pairs, we will exclude the first two angular bins in our curve fitting. We check the effect of the asymmetric distribution of the angular correlation function in the Section 5.3.4.

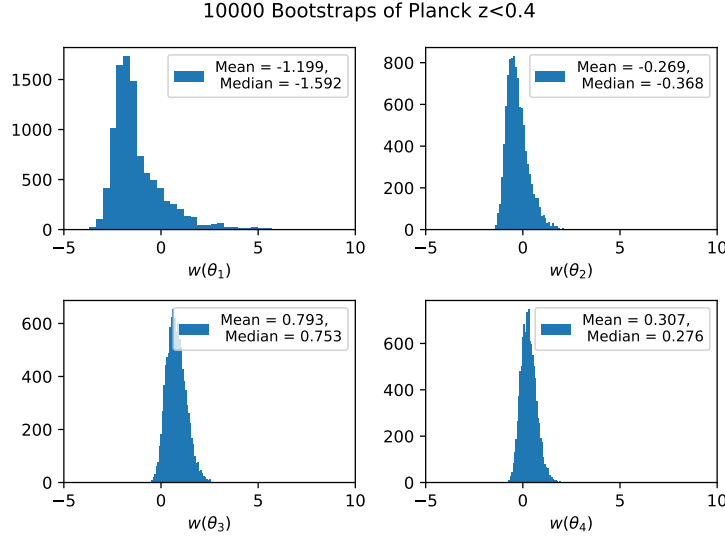


FIGURE 5.10: Distribution of angular two-point correlation function of 10,000 bootstrap resamples of clusters with redshift $z < 0.4$ of the first 4 angular bins. The high asymmetric distribution in the first two angular bins is due to the few number of pairs of clusters.

We perform two different fits of the angular correlation function of Planck clusters using power law: $w(\theta) = a\theta^b$. In the first case (dashed line), a and b are free parameters; and in the second case (red line), a is free parameter and fixed $b = -1$. We fix $b = -1$ in the second case in accordance with the prediction of the angular correlation function of *Planck* clusters.

The results of the two fits of the angular correlation function of *Planck* clusters is illustrated in Figure 5.11. As can be seen the first curve fitting (red line) is: $a = 1.44 \pm 0.48$, $b = -2.24 \pm 0.54$, and $\chi^2 = 2.27$. The second curve fitting with parameter fixed $b = -1$, we got $a = 0.27 \pm 0.14$, and $\chi^2 = 4.86$. The second fit has very high uncertainty on the parameter of the fit. However, the error of the second fit is lower than the error of the first fit. This is because we fitted with less parameter.

As we presented in Section 5.2.3, the angular two-point correlation function can be related to the spatial correlation function using the Limber's equation. We use equation 5.17 with selection function of *Planck* to make the prediction of the angular correlation function of *Planck* clusters.

As we mention above Hong et al. (2012) showed that the correlation length of selected SDSS clusters depends on the richness of clusters (higher richness means higher correlation length) and the power index is almost the same for all cluster sub-samples. We choose $r_0 = 20 h^{-1} \text{ Mpc}$ and $\gamma = 2$ because *Planck* has detected massive clusters (similar to high richness Planck Collaboration et al. (2014c)) with the mean mass of $5.27 \times 10^{14} M_\odot$ for redshift $z < 0.4$ and $\text{SNR} \geq 6$. Then, we projected the spatial two-point correlation following the depth of selection function of *Planck*.

We plot the prediction of angular correlation function of *Planck* SZ clusters

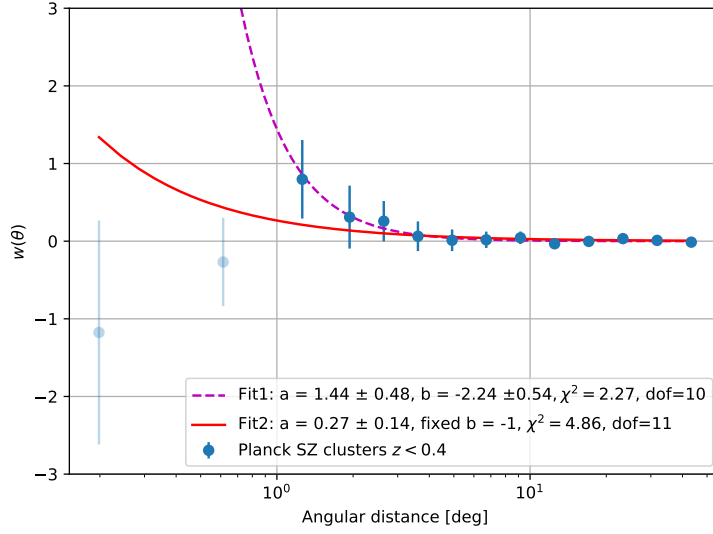


FIGURE 5.11: The angular two-point correlation function estimated from *Planck* clusters with redshift $z < 0.4$ (blue points). The two fitting lines are represented which exclude the first two angular bins. Fit 1 with two parameters (red line) cannot be considered due to the lack of data at small angles. In fit 2 (red line) the slope b is fixed to $b = -1$.

with redshift $z < 0.4$ in Figure 5.12 (green points), and the fit by a power law $w(\theta) = a\theta^b$ with $a = 0.37$, and $b \approx -1$ (green line), as expected (equation 5.13) with $\gamma = 2$.

We plot the prediction to compare with the angular correlation of *Planck* clusters with $z < 0.4$ in Figure 5.13. We fix $b = -1$ for the fitting line of the prediction. As we can see that the prediction is just slightly above the angular correlation of *Planck* clusters.

To conclude, we got a indication of clustering signal of *Planck* clusters with redshift $z < 0.4$. The angular correlation of *Planck* clusters is close to the prediction.

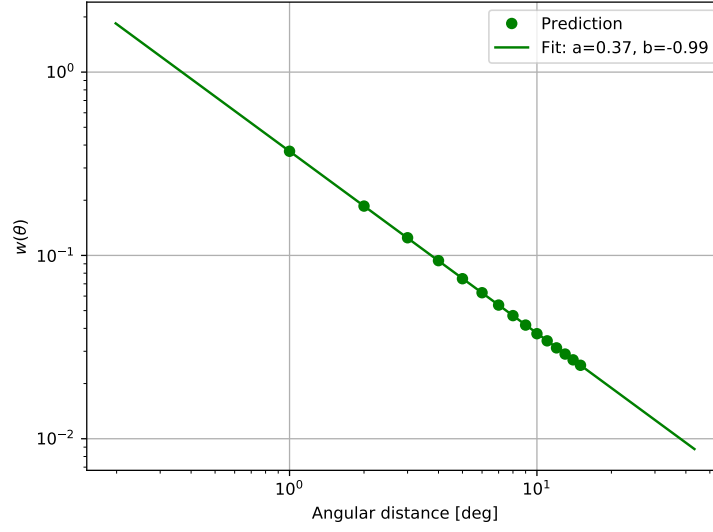


FIGURE 5.12: The prediction of the angular two-point correlation function of *Planck* clusters with redshift $z < 0.4$ (green points). The green line is the fitting line by a power law $w(\theta) = a\theta^b$.

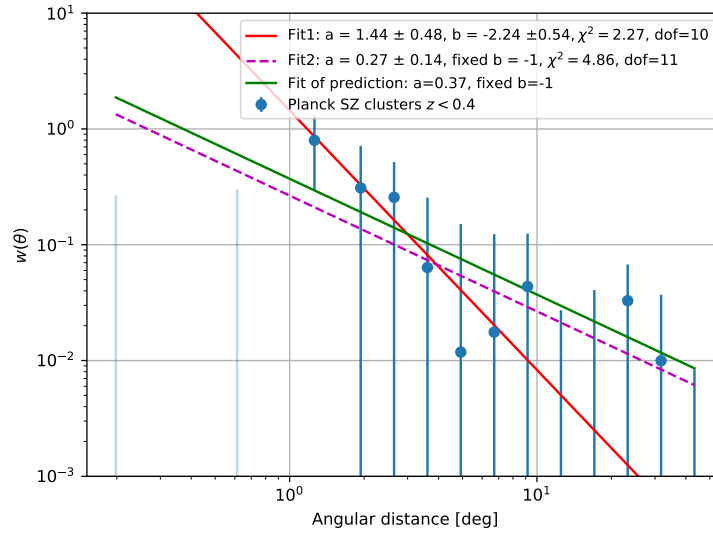


FIGURE 5.13: The angular two-point correlation function measured from the *Planck* clusters with redshift $z < 0.4$ (same plot of Figure 5.11 in log scale). The green line is the fitting line of the predicted angular correlation function of *Planck* clusters in the same redshift range. We get an amplitude of the second fit (dashed line) with fixed $b = -1$ which is comparable to the prediction of the *Planck* reference model.

5.3.4 Redshift dependence

Galaxy clusters are distributed at very large scale of the universe. Along the line of sight, two galaxy clusters are distributed on small angular distance could have very different redshifts i.e. very different distances. The angular correlation function is only based on the angular separation of clusters, but we can use the redshift of clusters to group them with respect to z as the third dimension. Moreover, we mentioned in the previous section that the Abell clusters used in the study of Bahcall and Soneira (1983) have redshift $z < 0.2$. Therefore, we divided the 442 *Planck* clusters into 2 groups:

- Redshift bin $0 < z < 0.2$: 243 clusters.
- Redshift bin $0.2 \leq z < 0.4$: 199 clusters

The statistics (mean and median) of 10,000 bootstraps of angular two-point correlation function of all 14 angular bins of *Planck* clusters in different redshift groups are shown in Table A.1 in Appendix A.

Low redshift sample

The two-point angular correlation function of low redshift clusters with $z < 0.2$ is shown in Figure 5.14 (orange points). We exclude the first two bins as we did with *Planck* clusters with $z < 0.4$ in Figure 5.11 from previous the section. High angular correlation of this cluster group can be seen at angular distance from 1 to 10 degrees. At higher angular distance, the angular correlation of this cluster group is approaching zero.

The yellow line is the power law of angular correlation function of 1547 Abell clusters (Abell 1958) as studied by Bahcall and Soneira (1983). They used rich clusters which have redshift estimates smaller than $z = 0.2$. They found that the angular correlation function can be approximated by a mean power law relation of the form: $w(\theta) = 0.8\theta^{-1}$. The angular correlation of *Planck* clusters is compatible with the angular correlation of Abell clusters.

We fitting the same power law model as before, first with both parameters free, and then with b fixed to -1 . We got the first curve fit (magenta dashed line) with $a = 1.59 \pm 0.72$ and $b = -1.41 \pm 0.33$. The second fit (red line) with $a = 0.83 \pm 0.27$ with fixed $b = -1$ is compatible with the result of Bahcall and Soneira for Abell clusters. The result from this fit (3σ) indicates a significant clustering signal for this group.

In Figure 5.15, we plot the power law of the predicted angular correlation function of *Planck* (blue line) to compare with the angular correlation of *Planck* in the same redshift range $z < 0.2$. As we can see that the prediction is below, and also close to the angular correlation of *Planck* clusters (red line).

The coefficient matrix of correlation function of *Planck* clusters with redshift $z < 0.2$ is shown in Figure A.2 in Appendix A.

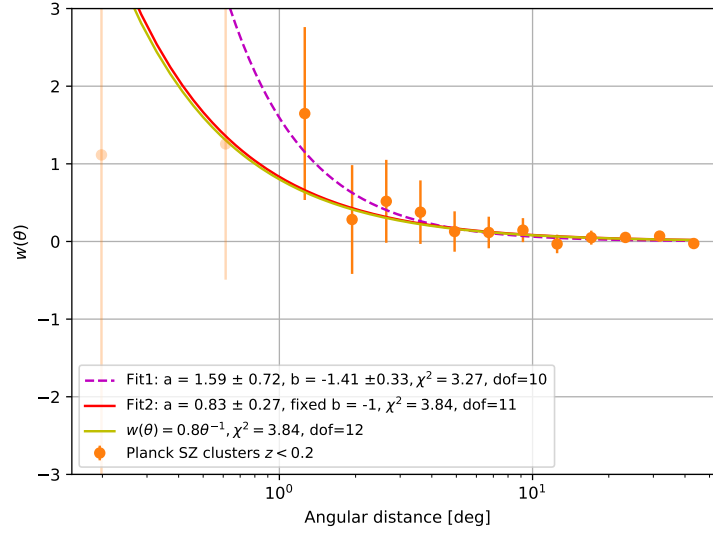


FIGURE 5.14: The angular two-point correlation function of *Planck* clusters with redshift $z < 0.2$. The fitting lines are fitted excluding the first two angular bins. The yellow line is the power law of the angular correlation function of Abell clusters from Bahcall and Soneira.

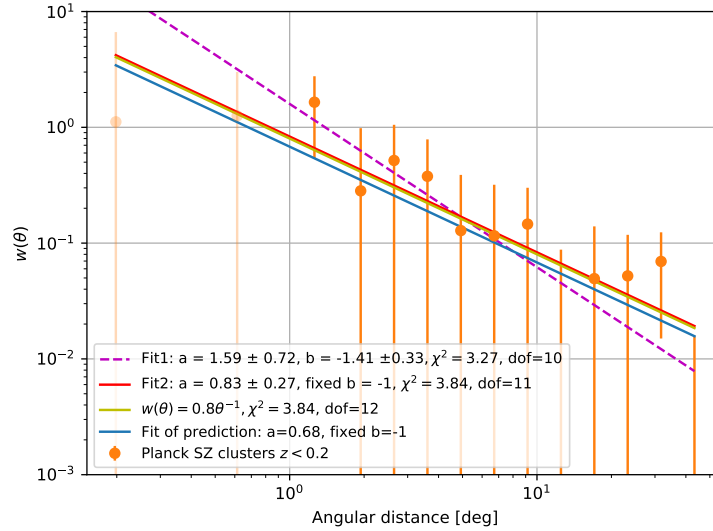


FIGURE 5.15: The angular two-point correlation function of *Planck* clusters with redshift $z < 0.2$ in log-log scale. The blue line represents the power law of the predicted angular correlation in the same redshift range.

High redshift sample

The two-point angular correlation function of *Planck* clusters with $0.2 \leq z < 0.4$ is shown in Figure 5.16. Most of angular distance bins indicate no or negative correlation of this cluster group except at angular distance from 2 to 3 degrees.

There are no pairs of clusters in the first two bins and 5 pairs of clusters in the third bin in this high redshift group. Therefore, we exclude the first three bins in our curve fitting. We obtain the two curve fits with high uncertainty on the fit parameters of the correlation function of these clusters. The first fit gives $a = 14.27 \pm 18.16$, and $b = 3.8 \pm 1.66$. The second fit gives $a = 0.27 \pm 0.14$.

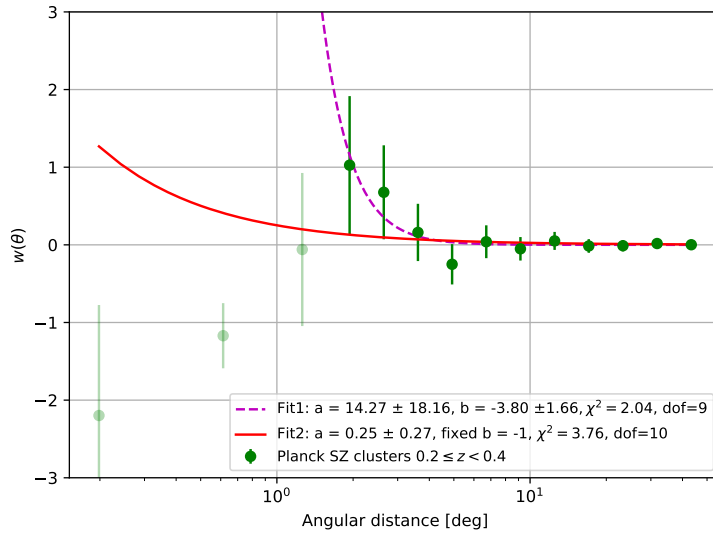


FIGURE 5.16: Angular two-point correlation function of *Planck* clusters with redshift $0.2 \leq z < 0.4$. The fitting lines (red and dashed magenta lines) are derived excluding the first three angular bins.

In Figure 5.17 we plot the prediction of the angular correlation function of *Planck* in the same redshift range $0.2 < z < 0.4$. We can see that the prediction is slightly higher, but still close to the angular correlation of *Planck* clusters.

The coefficient matrix of correlation function of *Planck* clusters with redshift $0.2 < z < 0.4$ is shown in Figure A.3 in appendix A.

Overall, the selection of redshift help us to gain clustering signal by eliminating the high redshift clusters. We obtained the clustering signal of *Planck* clusters with redshift $z < 0.2$ using the two-point angular correlation function. This angular correlation is compatible with the angular correlation function of Abell clusters with same range of redshift. We don't detect clustering signal of *Planck* clusters with redshift $0.2 \leq z < 0.4$. Our results are compatible with the prediction of the angular correlation function of *Planck* clusters in all redshift groups.

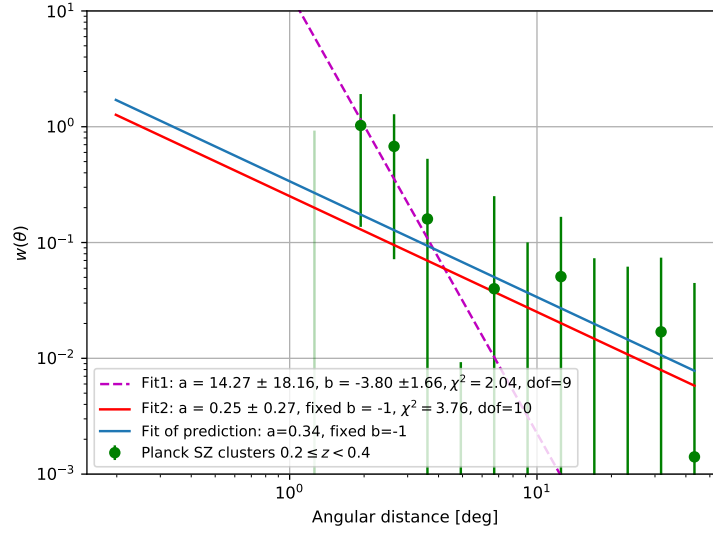


FIGURE 5.17: The angular two-point correlation function of *Planck* clusters with redshift $0.2 \leq z < 0.4$ in log-log scale. The blue line is the power law of the predicted angular correlation of *Planck* in the same redshift range.

Null test

The clustering signal of *Planck* clusters with redshift $z < 0.2$ obtained above which is excluded the first two angular bins. In this section we will clarify how the low number of pairs of clusters in the first angular bins affect the fit to the angular correlation function. The clustering signal of clusters with redshift $z < 0.2$ will be tested using the null test.

From the random catalog which was used to estimate the angular correlation of SZ clusters, we keep only clusters with redshifts $z < 0.2$. We randomly select 250 random clusters from these clusters to create a mock catalog with no clustering, and 2500 other clusters to create new random catalog for estimation of the two-point angular correlation function. Next, we estimate the angular two-point correlation function of the mock cluster catalog and fit it using model $w(\theta) = a \times \theta^{-1}$. We repeat this step in 5000 runs.

Figure 5.18 shows the mean of the angular two-point correlation function of 5000 mock catalogs. The red cross points show the median of angular correlation of 5000 mock catalogs. As we can see the mean of angular correlation function of 5000 mock catalogs is compatible with 0. However, the median values of the first three angular bins are negative due to non symmetric distribution of the angular correlation in these bins. It can be clearly observed in Figure 5.19. Especially, the first angular bin has the most non symmetric distribution of angular correlation function. This is similar to what we saw with the angular correlation function of re-sampled catalogs of *Planck* clusters with redshift $z < 0.4$ as we presented in the last section. We also checked with larger mock cluster catalogs (500 clusters in each catalog), the asymmetry of the angular correlation function in the first bins is significantly

reduced.

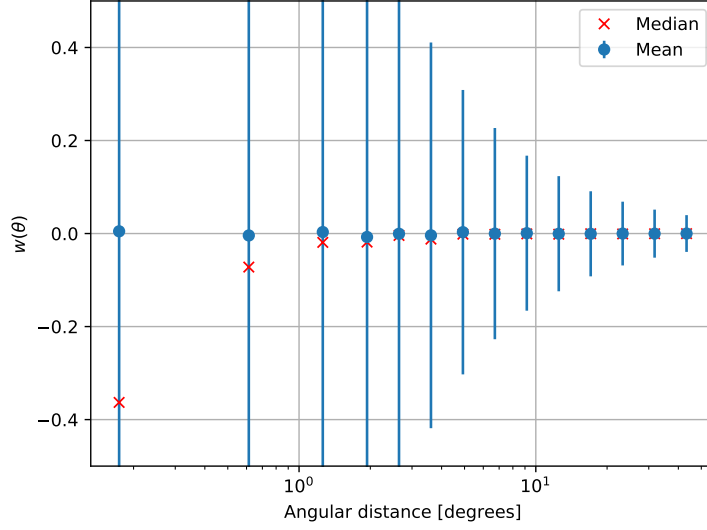


FIGURE 5.18: The mean and median of angular correlation function of 5000 mock cluster catalogs.

For this reason, we need to exclude at least the first two angular bins in our curve fit to neglect the bias effect. As shown in Figure 5.20, the bias of the curve fit is markedly decreased when excluding the first two angular bins in the curve fit. Besides, it can be seen by comparing the data of the histogram of the fit in Figure 5.20(b) with the result of the fit on clusters with $z < 0.2$ that under the null hypothesis the probability to obtain fitting parameter $a > 0.833$ is less than $1/5000$.

To summarize, the lack of pairs of clusters in the first two angular bins ultimately causes the bias in the curve fit of the two-point angular correlation function. This effect can be corrected by excluding these angular bins. The null test confirmed our clustering signal of clusters with redshift $z < 0.2$.

5.3.5 Conclusions

We have studied the angular correlation of *Planck* SZ cluster catalog. We restricted to clusters with redshift estimates and $SNR \geq 6$. The data are too scarce to explore small angular scales. This results in the slope of the red curve of the fit being erratic, and the 2 parameters fit is useless. When we fix the slope to $b = -1$, we obtain the amplitude of the fit which is compatible with the prediction, and follows the same variation with redshift:

- Clusters with redshift $z < 0.4$: we get $a = 0.27 \pm 0.14$, and the prediction $a = 0.37$.
- Clusters with redshift $z < 0.2$: we get $a = 0.83 \pm 0.27$, and the prediction $a = 0.68$.

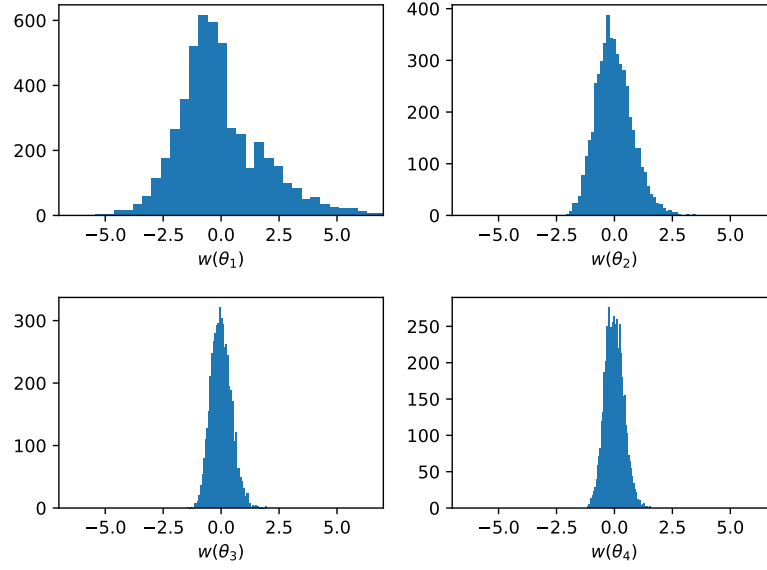
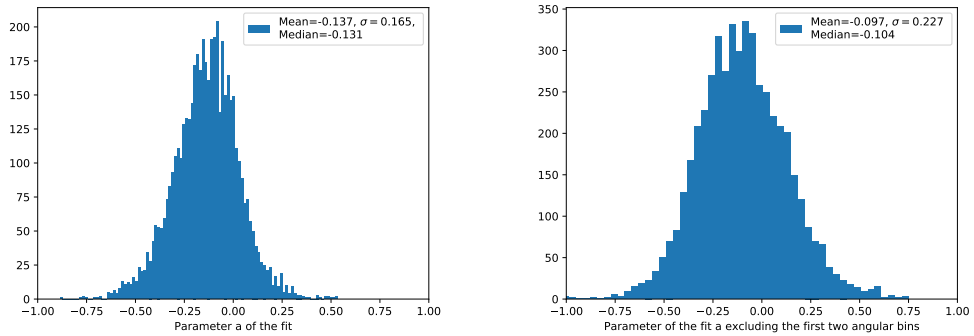


FIGURE 5.19: The angular correlation function of the first four angular bins of 5000 mock cluster catalogs.



(a) Using all 14 bins in the curve fit.

(b) Excluding the first two angular bins in the fit.

FIGURE 5.20: The parameter fit a of the angular correlation function of 5000 mock cluster catalogs. The bias of the fit is significantly reduced after we exclude the first two angular bins.

- Clusters with redshift $0.2 < z < 0.4$: we get $a = 0.25 \pm 0.27$, and the prediction $a = 0.34$.

The separation in redshift helped us to find a significant clustering of low redshift cluster group $z < 0.2$ because it reduces the dilution of distance clusters. Besides, the angular correlation of these clusters is compatible with the power law of the angular correlation of Abell cluster in the same range of redshift as studied by Bahcall and Soneira (1983).

In the near future, the large-scale structure surveys from experiments such as *Euclid* and LSST will detect many more clusters. We can make full use of this data by combining these surveys with *Planck* SZ data to construct multi-wavelength catalogs in order to improve our understanding of the evolution of the large-scale structure of the universe.

We have the opportunity to explore the potential of these future surveys with the *Euclid* flagship dark matter halo catalog as presented in next section.

5.4 The two-point correlation function of the Euclid Flagship dark matter halo catalog

The discovery of the accelerated expansion of the Universe is a remarkable event in our history. This expansion is believed to be caused by dark energy, which is the main component of our Universe ($\sim 70\%$). On the other hand, dark matter contributes about 20% to the total density of our universe. However, the nature of these two components is still unknown. *Euclid* is a future space mission that will map the large-scale structure of our universe covering the cosmic time of about the last 10 billion years.

Euclid will use two cosmological probes to study dark energy and dark matter: Galaxy clustering and weak lensing. *Euclid* is expected to find about 100,000 galaxy clusters. Sartoris et al. (2016) showed that *Euclid* clusters will be extremely powerful in constraining the amplitude of matter density Ω_m and the matter power spectrum σ_8 .

In this section we show the result on the two-point correlation function of the *Euclid* Flagship dark matter halo simulation. The evolution of galaxy clustering through cosmic time is shown by the power law of the two-point correlation. We will quantify the evolution of the clustering of *Euclid* simulation clusters using the power law of correlation function in different redshifts.

5.4.1 Euclid Flagship dark matter halo catalog

The *Euclid* Flagship dark matter halo catalog is a N-body simulation halo catalog. It was generated at the University of Zürich using the *Rockstar* (Robust Overdensity Calculation using K-Space Topologically Adaptive Refinement) halo finder (Behroozi et al., 2013). *Rockstar* is a halo finder algorithm for identifying dark matter halos, substructures, and tidal features. The *Euclid* flagship dark matter halo catalog is a full sky catalog in which the total number of halos is about 44 billion. The cosmological parameters that have been used in the simulation are shown in Table 5.2.

TABLE 5.2: Cosmological parameters used in the *Euclid* Flagship dark matter halo simulation.

Parameter	Symbol	Value
Total matter density	Ω_m	0.319
Baryon density	Ω_b	0.049
Cosmological constant	Ω_Λ	0.681
Rms matter fluctuation	σ_8	0.83
Scalar spectral index	n_s	0.96
Dimensionless Hubble parameter	h	0.67

5.4.2 Data selection

The *Euclid* flagship dark matter halo catalog is a full sky simulation which is very huge catalog with about 44 billion halos. However, we only select halos which have the number of particles greater than 40,000 or equivalent to halos mass larger than $9.6 \times 10^{13} M_{\odot}$. This minimum halo mass is of the order of the mass of galaxy clusters. At this step, we get 266,028 halos.

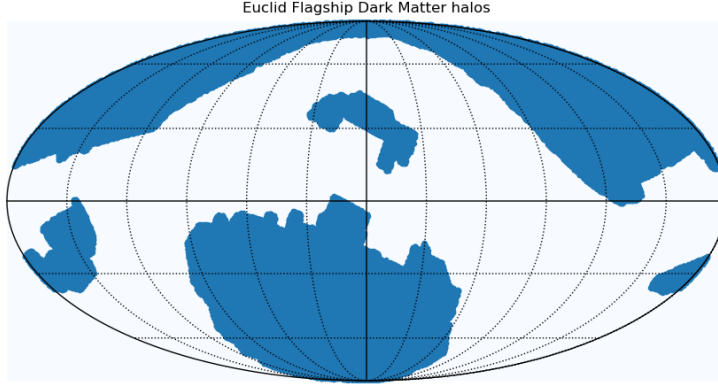


FIGURE 5.21: Distribution of *Euclid* Flagship dark matter halos (blue) after applying the *Euclid* survey mask and star mask (white area).

The *Euclid* Wide Survey will observe about 15,000 square degrees of the sky. It will avoid the sky areas which are contaminated by light from our Galaxy and our Solar System. Hervé Aussel (CEA) of the *Euclid* consortium has created the *Euclid* survey mask and star mask of the Wide Survey Area of galaxy catalogue for Science Performance Verification (SPV)³. Thanks to him, we can apply these masks to our halo catalog to get the same sky coverage as *Euclid* will observe. Thus we get 104,372 Flagship dark matter halos after applying these masks. Figure 5.21 shows the distribution of *Euclid* Flagship dark matter halos (blue points) applied the *Euclid* survey mask and star mask (white areas).

We generate a uniform random catalog over the sky. Then we also apply the survey mask and star mask to this random catalog. There are a total of 1,038,714 random clusters. We randomly draw redshifts from data catalog to create redshifts for random catalog.

5.4.3 Results

We divide our sample into different redshift bins with $\Delta z = 0.2$. Table 5.3 presents the number of *Euclid* flagship dark matter halos in the redshift bins. The first redshift bin has the lowest number of halos. The highest number of

³<https://Euclid.roe.ac.uk/issues/7760>

halos is in redshift range $0.4 < z < 0.6$. We only analyze the correlation of clusters in redshift range from 0 to 0.8 because when increasing redshift the number of halos decreases gradually. Therefore, we can have a prediction of the correlation functions of the higher redshift bins based on the results from the lower redshift groups.

TABLE 5.3: Number of selected *Euclid* flagship dark matter halos in different redshift bins

	Redshift	Number of halos
1	$z < 0.2$	5249
2	$0.2 < z < 0.4$	21,927
3	$0.4 < z < 0.6$	28,217
4	$0.6 < z < 0.8$	22,355
5	$0.8 < z < 1.0$	14,331

Figure 5.22 shows the distribution of *Euclid* flagship dark matter halo mass for redshifts from 0 to 0.8. We can see that most of the halos have the mass of 14 to 14.2 $\log_{10}(M_{\odot})$ in all selected redshift groups.

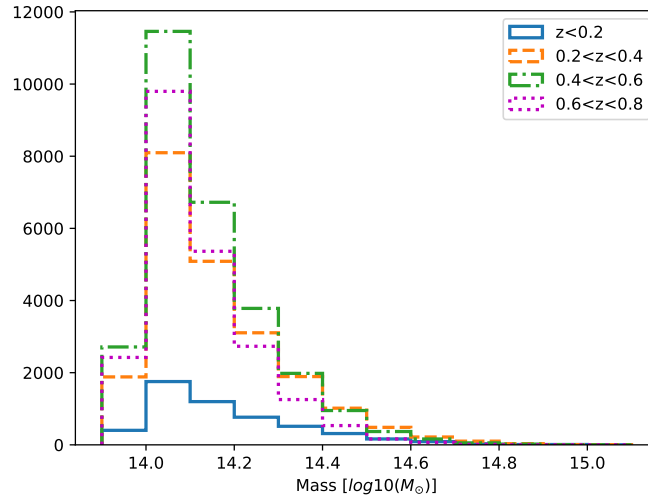


FIGURE 5.22: Distribution of *Euclid* Flagship dark matter halos mass in redshift range [0-0.8].

The predicted correlation functions of matter computed from the linear matter power spectrum using the *Euclid* flagship cosmological model at different redshifts are illustrated in Figure 5.23. As can be seen in this figure the correlation function of matter is evolved with redshifts. On scales below $\sim 80 h^{-1} \text{ Mpc}$, the correlation of matter decreases as redshift increases. On scales from 80 to $112 h^{-1} \text{ Mpc}$, we can see the peaks of the correlation functions on the same distance for all redshifts which are the typical BAO signals.

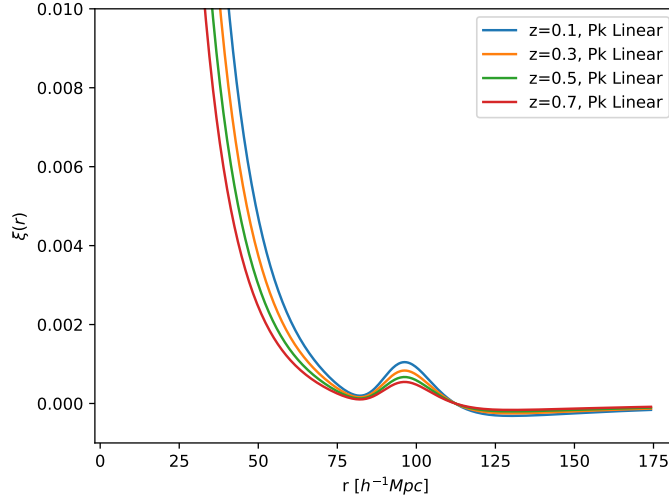


FIGURE 5.23: The predicted correlation function of matter computed from the linear matter power spectrum at different redshifts. We use the *Euclid* flagship cosmological parameters as shown in Table 5.2.

The correlation functions of *Euclid* Flagship dark matter halos in different redshift groups are shown in Figure 5.24. The error bars are computed using bootstrap method. The coefficient correlation matrices of the two-point correlation function of *Euclid* flagship dark matter halos are shown in appendix B. As can be seen in Figure 5.24, the separation of halos in redshift impacts directly to the spatial correlation of our sample. At distance scale $r < 60 h^{-1} \text{ Mpc}$, the highest correlation of *Euclid* flagship dark matter halos is obtained in the redshift bin $0.6 < z < 0.8$, followed by the redshift bin $0.4 < z < 0.6$, and $0.2 < z < 0.6$. The lowest correlation is detected in the lowest redshift bin $z < 0.2$.

We obtain high positive spatial correlation of our sample at spatial distance smaller than $80 h^{-1} \text{ Mpc}$ for all redshift bins. At distance larger than $120 h^{-1} \text{ Mpc}$ the correlation of *Euclid* flagship dark matter halos is anti-correlated. On the zoom box of the same plot, we observe the bumps in the correlation at spatial distance from 90 to $110 h^{-1} \text{ Mpc}$ for all redshift bins except redshift bin $z < 0.2$. These bumps which corresponds to BAO signals of the clustering as predicted from the correlation function of matter as shown in Figure 5.23. We present in detail of how to fit these BAO signals in the next section. The BAO signal on the first redshift bin is weak with larger error bars due to lower number of halos compared to the other groups.

The difference amplitude of the correlation function of *Euclid* flagship dark matter halos and the predicted correlation function of matter is due to the halo bias. The higher redshift halos have higher bias (Sridhar et al., 2017). We will go into detail about this bias in Section 5.4.6.

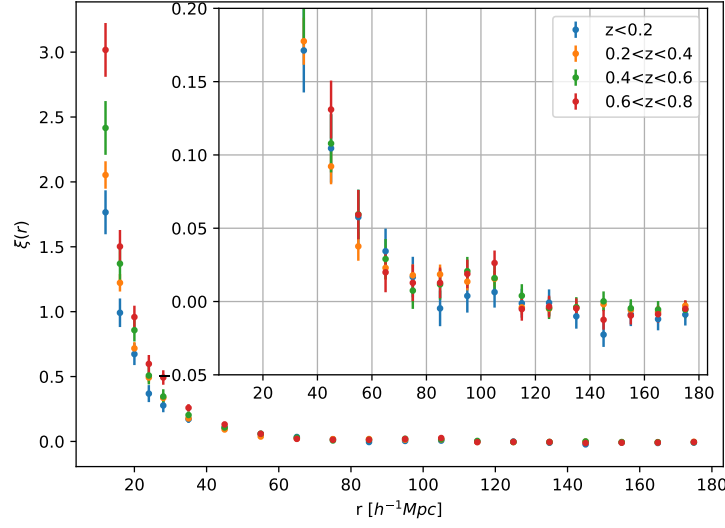


FIGURE 5.24: The correlation functions of *Euclid* flagship dark matter halos in different redshift groups. The box inside is a zoom of the correlation to magnify the BAO peaks.

5.4.4 Fitting power law

First, we analyze the correlation on scale smaller than $80 h^{-1} \text{ Mpc}$. The studies from Bahcall and Soneira (1983), Croft et al. (1997), Peacock and West (1992), Nichol et al. (1992), Gonzalez et al. (2002), and Bahcall et al. (2003) have shown that the correlation of clusters can be fitted by the power law on scales $r < 60 h^{-1} \text{ Mpc}$. Therefore, we apply the curve fit over the same scales to the correlation of *Euclid* dark matter halos using the power law $\xi(r) = (r/r_0)^\gamma$ (Equation 5.12). Figure 5.25 shows the correlation at different redshifts and the best fit of correlation function using the power law.

We can clearly see that the correlation length increases with redshifts. The power law index also increases with redshifts, except in redshift bin $0.4 < z < 0.6$ the power law index is slightly larger than in redshift bin $0.6 < z < 0.8$. In comparison with the power law obtained of MaxBCG clusters (Estrada et al., 2009), the correlation lengths of *Euclid* Flagship DM halos are in the same range.

Table 5.4 shows the value of the power index, and the correlation length, and value of χ^2 at different redshifts. As can be seen from this table, the correlation length increases as redshift increases. The scaling exponent doesn't change much over redshift groups.

5.4.5 Fitting BAO

At spatial scales larger than $80 h^{-1} \text{ Mpc}$ we apply a specific fitting function to obtain the fit of the BAO bumps on the correlation. We follow the method as presented in Padmanabhan et al. (2012), and Xu et al. (2012) to fit the BAO

5.4. The two-point correlation function of the Euclid Flagship dark matter halo catalog

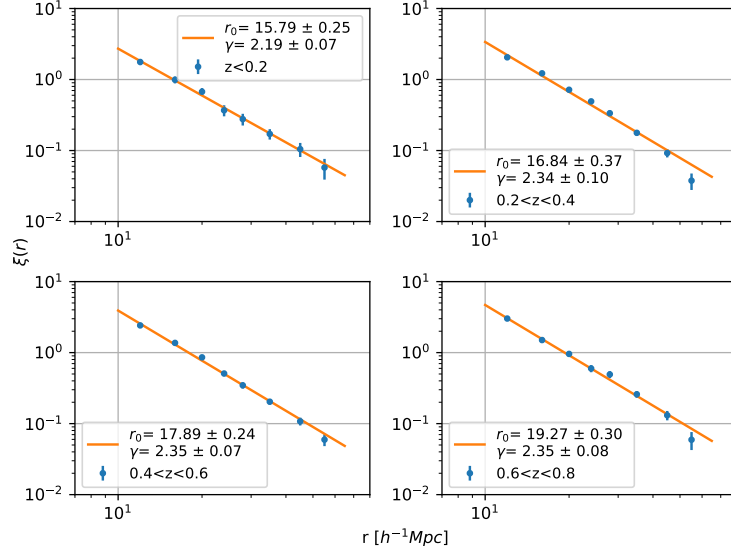


FIGURE 5.25: The correlation of *Euclid* dark matter halos (blue dots) and the power law fitting lines (orange lines) over scales $R < 60 h^{-1} \text{ Mpc}$.

TABLE 5.4: The best fit results of the power law of the correlation function of *Euclid* dark matter halos over scales $R < 60 h^{-1} \text{ Mpc}$.

Redshift	r_0	γ	χ^2
$z < 0.2$	15.79 ± 0.25	2.19 ± 0.07	1.63
$0.2 < z < 0.4$	16.84 ± 0.37	$2.34 \pm .010$	14.94
$0.4 < z < 0.6$	17.89 ± 0.24	2.35 ± 0.07	6.08
$0.6 < z < 0.8$	19.27 ± 0.3	2.35 ± 0.08	4.99

signal detected in the two-point correlation of *Euclid* flagship dark matter halos. The two-point correlation fitting model can be described as:

$$\xi^{fit}(r) = B^2 \xi_m(\alpha r) + A(r), \quad (5.18)$$

where $A(r)$ is used to help marginalize out the unmodeled broadband signal in the correlation function:

$$A(r) = \frac{a_1}{r^2} + \frac{a_2}{r} + a_3, \quad (5.19)$$

where: α is the scale dilation parameter which provides a measure of any isotropic shifts in the position of the BAO peak in the data compared to the fiducial cosmological model (we fix $\alpha = 1$ because we study the correlation of simulation data with known fiducial model); B^2 is a large-scale bias term; a_1 , a_2 , and a_3 are the linear nuisance parameters. The correlation template $\xi_m(r)$ in Equation 5.18 is defined by:

$$\xi_m(r) = \int \frac{k^2 dk}{2\pi^2} P_m(k) j_0(kr) e^{-k^2 a^2} \quad (5.20)$$

where: $j_0(kr)$ is the zeroth-order spherical Bessel function, $a = 1h^{-1}$ Mpc a scale small enough such that the effects of the damping will not be significant in our fit, the exponential term is used to damp the oscillatory transform kernel $j_0(kr)$ at high- k to induce better numerical convergence in the integration. The template power spectrum $P_m(k)$ is defined by interpolating between the linear theory power spectrum and non-linear power spectrum at a given redshift z :

$$P_m(k) = [P_{lin}(k) - P_{smooth}(k)] e^{-k^2 \Sigma_{nl}^2 / 2} + P_{smooth}(k), \quad (5.21)$$

where $P_{smooth}(k)$ is the power spectrum with no-wiggle as described in Eisenstein and Hu (1998b), Σ_{nl} is a smooth parameter that is used to model the degradation in the acoustic peak due to non-linear evolution (Eisenstein et al., 2007).

Figure 5.26 illustrates the effect of Σ_{nl} to the width and the height of the BAO signal on the correlation function which is computed from the power spectrum using the *Euclid* flagship cosmological parameters in Table 5.2. In our work, we generate the linear power spectrum using classy which is a Python wrapper of CLASS (Cosmic Linear Anisotropy Solving System). CLASS is a set of Boltzmann codes to simulate the evolution of linear perturbations in the universe and to compute CMB and large-scale structure observables (Lesgourgues, 2011). For a given redshift $z = 0.3$, by adding the non-linear power spectrum the BAO signal on the two-point correlation is broaden when we increase the value of Σ_{nl} .

The effect of the smooth parameter is important in our study. Therefore, we fix this parameter with different values to obtain the best fit value of BAO fit and χ^2 of the fit. Then we will compare these values to get the optimal values of the fits.

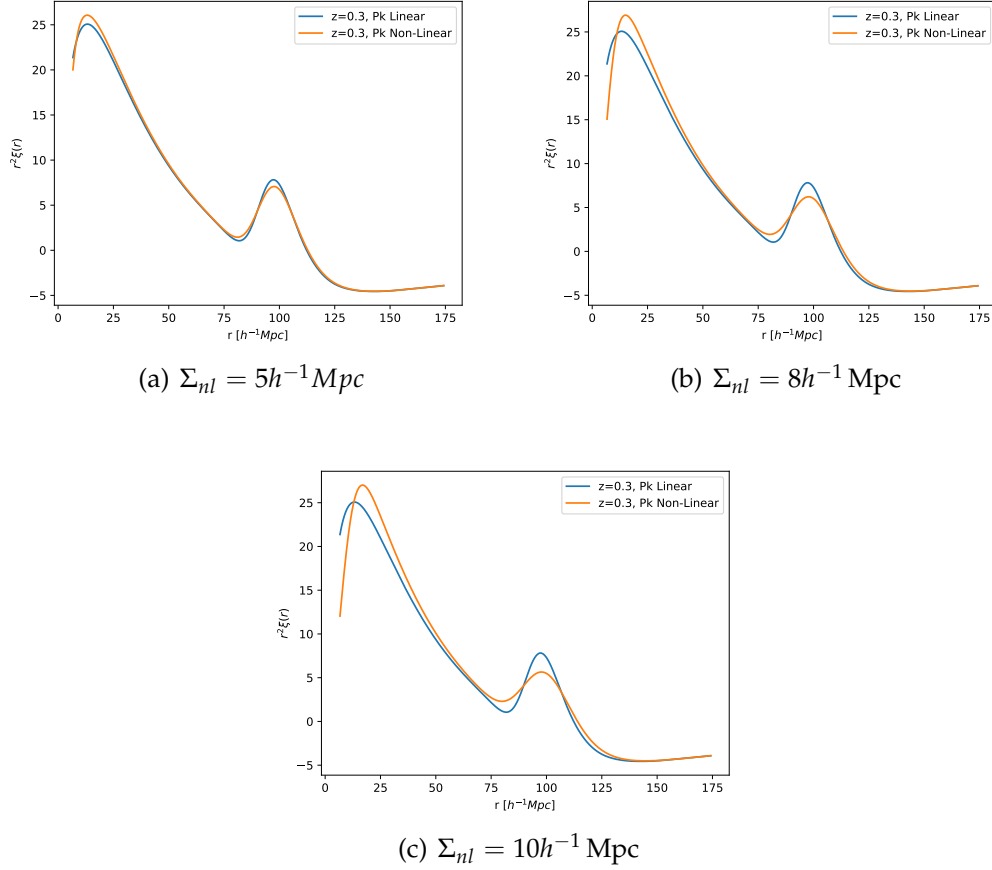


FIGURE 5.26: The effect of varying the smooth parameter Σ_{nl} to the correlation function and the BAO signal. The blue lines are the correlation function computed from the linear matter power spectrum. The orange lines are the correlation function computed from non-linear matter power spectrum. We multiply $\xi(r)$ by r^2 to magnify the BAO peaks. We use the *Euclid* flagship cosmological parameters.

The two-point correlation function of *Euclid* flagship dark matter halos and the BAO fitting lines ($\Sigma_{nl} = 4 h^{-1} \text{Mpc}$) are shown in Figure 5.27. Our BAO fitting lines are fitted very well with the correlation function of *Euclid* flagship dark matter halos and the BAO peaks for the redshift groups larger with $z > 0.2$. For the clusters with redshifts $z < 0.2$, as we mentioned above the BAO signal is not trivial. In comparison with other redshift groups, the BAO fitting line of the correlation function at this redshift bin also shows that the BAO signal is insignificant.

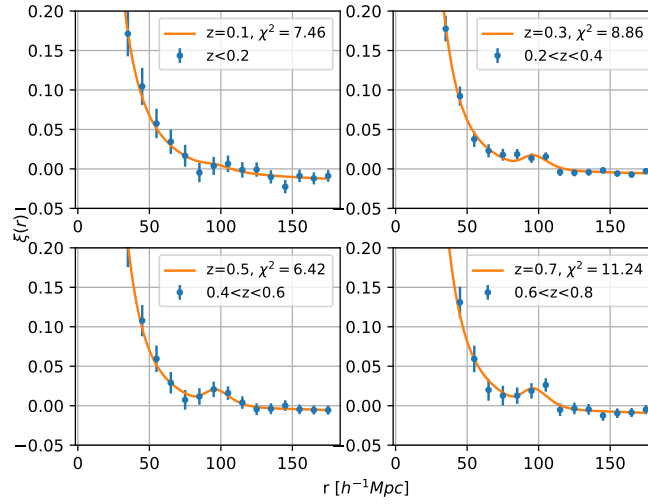


FIGURE 5.27: The correlation function of *Euclid* flagship dark matter halos (blue points) and the BAO fitting lines (orange lines). In this case, the smooth parameter $\Sigma_{nl} = 4 h^{-1} \text{Mpc}$.

We show in Figure 5.28 the BAO fitting lines using the BAO template with $\Sigma_{nl} = 10 h^{-1} \text{Mpc}$. In this case, the BAO peaks are not fitted well in all redshift groups compared to the BAO template with $\Sigma_{nl} = 4 h^{-1} \text{Mpc}$. The χ^2 values of these fit are also much higher. Table 5.5 shows the values of χ^2 of the fit for different values of Σ_{nl} . The bold number in each column of χ^2 corresponds to the lowest value for different redshift groups.

We can see that the BAO fit is optimal for the lowest redshift group using the BAO template with smooth parameter $\Sigma_{nl} = 0 h^{-1} \text{Mpc}$. In other words, a simple model of the linear power spectrum gives the best fitting on the correlation of dark matter halos at low redshift.

On the other hand, the BAO templates with $\Sigma_{nl} = 4 h^{-1} \text{Mpc}$ gives the best BAO fits with the lowest values of χ^2 for high redshift groups $0.4 < z < 0.6$ and $0.6 < z < 0.8$. For the redshift group $0.2 < z < 0.4$, we obtain the best fit using the BAO template with $\Sigma_{nl} = 6 h^{-1} \text{Mpc}$. Moreover, using the BAO templates with high values of Σ_{nl} obtain worse fitting as we already saw in Figure 5.28. The best fit parameters of the BAO fit are shown in Table B.1 in Appendix B.

The corresponding of the smooth parameter Σ_{nl} for each group is: 0, 6, 4 and $4 h^{-1} \text{Mpc}$

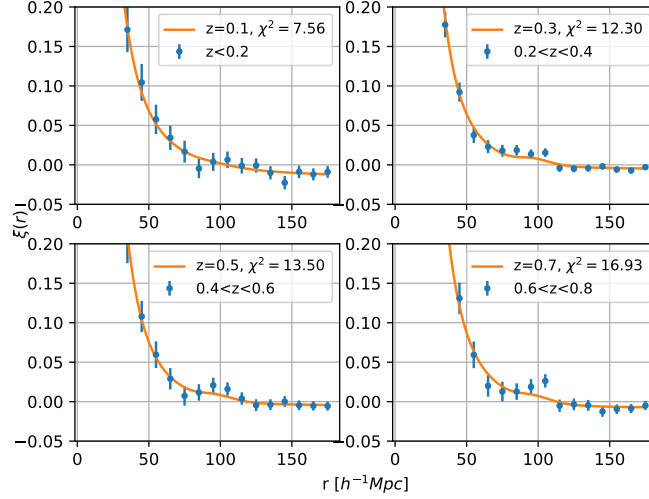


FIGURE 5.28: The correlation function of *Euclid* flagship dark matter halos (blue points) and the BAO fitting lines (orange lines). In this case, the smooth parameter $\Sigma_{nl} = 10 h^{-1} \text{Mpc}$.

TABLE 5.5: Values of χ^2 of the BAO fit when vary the value of the smooth parameter Σ_{nl} . The lowest χ^2 value in each redshift groups are bold.

$\Sigma_{nl} [h^{-1} \text{Mpc}]$	$\chi^2 - z < 0.2$	$\chi^2 - 0.2 < z < 0.4$	$\chi^2 - 0.4 < z < 0.6$	$\chi^2 - 0.6 < z < 0.8$
0	7.428	9.319	6.458	11.302
1	7.430	9.284	6.452	11.293
2	7.437	9.184	6.436	11.269
3	7.448	9.036	6.419	11.244
4	7.462	8.861	6.418	11.239
5	7.477	8.679	6.490	11.339
6	7.448	8.521	6.812	11.757
7	7.495	8.611	7.704	12.720
8	7.507	9.359	9.388	14.179
9	7.531	10.747	11.521	15.716
10	7.564	12.296	13.500	16.930

5.4.6 Discussion on bias evolution

As we mentioned in chapter 2, halos are the bias tracer of the "background" dark matter field with a bias $b(M, z)$:

$$b^2(M, z) = \frac{\xi_h(r)}{\xi_{DM}(r)} \quad (5.22)$$

Basilakos et al. (2008) and Sridhar et al. (2017) showed that the halo bias evolves with redshift, i.e. that the halo bias increases with z . Figure 5.29 shows the halo bias of *Euclid* flagship dark matter halos as a function of redshift. On large scales there is no estimation of halo bias at some redshift groups because of the negative values of the division of the two-point correlation functions. Over all scales, the lower redshift group has the smaller bias. This is especially true over the scales $r < 50 h^{-1} \text{Mpc}$. The halo bias on these scales are from 2 and 4 and quite the same values among each the redshift group. On scales $r > 80 h^{-1} \text{Mpc}$, the halo bias increase significantly.

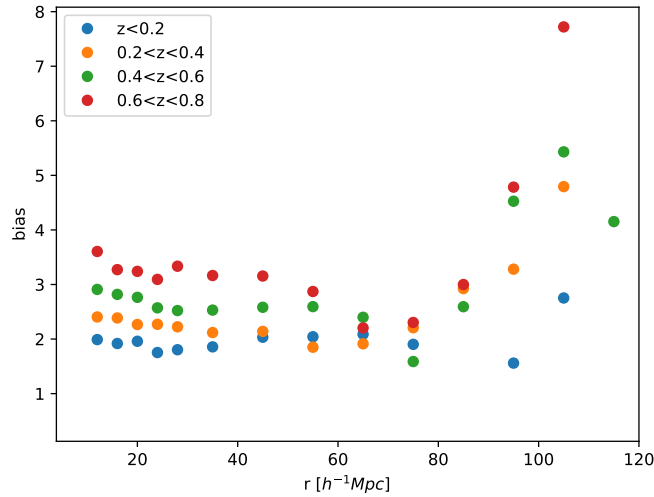


FIGURE 5.29: Halo bias as a function of redshift.

In summary, the amplitude of the matter correlation decreases with redshift, and the halo bias increases with redshift. As a result, the amplitude of the correlation of *Euclid* dark matter halos increases with redshift. Our results are consistent with the studies of Basilakos et al. (2008) and Sridhar et al. (2017).

5.4.7 Conclusions

We have studied the correlation of *Euclid* flagship dark matter halos which applied the *Euclid* survey mask and the star mask. We divided our sample into 4 different redshift bins. Here are the main results:

- The correlation functions of *Euclid* are positive and change over redshifts on distance scales $r < 60 h^{-1}$ Mpc. On these scale the correlation can be fitted well by a power law as given in Equation 5.12.
- The correlation length of the power law of the correlation function of halos evolves with redshift.
- The amplitude of the correlation function of *Euclid* increases with redshift which can be explained as the evolution of halo bias. Our results are consistent with Basilakos et al. (2008) and Sridhar et al. (2017).
- On the scales from 80 to 112 h^{-1} Mpc we observe the BAO peaks in the correlation of *Euclid* flagship dark matter halos with redshift $z > 0.2$. These peaks are well fitted using the BAO templates which are the prediction computed from the matter power spectrum using the cosmological model from Euclid simulation.
- The fit of BAO peaks strongly depends on the smooth parameter Σ_{nl} which varies the height and the width of the BAO peak. In practice, if we fit the BAO signal from the measurement of real data, we also need to make the scale dialation parameter α as a free parameter. In our work, we set $\alpha = 1$ because we know the position of BAO peaks based on cosmological model used in the simulation.

5.5 Conclusions

Galaxy clusters have been used to study the large-scale structure of the universe over the last decades. Through optical, X-ray, and SZ surveys thousands of clusters have been detected at close to very far distances. In this picture of the universe, galaxy clusters exhibit as one of the largest structures of the universe which are bound through gravity. The quantitative measurement of the clustering can be done through the statistics of the two-point correlation function in both spatial and projected angular scales. Using the two-point correlation, the large-scale clustering of galaxy clusters is well described by a power law $\xi(r) = (r/r_0)^{-\gamma}$ over scales $r < 60 h^{-1}$ Mpc. The correlation length r_0 is from 14 to 30 h^{-1} Mpc, which depends on the cluster richness as well on the analyzed samples. The power law index γ ranges from 1.6 to 2.1 and depends on the samples used. In some cases, for example when there is a lack of redshift measurement of cluster samples or when samples are small, the angular two-point correlation can also be used to study the clustering of galaxy clusters. The angular correlation function can be related to the spatial correlation function through Limber's approximation. On larger scales $r \approx 100 h^{-1}$ Mpc, the baryon acoustic oscillations feature was detected using galaxies and galaxy clusters, and can be used as the cosmological standard ruler to measure the expansion of the universe.

We have studied the angular two-point correlation of the *Planck* SZ cluster catalog. We obtained a hint of significant clustering of galaxy clusters with

redshift $z < 0.4$ and $SNR > 6$. When we split the sample into 2 redshift groups, we do not find significant clustering of galaxy clusters with $0.2 < z < 0.4$. However, we obtained a significant signal for clusters with $z < 0.2$. The correlation of this cluster group is also compatible with the correlation of Abell clusters as studied by Bahcall and Soneira (1983). Moreover, the prediction of the correlation function of *Planck* SZ clusters is also compatible with our results.

Using the *Euclid* flagship dark matter halo simulation catalog, we explored the potential of measuring the two-point correlation function. We found that the correlation length of *Euclid* dark matter halos changes with redshift: for higher redshifts we obtain a larger correlation length. We derived the BAO peaks that are compatible with the prediction from non-linear evolution of matter. Furthermore, we also found that the halo bias evolves with redshift, which is an indication for the underlying dark matter distribution. Our results also demonstrate the potential of studying the large-scale structure through future surveys, such as they are going to be performed by *Euclid* and LSST, which are expected to find of the order of 100,000 galaxy clusters.

Chapter 6

Conclusions and outlook

6.1 Conclusions

In this thesis, I have studied the large-scale structure of the universe using galaxy clusters, in particular with the *Planck* SZ cluster catalog and the dark matter halo catalog of the Flagship simulation for *Euclid*.

Many studies in recent history have used galaxy clusters as a tracer of the large-scale structure of the universe. The most common tool to quantify the clustering of large-scale structure is the two-point correlation function in spatial scales $\xi(r)$ or in angular scales $w(\theta)$. On large scales, the two-point correlation function can be approximated by a power law $\xi(r) = (r/r_0)^\gamma$. The correlation length r_0 and the power law index γ varies depending on the richness of galaxy clusters and redshift.

Planck was a space mission (2009-2013) of ESA to measure the temperature anisotropies of the CMB at microwave and infrared wavelengths. The *Planck* SZ catalog is an all-sky catalog of galaxy clusters detected during 29 months of observation of *Planck*. Using the angular two-point correlation function we found an indication of a clustering signal of galaxy clusters with redshift $z < 0.4$ and $SNR \geq 6$. We also obtained a significant clustering signal of clusters with $z < 0.2$ and $SNR \geq 6$. The angular two-point correlation function of *Planck* detected galaxy clusters is well described by a power law $w(\theta) = a \times \theta^{-1}$. The angular correlation of *Planck* galaxy clusters is very close to our prediction.

Euclid is a space mission of ESA that will be launched in 2022 to investigate the accelerating expansion of the Universe using two main cosmological probes: Weak Gravitational Lensing and Baryonic Acoustic Oscillations. Its surveys will cover about $15,000 \text{ deg}^2$ of the sky and will be expected to detect about 100,000 galaxy clusters up to redshift $z = 2.0$. I had the opportunity to explore the potential of the two-point correlation function using the *Euclid* flagship dark matter halo simulation catalog with the survey mask applied. The correlation of *Euclid* flagship dark matter halos evolves with redshifts, and can be well fitted using a power law $\xi(r) = (r/r_0)^\gamma$ over scales smaller than $60 h^{-1} \text{ Mpc}$ in all redshift groups. The BAO signature on scales from 80 to $125 h^{-1} \text{ Mpc}$ was detected in redshift groups $0.2 < z < 0.4$, $0.4 < z < 0.6$, and $0.6 < z < 0.8$. These BAO signatures are consistent with the prediction from non-linear matter evolution.

The detection of the BAO signal using this catalog was an important test for *Euclid* to demonstrate that this mission will help accurately measuring the Hubble parameter and that through *Euclid*'s measurements we will be able to put strong constraints on the properties of dark energy.

In the frame of the validation of *Euclid* external simulation data in the context of the Scientific Challenge SC3 of the *Euclid* consortium, the results of the unit test showed that the code of the external simulator works properly. The properties of the output are simulated as expected. The results of this work showed that the unit tests are useful for the next simulation stages when the team will re-factorize the simulation code. This validation work also helped me to learn how to simulate an astronomical image, how to measure the photometry of stars and galaxies, and how to use *SExtractor* to detect sources in an image.

6.2 Outlook

The results on the two-point correlation function of the *Planck* SZ cluster catalog and the dark matter halo catalog will be valuable in the analysis of the large-scale structure of the universe with galaxy clusters for the upcoming surveys such as those to be conducted by *Euclid* and LSST. I am preparing an article to present our results of the two-point correlation function of *Planck* SZ cluster catalog.

The measurement of BAO is a powerful probe of dark matter and dark energy which will be exploited with *Euclid*. This thesis also demonstrates that the *Euclid* mission will indeed significantly advance our knowledge about the cosmology of our Universe, especially measuring the expansion rate of the universe through BAO signatures. *Euclid* will therefore be able to put significant constraints on the properties of dark energy.

The future large surveys such as LSST, *Euclid*, WFIRST with much larger number of galaxies, clusters and especially at higher redshifts will provide us a significant improvement at pixel level on the measurement of constraining cosmological parameters (Chary et al., 2019). These improvements can be obtained using baryon acoustic oscillation signatures, weak gravitational lensing, and statistics of clustering. Combining the data from these surveys with the observable cosmological probes will enable us to investigate the nature of dark matter and dark energy with far smaller uncertainties (Rhodes et al., 2017), (Capak et al., 2019).

Appendix A

The angular two-point correlation function of *Planck* SZ clusters and their coefficient correlation matrices

The values of diagonal elements of the coefficient matrix are equal to 1 and are masked in these following figures.

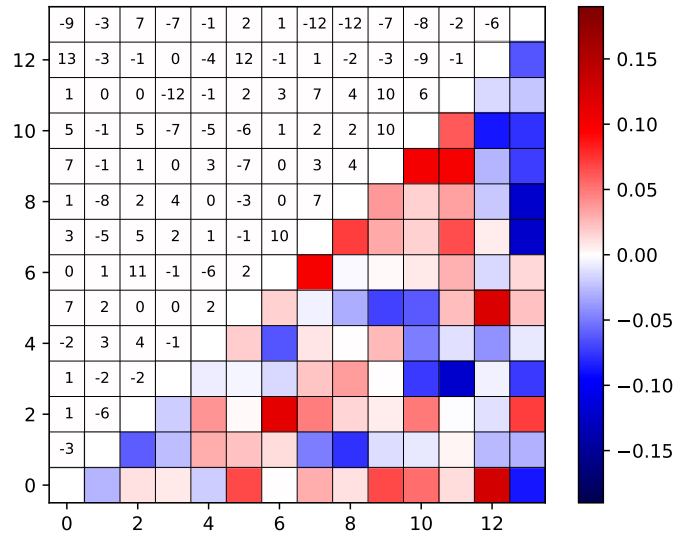


FIGURE A.1: Coefficient correlation matrix of the angular two-point correlation function of *Planck* clusters with $z < 0.4$ and $SNR > 6$. The values in each box on the left above the diagonal are multiplied by 100.

The coefficient matrix of the angular two-point correlation function of *Planck* clusters with redshift $0.2 < z < 0.4$ is presented in Figure A.3.

The statistics of the angular correlation measured from the *Planck* SZ catalog bootstrap resamples are shown in table A.1.

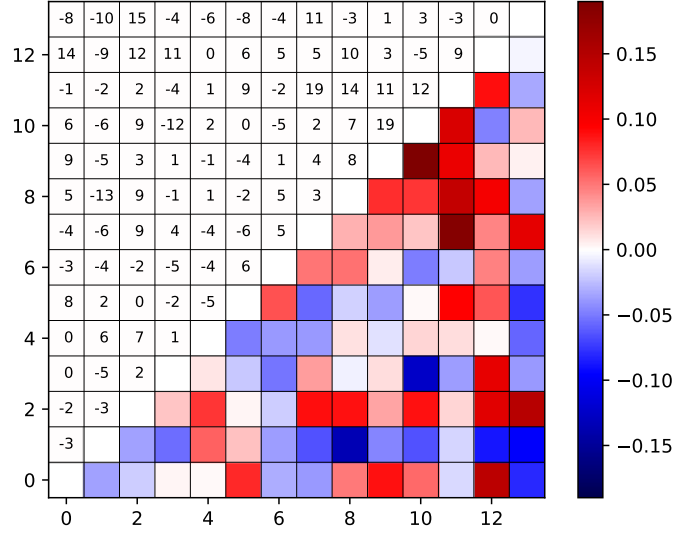


FIGURE A.2: Coefficient correlation matrix of the angular two-point correlation function of *Planck* clusters with $z < 0.2$ and $SNR > 6$. The values in each box on the left above the diagonal are multiplied by 100.

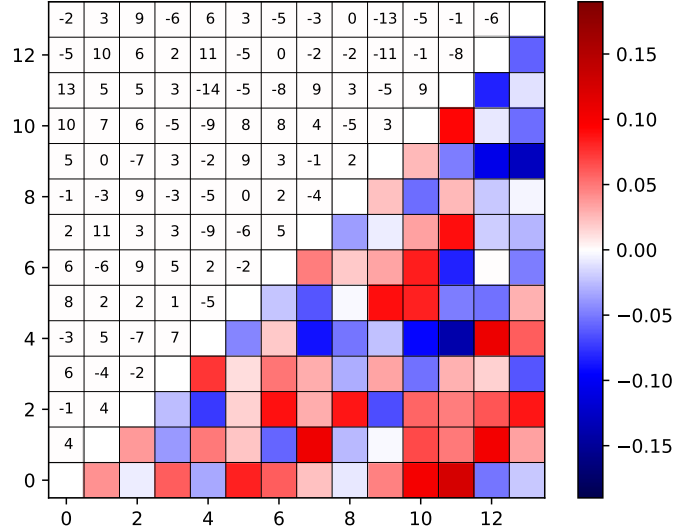


FIGURE A.3: Coefficient correlation matrix of correlation function of *Planck* clusters with $0.2 < z < 0.4$ and $SNR > 6$. The values in each box on the left above the diagonal are multiplied by 100

TABLE A.1: Statistics of the angular two-point correlation function of *Planck* clusters in all 14 angular bins of different redshift groups from 10,000 bootstrap resamples.

Redshift	$z \leq 0.4$		$z < 0.2$		$0.2 \leq z < 0.4$	
$w(\theta_i)$	Mean	Median	Mean	Median	Mean	Median
θ_1	-1.199	-1.592	1.142	-1.157	-2.196	-2.198
θ_2	-0.269	-0.368	1.288	0.923	-1.165	-1.17
θ_3	0.793	0.753	1.658	1.538	-0.056	-0.212
θ_4	0.307	0.276	0.277	0.174	1.03	0.923
θ_5	0.255	0.237	0.517	0.455	0.672	0.596
θ_6	0.058	0.047	0.382	0.346	0.159	0.129
θ_7	0.009	0.004	0.124	0.106	-0,256	-0,271
θ_8	0.015	0.013	0.112	0.101	0.039	0.032
θ_9	0.042	0.040	0.142	0.136	-0.054	-0.059
θ_{10}	-0.036	-0.037	-0.038	-0.041	0.046	0.044
θ_{11}	-0.005	-0.006	0.045	0.043	-0.019	-0.020
θ_{12}	0.031	0.030	0.048	0.045	-0.015	-0.020
θ_{13}	0.007	0.007	0.066	0.064	0.012	0.011
θ_{14}	-0.015	-0.015	-0.031	-0.031	-0.004	-0.003

Appendix B

Coefficient matrix of the two-point correlation of *Euclid* dark matter halo catalog

TABLE B.1: The best fit parameters and their uncertainties of the BAO fit in different redshift groups.

Redshift	B	a_1	a_2	a_3
$z < 0.2$	1.92 ± 1.19	132 ± 182	0.97 ± 3.1	-0.022 ± 0.012
$0.2 < z < 0.4$	3.96 ± 0.42	-168 ± 110	4.67 ± 1.85	-0.025 ± 0.007
$0.4 < z < 0.6$	4.74 ± 0.43	-180 ± 106	4.99 ± 1.78	-0.026 ± 0.007
$0.6 < z < 0.8$	5.71 ± 0.83	-210 ± 203	5.90 ± 3.46	-0.033 ± 0.014

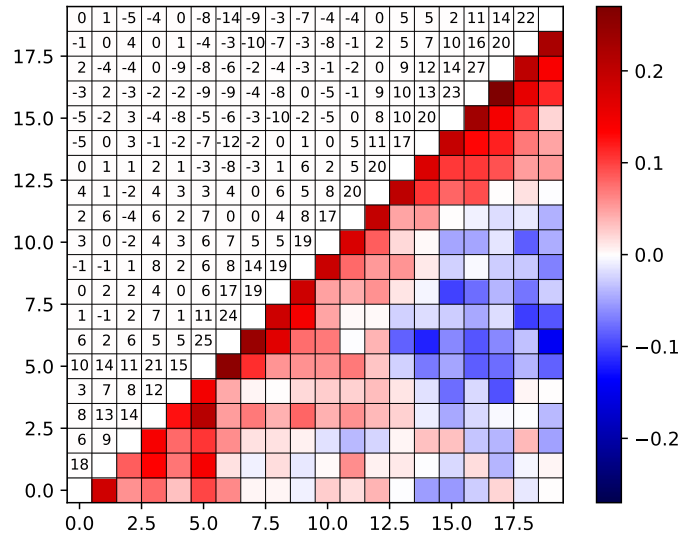


FIGURE B.1: Coefficient correlation matrix of the two-point correlation function of *Euclid* dark matter halos $z < 0.2$. The values in each box on the left above the diagonal are multiplied by 100.

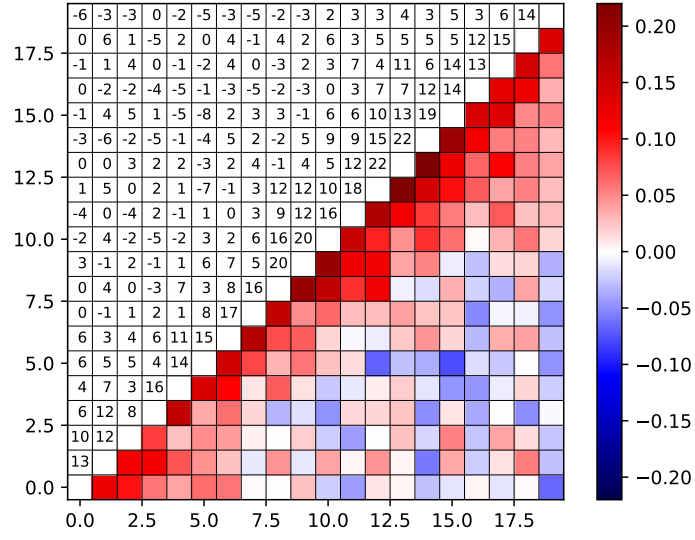


FIGURE B.2: Coefficient correlation matrix of the two-point correlation function of *Euclid* dark matter halos with $0.2 < z < 0.4$. The values in each box on the left above the diagonal are multiplied by 100.

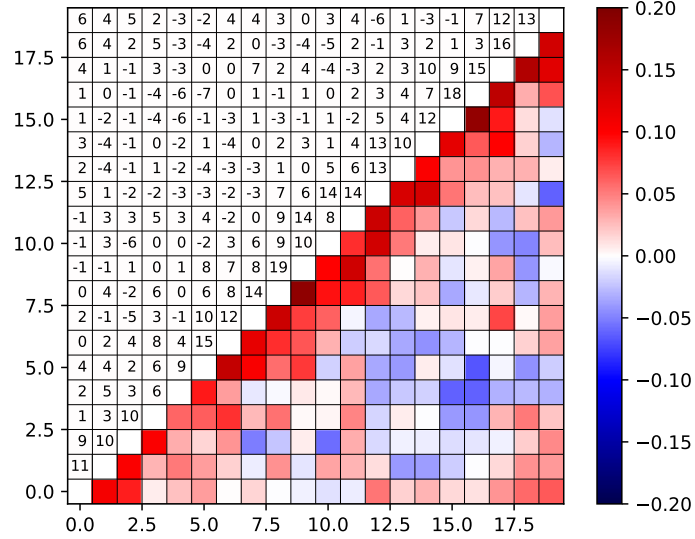


FIGURE B.3: Coefficient correlation matrix of the two-point correlation function of *Euclid* dark matter halos with $0.4 < z < 0.6$. The values in each box on the left above the diagonal are multiplied by 100.

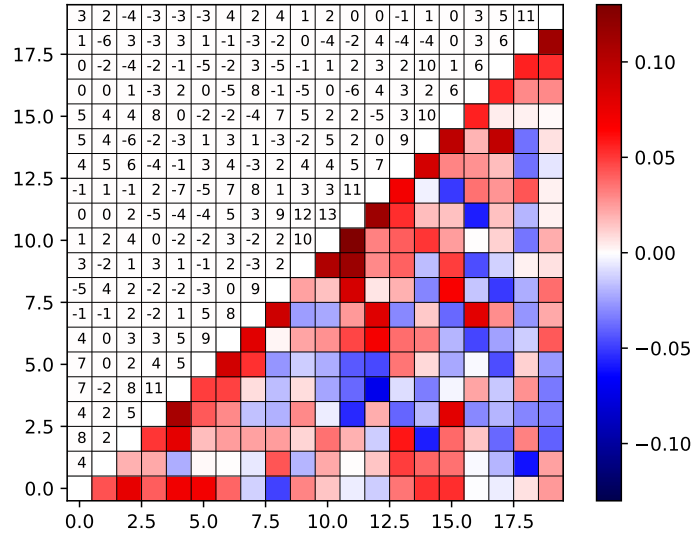


FIGURE B.4: Coefficient correlation matrix of the two-point correlation function of *Euclid* dark matter halos with $0.6 < z < 0.8$. The values in each box on the left above the diagonal are multiplied by 100.

Bibliography

- Abbott, B. P. et al. (2016). “Observation of Gravitational Waves from a Binary Black Hole Merger”. In: *Physical Review Letters* 116.6, 061102, p. 061102. DOI: [10.1103/PhysRevLett.116.061102](https://doi.org/10.1103/PhysRevLett.116.061102). arXiv: [1602.03837](https://arxiv.org/abs/1602.03837) [gr-qc].
- Abbott, B. P. et al. (2017a). “A gravitational-wave standard siren measurement of the Hubble constant”. In: *Nature* 551, pp. 85–88. DOI: [10.1038/nature24471](https://doi.org/10.1038/nature24471). arXiv: [1710.05835](https://arxiv.org/abs/1710.05835).
- (2017b). “GW170817: Observation of Gravitational Waves from a Binary Neutron Star Inspiral”. In: *Physical Review Letters* 119.16, 161101, p. 161101. DOI: [10.1103/PhysRevLett.119.161101](https://doi.org/10.1103/PhysRevLett.119.161101). arXiv: [1710.05832](https://arxiv.org/abs/1710.05832) [gr-qc].
- (2017c). “Multi-messenger Observations of a Binary Neutron Star Merger”. In: *ApJ* 848, L12, p. L12. DOI: [10.3847/2041-8213/aa91c9](https://doi.org/10.3847/2041-8213/aa91c9). arXiv: [1710.05833](https://arxiv.org/abs/1710.05833) [astro-ph.HE].
- Abell, G. O. (1958). “The Distribution of Rich Clusters of Galaxies.”. In: *ApJS* 3, p. 211. DOI: [10.1086/190036](https://doi.org/10.1086/190036).
- Abell, G. O., H. G. Corwin Jr., and R. P. Olowin (1989a). “A catalog of rich clusters of galaxies”. In: *ApJS* 70, pp. 1–138. DOI: [10.1086/191333](https://doi.org/10.1086/191333).
- (1989b). “A catalog of rich clusters of galaxies”. In: *ApJS* 70, pp. 1–138. DOI: [10.1086/191333](https://doi.org/10.1086/191333).
- Alam, Shadab et al. (2017). “The clustering of galaxies in the completed SDSS-III Baryon Oscillation Spectroscopic Survey: cosmological analysis of the DR12 galaxy sample”. In: *MNRAS* 470.3, pp. 2617–2652. DOI: [10.1093/mnras/stx721](https://doi.org/10.1093/mnras/stx721). arXiv: [1607.03155](https://arxiv.org/abs/1607.03155) [astro-ph.CO].
- Allen, S. W., A. E. Evrard, and A. B. Mantz (2011). “Cosmological Parameters from Observations of Galaxy Clusters”. In: *ARA&A* 49, pp. 409–470. DOI: [10.1146/annurev-astro-081710-102514](https://doi.org/10.1146/annurev-astro-081710-102514). arXiv: [1103.4829](https://arxiv.org/abs/1103.4829) [astro-ph.CO].
- Amelio, G. F., M. F. Tompsett, and G. E. Smith (1970). “Experimental Verification of the Charge Coupled Device Concept”. In: *Bell System Technical Journal* 49.4, pp. 593–600. DOI: [10.1002/j.1538-7305.1970.tb01791.x](https://doi.org/10.1002/j.1538-7305.1970.tb01791.x). eprint: <https://onlinelibrary.wiley.com/doi/pdf/10.1002/j.1538-7305.1970.tb01791.x>. URL: <https://onlinelibrary.wiley.com/doi/abs/10.1002/j.1538-7305.1970.tb01791.x>.
- Ata, Metin et al. (2018). “The clustering of the SDSS-IV extended Baryon Oscillation Spectroscopic Survey DR14 quasar sample: first measurement of baryon acoustic oscillations between redshift 0.8 and 2.2”. In: *MNRAS* 473.4, pp. 4773–4794. DOI: [10.1093/mnras/stx2630](https://doi.org/10.1093/mnras/stx2630). arXiv: [1705.06373](https://arxiv.org/abs/1705.06373) [astro-ph.CO].
- Bahcall, N. A. and R. M. Soneira (1983). “The spatial correlation function of rich clusters of galaxies”. In: *ApJ* 270, pp. 20–38. DOI: [10.1086/161094](https://doi.org/10.1086/161094).

- Bahcall, N. A., L. M. Lubin, and V. Dorman (1995). “Where is the Dark Matter?”. In: *ApJ* 447, p. L81. DOI: [10.1086/309577](#). eprint: [astro-ph/9506041](#).
- Bahcall, Neta A. et al. (2003). “The Richness-dependent Cluster Correlation Function: Early Sloan Digital Sky Survey Data”. In: *ApJ* 599, pp. 814–819. DOI: [10.1086/379599](#). arXiv: [astro-ph/0307102](#) [[astro-ph](#)].
- Barkhouse, W. A. et al. (2006). “ChAMP Serendipitous Galaxy Cluster Survey”. In: *ApJ* 645, pp. 955–976. DOI: [10.1086/504457](#). arXiv: [astro-ph/0603521](#) [[astro-ph](#)].
- Bartlett, J. G. (1997). “Galaxy Clusters in Cosmology: Cluster abundance as a probe of structure formation”. In: *From Quantum Fluctuations to Cosmological Structures*. Ed. by D. Valls-Gabaud et al. Vol. 126. Astronomical Society of the Pacific Conference Series, p. 365. eprint: [astro-ph/9703090](#).
- Basak, Soumen and Jacques Delabrouille (2013). “A needlet ILC analysis of WMAP 9-year polarization data: CMB polarization power spectra”. In: *MNRAS* 435.1, pp. 18–29. DOI: [10.1093/mnras/stt1158](#). arXiv: [1204.0292](#) [[astro-ph.CO](#)].
- Basilakos, S. et al. (2003). “Comparison between optical and X-ray cluster detection methods”. In: *arXiv e-prints*, [astro-ph/0310249](#), [astro-ph/0310249](#). arXiv: [astro-ph/0310249](#) [[astro-ph](#)].
- Basilakos, S., M. Plionis, and C. Ragone-Figueroa (2008). “The Halo Mass-Bias Redshift Evolution in the Λ CDM Cosmology”. In: *ApJ* 678.2, pp. 627–634. DOI: [10.1086/586725](#). arXiv: [0801.3889](#) [[astro-ph](#)].
- Basilakos, Spyros and Manolis Plionis (2004). “Modelling the two-point correlation function of galaxy clusters in the Sloan Digital Sky Survey”. In: *MNRAS* 349, pp. 882–888. DOI: [10.1111/j.1365-2966.2004.07559.x](#). arXiv: [astro-ph/0304551](#) [[astro-ph](#)].
- Battistelli, Elia S. et al. (2016). “Galaxy clusters as probes for cosmology and dark matter”. In: *International Journal of Modern Physics D* 25, 1630023, p. 1630023. DOI: [10.1142/S0218271816300238](#). arXiv: [1609.01110](#) [[astro-ph.CO](#)].
- Baugh, C. M. (1996). “The real-space correlation function measured from the APM Galaxy Survey”. In: *MNRAS* 280, pp. 267–275. DOI: [10.1093/mnras/280.1.267](#). arXiv: [astro-ph/9512011](#) [[astro-ph](#)].
- Baugh, C. M. and G. Efstathiou (1993). “The Three-Dimensional Power Spectrum Measured from the APM Galaxy Survey - Part One - Use of the Angular Correlation Function”. In: *MNRAS* 265, p. 145. DOI: [10.1093/mnras/265.1.145](#).
- Bautista, Julian E. et al. (2017). “Measurement of baryon acoustic oscillation correlations at $z = 2.3$ with SDSS DR12 Ly α -Forests”. In: *A&A* 603, A12, A12. DOI: [10.1051/0004-6361/201730533](#). arXiv: [1702.00176](#) [[astro-ph.CO](#)].
- Bautista, Julian E. et al. (2018). “The SDSS-IV Extended Baryon Oscillation Spectroscopic Survey: Baryon Acoustic Oscillations at Redshift of 0.72 with the DR14 Luminous Red Galaxy Sample”. In: *ApJ* 863.1, 110, p. 110. DOI: [10.3847/1538-4357/aacea5](#). arXiv: [1712.08064](#) [[astro-ph.CO](#)].
- Beckmann, V. and C. R. Shrader (2012). *Active Galactic Nuclei*. DOI: [10.1002/9783527666829](#).

- Behroozi, Peter S., Risa H. Wechsler, and Hao-Yi Wu (2013). "The ROCKSTAR Phase-space Temporal Halo Finder and the Velocity Offsets of Cluster Cores". In: *ApJ* 762, 109, p. 109. DOI: [10.1088/0004-637X/762/2/109](#). arXiv: [1110.4372 \[astro-ph.CO\]](#).
- Benítez, N. et al. (2015). "J-PAS: The Javalambre-Physics of the Accelerated Universe Astrophysical Survey". In: *Highlights of Spanish Astrophysics VIII*. Ed. by A. J. Cenarro et al., pp. 148–153.
- Berlind, Andreas A. et al. (2006). "Percolation Galaxy Groups and Clusters in the SDSS Redshift Survey: Identification, Catalogs, and the Multiplicity Function". In: *The Astrophysical Journal Supplement Series* 167, pp. 1–25. DOI: [10.1086/508170](#). arXiv: [astro-ph/0601346 \[astro-ph\]](#).
- Bertin, E. and S. Arnouts (1996). "SExtractor: Software for source extraction.". In: *A&AS* 117, pp. 393–404. DOI: [10.1051/aas:1996164](#).
- Beutler, F. et al. (2011). "The 6dF Galaxy Survey: baryon acoustic oscillations and the local Hubble constant". In: *MNRAS* 416, pp. 3017–3032. DOI: [10.1111/j.1365-2966.2011.19250.x](#). arXiv: [1106.3366](#).
- Blake, C. et al. (2011). "The WiggleZ Dark Energy Survey: mapping the distance-redshift relation with baryon acoustic oscillations". In: *MNRAS* 418, pp. 1707–1724. DOI: [10.1111/j.1365-2966.2011.19592.x](#). arXiv: [1108.2635](#).
- Blanchard, A., Z. Sakr, and S. Ilić (2018). "Cosmological cluster tension". In: *arXiv e-prints*. arXiv: [1805.06976](#).
- Bleem, L. E. et al. (2015). "Galaxy Clusters Discovered via the Sunyaev-Zel'dovich Effect in the 2500-Square-Degree SPT-SZ Survey". In: *The Astrophysical Journal Supplement Series* 216, 27, p. 27. DOI: [10.1088/0067-0049/216/2/27](#). arXiv: [1409.0850 \[astro-ph.CO\]](#).
- Bock, J. J. et al. (1995). "A Novel Bolometer for Infrared and Millimeter-Wave Astrophysics". In: *Space Science Reviews* 74, pp. 229–235. DOI: [10.1007/BF00751274](#).
- Böhringer, H. et al. (2000). "The Northern ROSAT All-Sky (NORAS) Galaxy Cluster Survey. I. X-Ray Properties of Clusters Detected as Extended X-Ray Sources". In: *The Astrophysical Journal Supplement Series* 129, pp. 435–474. DOI: [10.1086/313427](#). arXiv: [astro-ph/0003219 \[astro-ph\]](#).
- Böhringer, H. et al. (2004). "The ROSAT-ESO Flux Limited X-ray (REFLEX) Galaxy cluster survey. V. The cluster catalogue". In: *A&A* 425, pp. 367–383. DOI: [10.1051/0004-6361:20034484](#). eprint: [astro-ph/0405546](#).
- Bonamente, Massimiliano et al. (2012). "Comparison of pressure profiles of massive relaxed galaxy clusters using the Sunyaev-Zel'dovich and x-ray data". In: *New Journal of Physics* 14, 025010, p. 025010. DOI: [10.1088/1367-2630/14/2/025010](#). arXiv: [1112.1599 \[astro-ph.CO\]](#).
- Bond, J. R. et al. (1991). "Excursion set mass functions for hierarchical Gaussian fluctuations". In: *ApJ* 379, pp. 440–460. DOI: [10.1086/170520](#).
- Borgani, S. (2008). "Cosmology with Clusters of Galaxies". In: *A Pan-Chromatic View of Clusters of Galaxies and the Large-Scale Structure*, edited by M. Plionis, O. López-Cruz and D. Hughes. *Lecture Notes in Physics* Vol. 740. 474 p. 24 illus. in color., Hardcover, ISBN: 978-1-4020-6940-6. Published by Springer,

- Dordrecht, The Netherlands, 2008, p.287. Ed. by M. Plionis, O. López-Cruz, and D. Hughes, p. 24. DOI: 10.1007/978-1-4020-6941-3_9.*
- Borgani, S., M. Plionis, and V. Kolokotronis (1999). "Cosmological constraints from the clustering properties of the X-ray Brightest Abell-type Cluster sample". In: *MNRAS* 305, pp. 866–874. DOI: 10.1046/j.1365-8711.1999.02468.x. eprint: astro-ph/9812417.
- Borgani, Stefano and Luigi Guzzo (2001). "X-ray clusters of galaxies as tracers of structure in the Universe". In: *Nature* 409.6816, pp. 39–45. DOI: 10.1038/409039A0. arXiv: astro-ph/0012439 [astro-ph].
- Botzler, C. S. et al. (2004). "Finding structures in photometric redshift galaxy surveys: an extended friends-of-friends algorithm". In: *MNRAS* 349, pp. 425–439. DOI: 10.1111/j.1365-2966.2004.07468.x. eprint: astro-ph/0312018.
- Bougoin, M. et al. (2017). "The SiC structure of the EUCLID NISP instrument". In: *Society of Photo-Optical Instrumentation Engineers (SPIE) Conference Series*. Vol. 10562. Society of Photo-Optical Instrumentation Engineers (SPIE) Conference Series, 105624J. DOI: 10.1117/12.2296060.
- Bower, R. G., J. R. Lucey, and R. S. Ellis (1992). "Precision Photometry of Early Type Galaxies in the Coma and Virgo Clusters - a Test of the Universality of the Colour / Magnitude Relation - Part Two - Analysis". In: *MNRAS* 254, p. 601. DOI: 10.1093/mnras/254.4.601.
- Boyle, W. S. and G. E. Smith (1970). "Charge Coupled Semiconductor Devices". In: *Bell System Technical Journal* 49.4, pp. 587–593. DOI: 10.1002/j.1538-7305.1970.tb01790.x. eprint: https://onlinelibrary.wiley.com/doi/pdf/10.1002/j.1538-7305.1970.tb01790.x. URL: https://onlinelibrary.wiley.com/doi/abs/10.1002/j.1538-7305.1970.tb01790.x.
- Byram, E. T., T. A. Chubb, and H. Friedman (1966). "Cosmic X-ray Sources, Galactic and Extragalactic". In: *Science* 152, pp. 66–71. DOI: 10.1126/science.152.3718.66.
- Calzetti, D., M. Giavalisco, and A. Meiksin (1992). "The shape of the two-point correlation function - Evidence for a double power law". In: *ApJ* 398, pp. 429–440. DOI: 10.1086/171867.
- Capak, P. et al. (2019). "Enhancing LSST Science with Euclid Synergy". In: *arXiv e-prints*, arXiv:1904.10439, arXiv:1904.10439. arXiv: 1904.10439 [astro-ph.IM].
- Carlstrom, John E., Gilbert P. Holder, and Erik D. Reese (2002). "Cosmology with the Sunyaev-Zel'dovich Effect". In: *Annual Review of Astronomy and Astrophysics* 40, pp. 643–680. DOI: 10.1146/annurev.astro.40.060401.093803. arXiv: astro-ph/0208192 [astro-ph].
- Chary, R. et al. (2019). "Joint Survey Processing of LSST, Euclid and WFIRST: Enabling a broad array of astrophysics and cosmology through pixel level combinations of datasets". In: *arXiv e-prints*, arXiv:1910.01259, arXiv:1910.01259. arXiv: 1910.01259 [astro-ph.GA].
- Chluba, Jens (2018). "Future Steps in Cosmology using Spectral Distortions of the Cosmic Microwave Background". In: *arXiv e-prints*, arXiv:1806.02915, arXiv:1806.02915. arXiv: 1806.02915 [astro-ph.CO].

- Coil, Alison L. (2013). "The Large-Scale Structure of the Universe". In: *Planets, Stars and Stellar Systems Vol. 6, by Oswalt, Terry D.; Keel, William C.*, ISBN 978-94-007-5608-3. Springer Science+Business Media Dordrecht, 2013, p. 387. Ed. by Terry D. Oswalt and William C. Keel, p. 387. DOI: [10.1007/978-94-007-5609-0_8](#).
- Cole, Shaun and Cedric Lacey (1996). "The structure of dark matter haloes in hierarchical clustering models". In: *MNRAS* 281, p. 716. DOI: [10.1093/mnras/281.2.716](#). arXiv: [astro-ph/9510147](#) [astro-ph].
- Cole, Shaun et al. (2005). "The 2dF Galaxy Redshift Survey: power-spectrum analysis of the final data set and cosmological implications". In: *MNRAS* 362, pp. 505–534. DOI: [10.1111/j.1365-2966.2005.09318.x](#). arXiv: [astro-ph/0501174](#) [astro-ph].
- Collins, C. A., N. H. Heydon-Dumbleton, and H. T. MacGillivray (1989). "The Edinburgh/Durham Southern Galaxy Catalogue. I - First results on the galaxy angular correlation function". In: *MNRAS* 236, 7P–12P. DOI: [10.1093/mnras/236.1.7P](#).
- Collins, C. A. et al. (2000). "The ROSAT-ESO Flux-Limited X-ray (REFLEX) galaxy cluster survey - II. The spatial correlation function". In: *MNRAS* 319, pp. 939–948. DOI: [10.1046/j.1365-8711.2000.03918.x](#). arXiv: [astro-ph/0008245](#) [astro-ph].
- Connolly, A. J. et al. (2002). "The Angular Correlation Function of Galaxies from Early Sloan Digital Sky Survey Data". In: *ApJ* 579, pp. 42–47. DOI: [10.1086/342787](#). eprint: [astro-ph/0107417](#).
- Courtin, J. et al. (2011). "Imprints of dark energy on cosmic structure formation - II. Non-universality of the halo mass function". In: *MNRAS* 410, pp. 1911–1931. DOI: [10.1111/j.1365-2966.2010.17573.x](#). arXiv: [1001.3425](#) [astro-ph.CO].
- Croft, R. A. C. et al. (1997). "The richness dependence of galaxy cluster correlations: results from a redshift survey of rich APM clusters". In: *MNRAS* 291, pp. 305–313. DOI: [10.1093/mnras/291.2.305](#). arXiv: [astro-ph/9701040](#) [astro-ph].
- Dalton, G. B. et al. (1994). "The Two-Point Correlation Function of Rich Clusters of Galaxies - Results from an Extended APM Cluster Redshift Survey". In: *MNRAS* 271, p. L47. DOI: [10.1093/mnras/271.1.L47](#). eprint: [astro-ph/9407076](#).
- Dalton, G. B. et al. (1997). "The APM Galaxy Survey - V. Catalogues of galaxy clusters". In: *MNRAS* 289, pp. 263–284. DOI: [10.1093/mnras/289.2.263](#). arXiv: [astro-ph/9701180](#) [astro-ph].
- Davis, M. and P. J. E. Peebles (1983a). "A survey of galaxy redshifts. V - The two-point position and velocity correlations". In: *ApJ* 267, pp. 465–482. DOI: [10.1086/160884](#).
- (1983b). "A survey of galaxy redshifts. V - The two-point position and velocity correlations". In: *ApJ* 267, pp. 465–482. DOI: [10.1086/160884](#).
- de Haan, T. et al. (2016). "Cosmological Constraints from Galaxy Clusters in the 2500 Square-degree SPT-SZ Survey". In: *ApJ* 832.1, 95, p. 95. DOI: [10.3847/0004-637X/832/1/95](#). arXiv: [1603.06522](#) [astro-ph.CO].

- de Jong, Jelte T. A. et al. (2013). “The Kilo-Degree Survey”. In: *Experimental Astronomy* 35, pp. 25–44. DOI: [10.1007/s10686-012-9306-1](https://doi.org/10.1007/s10686-012-9306-1). arXiv: [1206.1254](https://arxiv.org/abs/1206.1254) [astro-ph.CO].
- Debray, B. et al. (2006). “The Besançon Model of our Galaxy: a simulation tool towards the Virtual Observatory”. In: *Astronomical Data Analysis Software and Systems XV*. Ed. by C. Gabriel et al. Vol. 351. Astronomical Society of the Pacific Conference Series, p. 224.
- Delabrouille, J., J. F. Cardoso, and G. Patanchon (2003). “Multidetector multicomponent spectral matching and applications for cosmic microwave background data analysis”. In: *MNRAS* 346.4, pp. 1089–1102. DOI: [10.1111/j.1365-2966.2003.07069.x](https://doi.org/10.1111/j.1365-2966.2003.07069.x). arXiv: [astro-ph/0211504](https://arxiv.org/abs/astro-ph/0211504) [astro-ph].
- DES Collaboration et al. (2018). “Cosmological Constraints from Multiple Probes in the Dark Energy Survey”. In: *arXiv e-prints*, arXiv:1811.02375, arXiv:1811.02375. arXiv: [1811.02375](https://arxiv.org/abs/1811.02375) [astro-ph.CO].
- Despali, Giulia et al. (2016). “The universality of the virial halo mass function and models for non-universality of other halo definitions”. In: *MNRAS* 456, pp. 2486–2504. DOI: [10.1093/mnras/stv2842](https://doi.org/10.1093/mnras/stv2842). arXiv: [1507.05627](https://arxiv.org/abs/1507.05627) [astro-ph.CO].
- Dicke, R. H. et al. (1965). “Cosmic Black-Body Radiation.”. In: *ApJ* 142, pp. 414–419. DOI: [10.1086/148306](https://doi.org/10.1086/148306).
- Dodd, R. J. and H. T. MacGillivray (1986). “Automated detection of clusters of galaxies”. In: *AJ* 92, pp. 706–712. DOI: [10.1086/114206](https://doi.org/10.1086/114206).
- Douspis, Marian, Laura Salvati, and Nabila Aghanim (2019). “On the tension between Large Scale Structures and Cosmic Microwave Background”. In: *arXiv e-prints*, arXiv:1901.05289, arXiv:1901.05289. arXiv: [1901.05289](https://arxiv.org/abs/1901.05289) [astro-ph.CO].
- du Mas des Bourboux, Héliion et al. (2017). “Baryon acoustic oscillations from the complete SDSS-III Ly α -quasar cross-correlation function at $z = 2.4$ ”. In: *A&A* 608, A130, A130. DOI: [10.1051/0004-6361/201731731](https://doi.org/10.1051/0004-6361/201731731). arXiv: [1708.02225](https://arxiv.org/abs/1708.02225) [astro-ph.CO].
- Ebeling, H. and G. Wiedenmann (1993). “Detecting structure in two dimensions combining Voronoi tessellation and percolation”. In: *Phys. Rev. E* 47 (1), pp. 704–710. DOI: [10.1103/PhysRevE.47.704](https://doi.org/10.1103/PhysRevE.47.704). URL: <https://link.aps.org/doi/10.1103/PhysRevE.47.704>.
- Ebeling, H. et al. (1996). “Properties of the X-ray-brightest Abell-type clusters of galaxies (XBACs) from ROSAT All-Sky Survey data - I. The sample”. In: *MNRAS* 281, pp. 799–829. DOI: [10.1093/mnras/281.3.799](https://doi.org/10.1093/mnras/281.3.799). eprint: [astro-ph/9602080](https://arxiv.org/abs/astro-ph/9602080).
- Efron, B. (1982). *The Jackknife, the Bootstrap and other resampling plans*.
- Efron, Bradley (1979). “Bootstrap Methods: Another Look at the Jackknife”. In: *The Annals of Statistics* 7. DOI: [10.1214/aos/1176344552](https://doi.org/10.1214/aos/1176344552).
- Efstathiou, G. (1993). “Galaxy Clustering on Large Scales”. In: *Proceedings of the National Academy of Science* 90, pp. 4859–4866. DOI: [10.1073/pnas.90.11.4859](https://doi.org/10.1073/pnas.90.11.4859).
- Efstathiou, G. et al. (1985). “Numerical techniques for large cosmological N-body simulations”. In: *ApJS* 57, pp. 241–260. DOI: [10.1086/191003](https://doi.org/10.1086/191003).

- Einasto, Jaan (2001). “Large scale structure”. In: *New Astronomy Reviews* 45, pp. 355–372. DOI: [10.1016/S1387-6473\(00\)00158-5](#). arXiv: [astro-ph/0011332](#) [[astro-ph](#)].
- Einstein, A. (1915). “Die Feldgleichungen der Gravitation”. In: *Sitzungsberichte der Königlich Preußischen Akademie der Wissenschaften (Berlin)*, Seite 844–847.
- Eisenstein, D. J. and W. Hu (1998a). “Baryonic Features in the Matter Transfer Function”. In: *ApJ* 496, pp. 605–614. DOI: [10.1086/305424](#). eprint: [astro-ph/9709112](#).
- (1998b). “Baryonic Features in the Matter Transfer Function”. In: *ApJ* 496, pp. 605–614. DOI: [10.1086/305424](#). eprint: [astro-ph/9709112](#).
- Eisenstein, Daniel J. et al. (2005). “Detection of the Baryon Acoustic Peak in the Large-Scale Correlation Function of SDSS Luminous Red Galaxies”. In: *ApJ* 633, pp. 560–574. DOI: [10.1086/466512](#). arXiv: [astro-ph/0501171](#) [[astro-ph](#)].
- Eisenstein, Daniel J., Hee-Jong Seo, and Martin White (2007). “On the Robustness of the Acoustic Scale in the Low-Redshift Clustering of Matter”. In: *ApJ* 664, pp. 660–674. DOI: [10.1086/518755](#). arXiv: [astro-ph/0604361](#) [[astro-ph](#)].
- Eriksen, H. K. et al. (2008). “Joint Bayesian Component Separation and CMB Power Spectrum Estimation”. In: *ApJ* 676.1, pp. 10–32. DOI: [10.1086/525277](#). arXiv: [0709.1058](#) [[astro-ph](#)].
- Estrada, Juan, Emiliano Sefusatti, and Joshua A. Frieman (2009). “The Correlation Function of Optically Selected Galaxy Clusters in the Sloan Digital Sky Survey”. In: *ApJ* 692, pp. 265–282. DOI: [10.1088/0004-637X/692/1/265](#). arXiv: [0801.3485](#) [[astro-ph](#)].
- Farrens, S. et al. (2011). “Friends-of-friends groups and clusters in the 2SLAQ catalogue”. In: *MNRAS* 417, pp. 1402–1416. DOI: [10.1111/j.1365-2966.2011.19356.x](#). arXiv: [1106.5687](#) [[astro-ph.CO](#)].
- Fernández-Cobos, R. et al. (2012). “Multiresolution internal template cleaning: an application to the Wilkinson Microwave Anisotropy Probe 7-yr polarization data”. In: *MNRAS* 420.3, pp. 2162–2169. DOI: [10.1111/j.1365-2966.2011.20182.x](#). arXiv: [1106.2016](#) [[astro-ph.CO](#)].
- Fixsen, D. J. and J. C. Mather (2002). “The Spectral Results of the Far-Infrared Absolute Spectrophotometer Instrument on COBE”. In: *ApJ* 581, pp. 817–822. DOI: [10.1086/344402](#).
- Friedmann, A. (1922). “Über die Krümmung des Raumes”. In: *Zeitschrift für Physik* 10, pp. 377–386. DOI: [10.1007/BF01332580](#).
- Frieman, J. A., M. S. Turner, and D. Huterer (2008). “Dark energy and the accelerating universe.”. In: *Annual Review of Astronomy and Astrophysics* 46, pp. 385–432. DOI: [10.1146/annurev.astro.46.060407.145243](#). arXiv: [0803.0982](#) [[astro-ph](#)].
- Gal, Roy R. (2006). “Optical Detection of Galaxy Clusters”. In: *arXiv e-prints*, [astro-ph/0601195](#), [astro-ph/0601195](#). arXiv: [astro-ph/0601195](#) [[astro-ph](#)].
- Galilei, G. (1610). *Sidereus nuncius magna, longeque admirabilia spectacula pandens lunae facie, fixis innumeris, lacteo circulo, stellis nebulosis, ... Galileo Galileo : nuper a se reperti beneficio sunt observata in apprime vero in quatuor planetis*

- circa Iovis stellam disparibus intervallis, atque periodis, celeritate mirabili circumvolutis ... atque Medicea sidera nuncupandos decrevit.* DOI: [10.3931/e-rara-695](#).
- Gamow, G. (1948). "The Evolution of the Universe". In: *Nature* 162, pp. 680–682. DOI: [10.1038/162680a0](#).
- Giacconi, R. et al. (1972). "The Uhuru catalog of X-ray sources.". In: *ApJ* 178, pp. 281–308. DOI: [10.1086/151790](#).
- Gioia, I. M. and G. A. Luppino (1994). "The EMSS Catalog of X-Ray-selected Clusters of Galaxies. I. an Atlas of CCD Images of 41 Distant Clusters". In: *The Astrophysical Journal Supplement Series* 94, p. 583. DOI: [10.1086/192083](#). arXiv: [astro-ph/9405069](#) [[astro-ph](#)].
- Gladders, M. D. and H. K. C. Yee (2005). "The Red-Sequence Cluster Survey. I. The Survey and Cluster Catalogs for Patches RCS 0926+37 and RCS 1327+29". In: *ApJS* 157, pp. 1–29. DOI: [10.1086/427327](#). eprint: [astro-ph/0411075](#).
- Gladders, Michael D. and H. K. C. Yee (2000). "A New Method For Galaxy Cluster Detection. I. The Algorithm". In: *AJ* 120, pp. 2148–2162. DOI: [10.1086/301557](#). arXiv: [astro-ph/0004092](#) [[astro-ph](#)].
- Gonzalez, Anthony H., Dennis Zaritsky, and Risa H. Wechsler (2002). "The Las Campanas Distant Cluster Survey Correlation Function". In: *ApJ* 571, pp. 129–135. DOI: [10.1086/339914](#). arXiv: [astro-ph/0201534](#) [[astro-ph](#)].
- Goto, T. et al. (2002). "The Cut-and-Enhance Method: Selecting Clusters of Galaxies from the Sloan Digital Sky Survey Commissioning Data". In: *AJ* 123, pp. 1807–1825. DOI: [10.1086/339303](#). eprint: [astro-ph/0112482](#).
- Hamilton, A. J. S. (1993). "Toward Better Ways to Measure the Galaxy Correlation Function". In: *ApJ* 417, p. 19. DOI: [10.1086/173288](#).
- Hasselfield, Matthew et al. (2013). "The Atacama Cosmology Telescope: Sunyaev-Zel'dovich selected galaxy clusters at 148 GHz from three seasons of data". In: *Journal of Cosmology and Astro-Particle Physics* 2013, 008, p. 008. DOI: [10.1088/1475-7516/2013/07/008](#). arXiv: [1301.0816](#) [[astro-ph.CO](#)].
- Herranz, D. et al. (2002). "Filtering techniques for the detection of Sunyaev-Zel'dovich clusters & in multifrequency maps". In: *MNRAS* 336, pp. 1057–1068. DOI: [10.1046/j.1365-8711.2002.05704.x](#). arXiv: [astro-ph/0203486](#) [[astro-ph](#)].
- Hewett, P. C. (1982). "The estimation of galaxy angular correlation functions". In: *MNRAS* 201, pp. 867–883. DOI: [10.1093/mnras/201.4.867](#).
- Hilton, Matt et al. (2018). "The Atacama Cosmology Telescope: The Two-season ACTPol Sunyaev-Zel'dovich Effect Selected Cluster Catalog". In: *The Astrophysical Journal Supplement Series* 235, 20, p. 20. DOI: [10.3847/1538-4365/aaa6cb](#). arXiv: [1709.05600](#) [[astro-ph.CO](#)].
- Hinshaw, G. et al. (2013). "Nine-year Wilkinson Microwave Anisotropy Probe (WMAP) Observations: Cosmological Parameter Results". In: *The Astrophysical Journal Supplement Series* 208, 19, p. 19. DOI: [10.1088/0067-0049/208/2/19](#). arXiv: [1212.5226](#) [[astro-ph.CO](#)].
- Holwerda, B. W. (2005). "Source Extractor for Dummies v5". In: *arXiv e-prints*, [astro-ph/0512139](#), [astro-ph/0512139](#). arXiv: [astro-ph/0512139](#) [[astro-ph](#)].

- Hong, T. et al. (2012). "The Correlation Function of Galaxy Clusters and Detection of Baryon Acoustic Oscillations". In: *ApJ* 749, 81, p. 81. DOI: [10.1088/0004-637X/749/1/81](#). arXiv: [1202.0640 \[astro-ph.CO\]](#).
- Howell, S. B. (2000). *Handbook of CCD Astronomy*.
- Hubble, E. (1929). "A Relation between Distance and Radial Velocity among Extra-Galactic Nebulae". In: *Proceedings of the National Academy of Science* 15, pp. 168–173. DOI: [10.1073/pnas.15.3.168](#).
- Hubble, E. P. (1925). "Cepheids in spiral nebulae". In: *The Observatory* 48, pp. 139–142.
- Huchra, J. P. and M. J. Geller (1982). "Groups of galaxies. I - Nearby groups". In: *ApJ* 257, pp. 423–437. DOI: [10.1086/160000](#).
- Huterer, Dragan and Daniel L. Shafer (2018). "Dark energy two decades after: observables, probes, consistency tests". In: *Reports on Progress in Physics* 81, 016901, p. 016901. DOI: [10.1088/1361-6633/aa997e](#). arXiv: [1709.01091 \[astro-ph.CO\]](#).
- Ibata, R. A. et al. (2017). "The Canada-France Imaging Survey: First Results from the u-Band Component". In: *ApJ* 848, 128, p. 128. DOI: [10.3847/1538-4357/aa855c](#). arXiv: [1708.06356](#).
- Inserra, C. et al. (2018). "Euclid: Superluminous supernovae in the Deep Survey". In: *A&A* 609, A83, A83. DOI: [10.1051/0004-6361/201731758](#). arXiv: [1710.09585 \[astro-ph.CO\]](#).
- Janesick, J. and M Blouke (1987). "Sky on a Chip: The Fabulous CCD". In: *Sky and Telescope* 74, pp. 238–282.
- Jenkins, A. et al. (2001). "The mass function of dark matter haloes". In: *MNRAS* 321, pp. 372–384. DOI: [10.1046/j.1365-8711.2001.04029.x](#). eprint: [astro-ph/0005260](#).
- Kaiser, N. (1984). "On the spatial correlations of Abell clusters". In: *ApJ* 284, pp. L9–L12. DOI: [10.1086/184341](#).
- (1986). "Evolution and clustering of rich clusters". In: *MNRAS* 222, pp. 323–345. DOI: [10.1093/mnras/222.2.323](#).
- (1987). "Clustering in real space and in redshift space". In: *MNRAS* 227, pp. 1–21. DOI: [10.1093/mnras/227.1.1](#).
- Kaiser, N. et al. (2002). "Pan-STARRS: A Large Synoptic Survey Telescope Array". In: *Survey and Other Telescope Technologies and Discoveries*. Ed. by J. A. Tyson and S. Wolff. Vol. 4836. "Survey and Other Telescope Technologies and Discoveries. Edited by Tyson, J. Anthony; Wolff, Sidney. Proceedings of the SPIE.", pp. 154–164. DOI: [10.1117/12.457365](#).
- Karachentsev, I. D. and O. G. Kashibadze (2006). "Masses of the local group and of the M81 group estimated from distortions in the local velocity field". In: *Astrophysics* 49, pp. 3–18. DOI: [10.1007/s10511-006-0002-6](#).
- Kepner, Jeremy et al. (1999). "An Automated Cluster Finder: The Adaptive Matched Filter". In: *ApJ* 517, pp. 78–91. DOI: [10.1086/307160](#). arXiv: [astro-ph/9803125 \[astro-ph\]](#).
- Kerscher, Martin, István Szapudi, and Alexander S. Szalay (2000). "A Comparison of Estimators for the Two-Point Correlation Function". In: *ApJ* 535, pp. L13–L16. DOI: [10.1086/312702](#). arXiv: [astro-ph/9912088 \[astro-ph\]](#).

- Kilbinger, Martin et al. (2013). “CFHTLenS: combined probe cosmological model comparison using 2D weak gravitational lensing”. In: *MNRAS* 430, pp. 2200–2220. DOI: [10.1093/mnras/stt041](#). arXiv: [1212.3338 \[astro-ph.CO\]](#).
- Kim, R. S. J. et al. (2002). “Detecting Clusters of Galaxies in the Sloan Digital Sky Survey. I. Monte Carlo Comparison of Cluster Detection Algorithms”. In: *AJ* 123, pp. 20–36. DOI: [10.1086/324727](#). eprint: [astro-ph/0110259](#).
- Knebe, A. et al. (2011). “Halo es gone MAD: The Halo-Finder Comparison Project”. In: *MNRAS* 415, pp. 2293–2318. DOI: [10.1111/j.1365-2966.2011.18858.x](#). arXiv: [1104.0949](#).
- Koester, B. P. et al. (2007). “MaxBCG: A Red-Sequence Galaxy Cluster Finder”. In: *ApJ* 660, pp. 221–238. DOI: [10.1086/512092](#). eprint: [astro-ph/0701268](#).
- Kotov, O. and A. Vikhlinin (2006). “Chandra Sample of Galaxy Clusters at $z = 0.4-0.55$: Evolution in the Mass-Temperature Relation”. In: *ApJ* 641, pp. 752–755. DOI: [10.1086/500553](#). arXiv: [astro-ph/0511044 \[astro-ph\]](#).
- Labatie, Antoine et al. (2010). “Uncertainty in 2-point correlation function estimators and BAO detection in SDSS DR7”. In: *arXiv e-prints*, arXiv:1009.1232, arXiv:1009.1232. arXiv: [1009.1232 \[astro-ph.CO\]](#).
- Lacey, C. and S. Cole (1993). “Merger rates in hierarchical models of galaxy formation”. In: *MNRAS* 262, pp. 627–649. DOI: [10.1093/mnras/262.3.627](#).
- Landy, S. D. and A. S. Szalay (1993). “Bias and variance of angular correlation functions”. In: *ApJ* 412, pp. 64–71. DOI: [10.1086/172900](#).
- LaRoque, S. J. et al. (2006). “X-Ray and Sunyaev-Zel’dovich Effect Measurements of the Gas Mass Fraction in Galaxy Clusters”. In: *ApJ* 652, pp. 917–936. DOI: [10.1086/508139](#). eprint: [astro-ph/0604039](#).
- Laureijs, R. et al. (2011). “Euclid Definition Study Report”. In: *arXiv e-prints*. arXiv: [1110.3193 \[astro-ph.CO\]](#).
- Lavaux, G. et al. (2004). “Sunyaev-Zel’dovich polarization as a probe of the intracluster medium”. In: *MNRAS* 347, pp. 729–739. DOI: [10.1111/j.1365-2966.2004.07265.x](#). eprint: [astro-ph/0307293](#).
- Leach, S. M. et al. (2008). “Component separation methods for the PLANCK mission”. In: *A&A* 491.2, pp. 597–615. DOI: [10.1051/0004-6361:200810116](#). arXiv: [0805.0269 \[astro-ph\]](#).
- Leibundgut, Bruno and Jesper Sollerman (2002). “A cosmological surprise: the universe accelerates”. In: *arXiv e-prints*, astro-ph/0204492, astro-ph/0204492. arXiv: [astro-ph/0204492 \[astro-ph\]](#).
- Lemaître, G. (1927). “Un Univers homogène de masse constante et de rayon croissant rendant compte de la vitesse radiale des nébuleuses extra-galactiques”. In: *Annales de la Société Scientifique de Bruxelles* 47, pp. 49–59.
- Lesgourgues, Julien (2011). “The Cosmic Linear Anisotropy Solving System (CLASS) I: Overview”. In: *arXiv e-prints*, arXiv:1104.2932, arXiv:1104.2932. arXiv: [1104.2932 \[astro-ph.IM\]](#).
- Limber, D. N. (1953). “The Analysis of Counts of the Extragalactic Nebulae in Terms of a Fluctuating Density Field.”. In: *ApJ* 117, p. 134. DOI: [10.1086/145672](#).

- Linde, A. (2014). “Inflationary Cosmology after Planck 2013”. In: *arXiv e-prints*. arXiv: [1402.0526 \[hep-th\]](#).
- Lobo, C. et al. (2000). “EISily looking for distant clusters of galaxies - a new algorithm and its application to the EIS-wide data”. In: *A&A* 360, pp. 896–910. eprint: [astro-ph/0006431](#).
- LSST Dark Energy Science Collaboration (2012). “Large Synoptic Survey Telescope: Dark Energy Science Collaboration”. In: *arXiv e-prints*. arXiv: [1211.0310 \[astro-ph.CO\]](#).
- LSST Science Collaboration et al. (2009). “LSST Science Book, Version 2.0”. In: *arXiv e-prints*. arXiv: [0912.0201 \[astro-ph.IM\]](#).
- Lumsden, S. L. et al. (1992). “The Edinburgh-Durham Southern Galaxy Catalogue. IV - The Cluster Catalogue”. In: *MNRAS* 258, pp. 1–22. DOI: [10.1093/mnras/258.1.1](#).
- Maddox, S. J. et al. (1990). “The APM galaxy survey. I - APM measurements and star-galaxy separation”. In: *MNRAS* 243, pp. 692–712.
- Mana, Annalisa et al. (2013). “Combining clustering and abundances of galaxy clusters to test cosmology and primordial non-Gaussianity”. In: *MNRAS* 434.1, pp. 684–695. DOI: [10.1093/mnras/stt1062](#). arXiv: [1303.0287 \[astro-ph.CO\]](#).
- Markevitch, M. (1998). “The L_X -T Relation and Temperature Function for Nearby Clusters Revisited”. In: *ApJ* 504, pp. 27–34. DOI: [10.1086/306080](#). eprint: [astro-ph/9802059](#).
- Maughan, B. J. et al. (2012). “Self-similar scaling and evolution in the galaxy cluster X-ray luminosity-temperature relation”. In: *MNRAS* 421, pp. 1583–1602. DOI: [10.1111/j.1365-2966.2012.20419.x](#). arXiv: [1108.1200 \[astro-ph.CO\]](#).
- Melin, J. B., J. G. Bartlett, and J. Delabrouille (2006). “Catalog extraction in SZ cluster surveys: a matched filter approach”. In: *A&A* 459, pp. 341–352. DOI: [10.1051/0004-6361:20065034](#). arXiv: [astro-ph/0602424 \[astro-ph\]](#).
- Melin, J. B. et al. (2012). “A comparison of algorithms for the construction of SZ cluster catalogues”. In: *A&A* 548, A51, A51. DOI: [10.1051/0004-6361/201015689](#). arXiv: [1210.1416 \[astro-ph.CO\]](#).
- Mighell, K. J. (1999). “CCD Aperture Photometry”. In: *Precision CCD Photometry*. Ed. by E. R. Craine, D. L. Crawford, and R. A. Tucker. Vol. 189. Astronomical Society of the Pacific Conference Series, p. 50.
- Mo, H. J. and S. D. M. White (1996). “An analytic model for the spatial clustering of dark matter haloes”. In: *MNRAS* 282, pp. 347–361. DOI: [10.1093/mnras/282.2.347](#). eprint: [astro-ph/9512127](#).
- Moscardini, L. et al. (2000). “The correlation function of X-ray galaxy clusters in the ROSAT All-Sky Survey 1 Bright Sample”. In: *MNRAS* 314, pp. 647–656. DOI: [10.1046/j.1365-8711.2000.03372.x](#). eprint: [astro-ph/9904282](#).
- Murray, S. G., C. Power, and A. S. G. Robotham (2013). “HMFcalc: An online tool for calculating dark matter halo mass functions”. In: *Astronomy and*

- Computing* 3, pp. 23–34. DOI: [10.1016/j.ascom.2013.11.001](https://doi.org/10.1016/j.ascom.2013.11.001). arXiv: [1306.6721](https://arxiv.org/abs/1306.6721) [[astro-ph.C0](#)].
- Nichol, R. C. et al. (1992). “The Edinburgh-Durham Southern Galaxy Catalogue. V - The cluster correlation function”. In: *MNRAS* 255, 21P–24P. DOI: [10.1093/mnras/255.1.21P](https://doi.org/10.1093/mnras/255.1.21P).
- Norberg, P. et al. (2002). “The 2dF Galaxy Redshift Survey: the dependence of galaxy clustering on luminosity and spectral type”. In: *MNRAS* 332, pp. 827–838. DOI: [10.1046/j.1365-8711.2002.05348.x](https://doi.org/10.1046/j.1365-8711.2002.05348.x). eprint: [astro-ph/0112043](https://arxiv.org/abs/astro-ph/0112043).
- Norberg, P. et al. (2009). “Statistical analysis of galaxy surveys - I. Robust error estimation for two-point clustering statistics”. In: *MNRAS* 396, pp. 19–38. DOI: [10.1111/j.1365-2966.2009.14389.x](https://doi.org/10.1111/j.1365-2966.2009.14389.x). arXiv: [0810.1885](https://arxiv.org/abs/0810.1885) [[astro-ph](#)].
- Olsen, L. F. et al. (1999). “ESO imaging survey. II. Searching for distant clusters of galaxies”. In: *A&A* 345, pp. 681–690. eprint: [astro-ph/9803338](https://arxiv.org/abs/astro-ph/9803338).
- O’Raifeartaigh, Cormac et al. (2018). “One hundred years of the cosmological constant: from “superfluous stunt” to dark energy”. In: *European Physical Journal H* 43.1. DOI: [10.1140/epjh/e2017-80061-7](https://doi.org/10.1140/epjh/e2017-80061-7). arXiv: [1711.06890](https://arxiv.org/abs/1711.06890) [[physics.hist-ph](#)].
- Padmanabhan, N. et al. (2012). “A 2 per cent distance to $z = 0.35$ by reconstructing baryon acoustic oscillations - I. Methods and application to the Sloan Digital Sky Survey”. In: *MNRAS* 427, pp. 2132–2145. DOI: [10.1111/j.1365-2966.2012.21888.x](https://doi.org/10.1111/j.1365-2966.2012.21888.x). arXiv: [1202.0090](https://arxiv.org/abs/1202.0090).
- Park, C. and S. Lee (1998). “Correlation Functions of the APM Clusters of Galaxies”. In: *Journal of Korean Astronomical Society* 31, pp. 105–108. eprint: [astro-ph/9809372](https://arxiv.org/abs/astro-ph/9809372).
- Peacock, J. A. and M. J. West (1992). “The power spectrum of Abell cluster correlations”. In: *MNRAS* 259, pp. 494–504. DOI: [10.1093/mnras/259.3.494](https://doi.org/10.1093/mnras/259.3.494).
- Peacock, John A. et al. (2001). “A measurement of the cosmological mass density from clustering in the 2dF Galaxy Redshift Survey”. In: *Nature* 410, pp. 169–173. arXiv: [astro-ph/0103143](https://arxiv.org/abs/astro-ph/0103143) [[astro-ph](#)].
- Peebles, P. J. E. (1980). *The large-scale structure of the universe*.
- (1986). “The mean mass density of the Universe”. In: *Nature* 321, pp. 27–32. DOI: [10.1038/321027a0](https://doi.org/10.1038/321027a0).
- Peebles, P. J. E. and M. G. Hauser (1974). “Statistical Analysis of Catalogs of Extragalactic Objects. III. The Shane-Wirtanen and Zwicky Catalogs”. In: *ApJS* 28, p. 19. DOI: [10.1086/190308](https://doi.org/10.1086/190308).
- Penzias, A. A. and R. W. Wilson (1965). “A Measurement of Excess Antenna Temperature at 4080 Mc/s.”. In: *ApJ* 142, pp. 419–421. DOI: [10.1086/148307](https://doi.org/10.1086/148307).
- Perlman, Eric S. et al. (2002). “The WARPS Survey. VI. Galaxy Cluster and Source Identifications from Phase I”. In: *The Astrophysical Journal Supplement Series* 140, pp. 265–301. DOI: [10.1086/339685](https://doi.org/10.1086/339685). arXiv: [astro-ph/0112190](https://arxiv.org/abs/astro-ph/0112190) [[astro-ph](#)].
- Perlmutter, S. and B. P. Schmidt (2003). “Measuring Cosmology with Supernovae”. In: *Supernovae and Gamma-Ray Bursters. Edited by K. Weiler, Lecture*

- Notes in Physics*, vol. 598, p.195-217. Ed. by K. Weiler, pp. 195–217. DOI: [10.1007/3-540-45863-8_11](#).
- Perlmutter, S. et al. (1999). “Measurements of Ω and Λ from 42 High-Redshift Supernovae”. In: *ApJ* 517, pp. 565–586. DOI: [10.1086/307221](#). eprint: [astro-ph/9812133](#).
- Piffaretti, R. et al. (2011). “The MCXC: a meta-catalogue of x-ray detected clusters of galaxies”. In: *A&A* 534, A109, A109. DOI: [10.1051/0004-6361/201015377](#). arXiv: [1007.1916 \[astro-ph.CO\]](#).
- Planck Collaboration et al. (2011a). “Planck early results. I. The Planck mission”. In: *A&A* 536, A1, A1. DOI: [10.1051/0004-6361/201116464](#). arXiv: [1101.2022 \[astro-ph.IM\]](#).
- Planck Collaboration et al. (2011b). “Planck early results. X. Statistical analysis of Sunyaev-Zeldovich scaling relations for X-ray galaxy clusters”. In: *A&A* 536, A10, A10. DOI: [10.1051/0004-6361/201116457](#). arXiv: [1101.2043 \[astro-ph.CO\]](#).
- Planck Collaboration et al. (2011c). “Planck early results. XI. Calibration of the local galaxy cluster Sunyaev-Zeldovich scaling relations”. In: *A&A* 536, A11, A11. DOI: [10.1051/0004-6361/201116458](#). arXiv: [1101.2026 \[astro-ph.CO\]](#).
- Planck Collaboration et al. (2013). “Planck intermediate results. X. Physics of the hot gas in the Coma cluster”. In: *A&A* 554, A140, A140. DOI: [10.1051/0004-6361/201220247](#). arXiv: [1208.3611 \[astro-ph.CO\]](#).
- Planck Collaboration et al. (2014a). “Planck 2013 results. XVI. Cosmological parameters”. In: *A&A* 571, A16, A16. DOI: [10.1051/0004-6361/201321591](#). arXiv: [1303.5076](#).
- (2014b). “Planck 2013 results. XX. Cosmology from Sunyaev-Zeldovich cluster counts”. In: *A&A* 571, A20, A20. DOI: [10.1051/0004-6361/201321521](#). arXiv: [1303.5080](#).
- Planck Collaboration et al. (2014c). “Planck 2013 results. XXIX. The Planck catalogue of Sunyaev-Zeldovich sources”. In: *A&A* 571, A29, A29. DOI: [10.1051/0004-6361/201321523](#). arXiv: [1303.5089 \[astro-ph.CO\]](#).
- Planck Collaboration et al. (2015). “Planck 2013 results. XXXII. The updated Planck catalogue of Sunyaev-Zeldovich sources”. In: *A&A* 581, A14, A14. DOI: [10.1051/0004-6361/201525787](#). arXiv: [1502.00543](#).
- Planck Collaboration et al. (2016a). “Planck 2015 results. I. Overview of products and scientific results”. In: *A&A* 594, A1, A1. DOI: [10.1051/0004-6361/201527101](#). arXiv: [1502.01582](#).
- Planck Collaboration et al. (2016b). “Planck 2015 results. XIII. Cosmological parameters”. In: *A&A* 594, A13, A13. DOI: [10.1051/0004-6361/201525830](#). arXiv: [1502.01589](#).
- (2016c). “Planck 2015 results. XXIV. Cosmology from Sunyaev-Zeldovich cluster counts”. In: *A&A* 594, A24, A24. DOI: [10.1051/0004-6361/201525833](#). arXiv: [1502.01597](#).
- Planck Collaboration et al. (2016d). “Planck 2015 results. XXVII. The second Planck catalogue of Sunyaev-Zeldovich sources”. In: *A&A* 594, A27, A27. DOI: [10.1051/0004-6361/201525823](#). arXiv: [1502.01598 \[astro-ph.CO\]](#).

- Planck Collaboration et al. (2018a). “Planck 2018 results. I. Overview and the cosmological legacy of Planck”. In: *arXiv e-prints*. arXiv: [1807.06205](#).
- Planck Collaboration et al. (2018b). “Planck 2018 results. VI. Cosmological parameters”. In: *arXiv e-prints*. arXiv: [1807.06209](#).
- Planck Collaboration et al. (2018c). “Planck 2018 results. X. Constraints on inflation”. In: *arXiv e-prints*. arXiv: [1807.06211](#).
- Planck Collaboration, et al. (2016). “Planck 2015 results. XI. CMB power spectra, likelihoods, and robustness of parameters”. In: *Astron. Astrophys.* 594, A11. DOI: [10.1051/0004-6361/201526926](#). arXiv: [1507.02704 \[astro-ph.CO\]](#).
- Pons-Bordería, M.-J. et al. (1999). “Comparing Estimators of the Galaxy Correlation Function”. In: *ApJ* 523, pp. 480–491. DOI: [10.1086/307754](#). eprint: [astro-ph/9906344](#).
- Postman, M., M. J. Geller, and J. P. Huchra (1986). “The cluster-cluster correlation function”. In: *AJ* 91, pp. 1267–1273. DOI: [10.1086/114101](#).
- Postman, Marc et al. (1996). “The Palomar Distant Clusters Survey. I. The Cluster Catalog”. In: *AJ* 111, p. 615. DOI: [10.1086/117811](#). arXiv: [astro-ph/9511011 \[astro-ph\]](#).
- Press, W. H. and P. Schechter (1974). “Formation of Galaxies and Clusters of Galaxies by Self-Similar Gravitational Condensation”. In: *ApJ* 187, pp. 425–438. DOI: [10.1086/152650](#).
- Puddu, E. et al. (2001). “Photometric validation of a model independent procedure to extract galaxy clusters”. In: *A&A* 379, pp. 426–435. DOI: [10.1051/0004-6361:20011316](#). eprint: [astro-ph/0110321](#).
- Quenouille, M. H. (1956). “Notes on Bias in Estimation”. In: *Biometrika* 43.3/4, pp. 353–360. ISSN: 00063444. URL: <http://www.jstor.org/stable/2332914>.
- Ramella, M. et al. (2002). “The UZC-SSRS2 Group Catalog”. In: *AJ* 123, pp. 2976–2984. DOI: [10.1086/340357](#). eprint: [astro-ph/0202326](#).
- Reichardt, C. L. et al. (2013). “Galaxy Clusters Discovered via the Sunyaev-Zel’dovich Effect in the First 720 Square Degrees of the South Pole Telescope Survey”. In: *ApJ* 763, 127, p. 127. DOI: [10.1088/0004-637X/763/2/127](#). arXiv: [1203.5775](#).
- Reid, B. A. et al. (2012). “The clustering of galaxies in the SDSS-III Baryon Oscillation Spectroscopic Survey: measurements of the growth of structure and expansion rate at $z = 0.57$ from anisotropic clustering”. In: *MNRAS* 426, pp. 2719–2737. DOI: [10.1111/j.1365-2966.2012.21779.x](#). arXiv: [1203.6641](#).
- Reiprich, T. H. and H. Böhringer (2002). “The Mass Function of an X-Ray Flux-limited Sample of Galaxy Clusters”. In: *ApJ* 567, pp. 716–740. DOI: [10.1086/338753](#). eprint: [astro-ph/0111285](#).
- Rhodes, Jason et al. (2017). “Scientific Synergy between LSST and Euclid”. In: *ApJS* 233.2, 21, p. 21. DOI: [10.3847/1538-4365/aa96b0](#). arXiv: [1710.08489 \[astro-ph.IM\]](#).
- Riess, A. G. et al. (1998). “Observational Evidence from Supernovae for an Accelerating Universe and a Cosmological Constant”. In: *AJ* 116, pp. 1009–1038. DOI: [10.1086/300499](#). eprint: [astro-ph/9805201](#).

- Riess, Adam G. et al. (2016). “A 2.4% Determination of the Local Value of the Hubble Constant”. In: *ApJ* 826, 56, p. 56. DOI: [10.3847/0004-637X/826/1/56](#). arXiv: [1604.01424 \[astro-ph.CO\]](#).
- Riess, Adam G. et al. (2018). “Milky Way Cepheid Standards for Measuring Cosmic Distances and Application to Gaia DR2: Implications for the Hubble Constant”. In: *ApJ* 861.2, 126, p. 126. DOI: [10.3847/1538-4357/aac82e](#). arXiv: [1804.10655 \[astro-ph.CO\]](#).
- Romer, A. K. et al. (2000). “The Bright SHARC Survey: The Cluster Catalog”. In: *The Astrophysical Journal Supplement Series* 126, pp. 209–269. DOI: [10.1086/313302](#). arXiv: [astro-ph/9907401 \[astro-ph\]](#).
- Rosati, P. et al. (1995). “A first determination of the surface density of galaxy clusters at very low x-ray fluxes”. In: *ApJ* 445, pp. L11–L14. DOI: [10.1086/187877](#). eprint: [astro-ph/9503064](#).
- Rosati, P., S. Borgani, and C. Norman (2002). “The Evolution of X-ray Clusters of Galaxies”. In: *ARA&A* 40, pp. 539–577. DOI: [10.1146/annurev.astro.40.120401.150547](#). eprint: [astro-ph/0209035](#).
- Ross, Ashley J. et al. (2015). “The clustering of the SDSS DR7 main Galaxy sample - I. A 4 per cent distance measure at $z = 0.15$ ”. In: *MNRAS* 449.1, pp. 835–847. DOI: [10.1093/mnras/stv154](#). arXiv: [1409.3242 \[astro-ph.CO\]](#).
- Rowe, B. T. P. et al. (2015). “GALSIM: The modular galaxy image simulation toolkit”. In: *Astronomy and Computing* 10, pp. 121–150. DOI: [10.1016/j.ascom.2015.02.002](#). arXiv: [1407.7676 \[astro-ph.IM\]](#).
- Rozo, E. et al. (2015). “redMaPPer - III. A detailed comparison of the Planck 2013 and SDSS DR8 redMaPPer cluster catalogues”. In: *MNRAS* 450, pp. 592–605. DOI: [10.1093/mnras/stv605](#). arXiv: [1401.7716](#).
- Rykoff, E. S. et al. (2014). “redMaPPer. I. Algorithm and SDSS DR8 Catalog”. In: *ApJ* 785, 104, p. 104. DOI: [10.1088/0004-637X/785/2/104](#). arXiv: [1303.3562](#).
- Sachs, R. K. and A. M. Wolfe (1967). “Perturbations of a Cosmological Model and Angular Variations of the Microwave Background”. In: *ApJ* 147, p. 73. DOI: [10.1086/148982](#).
- Said, Najla et al. (2013). “New constraints on the dark energy equation of state”. In: *Phys. Rev. D* 88, 043515, p. 043515. DOI: [10.1103/PhysRevD.88.043515](#). arXiv: [1303.4353 \[astro-ph.CO\]](#).
- Sartoris, B. et al. (2016). “Next generation cosmology: constraints from the Euclid galaxy cluster survey”. In: *MNRAS* 459, pp. 1764–1780. DOI: [10.1093/mnras/stw630](#). arXiv: [1505.02165 \[astro-ph.CO\]](#).
- Scolnic, D. M. et al. (2018). “The Complete Light-curve Sample of Spectroscopically Confirmed SNe Ia from Pan-STARRS1 and Cosmological Constraints from the Combined Pantheon Sample”. In: *ApJ* 859.2, 101, p. 101. DOI: [10.3847/1538-4357/aab9bb](#). arXiv: [1710.00845 \[astro-ph.CO\]](#).
- Serjeant, S. (2010). *Observational Cosmology*.
- Shane, C. D. and C. A. Wirtanen (1967). In: *Pub. Lick Obs.* 22.
- Shectman, S. A. (1985). “Clusters of galaxies from the Shane-Wirtanen counts”. In: *ApJS* 57, pp. 77–90. DOI: [10.1086/190996](#).

- Sheth, R. K., H. J. Mo, and G. Tormen (2001). “Ellipsoidal collapse and an improved model for the number and spatial distribution of dark matter haloes”. In: *MNRAS* 323, pp. 1–12. DOI: [10.1046/j.1365-8711.2001.04006.x](#). eprint: [astro-ph/9907024](#).
- Slipher, V. M. (1913). “The radial velocity of the Andromeda Nebula”. In: *Lowell Observatory Bulletin* 2, pp. 56–57.
- Smoot, G. F. et al. (1992). “Structure in the COBE differential microwave radiometer first-year maps”. In: *ApJ* 396, pp. L1–L5. DOI: [10.1086/186504](#).
- Spergel, D. et al. (2015). “Wide-Field Infrared Survey Telescope-Astrophysics Focused Telescope Assets WFIRST-AFTA 2015 Report”. In: *arXiv e-prints*, arXiv:1503.03757, arXiv:1503.03757. arXiv: [1503.03757 \[astro-ph.IM\]](#).
- Spergel, D. N. (2005). “The Cosmic Microwave Background as a Cosmological Probe”. In: *The Cool Universe: Observing Cosmic Dawn*. Ed. by C. Lidman and D. Alloin. Vol. 344. Astronomical Society of the Pacific Conference Series, p. 29.
- Springel, Volker et al. (2005). “Simulations of the formation, evolution and clustering of galaxies and quasars”. In: *Nature* 435, pp. 629–636. DOI: [10.1038/nature03597](#). arXiv: [astro-ph/0504097 \[astro-ph\]](#).
- Sridhar, Srivatsan et al. (2017). “Evolution of the real-space correlation function from next generation cluster surveys. Recovering the real-space correlation function from photometric redshifts”. In: *A&A* 600, A32, A32. DOI: [10.1051/0004-6361/201629369](#). arXiv: [1612.02821 \[astro-ph.CO\]](#).
- Staniszewski, Z. et al. (2009). “Galaxy Clusters Discovered with a Sunyaev-Zel’dovich Effect Survey”. In: *ApJ* 701, pp. 32–41. DOI: [10.1088/0004-637X/701/1/32](#). arXiv: [0810.1578 \[astro-ph\]](#).
- Szapudi, I. and A. S. Szalay (1998). “A New Class of Estimators for the N-Point Correlations”. In: *ApJ* 494, pp. L41–L44. DOI: [10.1086/311146](#).
- The Dark Energy Survey Collaboration (2005). “The Dark Energy Survey”. In: *arXiv e-prints*, astro-ph/0510346, astro-ph/0510346. arXiv: [astro-ph/0510346 \[astro-ph\]](#).
- The Planck Collaboration (2006). “The Scientific Programme of Planck”. In: *arXiv Astrophysics e-prints*. eprint: [astro-ph/0604069](#).
- Tinker, Jeremy et al. (2008). “Toward a Halo Mass Function for Precision Cosmology: The Limits of Universality”. In: *ApJ* 688, pp. 709–728. DOI: [10.1086/591439](#). arXiv: [0803.2706 \[astro-ph\]](#).
- Tinker, Jeremy L. et al. (2005). “On the Mass-to-Light Ratio of Large-Scale Structure”. In: *ApJ* 631.1, pp. 41–58. DOI: [10.1086/432084](#). arXiv: [astro-ph/0411777 \[astro-ph\]](#).
- Totsuji, H. and T. Kihara (1969). “The Correlation Function for the Distribution of Galaxies”. In: *Publications of the Astronomical Society of Japan* 21, p. 221.
- Trujillo, I., A. W. Graham, and N. Caon (2001). “On the estimation of galaxy structural parameters: the Sérsic model”. In: *MNRAS* 326, pp. 869–876. DOI: [10.1046/j.1365-8711.2001.04471.x](#). eprint: [astro-ph/0102393](#).
- Tucker, D. L. et al. (2001). “VizieR Online Data Catalog: LCRS loose groups of galaxies (Tucker+, 2000)”. In: *VizieR Online Data Catalog* 213.

- Tukey, John W. (1958). "Abstracts of Papers". In: *Ann. Math. Statist.* 29.2, pp. 614–623. DOI: [10.1214/aoms/1177706647](https://doi.org/10.1214/aoms/1177706647). URL: <https://doi.org/10.1214/aoms/1177706647>.
- Tully, R. Brent et al. (2014). "The Laniakea supercluster of galaxies". In: *Nature* 513.7516, pp. 71–73. DOI: [10.1038/nature13674](https://doi.org/10.1038/nature13674). arXiv: [1409.0880](https://arxiv.org/abs/1409.0880) [astro-ph.CO].
- Vázquez, J. A., L. E. Padilla, and T. Matos (2018). "Inflationary Cosmology: From Theory to Observations". In: *arXiv e-prints*. arXiv: [1810.09934](https://arxiv.org/abs/1810.09934).
- Vikhlinin, A. et al. (2006). "Chandra Sample of Nearby Relaxed Galaxy Clusters: Mass, Gas Fraction, and Mass-Temperature Relation". In: *ApJ* 640, pp. 691–709. DOI: [10.1086/500288](https://doi.org/10.1086/500288). arXiv: [astro-ph/0507092](https://arxiv.org/abs/astro-ph/0507092) [astro-ph].
- Voges, W. et al. (1999). "The ROSAT all-sky survey bright source catalogue". In: *A&A* 349, pp. 389–405. eprint: [astro-ph/9909315](https://arxiv.org/abs/astro-ph/9909315).
- Watson, Douglas F., Andreas A. Berlind, and Andrew R. Zentner (2011). "A Cosmic Coincidence: The Power-law Galaxy Correlation Function". In: *ApJ* 738, 22, p. 22. DOI: [10.1088/0004-637X/738/1/22](https://doi.org/10.1088/0004-637X/738/1/22). arXiv: [1101.5155](https://arxiv.org/abs/1101.5155) [astro-ph.CO].
- Weinberg, David H. et al. (2013). "Observational probes of cosmic acceleration". In: *Physics Reports* 530, pp. 87–255. DOI: [10.1016/j.physrep.2013.05.001](https://doi.org/10.1016/j.physrep.2013.05.001). arXiv: [1201.2434](https://arxiv.org/abs/1201.2434) [astro-ph.CO].
- Wells, D. C., E. W. Greisen, and R. H. Harten (1981). "FITS - a Flexible Image Transport System". In: *A&AS* 44, p. 363.
- Wen, Z. L., J. L. Han, and F. S. Liu (2009). "Galaxy Clusters Identified from the SDSS DR6 and Their Properties". In: *ApJS* 183, pp. 197–213. DOI: [10.1088/0067-0049/183/2/197](https://doi.org/10.1088/0067-0049/183/2/197). arXiv: [0906.0803](https://arxiv.org/abs/0906.0803).
- Wright, T. (1750). "An Original Theory or New Hypothesis of the Universe". In: *An Original Theory or New Hypothesis of the Universe, London, Printed for the author by H. Chapelle*.
- Xu, X. et al. (2012). "A 2 per cent distance to $z = 0.35$ by reconstructing baryon acoustic oscillations - II. Fitting techniques". In: *MNRAS* 427, pp. 2146–2167. DOI: [10.1111/j.1365-2966.2012.21573.x](https://doi.org/10.1111/j.1365-2966.2012.21573.x). arXiv: [1202.0091](https://arxiv.org/abs/1202.0091).
- York, D. G. et al. (2000). "The Sloan Digital Sky Survey: Technical Summary". In: *AJ* 120, pp. 1579–1587. DOI: [10.1086/301513](https://doi.org/10.1086/301513). eprint: [astro-ph/0006396](https://arxiv.org/abs/astro-ph/0006396).
- Zentner, A. R. (2007). "The Excursion Set Theory of Halo Mass Functions, Halo Clustering, and Halo Growth". In: *International Journal of Modern Physics D* 16, pp. 763–815. DOI: [10.1142/S0218271807010511](https://doi.org/10.1142/S0218271807010511). eprint: [astro-ph/0611454](https://arxiv.org/abs/astro-ph/0611454).
- Zhang, Y. Y. et al. (2007). "Scaling relations and mass calibration of the X-ray luminous galaxy clusters at redshift ~ 0.2 : XMM-Newton observations". In: *A&A* 467, pp. 437–457. DOI: [10.1051/0004-6361:20066567](https://doi.org/10.1051/0004-6361:20066567). arXiv: [astro-ph/0702739](https://arxiv.org/abs/astro-ph/0702739) [astro-ph].
- Zheng, Zheng et al. (2002). "Do Distinct Cosmological Models Predict Degenerate Halo Populations?". In: *The Astrophysical Journal* 575.2, pp. 617–633. DOI: [10.1086/341434](https://doi.org/10.1086/341434). URL: <https://doi.org/10.1086%2F341434>.
- Zwicky, F. (1933). "Die Rotverschiebung von extragalaktischen Nebeln". In: *Helvetica Physica Acta* 6, pp. 110–127.

Zwicky, F. et al. (1961–1968). *Catalogue of galaxies and of clusters of galaxies*, Vol. I–VI.